

DEVELOPMENT
OF PIXEL DETECTORS
FOR THE INNER TRACKER UPGRADE
OF THE ATLAS EXPERIMENT

DISSERTATION BY NATASCHA SAVIĆ



DEVELOPMENT
OF PIXEL DETECTORS
FOR THE INNER TRACKER UPGRADE
OF THE ATLAS EXPERIMENT

Dissertation
an der Fakultät für Physik
der
Ludwig–Maximilians–Universität München

vorgelegt von
Natascha Savić
geboren in Tuzla, Bosnien und Herzegowina

München, den 20.12.2017



DISSERTATION

submitted to the Faculty of Physics of the
Ludwig–Maximilians–Universität München

by Natascha Savić

1st Referee: Priv. Doz. Dr. Richard Nisius

2nd Referee: Prof. Dr. Otmar Biebel

Date of submission: 20.12.2017

Date of oral examination: 02.03.2018

ZUSAMMENFASSUNG

Der “High Luminosity Large Hadron Collider” (HL-LHC) erweitert die Möglichkeiten für Entdeckungen und Präzisionsmessungen in der Teilchenphysik. Dieses Programm wird durch Fortschritte in Beschleuniger- und Detektortechnologien ermöglicht. Der LHC-Beschleunigerkomplex wird bis 2025 sukzessiv ausgebaut. Um die experimentellen Herausforderungen der erhöhten Luminosität von bis zu einem Faktor 7 in Bezug auf den Designwert des LHC, $10^{34} \text{cm}^{-2} \text{s}^{-1}$ zu erfüllen, wird das Spurendetektorsystem des ATLAS-Experiment vollständig ersetzt werden, um die Leistungsfähigkeit des vorliegenden Detektors aufrechtzuerhalten und zu verbessern.

Aufgrund des reduzierten Materialbudgets und der effizienten Ladungssammlung sowie hoher Nachweiseffizienz für geladene Teilchen sind dünne n^+ -in-p-planare Pixelmodule vielversprechende Kandidaten, um das neue Pixelsystem auszustatten.

Im Mittelpunkt dieser Arbeit stehen Pixelmodule, die mit $100 \mu\text{m}$ und $150 \mu\text{m}$ dicken Sensoren bestückt sind. Sie werden mithilfe von verschiedenen Untersuchungsmethoden charakterisiert. Insbesondere werden die Ladungssammlungs- und Pixeleffizienz vor und nach der Bestrahlung bis zum erwarteten maximalen Fluenzbereich im HL-LHC von $10^{16} \text{n}_{\text{eq}} \text{cm}^{-2}$ untersucht. Zusätzlich wird die Methode des transienten Stroms verwendet, um die Ladungssammlung und elektrische Feldeigenschaften als Funktion der Sensortiefe in $100 \mu\text{m}$ und $150 \mu\text{m}$ dicken Sensoren zu untersuchen. Im Zuge der Arbeit wird eine Studie über die Auswirkung unterschiedlicher Integrationen von Testmöglichkeiten in das Design, die IV-Messungen der Sensoren vor der Verbindung mit dem Auslesechip ermöglichen, durchgeführt. Angesichts der Tatsache, dass diese Strukturen eine Verringerung der Pixeleffizienz nach der Bestrahlung verursachen, wird die beste technologische Lösung mit Strahltestkampagnen untersucht.

Um auch bei hoher Teilchenmultiplizität des HL-LHC die aktuelle Okkupanz des Pixeldetektors nicht zu überschreiten, wurde in der ATLAS Kollaboration ein neuer Auslese-Chip mit einer Zellengröße von $50 \times 50 \mu\text{m}^2$ entwickelt, was zu einer höheren Granularität im Vergleich zur vorliegenden Chipzellengröße von $50 \times 250 \mu\text{m}^2$ führt. Sensoren, die mit dem aktuellen Auslese-Chip kompatibel sind, jedoch in kleinere Pixelzellen mit einer Größe von $50 \times 50 \mu\text{m}^2$ unterteilt sind, wurden entworfen und charakterisiert. Dadurch ist es möglich, erste Vorhersagen über die Leistung von kleinen Pixelzellen in der HL-LHC-Umgebung zu treffen.

ABSTRACT

The High Luminosity Large Hadron Collider (HL-LHC) project will extend the discovery reach and the capability for precision measurements in particle physics. Its program is enabled by advances in accelerator and detector technology. The LHC accelerator complex will undergo successive upgrades until 2025. To meet the experimental challenges of the increased instantaneous luminosity of up to a factor 7 with respect to the design value, $10^{34} \text{cm}^{-2} \text{s}^{-1}$, the ATLAS experiment will undergo a replacement of the tracker system to sustain and improve the performance of the present detector.

Due to the reduced material budget and the high charge collection and tracking efficiency, thin n^+ -in-p planar pixel modules are promising candidates to instrument parts of the new pixel system. Pixel modules assembled with $100 \mu\text{m}$ and $150 \mu\text{m}$ thick sensors are the focus of this thesis. They are characterised exploiting different methodologies. In particular, the charge collection and hit efficiencies are studied before and after irradiation up to the expected maximum fluence range in the HL-LHC of $10^{16} \text{n}_{\text{eq}} \text{cm}^{-2}$. Additionally, the transient current technique is used to investigate charge collection and electric field properties within the sensor depth of $100 \mu\text{m}$ and $150 \mu\text{m}$ thick sensors.

In the course of this thesis, a study is performed on the effect of different geometries of the biasing structures, necessary to perform IV measurements of the sensors before the interconnection to the readout chip. Given the fact that these structures cause a decrease of the hit efficiency after irradiation, the best technological solutions are investigated with beam test campaigns.

To maintain the present level of occupancy also at the high particle multiplicity of the HL-LHC, a new readout chip was developed with a chip cell size of $50 \times 50 \mu\text{m}^2$, resulting in a higher granularity with respect to the present chip cell size of $50 \times 250 \mu\text{m}^2$. Sensors compatible with the current readout chip but subdivided into smaller pixel cells of $50 \times 50 \mu\text{m}^2$ size were designed and are characterised to make first predictions for the performance of small pixel cells in the HL-LHC environment.

TABLE OF CONTENTS

1	The Large Hadron Collider and the ATLAS experiment	3
1.1	The LHC complex and performance	4
1.2	The ATLAS experiment	5
1.3	Accelerator and detector upgrade	9
1.3.1	Physics motivation	9
1.3.2	Accelerator upgrade	10
1.3.3	ATLAS upgrade	11
2	Theory of silicon particle detectors	13
2.1	Working principle	13
2.2	Properties of silicon used as a detector for charged particles	14
2.2.1	Doping	14
2.2.2	P-n junction	15
2.2.3	Depletion voltage and leakage current	16
2.2.4	Charge generation	17
2.2.5	Formation of electrical signal	19
2.3	Radiation damage in silicon	20
2.3.1	Impact of defects on silicon properties	21
2.3.2	Annealing of defects	23
2.4	Pixel detectors in particle physics	24
2.4.1	Pixel sensors	25
3	The ATLAS pixel detector	29
3.1	Present pixel detector	29
3.1.1	ATLAS readout chips	30
3.1.2	ATLAS pixel sensors	32

3.2	The ITk pixel detector	34
3.2.1	RD53A ATLAS readout chip	36
3.2.2	Planar module concept for the upgraded detector	36
3.2.3	Pixel module concept for the upgraded detector	38
4	Sensor and module characterisation methodology	39
4.1	Irradiation facilities	39
4.1.1	TRIGA Mark II reactor of Jožef Stefan Institute	39
4.1.2	Compact Cyclotron at Karlsruhe Institute of Technology	40
4.1.3	Cyclotron at the University of Birmingham	41
4.1.4	CERN-PS irradiation facility	42
4.2	Methodology for sensor characterisation	43
4.2.1	IV measurements	43
4.2.2	Edge transient current technique	44
4.3	Methodology for module characterisation	50
4.3.1	Charge collection measurements	55
4.3.2	Beam test measurements with particle beams	56
5	Production and performance of thin planar n⁺-in-p pixel sensors	65
5.1	Production and processing	65
5.1.1	CiS productions	65
5.1.2	MPP/HLL productions	68
5.1.3	ADVACAM productions	70
5.1.4	Overview of the modules and the irradiations performed on them	72
5.2	Performance of thin sensors	75
5.2.1	IV characteristics	75
5.2.2	Charge collection	80
5.2.3	Electric field properties	97
5.2.4	Hit efficiency	97
5.2.5	Hit efficiency at the sensor edge	115
5.2.6	Hit efficiency and charge collection at high pseudorapidity	119
5.2.7	Power dissipation	123
6	Conclusions and outlook	125
	Acknowledgements	129
	List of figures	131
	List of tables	140
	Bibliography	141

OVERVIEW

Pixel modules based on the thin n^+ -in-p planar pixel module technology are investigated in terms of their performance in a high occupancy and high irradiation environment. Three main innovations provide the basis for the thin n-in-p module concept for the ATLAS upgrade: thin sensors, smaller pixel cell sizes and reduced inactive edges.

Chapter 1: The first chapter serves as an introduction to the LHC accelerator and the ATLAS experiment. The accelerator and detector upgrade are motivated and the three-stage upgrade plan is described. The experimental challenges and requirements are discussed.

Chapter 2: A theoretical background of silicon particle detectors is given, with a focus on general properties of semiconductors. In particular this chapter is focused on the damages induced in the silicon sensors after irradiation. Moreover, the main design concepts of pixel detectors are summarised.

Chapter 3: An introduction to the ATLAS pixel detector is given, presenting the present tracking system and the one foreseen for the HL-LHC upgrade.

Chapter 4: In this chapter, the characterization methodology at bare sensor and module level are discussed with a focus on beam test measurements and characterisation by the transient current technique. Furthermore, the irradiation facilities are presented.

Chapter 5: The production and performance of thin n^+ -in-p planar pixel modules is presented in this chapter. The most relevant properties of pixel detectors for particle detection are investigated, primarily in terms of charge collection and hit efficiency obtained by beam test studies and charge collection and electric field properties obtained by measurements with the transient current technique.

Chapter 6: The main results investigated for the presented pixel module concept are summarised along with an outlook to further developments for the ATLAS ITk pixel system.

THE LARGE HADRON COLLIDER AND THE ATLAS EXPERIMENT

Located at the border between Switzerland and France near the Swiss city of Geneva, the Large Hadron Collider (LHC) [1] at the Conseil Européen pour la Recherche Nucléaire (CERN)¹ is pushing the limits of human knowledge, and opening up a new window, which will potentially allow us a glimpse into physics beyond the Standard Model (SM). With a circumference of 27 km, the LHC is presently the largest and most powerful accelerator worldwide dedicated to research in high energy physics. It is situated 45 m to 170 m below ground in the same tunnel used for the Large Electron Positron collider (LEP). In the LHC, proton collisions with a center-of-mass energy of 14 TeV at a nominal luminosity of $10^{34}\text{cm}^{-2}\text{s}^{-1}$ and lead ion collisions with a center-of-mass energy of 1.15 PeV at a nominal luminosity of $10^{27}\text{cm}^{-2}\text{s}^{-1}$ are possibly resulting in a production of new and unknown particles. The main goals are to understand and investigate fundamental processes in nature and to quantify already known processes of existing theories. This knowledge is crucial to understand the fundamental structure of the universe. The LHC is a two-ring superconducting hadron accelerator, which keeps the two proton or lead ion beams in place and focuses them in order to collide in one of the four Interaction Points (IPs) dedicated for the hadron collisions. The four main experiments in the IPs are: **A Toroidal LHC Apparatus (ATLAS)** [2], **A Large Ion Collider Experiment (ALICE)** investigating the quark-gluon plasma in lead ion collisions [3], **Compact Muon Solenoid (CMS)** [4], **LHCb**, with b standing for bottom quarks. With the LHCb the charge conjugation and parity symmetry violation in the b-quark sector are investigated [5]. The ATLAS and CMS experiments are multipurpose detectors, which focus on the search for new physics obtained by proton-proton collisions. Their main goal is to search for new particles, as for example those predicted by the theory of Supersymmetry [6], and to increase the statistics for further investigations on the SM and Higgs-Mechanism, with the two detectors based on complementary technologies. This chapter is dedicated to the introduction to the LHC complex, with its accelerator systems in Section 1.1 and the ATLAS experiment in Section 1.2. In Section 1.3 the upgrade plans are presented for the accelerator complex as well as for the ATLAS experiment.

¹<http://cern.ch>

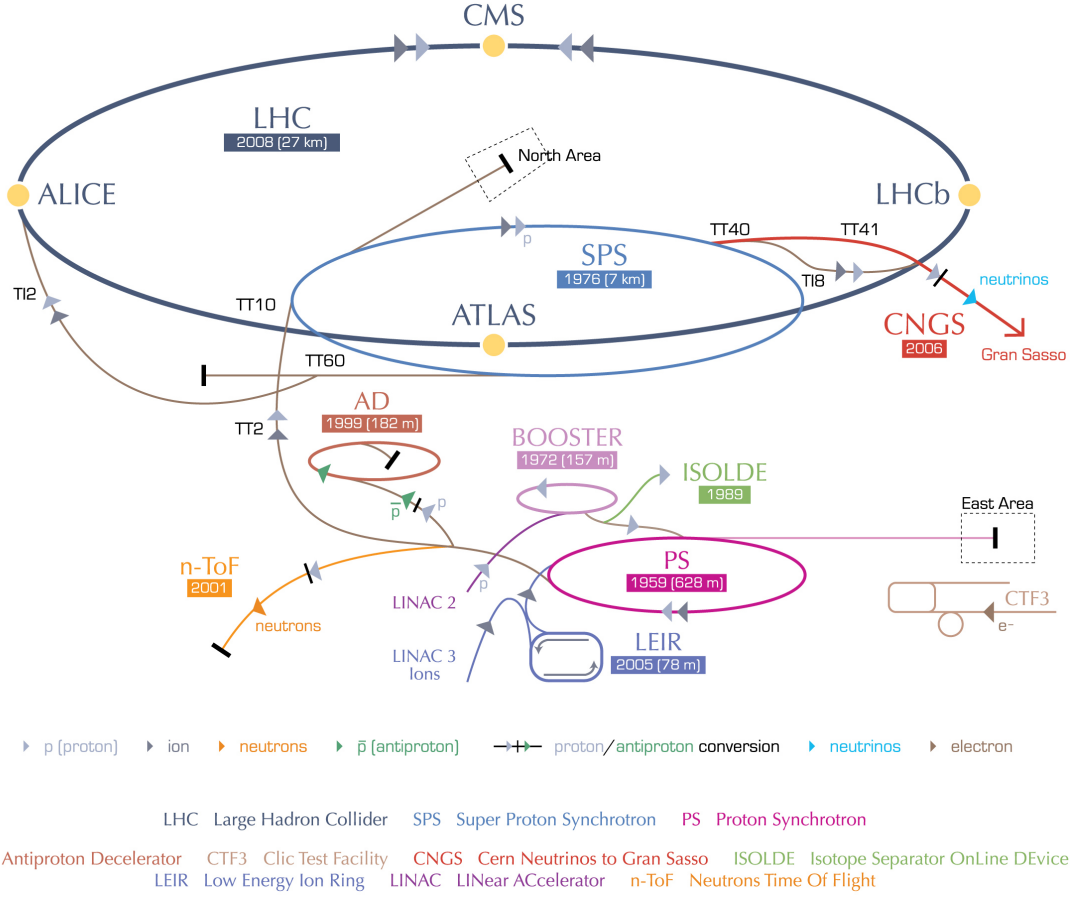


Figure 1.1: The LHC accelerator complex is composed of the LHC shown in black and smaller accelerators, which help boost the particles to their final energies. The image is taken from Ref. [7].

1.1 The LHC complex and performance

In the LHC complex the maximum center-of-mass energy of 14 TeV will be reached by various pre-accelerators starting from the Linear Accelerator 2 (LINCAC 2) up to the Super proton Synchrotron (SpS), boosting the energy of the particles from 50 MeV to higher levels of 450 GeV up to the injection into the LHC ring. The protons are extracted from an ionised hydrogen gas and then forwarded to the first accelerator LINAC 2 in the chain. An illustration of the LHC complex is given in Figure 1.1. Inside the LHC ring, the protons circulate in a two-ring structure in opposite directions until the desired collision energy is reached. A crucial parameter is the instantaneous luminosity, given by the beam intensity I per collision area A , that can be expressed in the following way, assuming the ideal case of identical round beams [8]:

$$\mathcal{L} = \frac{I}{A} = \frac{N_{e/s}}{\sigma_e} = \gamma \frac{N_b^2 n_b f_{rev}}{4\pi \epsilon_n \beta^*} R \quad , \quad R = 1/\sqrt{1 + \frac{\theta_c \sigma_z}{2\sigma}} \quad , \quad (1.1)$$

with $N_{e/s}$ as the number of events per second and σ_e the cross section of an event. Hence, the luminosity scales linearly with the number of events per second. The term γ is the Lorentz factor, N_b the number of particles per bunch and n_b the number of bunches per beam, which is for the

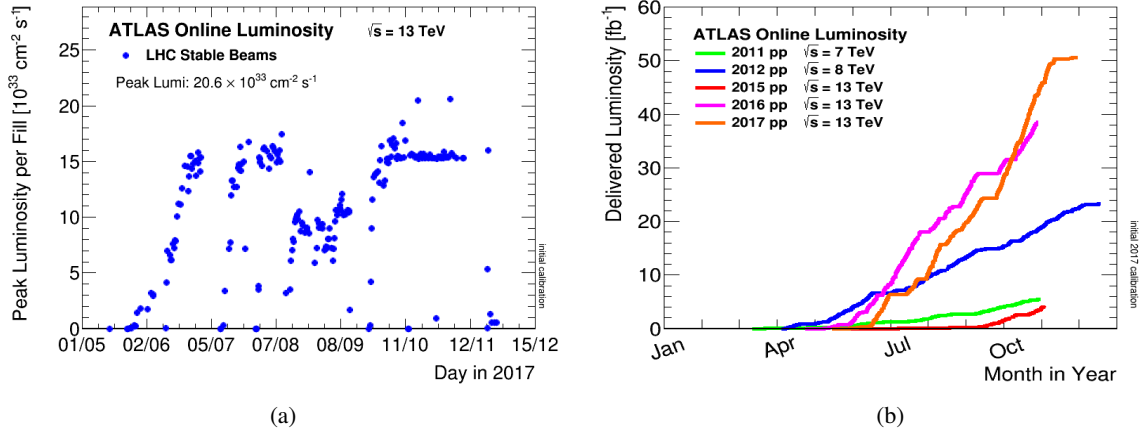


Figure 1.2: (a) peak instantaneous luminosity expressed in $10^{33} \text{ cm}^{-2} \text{ s}^{-1}$ at a center-of-mass energy of 13 TeV shown for the second half of 2017. (b) delivered integrated luminosity expressed in fb^{-1} as a function of time from the year 2011 up to now, year 2017, for the proton-proton collisions. The luminosity is obtained using counting rates evaluated by the luminosity detectors. Both figures show the luminosities, delivered to the ATLAS detector. The images are taken from Ref. [9].

nominal LHC value 2808 for 25 ns bunch spacing. Furthermore, f_{rev} represents the revolution frequency, which is nominally 11.2 kHz and ϵ_n the transverse normalised emittance with a value of $3.75 \mu\text{m}$ in the nominal LHC design. The term β^* is a beam geometry parameter describing the focal length at the collision point, which is 0.55 m in the nominal LHC. The geometrical reduction factor of the luminosity is given by R and has a value of 0.85 at nominal β^* . It depends on the crossing angle θ_c between colliding beams, and on σ , σ_z as the root mean square (RMS) of the beam sizes in the traverse and longitudinal directions. The time-integral of the instantaneous luminosity is the integrated luminosity and is a further value to characterise the performance of the accelerator with units, that are the reciprocal of those used for cross sections². In Figure 1.2, the peak instantaneous luminosity, delivered to the ATLAS detector in the second half of the year 2017, as well as the integrated luminosity from the year 2011 up to now is shown. This year, the instantaneous luminosity values of a factor two times larger than the nominal values were reached up to $2 \cdot 10^{34} \text{ cm}^{-2} \text{ s}^{-1}$. After 2011, the integrated luminosity per year increased from 5 fb^{-1} by a factor of 10 to above 50 fb^{-1} within six years. In this time period the center-of-mass energy was raised from 7 TeV in 2011 to 13 TeV in the year 2017. The increase of the center-of-mass energy is crucial in order to extend the discovery potential reach.

1.2 The ATLAS experiment

The ATLAS experiment [10] is one of the four large LHC experiments and its goal is to identify and measure a broad range of different particles originating from proton-proton, ion-ion or ion-proton collisions. Most of the produced particles decay shortly after their production into their decay

²cross sections are measured in units of barn $b = 10^{-24} \text{ cm}^2$

products, which are then recorded in the detector volume. It has a size of 25 m in diameter and 44 m in length in a forward-backward symmetrical design with multiple layers employing a variety of detector technologies. The layers are organised in such a way to cover as much solid angle around the interaction point as possible. The entire detector has a weight of 7 000 t and is situated in an about 80 m deep cavern in the LHC tunnel. The ATLAS detector is composed of three main subdetector systems: the Inner Detector (ID) subjected to a 2 T solenoidal magnetic field, the Electromagnetic and Hadronic Calorimeter (ECAL and HCAL) and the Muon Spectrometer (MS), situated in a toroidal 3.9 T magnetic field. All detector subsystems are divided into a central part, referred to as the barrel, and a forward part on each side of the barrel, referred to as the end-cap. The data output of the detector subsystem is combined in a trigger and data acquisition system (TDAQ). A cross-sectional schematic of the ATLAS Experiment is illustrated in Figure 1.3. In the following section, the different components together with their respective detection principles are shortly introduced with the main focus on the pixel detector, further expanded on in Chapter 3.

Inner detector

The Inner Detector [11] is composed of three different tracking systems: the Pixel Detector, the Semiconductor Tracker (SCT) and the Transition Radiation Tracker (TRT), which are surrounded by a solenoid magnet with a diameter of 2.5 m and a length of 5.3 m. The ID itself has a size of 2.3 m in diameter and 7 m in length and is dedicated to track and vertex reconstruction of charged particles. The main contribution to particle identification of the ID is the determination of the negative or positive electric charge and the momenta of the charged particles. Furthermore, it is intended to reconstruct the short-lived particles by their decay products. In order to achieve this, the Pixel Detector provides a high-granularity and a high-precision set of measurements with four barrel layers as close to the interaction point as possible, which is especially important to distinguish particles from different quark flavours, such as bottom and charm quarks, mostly embedded in jet structures, where jets are narrow cones of particles. Due to the short lifetime of B-hadrons of 1.6 ps, their travel distance from their primary vertex to the vertex of their decay, the secondary vertex, is around 500 μm . In the so-called b-tagging this characteristic is used to identify bottom quarks. For b-tagging high granularity and high-resolution tracking devices as close as possible to the beam pipe are crucial to, firstly, extrapolate particle trajectories backwards and to, secondly, allow for two-track separation of close by particles. The Pixel detector is described in more detail in the dedicated Chapter 3.

The middle layer of the ID is the Semiconductor Tracker [12, 13] and consists of four micro-strip silicon detector barrel layers at radii from 300 mm to 520 mm and two end-caps housing nine disks each. The SCT modules are composed of two sensor pairs forming a stereo angle of 40 mrad and glued on the top and the bottom of a central baseboard, which serves as a mechanical core and a thermal conductor at the same time. With this geometry design, the SCT contributes four additional space points with eight hits to the track reconstruction of the inner tracker. The electrodes are less finely spaced compared to the ones from the pixel detector and therefore result in a poorer spatial resolution. At the same time, it offers the advantage, that the cost for the SCT is reduced with the

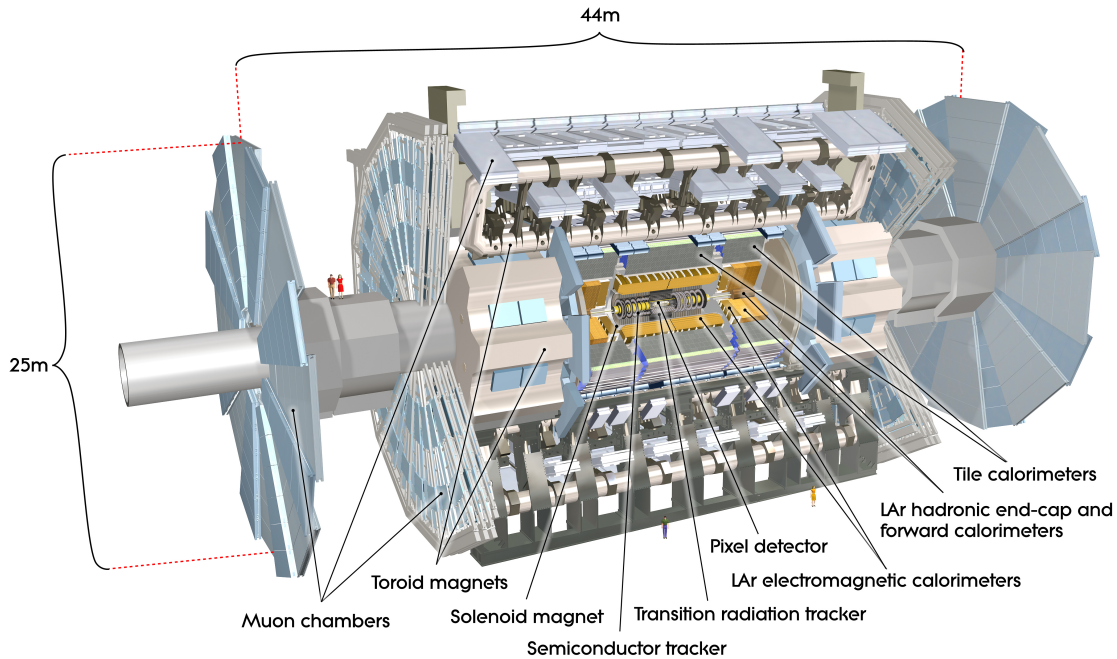


Figure 1.3: The cross section of the ATLAS Experiment with the Inner Detector, Calorimeter and the Muon Spectrometer (from inner to outer region). The image is taken from Ref. [16].

larger readout structures and allows for a larger area to be covered by silicon sensors.

The Transition Radiation Tracker [14, 15] is located in the outer part of the tracking volume and consists of one barrel layer with axial drift tubes and two end-caps with radial drift tubes. The drift tubes, conventionally referred to as straws, make up its basic element used for tracking. The 4 mm wide straws are filled with a gas mixture consisting of 70% Xe, 27% CO₂ and 3% O₂. The center of the straws is designed with gold-plated tungsten wires with a diameter of 0.03 mm. Transition radiation is emitted from ultra-relativistic particles when crossing the interface of the two media with different dielectric constants. With the TRT 36 additional space points are made available including additional information on the particle type and allow to distinguish between electrons and hadrons, such as pions, which are the lightest mesons consisting of one quark and one anti-quark.

Electromagnetic and hadronic calorimeter

In addition to the tracking information provided by the ID, it is crucial to determine the individual particle energy. The calorimeters are dedicated to the measurement of the energies of the particles and jets in the ATLAS detector. The calorimeter system [17, 18] is located outside the solenoid volume and is divided into an electromagnetic and hadronic calorimeter. The electromagnetic calorimeter is based on the sampling technology using active and passive absorber material to stop electrons and photons and measure their energy. Lead absorber plates are formed in an accordion design with Liquid Argon (LAr) filled between the absorber plates. The Liquid Argon represents the active medium with its very good intrinsic linear energy response and radiation tolerance.

In the hadronic calorimeter the end-cap sections (HEC) are designed with copper absorbers for electromagnetic showers and tungsten absorbers for hadronic showers (FCAL) filled with liquid Argon in between the absorber plates. In the case of the barrel regions, the selected materials are steel absorbers and plastic scintillators.

Muon spectrometer

The outer regions of the ATLAS detector are dedicated to the measurement of muon tracks with the muon spectrometer (MS) [19]. The muon tracks are bent by the toroidal magnetic field, which surrounds the MS and therefore allows for the measurement of the muon momentum and charge. Four different technologies are used, implemented from a radius of around 4 m up to the outermost part at a radius of about 11 m. To achieve high-precision tracking, the monitored drift tubes (MDTs) are implemented in the barrel region and the cathode drift chambers (CSC) in the end-cap region. Trigger information is obtained by the resistive plate chambers (RPC) located in the barrel region and the thin gap (multi-wire) chambers (TGC), located in the end-cap region.

Trigger and data acquisition system

An enormous amount of data is generated with a bunch-crossing every 25 ns and an event rate of 40 MHz. Therefore a dedicated trigger system [20] is needed, which aims to select only those hard-scatter events more interesting for physics analyses. The ATLAS trigger system is capable to reduce the event rate down to roughly 200 Hz with its composition of a first-level trigger system, Level-1 trigger, a High-Level trigger and a final event filter. The Level-1 trigger is purely hardware based and uses trigger information, obtained from the muon spectrometer and calorimeters and is capable to reduce the event rate to roughly 100 kHz. The High-Level trigger then performs a reconstruction process on regions of interest and provides a further reduction of the event rate down to roughly 3 kHz. The final event selection takes place in the event filter, where the event rate drops to roughly 200 Hz. With a mean ATLAS event size of around 1.5 MB, the data are stored at a rate of about 300 MB/s.

Coordinate system

In this subsection the cylindrical coordinate system of the ATLAS detector, used in this thesis, is introduced. The geometrical center of the ATLAS detector is defined as the IP with the beam line crossing the IP and being represented by the z axis. A point in the coordinate system around the beam line is identified by the radial distance r from the IP by the azimuth angle ϕ and the pseudorapidity η , which can be described in the following way:

$$\eta = -\ln\left(\tan\frac{\theta}{2}\right) \quad , \quad (1.2)$$

where θ is the angle between the particle direction and z axis. When a particle is generated in the IP, the pseudorapidity lies in a range between $\eta = 0$ and $\eta = \infty$. In the first case, the particle exits the IP with a direction perpendicular to the z axis and in the second case, the particle exits the IP

with a direction parallel to the z axis. Currently, a partial η coverage up to $|\eta| < 3.0$ in the pixel detector is ensured.

1.3 Accelerator and detector upgrade

To maximise the discovery potential at the LHC, a new phase with a high luminosity upgrade of the LHC is foreseen for 2025 [21]. The LHC will be renamed to High Luminosity LHC (HL-LHC) and will be operated at the maximum center-of-mass energy of 14 TeV and an increased instantaneous peak luminosity up to $7 \cdot 10^{34} \text{cm}^{-2} \text{s}^{-1}$ and accumulate an integrated luminosity up to 4000fb^{-1} . Assuming a bunch-crossing every 25 ns, one single bunch-crossing produces multiple separate events, so-called pile-up events. The pile-up events will increase to 200 from the current value of around 30-50. This will require an upgrade of the accelerators as well as the detectors to be able to operate after exposure to the increased particle fluences. In the following, the upgrade from the LHC to the HL-LHC is motivated together with a short description of the accelerator upgrade and the upgrade of the ATLAS detector.

1.3.1 Physics motivation

Following the successful discovery of the Higgs boson-like particle announced on July 4th in 2012 with a mass at about 125GeV^3 [22], the HL-LHC will have the potential to answer some key questions such as whether supersymmetry exists, how the nature of dark matter is described and whether there are undiscovered extra dimensions. The discovery of the boson consistent with the SM-Higgs boson, served as an important milestone in fundamental particle physics. The Standard Model of particle physics [23, 24] was completed and a new era of physics discovery at the LHC of determining the properties of the Higgs boson more precisely was begun. As the value of the Higgs boson mass is far below the Planck scale, it leads to the assumption that the SM is still incomplete at the TeV and Planck scale. Other problems are still unsolved, such as the existence of neutrino mass, although neutrinos are predicted from the SM to be massless and the existence of dark matter and dark energy, which is not explained by the SM. For this, different theories propose elegant solutions to explain this hierarchy problem. *Supersymmetry* (SUSY) [6] and *Extra dimensions* are two such proposed solutions. SUSY theories overcome the hierarchy problems with the existence of supersymmetric partners for each particle in the SM and especially address the dark matter problem of the missing mass in the universe. The weakly interacting massive particles (WIMPs) of dark matter are, as the naming suggests, not easily detectable and the SUSY theories offer the lightest super-symmetric particle (LSP), so-called *Neutralino*, as a WIMP candidate. The next decade of the LHC will push the energy frontier to find answers to unsolved questions.

The increase of the luminosity will lead to a higher collision rate and present a unique opportunity to increase the sensitivity to new physics, as well as allow for additional and more precise measurements. Precision measurements of the Higgs boson will be possible with the larger amount of data, such as for the Higgs rare decays, coupling to bosons and fermions and self-coupling. The

³mass units are stated with $c = \hbar = 1$

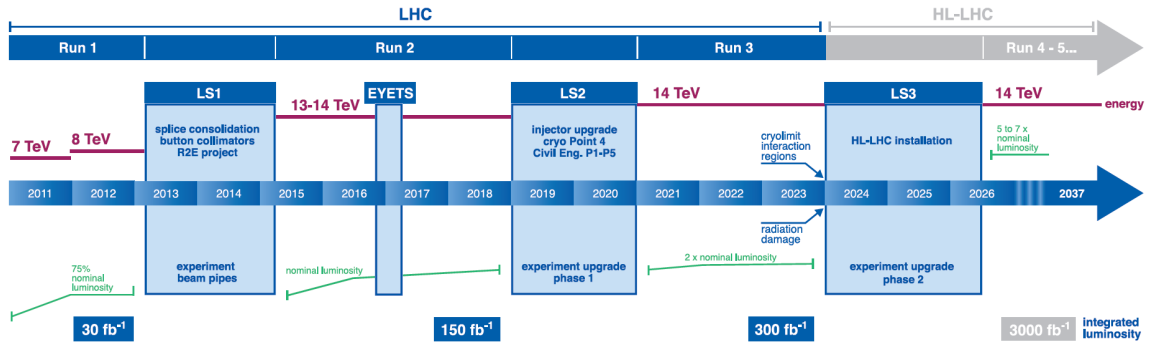


Figure 1.4: The LHC schedule for the upcoming high luminosity decade. The schedule plan starts from year 2011 and shows the energy of the collision in the upper red lines and the luminosity in the lower green lines. The first long shutdown (LS1) took place in 2013-2014, where the accelerator complex was upgraded to reach higher beam energies above 8 TeV (center-of-mass energy before LS1) and luminosities. The second long shutdown (LS2) is foreseen for 2019-2020, in which the luminosity will be consolidated and the LHC injectors and detectors will be upgraded. From 2026, after the third long shutdown (LS3) the LHC will be operated in the high luminosity configuration and will be named the HL-LHC from then on.

potential for the discovery of rare processes such as $H \rightarrow \mu\mu$ at the HL-LHC, as well as to further expand on vector boson fusion (VBF) production of $H \rightarrow \gamma\gamma$ and $H \rightarrow \tau\tau$ is high [2]. The two latter decays were already addressed in the current 7 TeV to 13 TeV analysis and are important for further precision measurements at higher energy scale. The Higgs production with top-pair $t\bar{t}H$ with $H \rightarrow \gamma\gamma$, which is a channel with an expected low signal rate, was measured with the increased luminosity in the current running period, Run-II, and is especially interesting. Next to the low signal rate channels WH/ZH , $H \rightarrow \gamma\gamma$, the $t\bar{t}H$ initial state is predicted with a signal-to-background ratio of around 20%, resulting in a cleaner signal compared to around 10% for ZH and around 2% for WH . Furthermore, it opens possibility for the top-Yukawa coupling to be precisely measured. With the final luminosity it will be further possible to investigate the Higgs self-coupling in the channels $HH \rightarrow \tau\tau bb$ and $HH \rightarrow \gamma\gamma bb$, which was never previously studied [2]. This is particularly important for further understanding of the Higgs mechanism. Furthermore, in the high pile-up environment, the b-tagging performance will be critical to maintain and is highly dependent on the performance of the innermost pixel layers. Due to this reason, the innermost layer is foreseen to be as close as possible to the beam line to enable the best possible performance on the two-track resolution, which will be additionally supported by a higher granularity of the pixel sensors.

1.3.2 Accelerator upgrade

The path towards HL-LHC, can be divided into three steps from the year 2011 until 2025: named Run-I (2011-2013), Run-II (2015-2018), Run-III (2021-2023) and Run-IV (from 2026 onwards). The running times are intervalled by long shutdowns for accelerator and detector maintenance in the periods of 2013-2014 for LS1, 2019-2020 for LS2 and 2024-2026 for LS3. The upgrade roadmap is illustrated in Figure 1.4. At the point of writing, the LHC is in its Run-II phase, in which it is operated with a bunch-crossing every 25 ns. In Run-III, the current center-of-mass energy of 13 TeV will be increased to its nominal energy of 14 TeV. The LS2 is foreseen in 2019 to replace the current

Table 1.1: High Luminosity LHC parameters with the nominal values of the LHC and the ones planned for HL-LHC [8]. Both configurations are shown for a bunch-spacing time of 25 ns.

Name and symbol	[Unit]	LHC for 25 ns	HL-LHC for 25 ns
Beam energy \sqrt{s}	[TeV]	14	14
Number of bunches n_b		2808	2808
Particles per bunch N_b	[10^{11}]	1.15	2.2
Revolution frequency f_{rev}	[kHz]	11.245	11.245
Normalised emittance ϵ_n	[μm]	3.75	2.5
Beta function at the IP β^*	[m]	0.55	0.15
Crossing angle θ_c	[μrad]	285	590
RMS bunch length σz	[cm]	7.55	7.55
RMS beam size at the IP σ^*	[μm]	16.7	13.6
Levelled factor \mathcal{L}	[$10^{34} \text{ cm}^{-2} \text{ s}^{-1}$]	1	5
Peak Luminosity $\mathcal{L}_{\text{peak}}$	[$10^{34} \text{ cm}^{-2} \text{ s}^{-1}$]	1.0	7.18
Pile-up $\langle\mu\rangle$	[events]	19	200

LINAC 2 pre-accelerator with the upgraded LINAC 4 [25] within the LHC complex. The LINAC 4 is able to accelerate protons up to 160 MeV instead of the previously possible 50 MeV in the LINAC 2. In the LS3 the LHC will be upgraded to its HL-LHC configuration with the aim to reach a peak luminosity of up to $7 \cdot 10^{34} \text{ cm}^{-2} \text{ s}^{-1}$, resulting in an increase of the integrated luminosity to 250 fb^{-1} per year. An upgrade of the components of the accelerator will be necessary. One of them is the replacement of the quadrupole magnets in the intersection regions, used to focus the beam on either the side of the ATLAS or CMS detectors. They exploit a key innovative technology providing fields beyond 10 T. The operational time after the LS3 is the HL-LHC phase and is called Run-IV. The parameters in the current LHC are displayed in Table 1.1 next to the respective parameters for the HL-LHC phase.

1.3.3 ATLAS upgrade

Along with the LHC upgrade efforts, the upgrade of the ATLAS experiment can be divided into three phases for the HL-LHC timeline. The first phase, Phase-0 was performed during the LS1, where the Insertable B-Layer (IBL) was inserted in the pixel detector as an additional layer, closer to the beam line than the innermost layer at that time (B-Layer). Together with a smaller beam pipe employing an inner radius of 2.4 cm, the additional pixel layer was introduced at a radius of 3.2 cm. The upgraded pixel modules, implemented in the IBL, are designed to be more radiation hard and with higher granularity for readout chip and sensor to withstand the development of the fluence and the larger number of pile-up events as the LHC was proceeding to Run-II. The upgraded IBL modules with a higher tracking and b-tagging efficiency are described in more detail in Chapter 3. To limit the increase of multiple scattering, even though additional material was introduced with the IBL, the cooling of sensor and electronics was improved with a new CO_2 system of reduced mass.

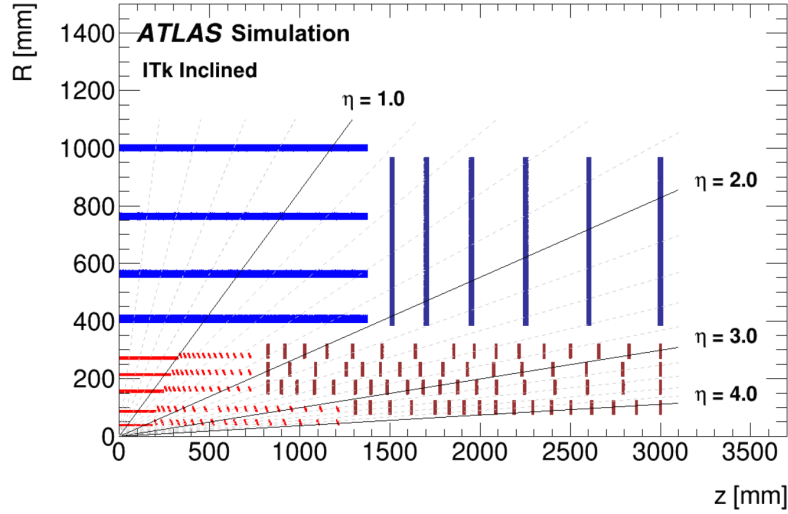


Figure 1.5: Schematic layout of the ITk of ATLAS for the HL-LHC phase, as presented in Ref. [2, 29]. The horizontal axis is parallel to the beam line, while the vertical axis represents the radial distance from the center of the detector, placed at point (0,0) in the figure. Only the active detector elements of the first quadrant are shown.

In the outer part of the detector a new neutron shielding was introduced in the muon spectrometer for a reduction of the background by 10-20%. The background arises from the increasing luminosity, which itself induces additional backgrounds from low-energy neutrons and photons [26]. For this, the beam pipe in the forward regions, originally made of steel, was replaced with an aluminium one. The Phase-I upgrade is scheduled for 2019-2020 during the LS2 and will concentrate on the upgrade of the outer parts of the ATLAS detector. The construction of New Small Wheels (NSW) will allow to improve the muon Level-1 trigger system to reduce the overall data-taking rate. This will be obtained by the further rejection of fake triggers. For full track reconstruction at the start of High-Level trigger, a new Fast Tracker (FTK), making use of the tracking information from the ID, will be incorporated into the first stages of the trigger system [27, 28].

For the last planned Phase-II upgrade [2, 29] during the LS3 from year 2024 on, major parts of the ATLAS detector will be replaced for the HL-LHC. For the muon system, a complete replacement of the readout electronics is foreseen, together with additional upgrades of the trigger systems, with the aim to increase the readout capabilities and the trigger rate. To cope with the increased occupancy in the HL-LHC, the Pixel Detector, the Semiconductor Tracker, as well as the Transition Radiation Tracker will be fully replaced with an all-silicon new Inner Tracker (ITk), illustrated in Figure 1.5. Compared to the current ID, the ITk will have a significant reduction in material budget. The ITk will ensure a complete $|\eta|$ coverage up to 4.0. The ITk will have the same performance as the current detector, but in the harsher environment of the HL-LHC. The overview of the planned design is given in detail in Section 3.2.

THEORY OF SILICON PARTICLE DETECTORS

Over the last 30 years solid state detectors have gained an important role with their excellent tracking capabilities for high energy physics experiments. In a regime of high particle multiplicity at hadron colliders, segmented semiconductor devices are a suitable technology for position sensitive detection, while keeping low cell occupancy. In the volume closest to the interaction point, pixel detectors are normally used thanks to their finer segmentation. The pixel cells define the granularity of the detector and provide a two-coordinate position sensitivity for the point of incidence together with a fast timing. From the particle trajectories, the basic properties of the traversing charged particle, like momentum and point of origin, can be evaluated. Up to now the pixel detectors at LHC have been built with a hybrid technology, where the sensing element (sensor) and the matching readout chip are processed independently and then connected. In this way the material and processes are individually optimised. This approach makes it possible to achieve fast enough readout and radiation hardness to cope with the LHC environment.

The following chapter introduces the fundamentals of solid state detectors based on silicon materials by focusing on the effects relevant for the investigations described in this thesis. For further reading on basic semiconductor physics, the interested reader is referred to Refs. [30–32]. The chapter begins with the working principle of silicon particle detectors in Section 2.1 and the properties of silicon used as a detector for charged particles in Section 2.2. Since in particle colliders, radiation interaction generates permanent or temporary damage in the silicon device, the resulting defects in silicon are introduced in Section 2.3. In the final section, Section 2.4, hybrid pixel detectors used in high energy particle physics applications are presented and a more detailed description is given on the sensor design itself.

2.1 Working principle

Solid state materials are classified by the way the atoms are arranged within the solid. Materials, in which atoms are randomly placed, are called amorphous. Materials, in which atoms are placed in a highly ordered structure, are called crystalline. Different to free atoms, where electrons are characterised by discrete energy levels, the crystalline structure forces the discrete energy levels to be merged into energy bands. Semiconductor materials are characterised by their forbidden energy

gap (E_g) between valence band and conduction band, $E_g = 1.12$ eV for silicon [32]. Only few electrons are thermally excited from the valence band into the conduction band at room temperature in intrinsic silicon. Therefore, there are only a few free charge carriers. The highest filled energy band is referred to as the valence band with the energy E_V , whereas the lowest partially filled energy band is referred to as the conduction band with the energy E_C . Depending on E_g , solid state materials are categorised into three main groups: conductor, semiconductor and insulator. In the case of no energy gap or overlapping energy levels and unfilled energy levels already at zero temperature $T = 0$ K, allowing for a free movement of the charge carriers within the energy bands, the solid material is conducting. On the contrary, in insulators the valence band is fully filled with a large energy difference to the conduction band and no increase of temperature will change its properties. At $T = 0$ K, a semiconductor behaves like an insulator. Due to its smaller energy gap, electrons from the valence band can be thermally excited and can overcome E_g to reach the conduction band. When electrons are excited to the conduction band, they move freely through the crystal into the occupied negative phase states (n) in the conduction band. The phase states in the valence band are left positive (p). The positive charge carriers in the valence band are called holes. The size of E_g is defined by the material properties of the semiconductor itself. The probability of the occupancy of a specific energy state in the band levels can be expressed by the Fermi-Dirac distribution:

$$f_e(E) = \frac{1}{e^{(E-E_F)/k_B T} + 1} \quad , \quad (2.1)$$

with k_B representing the Boltzmann constant and E_F the Fermi energy. The Fermi level is the highest occupied electron energy level at $T = 0$ K and lies between the valence and conduction band. At higher temperatures, electrons are able to occupy excited states above the Fermi level. These charge carriers are called intrinsic charge carriers and are found in intrinsic semiconductors, which are characterised by an equal carrier concentration of electrons and holes.

The material chosen for semiconductors in different application depends on availability and cost. Silicon as a semiconductor material meets the requirements of tracking detectors. Compared to other semiconductors with a smaller energy gap, such as germanium, a lower number of electrons are thermally excited in silicon. This results in lower noise.

2.2 Properties of silicon used as a detector for charged particles

2.2.1 Doping

In semiconductor devices intrinsic material is rarely used, due to its low electrical conductivity. With the introduction of impurities to the material, the electrical conductivity is increased selectively, also at low temperature, i.e. without thermal excitations. The significant benefit of semiconductors is the possibility of tailoring the conductivity by deliberately introducing impurities into the silicon lattice. This procedure is called doping and is performed either during crystal growth or afterwards in selected regions of the crystal. A silicon atom has four valence electrons. The conductivity is improved by doping with impurity elements with either three or five valence electrons. Phosphorus with five valence electrons requires less energy for the free electron, not bonded to the individual

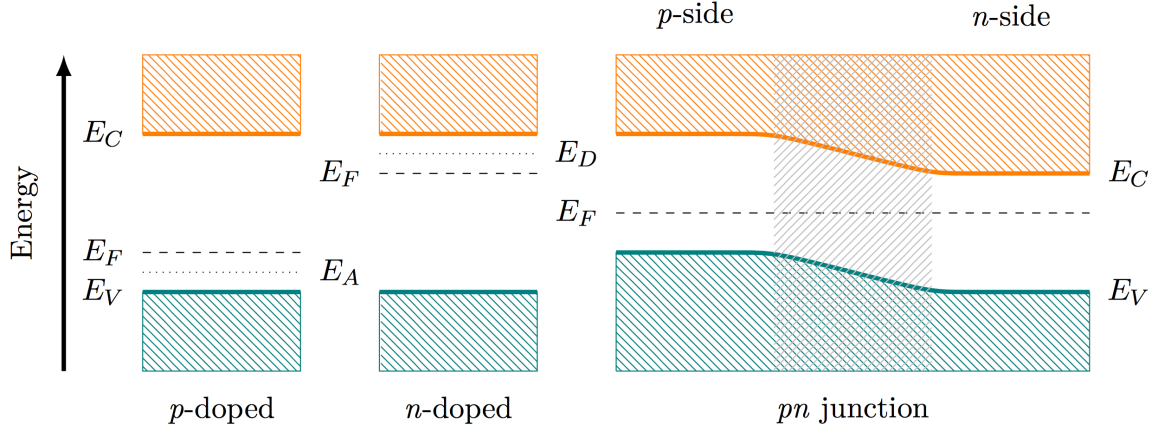


Figure 2.1: Schematics of the energy levels in p-type (left) and n-type (center) silicon. The valence band is shown in green colour, while the conduction band is shown in orange. With the introduction of donor electrons, the accompanied energy level E_D is created, while for the introduction of acceptor electrons E_A is created. Combining the differently doped segments results in a p-n junction with a balanced Fermi level in between the two segments. The sketch is taken from Ref. [33].

atoms in the silicon lattice, to be lifted to the conduction band. In fact, the addition of free electrons, the so-called electron *donors*, creates an energy level E_D in the band gap, close to the conduction band. With the addition of a further level in closest proximity to the conduction band, an excitation induced by temperature results in an excitation of the selectively added energy state. This leads to a shift of the Fermi energy towards E_D , as shown in Figure 2.1. Silicon doped in this way is called *n-type* silicon. Instead, Boron atoms with three valence electrons, acting as *acceptors*, are used to introduce additional holes into the crystal, which is accompanied by the creation of an additional energy level E_A close to the valence band and a shift of the Fermi energy towards it. This procedure transforms the material into a *p-type* silicon.

2.2.2 P-n junction

Combining the two differently doped parts, n-type and p-type, the resulting so-called p-n junction, will create a transition zone, where mobile charge carriers from one region diffuse into the differently doped region, as shown in Figure 2.1. Free electrons from the n-doped material will neutralise free holes in the p-doped material, while free holes from the p-doped material will neutralise with free electrons in the n-doped material. The potential inside the p-n junction can be expressed by the Poisson equation:

$$\Delta\phi = \frac{\rho}{\epsilon_{\text{Si}}\epsilon_0} = \frac{e_0}{\epsilon_{\text{Si}}\epsilon_0} (N_A - N_D) \quad \text{with} \quad \rho = e_0 (N_A - N_D) \quad , \quad (2.2)$$

with ϕ representing the electrostatic potential, $\epsilon_{\text{Si}} = 11.75$ the dielectric constant of silicon and $\epsilon_0 = 8.85 \cdot 10^{-12} \frac{\text{As}}{\text{Vm}}$ the vacuum permittivity. The term ρ represents the charge density, expressed by the elementary charge e_0 and N_A and N_D , the carrier concentrations in the respective regions. The concentration gradients of electron and holes in the p-n junction lead to the diffusion currents. Hence, immobile donor and acceptor ions are left without their reversely charged mobile charge

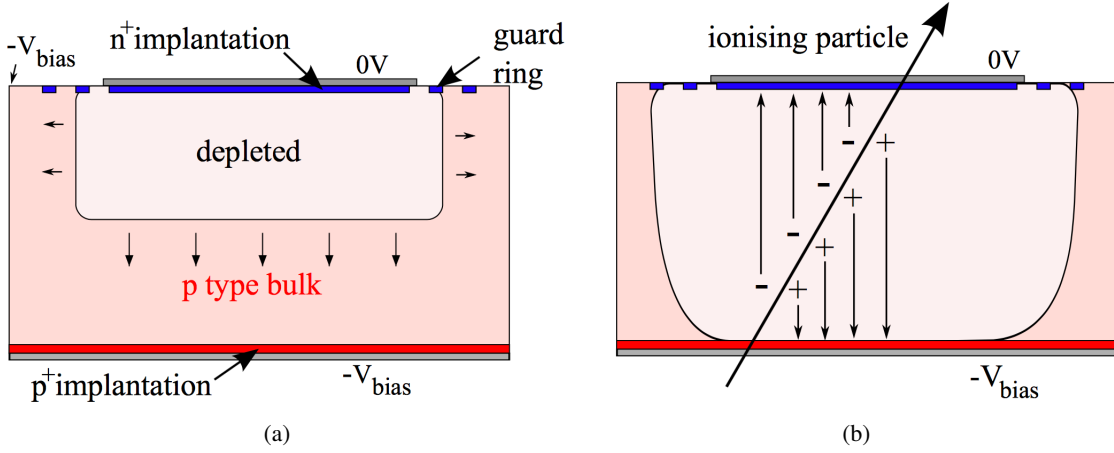


Figure 2.2: (a) depletion zone inside a silicon sensor with p-type bulk and (b) charge generation within the depleted bulk, taken from Ref. [34].

carriers creating a so-called *depletion region*. Fixed positively charged donor ions are created in the n-region, while fixed negatively charged acceptor ions are created in the p-region, respectively. The resulting so-called *space charge region* causes an electrical field counteracting the diffusion of charge carriers until a difference of the electrical potential is reached, which prevents further diffusion of the charge carriers. This built-in potential can be expressed in the following way:

$$\phi_{\text{bi}} = k_{\text{B}}T \ln\left(\frac{n_{0,\text{n}} \cdot p_{0,\text{p}}}{n_{\text{i}}^2}\right) \approx k_{\text{B}}T \ln\left(\frac{N_{\text{D}} \cdot N_{\text{A}}}{n_{\text{i}}^2}\right), \quad (2.3)$$

where $n_{0,\text{n}}$ represents the electron concentration in the n-type, $p_{0,\text{p}}$ the hole concentration in the p-type and n_{i} the intrinsic concentration. In the case of complete ionisation of donors and acceptors, the electron and hole concentrations are equal to N_{D} and N_{A} . The corresponding built-in voltage can then be written as:

$$U_{\text{bi}} = \frac{\phi_{\text{bi}}}{q} = \frac{k_{\text{B}}T}{q} \ln\left(\frac{N_{\text{D}} \cdot N_{\text{A}}}{n_{\text{i}}^2}\right), \quad (2.4)$$

with the charge q . Typical built-in voltages are in a range between 0.5 V and 1 V.

2.2.3 Depletion voltage and leakage current

Applying an external bias voltage to the p-n junction with a higher potential on the n-side than on the p-side (reverse biasing) increases the space charge region and consequently reduces the current flow through the p-n junction. In contrary, if a suitable positive voltage (forward biasing) is applied to the p-n junction, it supplies free electrons and holes with the extra energy they require to cross the junction. In this conditions, the width of the depletion layer around the p-n junction is decreased. The reverse bias voltage, needed to be applied to the semiconductor to extend the mobile-free charge carrier zone to the full depth of the sensor, is the *depletion voltage* and can be expressed as

$$U_{\text{depl}} = \frac{|N_{\text{eff}}|d^2}{2\epsilon_{\text{Si}}\epsilon_0} \quad \text{with} \quad N_{\text{eff}} = N_{\text{D}} - N_{\text{A}}, \quad (2.5)$$

with $N_{\text{eff}} = N_D - N_A$ as the effective doping concentration. In the silicon sensors, investigated in this thesis, the depleted region starts to extend from the n-type implants at the front side to the end of the space charge region defined by the end of the p-type bulk, which is at the backside of the sensor, as illustrated in Figure 2.2a. The depletion voltage is directly proportional to the squared thickness d of the device and to the bulk resistivity. For applied bias voltages exceeding the depletion voltage, the device is said to be *overdepleted*.

When a reverse bias voltage is applied, there is a probability of a quantum tunnelling of electrons from the valence band to the conduction band [35] in addition to thermal excitations of the charge carriers in an unbiased sensor. This results in a reverse current flow, the so-called *leakage current*. The leakage current is separated into two categories: The bulk generation current and the surface generation current. In both cases it is mostly due to charge carriers from crystal impurities. The surface generation current arises from defect states at the Si-SiO₂ interface. It is usually very small compared to other components of the current and is negligible in most of the cases, especially after irradiation. For an ideal junction, the reverse current is only determined by diffusion of charge carriers from the non-depleted region into the space charge zone. However, in reality, the dominant contribution comes from charge carriers originating from process and radiation-induced defects. Only defects in the space charge region contribute to the bulk generation current. Therefore, the width of the depleted area depends on the applied voltage. The resulting leakage current scales with the applied bias voltage. Furthermore, the leakage current is strongly dependent on temperature. The expected leakage current for a given T can be obtained from a measurement at a reference temperature T_{ref} by:

$$I_{\text{leak}}(T) = I_{\text{leak}}(T_{\text{ref}}) \left(\frac{T}{T_{\text{ref}}} \right)^2 \exp \left(-\frac{E_g}{2k_B} \left[\frac{1}{T} - \frac{1}{T_{\text{ref}}} \right] \right) , \quad (2.6)$$

with $I_{\text{leak}}(T_{\text{ref}})$ as the current measured at T_{ref} . According to this formula, the leakage current approximately doubles every 7 K. This relation also holds for devices irradiated to high fluences. It shows, that cooling is imperative to reduce the leakage current to an acceptable level.

For sufficiently high electric fields within the sensors, arising from high bias voltages applied, the carriers gain enough kinetic energy to generate additional electron-hole pairs by impact ionisation, finally leading to the breakdown of the sensor.

2.2.4 Charge generation

For detector operation, reverse biasing is ideal for signal charge collection. The number of free charge carriers in the sensitive volume of the semiconductor is reduced, allowing for a lower noise contribution to the actual measured charge. In high energy physics experiments the signal generation for most of the charged particles is approximated by the one of the minimum ionising particle (MIP). It has minimum mean energy loss, when passing through the semiconductor tracking material without losing all its energy at once and creating electron-hole pairs all along its path. The mean energy loss of the traversing charged particle is well-described by the Bethe-Bloch equation:

$$-\left\langle \frac{dE}{dx} \right\rangle = K z^2 \frac{Z}{A} \frac{1}{\beta^2} \left(\frac{1}{2} \ln \frac{2m_e c^2 \beta^2 \gamma^2 E_{\text{kin,max}}}{I^2} - \beta^2 + \dots \right) , \quad (2.7)$$

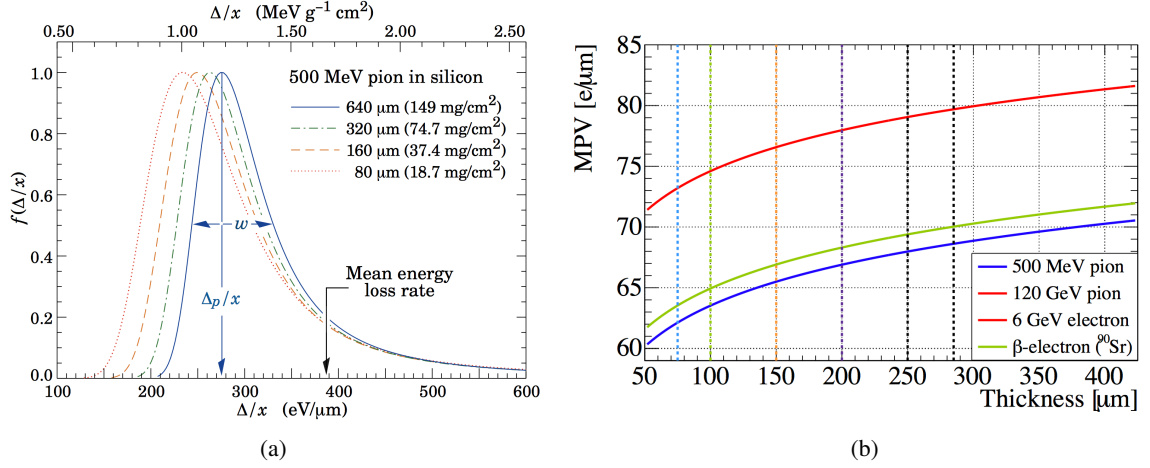


Figure 2.3: (a) example of the most probable energy loss of 500 MeV pions in silicon detectors of different sensor thicknesses. The width w is the full width at half maximum. The figure is taken from Ref. [36]. (b) the MPV of electron-hole pairs generated by particles of different energies as a function of the sensor thickness. The energies of the particles are given. The curves for electrons of 6 GeV and pions of 120 GeV, drawn in the same colour, coincide. The sensor thicknesses, shown as vertical lines, are highlighted with different colours, where in the scope of this thesis, the investigations are mainly focused on 100 μm and 150 μm thick sensors. The figure is taken from Ref. [37]

with $\frac{dE}{dx}$ representing the energy loss of the particle per length, K a constant, z the charge of the traversing particles in units of e , Z the atomic number of the absorption medium (14 for silicon) and A the atomic mass of the absorption medium (28 for silicon). The term $m_e c^2$ is the rest energy of the electron (0.511 MeV), β is the velocity of the traversing particle in units of the speed of light and $\gamma = 1/\sqrt{1 - \beta^2}$ is the Lorentz factor. Furthermore, the term $E_{\text{kin,max}}$ represents the maximum kinetic energy, which is transferred to an electron of the material in a single collision and I the mean excitation energy (173 eV for silicon [32]). The dots at the end of the equation are indicating additional correction terms, such as density corrections for high particle energies or shell corrections for lower particle energies [24]. The number of electron-hole pairs generated in the depleted sensor volume is obtained by the deposited energy from the traversing particle divided by 3.36 eV [32], which is the ionisation energy needed to create electron-hole pairs in silicon at 300 K. The ionisation energy is three times as large as the band gap energy of $E_g = 1.12$ GeV. For sensor thicknesses d the most probable value (MPV) of the created electron-hole pairs is described by the Landau-Vavilov distribution [36, 38, 39]:

$$MPV = \xi \left[\ln \frac{2m_e \beta^2 \gamma^2}{I} + \ln \frac{\xi}{I} + 0.200 - \beta^2 + \dots \right], \quad (2.8)$$

where $\xi = (K/2) \langle Z/A \rangle (d/\beta^2)$ MeV. For the example of 500 MeV pions the Landau-Vavilov distribution is calculated for different sensor thicknesses from Equation 2.8, adapted from Ref. [36] and shown in Figure 2.3a. For high energy particles, the Landau-Vavilov most probable energy loss reaches a Fermi plateau. The MPV of the deposited charge per μm equals the number of generated electron-hole pairs. It is shown in Figure 2.3b as a function of the sensor thickness for different particle types and energies relevant for this thesis. The sensor thicknesses are highlighted

with different colours, where the investigations of this thesis mainly focus on 100 μm (green) and 150 μm (orange) thick sensors. In sensors of this thickness range 70-80 electrons per μm are expected to be created by an incident MIP.

In presence of an applied reverse bias voltage, the created charge carriers drift under the influence of the electric field to their corresponding electrodes, i.e. the electrons drift to the n-doped region, connected to the higher potential. The drift velocity is expressed as a function of the electric field and for low electric field regions it can be written as:

$$\vec{v}_{e,h} = \pm \frac{q\tau_{\text{eff},e,h}}{m_{e,h}} \vec{E} = \pm \mu_{e,h} \vec{E} \quad (2.9)$$

for electrons and for holes with the respective sign. The term $\vec{v}_{e,h}$ represents the drift velocity of the charge carrier and $\tau_{\text{eff},e,h}$ the free mean time of the charge carrier between successive collisions, the so-called effective trapping time¹. The electric field is expressed by \vec{E} . The mobility μ is dependent on the doping and charge carrier concentration and temperature. It is considered constant in low field regions of $E < 1$ kV/cm, resulting in $\vec{v}_{e,h}$ being proportional to \vec{E} . At higher \vec{E} , the relation between $\vec{v}_{e,h}$ and \vec{E} deviates from linearity with $\vec{v}_{e,h}$ reaching a saturation value [40]. This effect is explained by the degradation of μ for $E > 1$ kV/cm. The charge carrier mobility as a function of \vec{E} is shown in Figure 2.4. It can be expressed in the following way [41]:

$$\mu = \frac{v_{\text{sat}}/E_C}{[1 + (E/E_C)^a]^{1/a}} \quad , \quad (2.10)$$

where v_{sat} is the value of the saturation drift velocity, E the absolute value of the electric field and E_C and a fitting parameters.

The saturation drift velocity of electrons is a factor of three higher than for holes, due to the lower hole mobility. Typical values of the electron and hole mobilities at saturation in silicon are $\mu_e = 1350 \text{ cm}^2/\text{Vs}$ and $\mu_h = 450 \text{ cm}^2/\text{Vs}$.

2.2.5 Formation of electrical signal

During the full drift time of the charge carriers in the electric field, a current I at the electrodes is induced, which is described by the Shockley-Ramo theorem [42, 43]:

$$I_{e,h} = Nq\vec{E}_w \vec{v}_{e,h} \quad , \quad (2.11)$$

where N the number of charge carriers and \vec{E}_w is the so-called weighting field of the considered electrode. With \vec{E}_w the electrostatic coupling between charge and electrode at a given detector depth is expressed. It is obtained from the weighting potential ϕ_w by:

$$\vec{E}_w = -\nabla\phi_w \quad , \quad (2.12)$$

¹The effective trapping time can be expressed as $\tau_{\text{eff},e,h} = \lambda_{e,h}/v_{\text{th},e,h}$. The probability of a charge to be trapped is proportional to the length in the material, the particle is traversing. It is represented by the effective trapping distance $\lambda_{e,h}$. The term $v_{\text{th},e,h}$ is the thermal velocity, which charge carriers acquire in between collisions. It is typically much larger than the drift velocity.

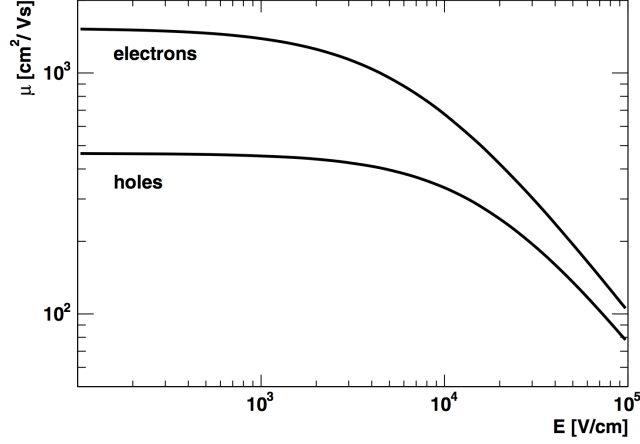


Figure 2.4: Charge carrier mobility shown as a function of the electric field. Figure taken from Ref. [30].

where ϕ_w is dimensionless and is defined to be 1 at the readout electrode and 0 at all other electrodes. In the ideal case of a fully depleted pad sensor with an active thickness of d and two parallel electrodes with lateral dimensions larger than d , the ϕ_w is linear along the sensor depth y . Consequently, the gradient of ϕ_w is defined to be constant with an absolute value of $\nabla\phi_w = \frac{1}{d}$. The induced current, resulting from generated electron-hole pairs inside the device at a time t and y can then be written as [44, 45]:

$$I(y, t) = I_e(y, t) + I_h(y, t) \approx e_0 N_{e,h} \frac{1}{d} \left[\vec{v}_e(y_e(t)) e^{-t/\tau_{\text{eff},e,h}} + \vec{v}_h(y_h(t)) e^{-t/\tau_{\text{eff},e,h}} \right] \quad , \quad (2.13)$$

with $I_e(y, t)$ as the current induced by electrons and $I_h(y, t)$ by holes, respectively. The number of trapped charge carriers over t can be expressed in the following way [46]:

$$dN = -N_0 \frac{1}{\lambda_{e,h}} dl = -N_0 \frac{1}{\tau_{\text{eff},e,h}} dt \quad \Rightarrow \quad N(t) = N_0 \exp\left(-\frac{t}{\tau_{\text{eff},e,h}}\right) \quad . \quad (2.14)$$

If the time of measurement is shorter than $\tau_{\text{eff},e,h}$, charge trapping does not influence the charge signal. The resulting induced current at the electrodes is amplified, shaped and read out by the front-end electronics.

2.3 Radiation damage in silicon

Properties, such as depletion voltage, leakage current and charge collection efficiency, of semiconductors are altered by particles penetrating through the material in a regime of high luminosity and high radiation doses. The non-ionising energy loss through high-energy particles scattering with silicon atoms of the crystalline lattice will harm the silicon sensors. Depending on the particle energy, the impact of the radiation damage varies: lower-energetic particles create point-like damage, where a single atom is displaced from its lattice position, while higher-energetic particles transferring an energy exceeding 2 keV, create cluster-like damage, where a number of atoms in a crystal volume with radius between 10 nm and 200 nm are damaged [48]. To compare the defects of the different particles induced in the silicon lattice structure, the radiation damage is scaled

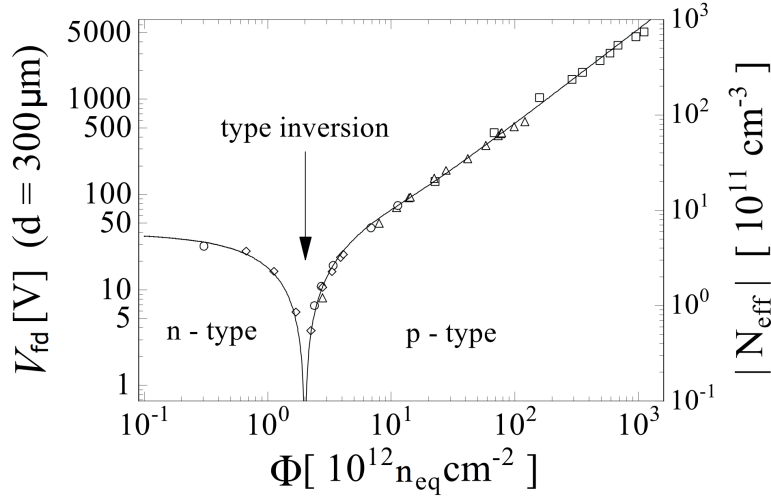


Figure 2.5: Depletion voltage of an n-type 300 μm thick sensor as a function of absolute effective doping concentration and irradiation fluence. Figure taken from Ref. [47].

according to the *non-ionizing energy loss* (NIEL) [49]. This is done under the assumption, that any displacement-damage-induced change in the material properties scales with the energy imparted in displacing collisions, irrespective of the type and interaction process of the imparting particle. To allow for a comparison of radiation damage, induced by different types of radiation, a normalisation needs to be applied. Therefore, a hardness factor κ is introduced for each particle and radiation type, which is normalised to mono-energetic 1 MeV neutrons. The equivalent irradiation fluence Φ_{eq} can then be expressed after scaling to the damage induced by a fluence of 1 MeV neutrons, instead of the actual fluence of particles received during irradiation Φ_{irr} , such:

$$\Phi_{\text{eq}} = \kappa \Phi_{\text{irr}} \quad . \quad (2.15)$$

2.3.1 Impact of defects on silicon properties

Radiation induced defects are categorised into *surface damage* and *bulk damage*. Surface damage is caused by ionising radiation such as photons, X-rays and charged particles and occurs in the Si-SiO₂ interface. Radiation-generated electrons will diffuse out of the oxide layer, while holes, with their much smaller mobility, will remain there, creating a positive charge region attracting electrons to the Si-SiO₂ interface and influencing the electric field in this area between the pixel implants. Consequently, to achieve, that the sensor performance is not influenced by surface damage, the changes in the electric field need to be taken into account in the sensor design. Instead, the bulk damage highly influences the sensor performance by altering the crystal structure properties. The change in the lattice structure is not reversible. High energetic particles damage the crystal lattice by displacing the atoms within the lattice, resulting in atoms between regular lattice sites, so-called *interstitials*, and empty lattice sites, so-called *vacancies*. When interacting inside the silicon bulk, the incident charged particle transfers energy to the nuclei, thus removing the atoms from the lattice, resulting in additional energy levels within the band gap, that act as recombination centers. The

amount of energy needed for the displacement is 13-20 eV per atom in silicon [50]. The vacancies in the crystal lead to an altered doping concentration within the silicon and reduce the charge carrier lifetime, as well as the measured charge in the case, that the drifting charge carriers are captured by the induced vacancies. The consequences are discussed in the following.

Effect on the depletion voltage Due to the fact, that a change in the effective doping concentration after irradiation has an impact on the depletion voltage, as shown in Equation 2.5, radiation in p-type material induces an increase of N_{eff} and consequently increases the voltage needed to be applied for fully depleting the sensor. An example of the depletion voltage as a function of the absolute effective doping concentration and irradiation fluence is shown for an n-type 300 μm thick sensor in Figure 2.5. In case of an n-type bulk material, which is implemented in the sensors of the current ATLAS pixel detector, the altering of the effective doping concentration results in a so-called *type inversion*, a change from an n-type to a p-type bulk material. This phenomena is explained by the radiation-induced constant removal of donor atoms and a generation of additional acceptor atoms, shifting the space charge first down to an intrinsic level and then up to the one of a p-type material. Therefore, in the n-type material, the depletion voltage first drops and then increases after type inversion. Instead, in the p-type material, the depletion voltage always increases with fluence.

Effect on the leakage current Radiation-induced defects increase the sensor current when interstitials or vacancies in the energy levels close to the band gap are generated. Electrons from the new energy levels are then able to be excited into the conduction band. The leakage current changes with particle fluence, as described by the linear function:

$$\Delta I_{\text{leak}} = \alpha \Delta \Phi V \quad , \quad (2.16)$$

with α as the proportionality factor for the current related damage rate, V the sensor volume and ΔI_{leak} the difference of the leakage current before and after irradiation to a fluence Φ . For detector operation, an increased leakage current after irradiation is bad, as it leads to an increased noise contribution and power consumption. Moreover, an increased leakage current results in constant heating and possible destruction of the sensor, due to the so-called *thermal runaway*. To decrease the leakage current after irradiation, the detector needs to be cooled.

Effect on the charge collection efficiency The radiation-induced recombination centers in the energy levels are able to capture the charge carriers (trapping) on their way to their corresponding electrode for a time of the order of μs and to re-emit them afterwards (de-trapping). The free charge carriers are trapped with a probability of $1/\tau_{\text{eff},e,h}$ (inverse trapping time). In case of a shorter trapping time than charge collection time, the height of the charge signal and the amount of collected charge are reduced. The degradation of the collected charge $Q_{e,h}$, arising from the induced trapping centers, can be expressed with Equation 2.14 by [30]:

$$Q_{e,h}(t) = Q_{0,e,h} \exp\left(-\frac{t}{\tau_{\text{eff},e,h}}\right) \quad \text{with} \quad \frac{1}{\tau_{\text{eff},e,h}(\Phi)} = \frac{1}{\tau_{\text{eff},e,h,\Phi=0}} + \beta_{\text{trap}}\Phi \quad (2.17)$$

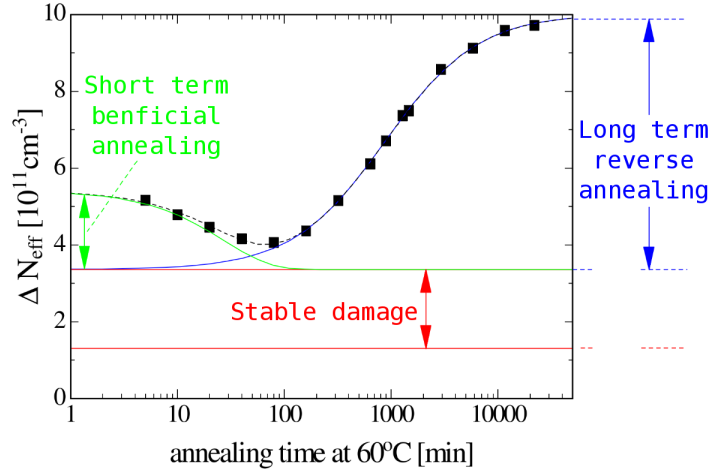


Figure 2.6: Variation of the effective doping concentration $|N_{\text{eff}}|$ as a function of time after annealing at 60°C . Figure taken from Ref. [51].

during t and $\tau_{\text{eff},e,h}$, inversely proportional to Φ . The term $\beta_{\text{trap}} > 0$ is a trapping related damage parameter. It is different for electrons and holes and dependent on the type of particle for irradiation. Hence, trapping of the charge carriers after high irradiation leads to a reduction of the charge collection efficiency, which is defined as the ratio of the collected charge after irradiation to the full collected charge before irradiation. It becomes especially relevant after an exposure to irradiation fluences above $10^{15} \text{ n}_{\text{eq}} \text{ cm}^{-2}$. The inefficiencies in charge collection significantly contribute to inefficiencies in particle detection in the tracking devices at the fluence levels expected at the HL-LHC.

2.3.2 Annealing of defects

Thermal energy allows for a growth of the mobility of the non-static interstitials or vacancies within the crystal and for partial restoration of the original crystal lattice structure over time. Radiation-induced interstitials recombine with the vacancies. This process is called *annealing*. Due to the fact, that the mobility increases with temperature, the speed of annealing depends on temperature. Consequently, annealing over t leads to a change of the effective doping concentration N_{eff} inside the sensor. The annealing is categorised into three types according to the Hamburg model [51]:

$$\Delta N_{\text{eff}}(\Phi_{\text{eq}}, t(T_a)) = N_a(\Phi_{\text{eq}}, t(T_a)) + N_c(\Phi_{\text{eq}}) + N_y(\Phi_{\text{eq}}, t(T_a)) \quad . \quad (2.18)$$

The annealing can be divided into time dependent and independent annealing. The damage constant N_c is only dependent on fluence, while the beneficial annealing N_a describes the behaviour on a short time scale and the reverse annealing N_y on a long time scale. In Figure 2.6, N_{eff} as a function of annealing time at a temperature of 60°C is shown. Up to a time of 80 min, beneficial annealing occurs with a decrease of N_{eff} , while afterwards reverse annealing occurs with an increase of N_{eff} , corresponding to an increase of the number of acceptor states. The depletion voltage increases with N_{eff} . Therefore, the depletion voltage is increased after reverse annealing with respect to the

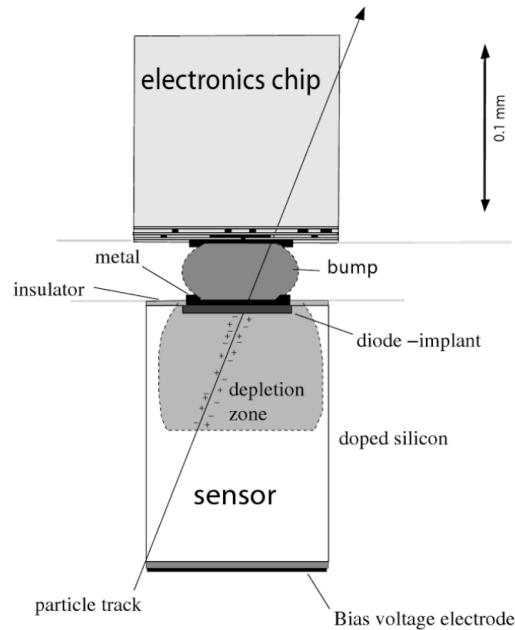


Figure 2.7: Schematic view of a pixel cell in a hybrid pixel detector. This detector is composed of a sensor and a readout chip interconnected via a bump ball in between the under bump metallisations on chip and sensor side. The figure is taken from Ref. [30].

beneficial annealing. Hence, it is mandatory to keep a controlled temperature below 0°C during detector operation to prevent reverse annealing. On the positive side, annealing is always beneficial for the leakage current, resulting in a decrease of the leakage current, scaled with the days of annealing, independent of beneficial or reverse annealing.

2.4 Pixel detectors in particle physics

Hybrid detectors are particularly beneficial in the LHC and the HL-LHC environment, given the fact, that they allow for a separate optimisation of the sensing and readout elements against radiation effects. A hybrid pixel detector is composed of a sensitive volume, the sensor, and a readout chip for processing the signal produced in the sensor. The fine segmentation results in good position resolution of the tracking devices. With solder bumps of diameter around $20\text{-}30\ \mu\text{m}$, which are deposited on each readout cell, a mechanical and electrical connection to the sensor cells is established. The interconnection method is known as *flip chipping*. For the deposition of the bump balls, an under bump metallisation (UBM) made of different metal alloys, depending on the production, is grown on the contact pads of both the readout chip and sensor side. On the UBMs on the chip side, bump balls are grown by electroplating with solder (Ag-Sn for most of the modules analysed in this thesis) and shaped into spheres by a reflow process. They create the electrical

Table 2.1: Example of a process flow for the production of n^+ -in-p silicon pixel sensors.

1	Thermal oxidation with SiO_2 on sensor surface
2	Photoresist layer on sensor front side
3	Photolithography on sensor front side for implant segmentation
4	Implantations of Phosphorus on sensor front side
5	Annealing of implanted ions for electrical activation
6	Silicon nitride and low temperature SiO_2 on sensor front side
7	Aluminium layer on the n^+ implants on sensor front side
8	Passivation layer on sensor surface in between the n^+ implants

connection between readout chip and sensor. To prevent from oxidation or diffusion of the bump balls into the UBM, gold is added in some productions on top of the UBM. The pixel cell size is defined by the size of the readout cell of the chip. For the currently implemented pixel sensors in the ATLAS detector, the pixel cells are $50 \times 250 \mu\text{m}^2$ and $50 \times 400 \mu\text{m}^2$. A schematics view of one pixel cell in a hybrid pixel detector is shown in Figure 2.7.

2.4.1 Pixel sensors

Pixel sensors, initially introduced as planar pixel sensors by the authors in Ref. [52], are composed of a lightly doped bulk material with highly doped implants on the sensor front (n^+) and backside (p^+) in the case of n^+ -in-n and n^+ -in-p planar sensors. The highly doped implants on the opposite sides with the lightly doped silicon bulk in between are characteristic for planar sensors.

The sensor is produced in such a way, that first the entire silicon surface of the wafer is polished by removing all natural oxide layers and then accurately thermally oxidised. As the next step, photoresist is deposited on the sensor surface and the front side is exposed to a mask to create openings in the photoresist in correspondence of the n^+ implants. The implanted ions are annealed to activate the dopants. Afterwards, silicon nitride and low temperature oxide (LTO) are deposited onto the front side of the wafer and etched away in a successive way in selected areas over the n^+ implants to allow for contacts of the implants through these isolation layers. Afterwards, a layer of aluminium is deposited over the pixel implants, to which it is contacted through the openings in the silicon oxide and nitride. As a last step, the sensor front side is protected with a passivation layer, left open in the area, where the contact to the chip bumps must be established [30]. The entire process flow for the production of n^+ -in-p silicon pixel sensors is summarised in Table 2.1. Electrons accumulate in these inter-pixel regions, being attracted by the fixed positive charge of the SiO_2 layer, especially after irradiation. This increases the amount of negative charge up to the n^+ pixel implantations and causes conducting n-channels between them, resulting in a creation of shorts on the sensor surface. To insulate the n^+ pixel implantations, a low dose Boron implantation is performed between the n^+ implants, leading to the creation of positive fixed charges, that compensate the electron layer. Three different solutions are presently available: p-stop, homogenous p-spray and moderated p-spray. In the solution of isolation by the p-stop method, a mask is used to create a p^+ layer in the central area between two implants, requiring an additional photolithographic step. Next

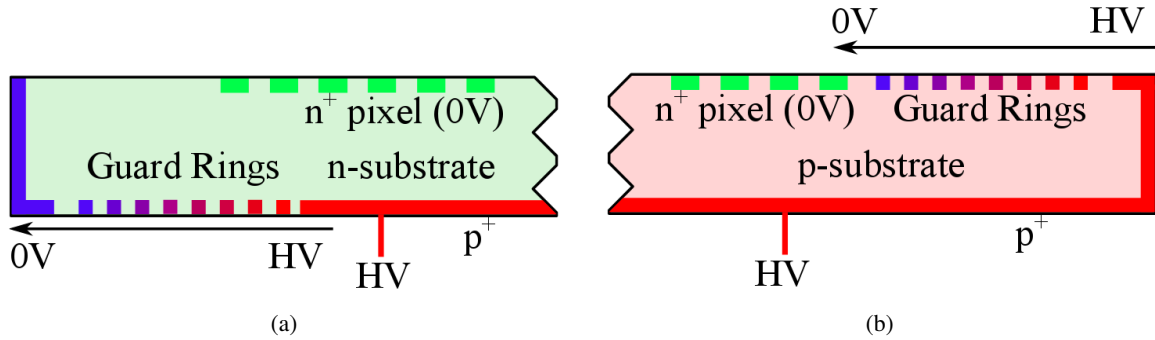


Figure 2.8: (a) n^+ -in- n sensor design with an n -type bulk and n^+ implants. The guard rings are situated on the backside. (b) n^+ -in- p sensor design with a p -type bulk and n^+ implants. Images taken from Ref. [53].

to the drawback in terms of cost due to an additional production step, it can be difficult to allocate space for the p^+ stop line for the small distances in between the pixels cells. The p -spray method prevents from these drawbacks with a homogenous low dose p -spray in between the pixel implants. However, the homogenous p -spray leads to a creation of high electric field regions between the p -doped silicon and the pixels. To prevent this problem, the doping concentration of the p -spray in the region close to the pixels can be reduced, the so-called moderated p -spray method. This method is currently employed in the ATLAS pixel detector.

Sensor concepts

The sensors are either built on an n -type or p -type material. In high energy physics either the n^+ -in- n or n^+ -in- p technologies are employed for pixel sensors. This is due to the fact, that n^+ implants act as the collecting electrode for electrons, generated in the bulk, in reverse bias mode. Electrons have a higher mobility compared to holes, resulting in a lower probability for the electrons to be trapped after irradiation. The n^+ -in- n technology is presently used in the ATLAS pixel detector, while the n^+ -in- p technology is foreseen to be implemented in the future ATLAS pixel detector. The layouts of both technologies are displayed in Figure 2.8, and discussed in more detail in the following chapter in Sections 3.1.2 and 3.2.2. One difference of the two technologies concerning the design is, that in the n^+ -in- n planar sensor technology the main junction is at the backside of the sensor, while in the n^+ -in- p planar sensor technology the main junction is located at the front side of the sensor. Consequently, the depletion in the different sensor types start at either the backside or the front side of the sensor. After irradiation of an n^+ -in- n sensor, type inversion changes the n -type bulk to a p -type bulk. The p - n junction moves to the front side and the depletion starts from the front side. Given the fact, that the main junction is on the backside, n^+ -in- n sensors need the guard ring structure, introduced in the following Section 2.4.1, to be implemented there, thus requiring a complete double-sided processing.

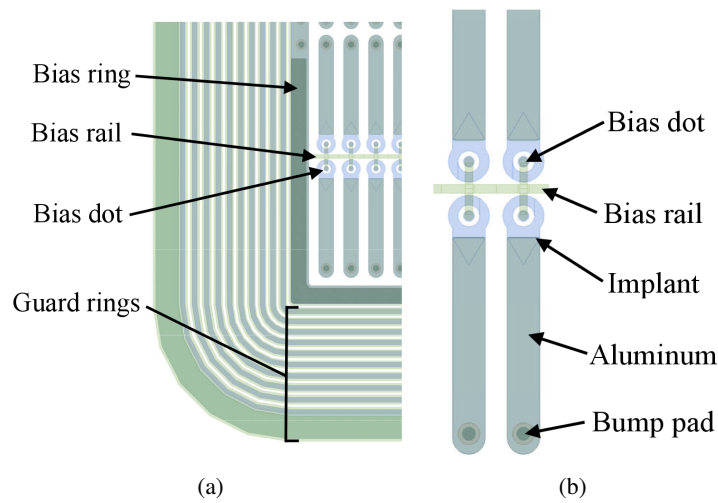


Figure 2.9: Layout of a pixel sensor: (a) cut-out of a sensor corner with GRs in the periphery of the active area of the sensor, (b) cut-out of four pixels from the active area of the sensor. A bias rail runs in between the short side of the pixels. It is situated on the same side as the bias dots, implemented either in an opening of the pixel implant (as shown in the figure) or in close proximity. Such design is called standard single punch-through design. On the other side of the pixel cell the bump pad for the interconnection to the readout channels is located. Images taken from Ref. [37].

Dedicated structures of the sensor

Guard ring (GR) structures are needed to achieve a smooth potential drop from the active area at ground to the region, where the high voltage is applied. In n^+ -in-p sensors the GRs are implemented on the front side, where the main junction is located. Increasing the number of GRs in the same area leads to smaller potential steps between them and to a reduction of the electric field.

The innermost GR is grounded for biasing purposes of the entire sensor and is therefore called *bias ring* (BR). Through the BR the electrical properties of sensors are tested before interconnection to readout chip. With this, rare damages are identified by increased leakage currents. The BR is connected to a *bias rail*, which runs between every second pixel column passing close to the pixel implants. The pixel implant itself derives its potential from the bias rail through a circular implant, the *bias dot*, which is located either in an opening of the pixel implant itself or in close proximity. The bias dots are always designed to be on the opposite site of the bump bond pads. The layout of the sensor surface with pixel implants and their biasing structure is shown in Figure 2.9.

To obtain an induction effect between different potentials, either in the area where the GRs are situated, or in the active area with the pixel implants, the so-called *punch-through effect* [30, 54] is used. With the punch-through effect the potential of the outer GRs decreases gradually from the ground potential of the innermost one, down to the value of the outermost one, that is very close to the negative high voltage applied at the backside. From the BR, the ground potential is transmitted to the connected bias rail and bias dots. The pixel implants are then lifted through the punch-through effect to a potential close to ground, but still negative. The potential difference between the bias dot and the pixel implant increases with the high voltage applied to the backside. This is due to the

fact, that the silicon bulk between the two parts acts like a dynamic resistance. After irradiation to high fluences, the punch-through design (p-t design) is found to influence the sensor hit efficiency, discussed in Section 5.2.4. The different biasing designs are presented in Section 5.1.

THE ATLAS PIXEL DETECTOR

In this chapter, the ATLAS pixel detector, the innermost sub-system immediately outside the LHC beam pipe, is described in more detail. Formerly built as a three-layer detector, the present ATLAS pixel detector was upgraded with a fourth layer, the Insertable B-Layer (IBL) [55], located closest to the interaction point. The three original layers, instrumented with ATLAS FE-I3 readout chips, interconnected to silicon n^+ -in-n planar sensors, are described together with the IBL components. The IBL modules are composed of ATLAS FE-I4 readout chips, successor of the FE-I3 readout chip, and sensors of two different technologies. The readout chips are described in Section 3.1.1, while the sensor technologies are described in Section 3.1.2. In addition to FE-I4 modules based on the planar sensor technology [52] and installed in the central region of the staves up to $|\eta| \approx 2.8$, the 3D sensor technology [56] is implemented in the modules covering the outer regions of the staves with $2.8 < |\eta| < 3.0$ [57].

The second part of the chapter focuses on the future ATLAS pixel detector for the ATLAS Phase II at HL-LHC, see Section 3.2. In this phase the ATLAS detector will have to cope with high irradiation fluences and higher occupancy of 200 inelastic proton-proton collisions per bunch crossing. The section begins with an introduction to the third generation readout chip, the RD53A, with smaller grid size and continues with a description of sensors with compatible pixel cell size implemented in the n^+ -in-p planar, the 3D and the CMOS technology. The thin n^+ -in-p planar pixel module concept was mainly developed at the Max-Planck-Institut für Physik (Werner-Heisenberg-Institut), from here on referred to as MPP, in collaboration with three semiconductor companies, see Section 5.1, and is introduced with a focus on small pixel cell sizes, thin sensors and sensors with reduced inactive areas in Section 3.2.2. All investigations and results presented in this thesis are based on the thin n^+ -in-p planar sensor technology.

3.1 Present pixel detector

The present pixel detector is made of 1456 modules, distributed in the three outer layers, named L_1 , L_2 and L_3 , at radii of $L_1 = 50.5$ mm, $L_2 = 88.5$ mm and $L_3 = 122.5$ mm. Additional 288 modules are located at the three disks at the forward and backward direction of the detector [58]. It was designed for an instantaneous luminosity of $10^{34} \text{cm}^{-2} \text{s}^{-1}$. Since during ATLAS Run 2 and

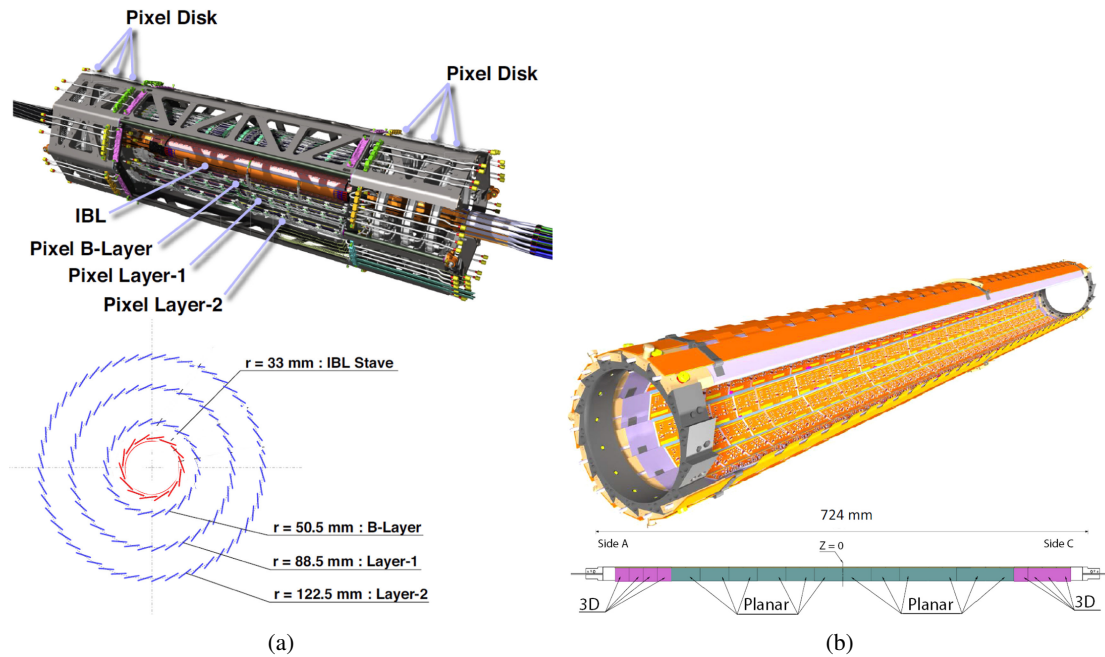


Figure 3.1: (a) (top) the current ATLAS pixel detector with its four layers and (bottom) the radial position of each layer. (b) (top) the IBL detector housing 14 staves depicted as a 3D schematic and (bottom) a sketch of the top-view of one IBL stave with the location of the two different module types. In the 3D schematic some staves are removed for a better visibility of the inner part of IBL. The images are adapted from Ref. [59].

Run 3, the luminosity is expected to increase up to a value twice the nominal one, resulting in a higher number of pile-up events, a fourth pixel layer was built to retain the performance of the pixel detector. The notions are introduced in Chapter 1. The additional IBL layer, with upgraded readout chip and sensor technology is located at a distance of 33.0 mm from the beam line. The 4-layer system of the pixel detector and the radial position of the barrel layers are illustrated in Figure 3.1a. With the insertion of the IBL and, hence, the addition of a further space point, the tracking performance was improved. Both pixel system are described in the following, starting with the readout chips and continuing with the pixel sensors.

3.1.1 ATLAS readout chips

In the three outer layers of the pixel detector, the FE-I3 front-end chip [60] is implemented in the 250 nm Complementary Metal Oxide Semiconductor (CMOS) technology and is used for the pixel readout. It is composed of 2880 readout cells with a $50 \times 400 \mu\text{m}^2$ pixel cell size, arranged in a 18×160 pixel matrix (18 rows and 160 columns) with an active area of $7.2 \times 10.8 \text{ mm}^2$. Rows describe the short direction of the pixel cell in y, while columns refer to the long pixel direction in x. In every readout channel an analogue component with a preamplifier is implemented and connected to each pixel via a bump ball. It amplifies the charge signal and processes it with a programmable discriminator threshold with an achievable minimum threshold value of 2.5 ke for single chip modules [61], where the height of the analog output signal is defined by the discharge of the feedback current. The discharge of the feedback current is nearly linear and results in a pulse

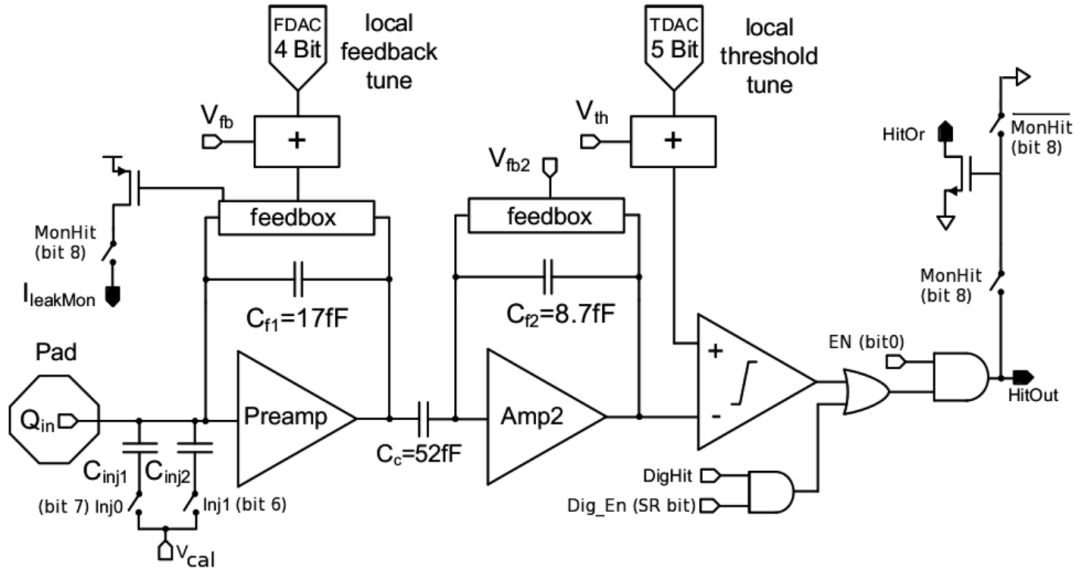


Figure 3.2: Schematic diagram of the FE-I4 pixel analog circuitry [66].

width proportional to the charge [10]. In addition, a digital circuitry is integrated recording the hit pixel address together with the period of time the signal is above threshold, in units of the chip clock of 25 ns. The width of the discriminator output, the Time over Threshold (ToT), of the hit is measured and stored in an 8-bit buffer at the chip periphery. A hit in a pixel is assigned for readout in case the trigger signal is matched within a timestamp interval of 25 ns. Since the FE-I3 readout chip is radiation hard up to a lifetime dose of 50 MRad or a fluence of 10^{15} $\text{n}_{\text{eq}} \text{cm}^{-2}$ [62], the successor, the FE-I4 readout chip [63], was designed to retain the performance in terms of occupancy and rate capabilities after an irradiation to a fluence of $5 \cdot 10^{15}$ $\text{n}_{\text{eq}} \text{cm}^{-2}$. This was achieved by avoiding minimal size transistors and systematically using GRs for analog and sensitive digital circuitry [64]. The FE-I4 readout chip is manufactured in 130 nm CMOS technology with an active chip surface of $16.8 \times 20.2 \text{ mm}^2$. With the increased number of 80 columns and 336 rows, the FE-I4 active chip surface with 26 880 pixels is larger than the one of the FE-I3, resulting in a reduction of the costs for flip chipping. The pixel pitch in the beam direction is reduced to $250 \mu\text{m}$, forming a pixel cell size of $50 \times 250 \mu\text{m}^2$, thus reducing the occupancy per channel at the same particle fluence. As for the FE-I3, it is composed of an analog and digital part, with two main differences: the amplifier of the analog component is optimized for low noise and low power operation with fast rise time, allowing for a decrease of the threshold down to 1 ke. The digital component is shared among four readout channels instead of a single one. The transmission data rate is with 160 Mb/s four times larger than in the FE-I3 chip [65]. Figure 3.2 illustrates the analog circuitry of a pixel in the FE-I4 chip in a two-stage amplifier configuration with a preamplifier and an amplifier. The amplification is done in two stages to provide enough gain in front of the discriminator. For analog calibration injection for tuning and testing capabilities, two selectable capacitors with two different capacitances are implemented.

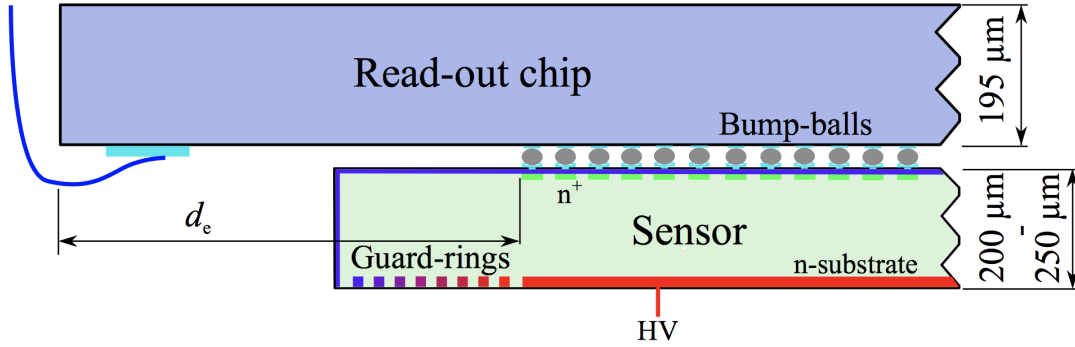


Figure 3.3: The present ATLAS module displaying a sensor in the thickness range from 200 μm (FE-I4 sensor) to 250 μm (FE-I3 sensor). Figure taken from Ref. [67].

3.1.2 ATLAS pixel sensors

The ATLAS pixel sensors are based on two silicon pixel technologies. The n^+ -in-n planar sensor technology is implemented in the sensors of the three outer layers of the pixel detector, as well as in 75% of the IBL, while sensors using the 3D sensor technology equip the outer parts of the IBL.

Planar sensors

The n^+ -in-n planar sensor technology is the sensor technology implemented in the ATLAS pixel detector. The FE-I3 pixel sensors of the three outer layers consist of a 250 μm thick n-doped bulk, while the upgraded pixel sensors of the IBL consist of a thinner 200 μm thick bulk. The bulk is made of oxygenated Float Zone (FZ) silicon for better resistance against charged particle radiation [68]. The front side of the sensor is highly doped with n^+ implants, defining the size of the pixel cell with the size of the n^+ implants. The isolation of the pixel implants is achieved with moderated p-spray, where a higher p-spray dose is implanted in the center area between two pixels through an opening of the nitride layer. The backside has a uniform p^+ implant and forms, together with the patterned n^+ implant on the front side, parallel electrodes. This is the key feature of the planar sensor technology for the present ATLAS module. The present ATLAS module is illustrated in Figure 3.3. In the outer three layers the modules are composed of a sensor interconnected to FE-I3 readout chips. The sensor has a pixel cell size of $50 \times 400 \mu\text{m}^2$ organised in a 328×144 pixel matrix plus additional slightly larger pixels in the outer 16 columns with a cell size of $50 \times 600 \mu\text{m}^2$. The sensor is manufactured in such a way, that it can be interconnected to a total of 16 readout chips. With this, it makes up an active sensor area of $16.4 \times 60.4 \text{ mm}^2$. In case of FE-I4 sensors, the sensors are designed to be interconnected to two readout chips with an active sensor area of $16.8 \times 40.9 \text{ mm}^2$ with two columns at the edge and two columns in the middle of the double chip employing longer pixel cells of $50 \times 500 \mu\text{m}^2$. As in the FE-I4 readout chip, the pixel pitch of the FE-I4 sensor is reduced to 250 μm in the beam direction, forming a compatible pixel cell size of $50 \times 250 \mu\text{m}^2$, to achieve a lower hit occupancy per pixel together with a better resolution in the beam direction. A biasing network [69], in which every single pixel is connected to a common BR via a bias dot, supplies the high voltage via the punch-through effect. In the FE-I3, as well as in the FE-I4 sensors,

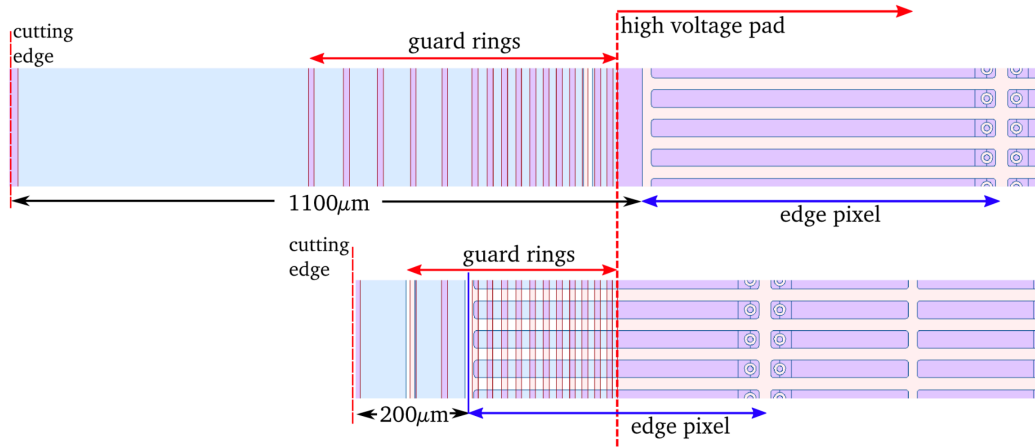


Figure 3.4: (top) the current ATLAS sensor design and (bottom) the IBL sensor design, adapted from Ref. [66]. The front side and the guard rings on the backside of the sensor are superimposed.

every pixel cell hosts its own bias dot. A difference between the two designs lies in the number of implemented GRs on the sensor backside, where the GRs control the potential drop from the high voltage applied in the area within the innermost GR on the backside, to the ground potential at the edges and the front side. The FE-I3 sensor hosts 22 GRs. This results in a dead area of 1.1 mm. Instead in the FE-I4 sensor, the inactive region was decreased to $200\mu\text{m}$ in the column direction and to $450\mu\text{m}$ in the row direction by reducing the number of GRs to 13 and by partially shifting the rings, situated on the backside, underneath the outermost n^+ implants, situated on the front side, see Figure 3.4. Consequently, the inactive area is smaller in the FE-I4 sensor.

3D sensors

In the planar sensor technology (Figure 3.5a) the minimum distance between the two electrodes is limited by the minimal achievable active thickness of the sensor. In contrary, the 3D sensor design exhibits a technology decoupling the active thickness of the sensor from the electrode spacing. With this, the drifting distance of the generated electron/hole pairs in the bulk is reduced without an effect on the charge signal. Before irradiation, the amount of collected charge is the same for planar and 3D sensors, as long as they employ the same sensor thickness. The IBL 3D sensor design is accomplished by inserting electrodes perpendicular to the sensor surface into the p-type bulk. The p-type substrate is chosen to prevent the bulk from type inversion after high irradiation fluences. The electrodes are produced by etching narrow columns into the bulk substrate using Deep Reactive Ion Etching (DRIE) [70] and subsequently doped with n^+ and p^+ implantations, where in a single pixel cell two n^+ columns are surrounded by in total six p^+ columns. An electric field is generated between oppositely doped neighbouring columns, as depicted in Figures 3.5b. The spacing between the n^+ columns defines the pixel cell size, while the spacing between the oppositely doped columns defines the charge collection distance. In the case of the modules implemented in the IBL, they employ the FE-I4 pixel cell size of $50\times 250\mu\text{m}^2$ and a charge collection distance of $67\mu\text{m}$. In the IBL, 25% of the modules are produced with the 3D sensor technology, populating

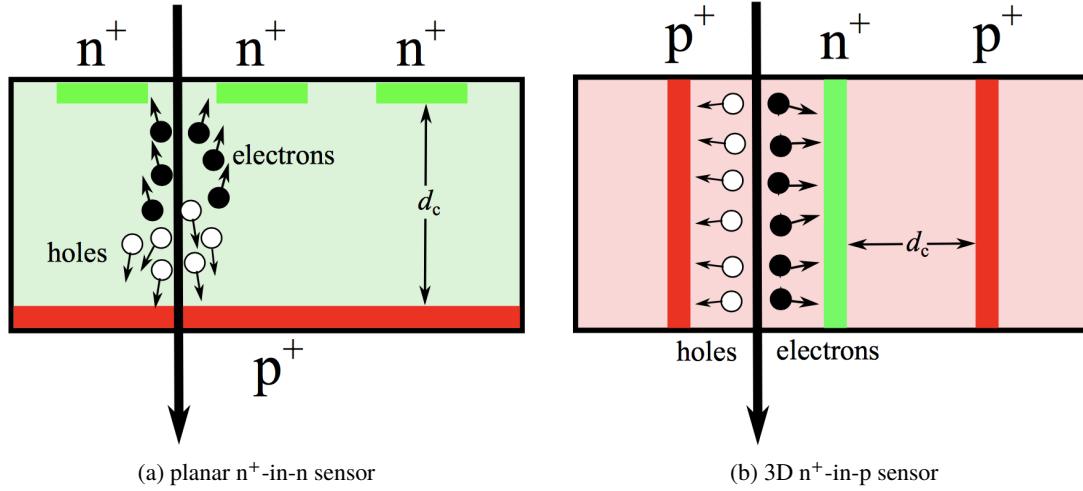


Figure 3.5: The two sensor technologies: (a) planar n^+ -in- n and (b) 3D n^+ -in- p sensors. The n^+ electrodes are illustrated in green, while the p^+ electrodes are coloured red. In the IBL, the charge collection distance d_c is $200 \mu\text{m}$ for the planar sensors and $67 \mu\text{m}$ for the 3D sensors. Images taken from Ref. [37].

the outer parts of the staves. The 3D modules of IBL employ $230 \mu\text{m}$ thick sensors and are produced by two silicon processing facilities: Centre Nacional de Microelectronica (CNM) [71] and Fondazione Bruno Kessler (FBK) [72]. Both sensor technologies are illustrated in Figure 3.6 and employ the double-sided processing, but mainly differ in the etching process of the doped columns. Etching of full-through columns is performed at FBK, while etching of partially-through columns of $210 \mu\text{m}$ length is performed at CNM. The partially-through column sensor design allows for a collection of the generated electron/hole pairs in the remaining column free and consequently active bulk of $20 \mu\text{m}$. As a drawback, the partially-through columns introduce a lower electric field after irradiation.

With its decoupled electrode spacing, 3D sensors are advantageous in terms of lower depletion voltages compared to the planar sensors, especially after high irradiation fluence. The resulting lower operational bias voltage leads to a decreased power dissipation. The main disadvantage is the low production yield of 60% calculated on 50 wafers [73] produced for the IBL, caused by the complex 3D sensor fabrication.

3.2 The ITk pixel detector

For the upcoming challenges posed by the HL-LHC especially for the innermost layers of the pixel detector, the currently implemented pixel technologies will not be capable to maintain their tracking and b-tagging performance. Consequently, the present pixel detector will be replaced using modules with upgraded sensor technologies. This will reduce the material budget and consequently the multiple scattering within the tracking devices. The total pixel detector surface, foreseen to be approximately 14 m^2 , will be almost 10 times larger compared to the current pixel detector employing a total surface of 1.73 m^2 [29]. The detector will employ modules with decreased sensor

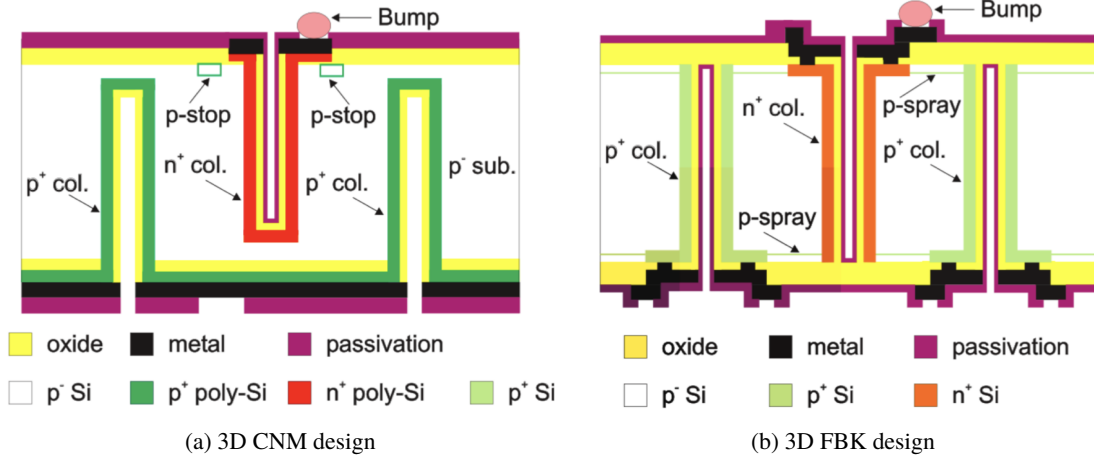


Figure 3.6: Schematics of the two 3D sensor options presently operational in the ATLAS IBL. The 3D sensor (a) with columns, etched partially through the bulk (CNM design) and (b) with full-through columns (FBK design). Both sensors are processed double-sided. The 3D sensor designs are taken from Ref. [66].

thicknesses, as well as finer pixel cell granularity. The new modules are designed to be able to withstand a radiation fluence in the order of $10^{16} \text{ n}_{\text{eq}} \text{ cm}^{-2}$. The future ATLAS pixel detector will consist of five barrel layers at radii of 39 mm, 99 mm, 160 mm, 220 mm and 279 mm for the five successive layers L_0 to L_4 [29]. Due to the harsh radiation environment over the full HL-LHC run period, the ITk detector will be built in such a way, that it will be possible to replace the two innermost pixel layers after around half the HL-LHC lifetime. In this scenario, the highest fluence in L_0 is expected to be $1.4 \cdot 10^{16} \text{ n}_{\text{eq}} \text{ cm}^{-2}$ and $3\text{-}4 \cdot 10^{15} \text{ n}_{\text{eq}} \text{ cm}^{-2}$ in L_1 . The fluence in the outer layers is expected to be $3 \cdot 10^{15} \text{ n}_{\text{eq}} \text{ cm}^{-2}$ [29]. An inclined layout option, with a pseudo-rapidity coverage up to $\eta = |4|$, is foreseen. A schematic of the pixel detector layout, designed to avoid long clusters and reduce the occupancy as well as the material crossed by charges particles, is shown in Figure 3.7. The 3D sensors are the baseline in the innermost layer and planar sensors in the four outermost layers. The planar sensors will be based on a thinner bulk of $100 \mu\text{m}$ in layer 1 (L_1) and of $150 \mu\text{m}$ in layer 2 to layer 4 ($L_2\text{-}L_4$). In the innermost layer (L_0) single, double and quad chip modules with single 3D sensors are foreseen. Instead, the remaining barrel layers will hold double and four chip modules employing the planar sensor technology with a novel module concept, mainly developed at MPP [74], based on thin n^+ -in-p planar pixel sensors. For a potential cost reduction, CMOS active devices are a promising candidate to instrument the large area of the fifth barrel layer. Close to the interaction point, a small pixel cell size and slim edge sensors are essential to cope with the increased particle density and to avoid a large fraction of inactive sensor area. In hybrid pixel modules not only sensors have to withstand the upcoming challenges, therefore a new readout chip, the RD53A readout chip [75], was developed. In the following, the RD53A readout chip is introduced together with the possible sensor technologies.

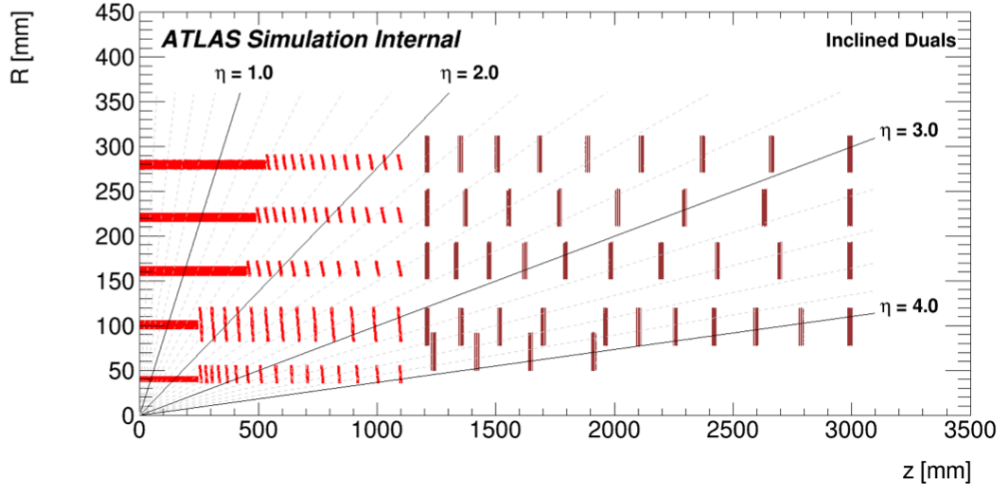


Figure 3.7: A possible schematic layout of the pixel detector for Phase II taken from Ref. [29]. It represents the inclined layout with a pseudo-rapidity coverage up to $\eta = |4|$. The horizontal axis is parallel to the beam line, while the vertical axis is the radius from the the beam line at $R = 0$ in the diagram. Only the active detector elements of the first quadrant are shown.

3.2.1 RD53A ATLAS readout chip

The RD53A readout chip is implemented in the 65 nm CMOS technology and developed by the RD53 Collaboration [76] to sustain three main challenges: radiation tolerance, high hit rate capabilities and stable low threshold operation. It is designed to be radiation tolerant at least up to a total dose of 500 MRad. To maintain the present level of occupancy also at the high particle multiplicity of the HL-LHC, the chip cell size is chosen to be $50 \times 50 \mu\text{m}^2$ with a larger number of readout channels with respect to the present readout chip. For the prototype the 76 800 readout channels are distributed over 400 columns and 192 rows resulting in a chip size of approximately $20 \times 10 \text{ mm}^2$. Furthermore, the output bandwidth will be increased up to 5.12 Gb/s per readout chip [29]. Low threshold operation to values down to 800 e will allow for detection of smaller signals [77]. The RD53A readout chip will be compatible with both $50 \times 50 \mu\text{m}^2$ and $25 \times 100 \mu\text{m}^2$ sensor cell sizes. After this first prototype, a final ATLAS readout chip will be developed with increased dimensions of approximately $20 \times 20 \text{ mm}^2$ to reduce cost and fabrication time. To reduce the amount of additional inactive material, a serial powering scheme will be implemented resulting in a reduced number of cables in the ITk.

3.2.2 Planar module concept for the upgraded detector

N⁺-in-p planar sensors The n⁺-in-p planar sensor technology is the chosen technology to be implemented in the modules instrumenting the detector layers L₁ to L₄ for the ITk. Due to its simplified process flow with a single-sided processing, it represents a cost-effective option with respect to the double-sided processed n⁺-in-n planar sensors currently implemented in the ATLAS pixel detector. The GR structure is implemented together with the n⁺ pixel implants on the front

side of the sensor. Since this side is interconnected to the readout chip, the ground potential of the readout chip is transferred to the pixel implants. With the GR situated at the sensor edge and being on a potential different to ground, sparks can occur between the readout chip and the sensor edge. This especially happens in case high bias voltages are applied after irradiation without protection measures. Different to the n^+ -in- n sensor technology, the module needs a further isolation layer between sensor and chip. Possible explored solutions are a Benzocyclobutene (BCB) deposition either on sensor or readout chip before interconnection or Parylene coating, performed at module level, to ensure operation at high bias voltages. The description of these technologies is given in more detail in Section 5.1.

Thin sensors As an important attribute for high hit efficiency and low power consumption after high irradiation fluences, the active thicknesses of the sensors need to be adjusted depending on the irradiation fluence they are exposed to. As discussed in Section 2.3.1, charge trapping in the silicon bulk occurs after high irradiation and is one of the main reasons for charge loss after irradiation. Reducing the sensor thickness results in a shorter collection time and hence in a lower probability for the charge to be trapped, while drifting to the electrodes. In addition, the needed operational bias voltage is reduced in thinner devices. As a result, the power dissipation is reduced, as well. Planar sensors with $150\ \mu\text{m}$ thickness are chosen to instrument L_2 - L_4 of the ITk, while for L_1 $100\ \mu\text{m}$ thick sensors are necessary to meet the requirements on the power dissipation at around half the LHC lifetime.

Slim and active edges Thin n^+ -in- p planar sensors can be processed with an extension of the backside implantation to the sensor edge. The side implantations can be performed thanks to trenches, that are etched at the sensor perimeter. With this process, the depleted region widens and creates activated vertical sides. The smoother field shape at the edges with respect to standard sensors without side activation also helps to decrease the number of GRs needed and consequently to increase the active area. This is important, given the fact, that in the ITk, sensors with slim edges of below $200\ \mu\text{m}$ are required especially in the innermost region close to the interaction point, to allow for minimal inactive areas at the peripheries of the module for high tracking efficiency.

Bias grid For the quality assurance of the sensor before interconnection to the readout chip, a biasing structure is implemented on the sensor front side. It allows for grounding all pixel implants of the sensor by an additional implementation of punch-through structures (p-t structures). It was measured, that the p-t structures induce a decrease of the collected charge in the area, where they are implemented, especially after irradiation, see Sections 5.2.2 and 5.2.4. As the resulting efficiency loss has an even larger effect on small pixel sizes, due to the fact that a larger fraction of the pixel cell is occupied by them, an alternative bias grid, created with a temporary layer, is investigated for the future sensor productions. The temporary layer is used for shorting all pixels to measure the leakage currents before interconnection and removed before further processing and interconnection to the readout chip. In this thesis, the focus is on the development and performance of bias grids with different implementations of p-t structures.

Smaller pixel cell size with RD53A To guarantee the compability of the sensor to the RD53A chip with a grid of $50 \times 50 \mu\text{m}^2$, as well as to maintain the performance of the pixel detector at high particle densities, the pixel cell size of the sensors is designed to be $50 \times 50 \mu\text{m}^2$ or $25 \times 100 \mu\text{m}^2$. The reduced pixel cell size will have the further benefit of a better position resolution in the ITk.

3.2.3 Pixel module concept for the upgraded detector

Along with the n^+ -in-p planar pixel modules, 3D modules are foreseen to instrument the future ATLAS pixel detector. Due to the higher operational voltage and the resulting higher power dissipation of planar pixel modules in a high radiation environment of around $10^{16} \text{ n}_{\text{eq}} \text{ cm}^{-2}$, the 3D sensor technology is chosen as the baseline for the innermost layer, L_0 . The relatively small area to be covered in the innermost layer can only be marginally affected by the lower yield and high production costs of 3D sensors. As well as for the planar pixel modules, the pixel cell size is assigned to be either $50 \times 50 \mu\text{m}^2$ or $25 \times 100 \mu\text{m}^2$, which further enhance their radiation hardness. This is explained with the fact, that at the same time the inter-electrode spacing, currently $67 \mu\text{m}$ in the FE-I4 compatible 3D sensors, will decrease to $28 \mu\text{m}$ or $35 \mu\text{m}$, depending on the pixel cell size chosen [78]. In both cases, this will result in a reduced trapping.

To further minimise the cost, CMOS devices [79] represent an option to cover the fifth barrel layer due to their estimated 4 times lower cost [29]. This technology is based on the approach, that pixel sensor and readout chip are integrated into one unit in contrast to hybrid pixel modules, where an expensive and labour-intensive interconnection procedure is needed. Since in terms of rate and radiation tolerance hybrid pixel modules are unrivaled, the CMOS technology is an option only for L_4 , an area with low occupancy and low irradiation level in the ITk.

SENSOR AND MODULE CHARACTERISATION

METHODOLOGY

In this chapter the experimental set-ups and methods used to characterise unirradiated and irradiated sensors before and after interconnection to readout chips are presented. The chapter begins with an introduction of the irradiation facilities used for the irradiation of the devices to high fluences. Afterwards, the chapter is divided into the introduction to characterisation methods for bare sensors, Section 4.2, and for modules, Section 4.3.

For bare sensors, the set-ups used for leakage current investigations, Section 4.2.1, as well as for charge collection and electric field examinations, are presented and discussed. The charge collection and electric field profiles are obtained by the edge transient current technique (Edge-TCT), with the measurement set-up being located at the Jožef Stefan Institute in Ljubljana. A discussion on how the data analysis is performed and a discussion of the statistical and systematic uncertainties in the obtained results, is conducted in Section 4.2.2.

For modules, the data acquisition (DAQ) systems are presented, employed in the tuning and operation of the pixel modules. It is followed by a description of the tuning procedure of the readout chips. The technique and the experimental set-up to measure the charge collection properties of the sensors at module level are summarised in Section 4.3.1. The chapter concludes with an overview of the facilities and equipment at beam tests in Section 4.3.2, including a discussion on the performed analysis methods to measure the performance of the module for the future ATLAS detector.

4.1 Irradiation facilities

4.1.1 TRIGA Mark II reactor of Jožef Stefan Institute

In the Reactor Centre of the Jožef Stefan Institute the TRIGA Mark II research reactor is hosted and is a light water pool reactor type, cooled by natural convection. It is used as source of neutrons in nuclear analytical techniques. Furthermore, neutron and gamma rays are used for irradiation of silicon detectors and related radiation damage studies of detector material and readout electronics for the ATLAS detector at CERN [80]. A continuous energy spectrum and a flux of fast neutrons

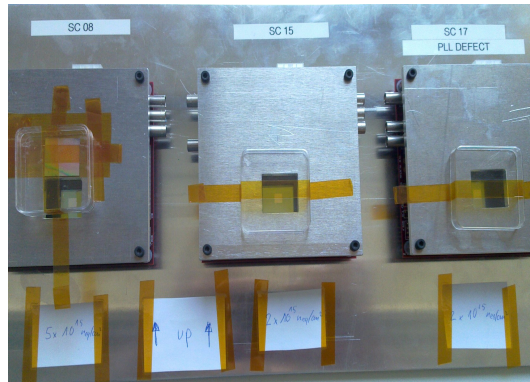


Figure 4.1: Photographs of the mountings of modules during irradiation at KIT. At KIT the modules are placed on an aluminium plate which is inserted into a cooling box. The modules are shielded by aluminium with an opening of $2 \times 2 \text{ cm}^2$ in the sensor area. A maximum number of two devices are placed behind each other.

with an energy larger than 100 keV allows for an irradiation up to $2 \cdot 10^{13} \text{ n}_{\text{eq}} \text{ cm}^{-2} \cdot \text{s}^{-1}$ at full reactor power of 250 kW in the very central channel out of 12 channels. There are 8 channels, in which the samples are vertically inserted and 4 horizontal channels [81]. The contribution of the fast neutrons is most significant to radiation damage for silicon detectors. It causes bulk damage in silicon through displacement of silicon atoms, leading to defects in the crystal lattice. Thermal neutrons with an energy smaller than 100 keV and gamma radiation do not have sufficient energy to displace a silicon atom. They can cause damage by triggering nuclear reactions with a release of fragments with sufficient energy. In pure silicon their contribution to bulk damage is small compared to fast neutrons [82].

The devices investigated in this thesis were irradiated in channel F19, where they are vertically inserted. In this channel the neutron flux is $1.5 \cdot 10^{12} \text{ n}_{\text{eq}} \text{ cm}^{-2} \cdot \text{s}^{-1}$ at full reactor power. For irradiation, the devices are placed inside irradiation tubes with a circular cross section of 2.2 cm diameter. The modules are irradiated without a printed circuit board (PCB) due to space and shielding limitations of the electrical components, which could lead to their activation. An irradiation to a fluence of $5 \cdot 10^{15} \text{ n}_{\text{eq}} \text{ cm}^{-2}$ takes approximately 50 minutes.

4.1.2 Compact Cyclotron at Karlsruhe Institute of Technology

The ZAG Zyklotron AG at the Forschungszentrum Karlsruhe of the Karlsruhe Institut für Technologie (KIT) is a proton compact cyclotron which provides a proton beam with a typical proton flux of $10^{11} \text{ p} \cdot \text{cm}^{-2} \cdot \text{s}^{-1}$ ($9 \cdot 10^{12} \text{ n}_{\text{eq}} \text{ cm}^{-2} \cdot \text{s}^{-1}$). The proton kinetic energy is 23 MeV [83]. During irradiation, the environment imitates the LHC operating conditions as close as possible. Fully assembled modules are set up in a thermally isolated box at -30°C and low humidity, ensured by a constant flow of cold nitrogen to avoid annealing during the irradiation.

The box is placed on a moving stage in front of the beam pipe in a distance of 30 cm. Full sensors and test-structures are stacked in frames inside the box. Maximum two device are placed behind each other, since the protons lose energy by passing through silicon. In contrast to the irradiation

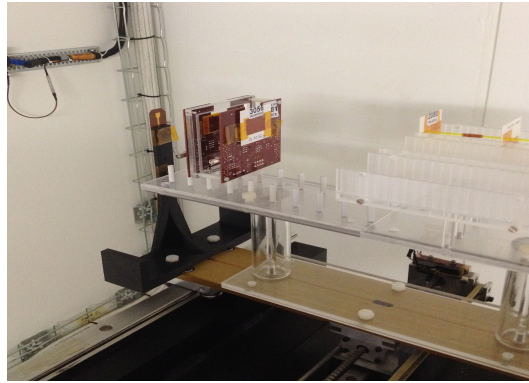


Figure 4.2: Photographs of the mountings of modules during irradiation at CERN-PS. At CERN multiple modules (in case of the shown irradiation in August 2015 there are two modules) are placed on a plastic frame behind each other fixed with plastic pins. The PCB does not have to be shielded, since the beam does not cover an area larger than $2 \times 2 \text{ cm}^2$.

at the TRIGA reactor the full modules including their PCBs, are irradiated directly avoiding the need to wire bond the chips to the PCBs again, as well as the possible consequent damage during handling. An aluminium mask is placed around the modules in front of the PCB cards, to shield the cards from activation with an opening at the area of the sensor. An image of three modules with aluminium shielding is shown in Figure 4.1. The box with the modules inside moves and is scanned along the surface of the modules. This achieves a uniform irradiation of the samples over a larger area than the one illuminated by the beam, with a spot size of around 7 mm diameter. The devices investigated in this thesis were irradiated to a maximum fluence of $5 \cdot 10^{15} \text{ n}_{\text{eq}} \text{ cm}^{-2}$ at ZAG. Higher fluences decrease the surviving probability due to damage induced in the readout chips by ionising radiation.

4.1.3 Cyclotron at the University of Birmingham

The Irradiation Facility at the University of Birmingham is using the Medical Physics MC40 cyclotron to provide a proton beam of 27 MeV, similar to the one at KIT. A $1 \mu\text{A}$ beam allows irradiated samples to receive a fluence in the range of $10^{15} \text{ n}_{\text{eq}} \text{ cm}^{-2}$ in 80 s with a fixed position of the beam. In case of a sample larger than the beam spot size of $1 \times 1 \text{ cm}^2$, the device is scanned with an automatic scanning system. With a typical current of 400 nA used for the irradiation of the devices investigated in this thesis, a fluence of $10^{15} \text{ n}_{\text{eq}} \text{ cm}^{-2}$ over the full sensor area is reached in 30 min. During irradiation the devices are kept in a temperature controlled cold box at -27°C , which continuously moves through the beam spot [84]. The chamber has a $150 \times 150 \mu\text{m}^2$ window on each side to allow beam entry and exit. The semiconductor sensors are mounted with kapton tapes on carbon fibre frames and then fixed on an aluminium plate, which is suspended from the chamber lid. Appropriately shaped nickel foils are placed in front of the samples to measure the fluence [85].

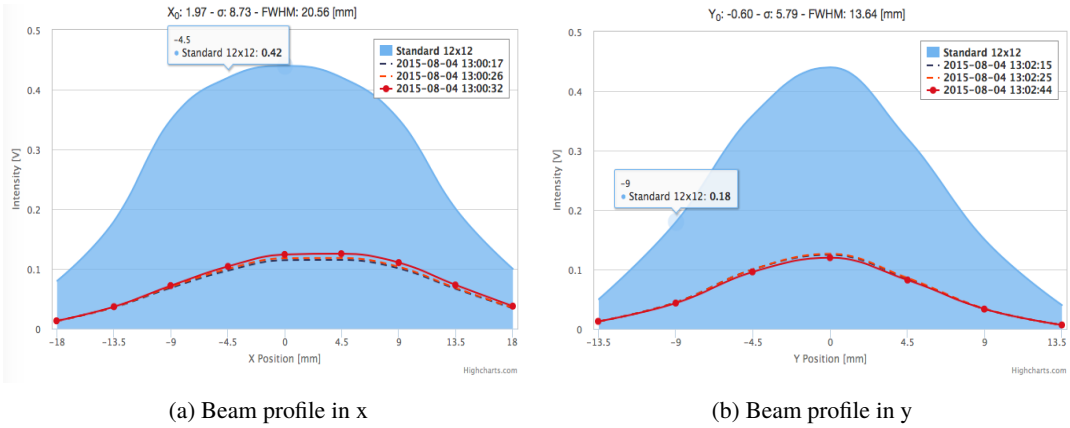


Figure 4.3: Measurements of the Beam Profile Monitor (BPM) at CERN-PS during irradiation for a module on August 4th in 2015. The sum of all voltages in the X and Y projections of the Gaussian beam profile is proportional to the integral of the proton spill. The integral of all readout channels corresponds to the beam intensity. The blue Gaussian is the beam shape at the focus position with a FWHM of $20.6 \times 13.6 \text{ mm}^2$, while the red line represents the last proton spill monitored. The beam profile in x is given in (a) and in y in (b).

4.1.4 CERN-PS irradiation facility

At the CERN proton synchrotron (CERN-PS) accelerator complex, the experimental zone, known as IRRAD, allows for the irradiation of samples in a proton beam. With a proton beam of 24 GeV proton energy and $1\text{-}3 \cdot 10^{13} \text{ n}_{\text{eq}} \text{ cm}^{-2} \cdot \text{h}^{-1}$ flux, it ensures a higher surviving probability of the modules irradiated to high fluences around $10^{16} \text{ n}_{\text{eq}} \text{ cm}^{-2}$. This is due to the lower total ionising dose (TID) given to the chip by the high energy protons, with respect to the 23-27 MeV protons at KIT and Birmingham. The irradiation takes place in the IRRAD bunker, which is subdivided into three zones according to the nature of samples to be irradiated: the first zone is dedicated to the irradiation of light materials, such as small silicon detectors. The devices are placed on tables, as shown in Figure 4.2, with remote-controlled stages, providing the possibility to position the device under test (DUT) with $\pm 0.1 \text{ mm}$ precision in the plane transversal to the beam axis [86]. For a better alignment within $\pm 0.025^\circ$, a possibility for rotation of the tables is additionally implemented. The size of samples possible during irradiation is about $2 \times 2 \text{ cm}^2$ limited by the beam spot allowing for a total irradiation of modules without dismounting them from their PCBs. The standard beam spot size covers an area of $12 \times 12 \text{ mm}^2$ and is made wider to maximum $2 \times 2 \text{ cm}^2$ by exploiting the natural divergence of the beam with an increased distance of the sample from the beam focus position. During irradiation, the profile of the proton beam is monitored by a custom-made Beam Profile Monitor (BPM). The beam has a maximum intensity of $5 \cdot 10^{11}$ protons per spill and the time duration between two spills is about 400 ms [87]. The output of the BPM is shown in Figure 4.3. It displays the last three proton spills as they are delivered from the proton synchrotron: the thick red curve is the last spill in the PS cycle, the other two lines are the two preceeding ones. This information is needed to get insight into the stability and variation from spill to spill. The blue Gaussian is the reference beam shape at the beam focus position with a FWHM of $12 \times 12 \text{ mm}^2$. An

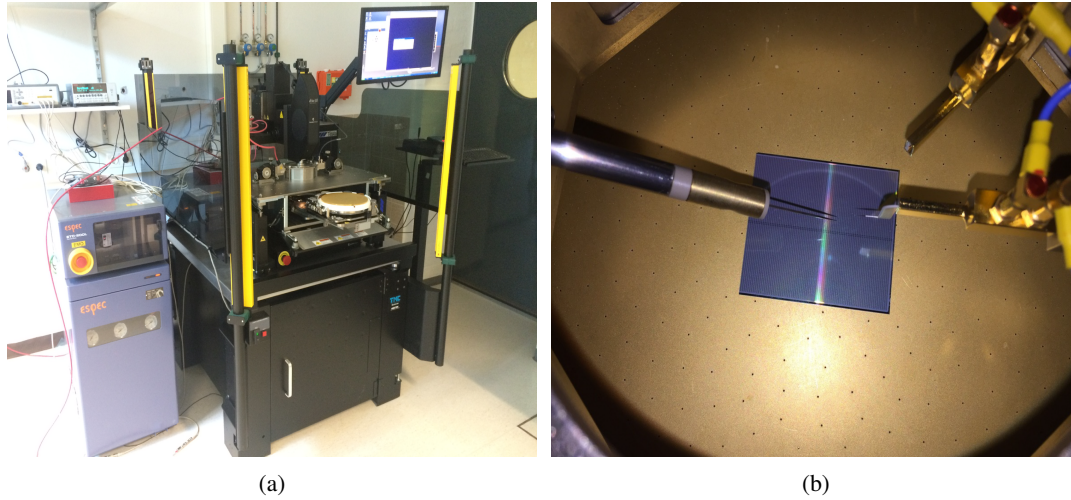


Figure 4.4: (a) the probe station and (b) the sensor inside the probe station placed at the center of the chuck with the HV-needle in contact with the sensor.

irradiation up to a fluence of $10^{16} \text{ n}_{\text{eq}} \text{ cm}^{-2}$ takes around 15 days due to the lower proton flux and is performed at room temperature.

4.2 Methodology for sensor characterisation

4.2.1 IV measurements

Before the interconnection of bare pixel sensors to readout chips, a first measurement of the leakage current of the bulk is performed as a function of bias voltage, named IV measurements. Measurements of bare sensors are possible, thanks to the implementation of the biasing structure. The measurements serve as an essential evaluation of the quality of the sensors of the different productions and allow for revealing defects of the devices, such as scratches on the surface of the devices that would result in high leakage currents. For the IV measurements, the APS200 TESLA semi-automatic 200 mm wafer probe station by Cascade Microtech, shown in Figure 4.4a, is used together with the Keithley 6517A or 6517B pico-amperimeters. The probe station offers the possibility to measure 4-inch to 8-inch wafers or diced sensors. Unirradiated sensors are measured at a temperature of 20°C , while the IV characteristics of irradiated sensors are tested in a range between -40°C and -25°C . The cooling system is connected to the probe station chuck, on which the sensor backside is placed. Through the chuck the high voltage is applied to the sensor backside. In turn, the sensor front side is kept at ground potential via the BR, which is contacted by a needle. The needle is placed on dedicated areas at the four corners of the BR, where the openings in the passivation layer are located to allow for electrical contact to the aluminium layer underneath. Ten consecutive measurements are performed at each voltage step to derive the mean and standard deviation of the leakage current.

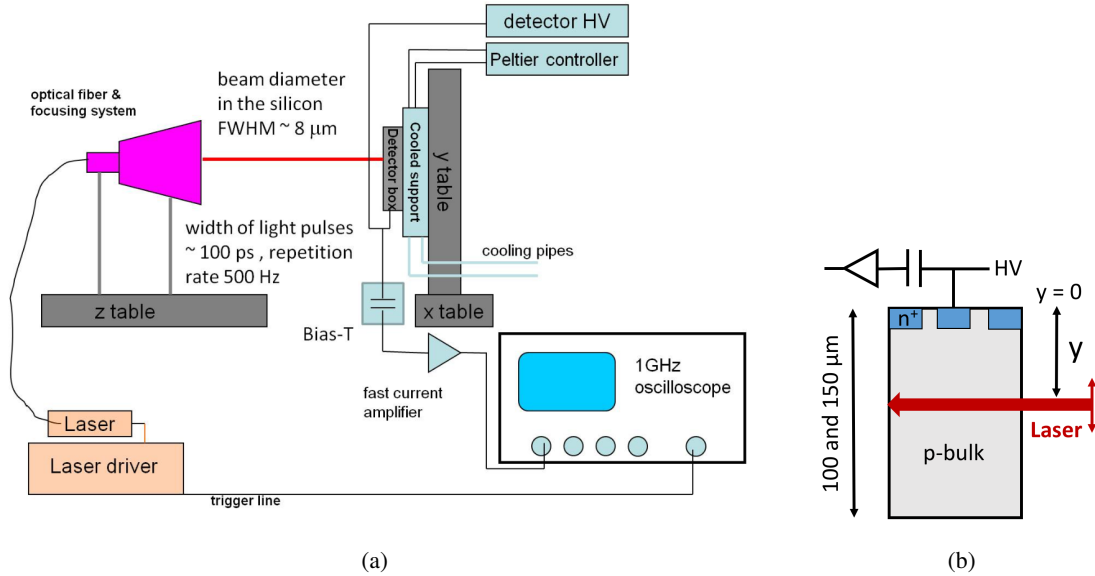


Figure 4.5: The Edge-TCT set-up from *Particulars* [88]: (a) schematics of the experimental set-up taken from Ref. [89] and (b) detector side view with an illustration of the laser beam penetrating at the detector edge.

4.2.2 Edge transient current technique

The edge transient current technique with a laser beam pointing at the sensor edge is a powerful method to get insights into the charge collection and electric field properties as a function of the sensor depth. The laser injection simulates a minimum ionising particle (MIP) in the real experiment. The extraction of the charge collection and velocity profile is based on the measurement of the time evolution of the induced current pulse. The technique, known as Edge-TCT, is described in this section, starting with an introduction to the instrumentation and data acquisition, followed by a description of the analysis chain.

Instrumentation and data acquisition

In Edge-TCT an infra-red laser with a small beam diameter of 8-12 μm at the focal point and a long penetration depth in silicon over 1 mm is directed onto the edge of the device. The device is a thin bare sensor of 100 μm and 150 μm thickness, and the laser beam is scanned along the sensor depth and the long direction of the pixel. The laser employs a wavelength of $\lambda = 1064 \text{ nm}$ with a pulse duration of 100 ps and 500 Hz repetition rate. The schematic of the Edge-TCT set-up is shown in Figure 4.5. Charge carriers, electron/hole pairs, are released inside the sensor and travel to their corresponding electrodes. An electrical signal induced by the movement of the charge carriers is amplified via an external 53 dB wideband charge amplifier [88]. The induced current pulse is analysed as a function of sensor depth to determine the collected charge, drift velocity and electric field in the pixel sensors.

Before measurements, sample preparation is performed. The sensor is precisely placed on top of

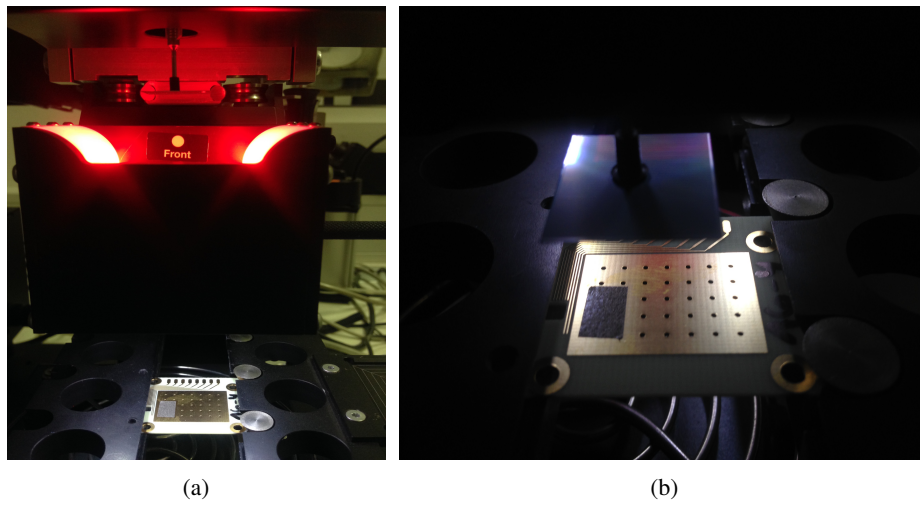


Figure 4.6: Placement of the sensor on the PCB via a manual component placement station [90] shown in (a) as a larger view and (b) as a zoom-in shortly before placing the sensor onto the PCB.

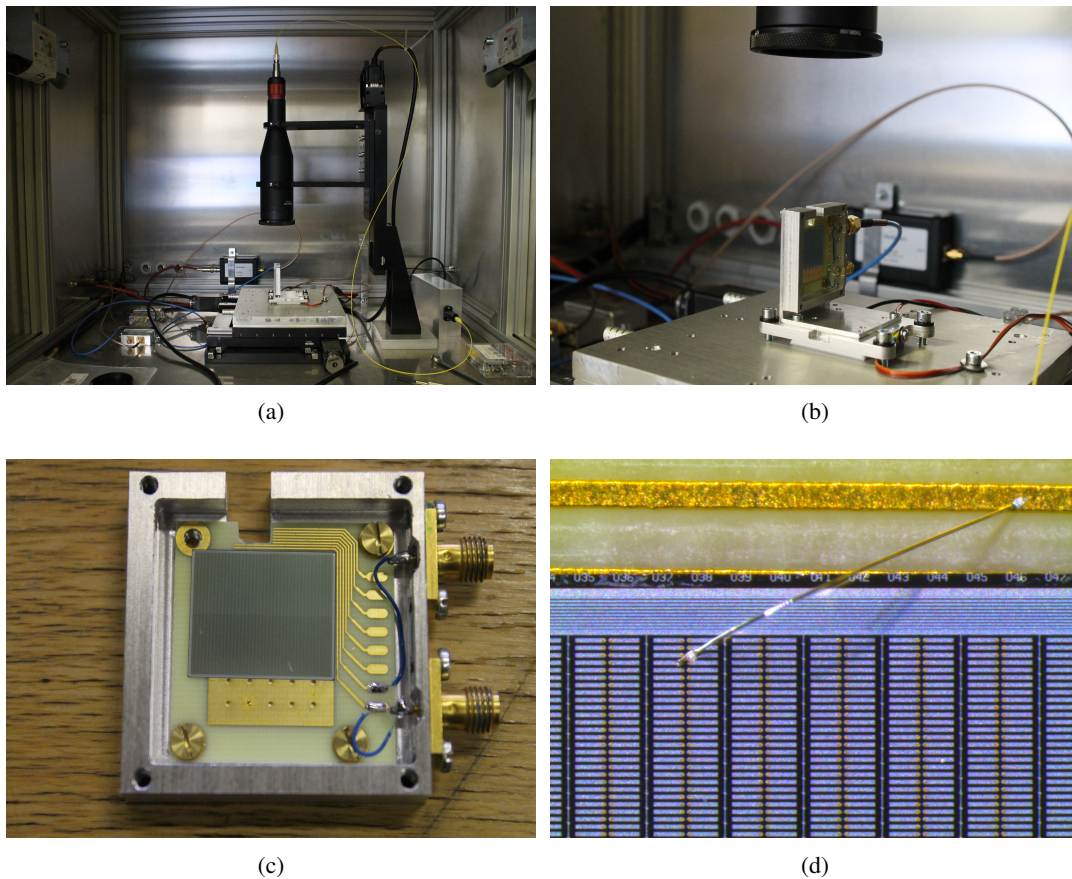


Figure 4.7: Photographs of the Edge-TCT set-up: (a) general view of the instrumentation, (b) placement of the detector with the laser beam pointing at its edge, (c) mounting of the device on a copper support and placement inside an aluminium frame with a connector for biasing and readout and (d) a microscope image of the sensor front side with one single pixel connected to readout via a wirebond.

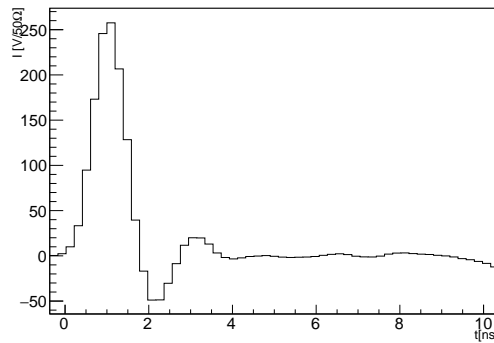


Figure 4.8: Induced current pulse at a position of $50 \mu\text{m}$ inside the sensor depth for a sensor with a thickness of $100 \mu\text{m}$ before irradiation. In the pulse shape, at increasing times, a peak, an undershoot and a tail is observed.

the PCB with a manual component placement station, illustrated in Figure 4.6. The sensor backside is glued to the PCB with a double-sided conductive tape, where the amount of glue-tape is chosen to cover $1/6$ of the sensor size to ensure appropriate hold but easy removal. Afterwards, the PCB with the sensor attached is screwed onto an aluminium support and fastened at the moving stage of the TCT set-up, as shown in Figure 4.7b. The support is thermally stabilized at room temperature for unirradiated samples and cooled to $-20^\circ \pm 0.1^\circ\text{C}$ via a $2 \times 40 \text{ W}$ Peltier element [88] for irradiated sensors using a custom made regulator. The position of the device in the laser beam is controlled by three orthogonal positioning stages in x (horizontal positioning along the long pixel side), y (vertical positioning along the sensor depth) and z (positioning along the laser beam) over the entire sensor thickness with sub- μm precision (Newport M-ILS100PP) [91]. The software, which allows for a remote control of the moving stages, high voltage supply, as well as acquiring the waveforms from the oscilloscope, is based on NI LabView¹.

All pixels on the front side are connected to high voltage via a wire bond attached to the BR, which is surrounding the pixels, while the sensor backside is set to ground. One single pixel is connected to readout and at the same time biased at high voltage via an additional wire bond on top of the $25 \mu\text{m}$ UBM opening on the pixel implant, which is shown in Figure 4.7d. The high voltage line from a Keithley 2410 high voltage power supply is connected to the PCB and a so-called Bias-T (Prosecong Pulse Labs, Model 5531) [92] decouples the AC current pulse from the DC high voltage through a capacitor and a resistor. The AC current pulse is then routed via a large-bandwidth amplifier (MITEQ AM-1309, 10 kHz-1 GHz) to a 1 GHz oscilloscope (LeCroy 950 WavePro), which averages over 400 laser pulses.

Ansatz of analysis

An example of the current pulse is shown in Figure 4.8 for a position $y = 50 \mu\text{m}$ inside an unirradiated sensor of $100 \mu\text{m}$ thickness. By integrating the induced current signal over time for

¹<http://www.ni.com/en-us/shop/labview.html>

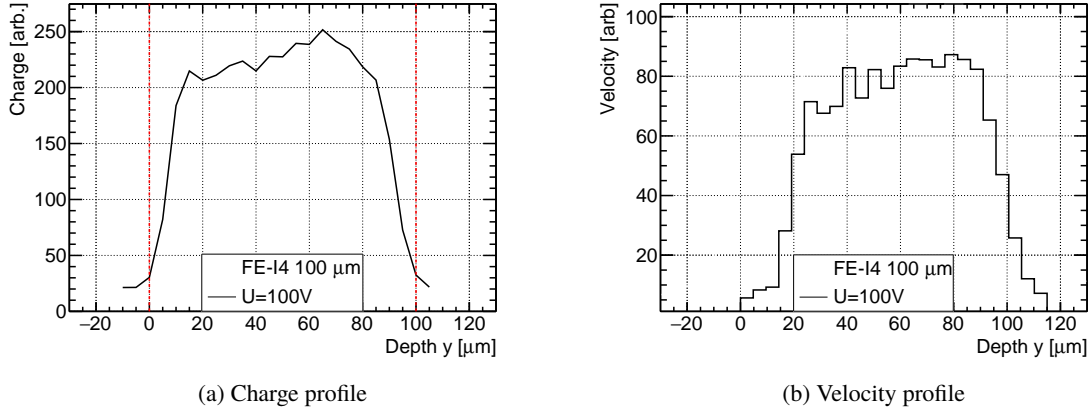


Figure 4.9: (a) collected charge (integrated current pulse over time) as a function of depth for a bias voltage of 100 V. The red lines indicate the sensor depth with front (lower depth numbers) and sensor backside. (b) charge carrier drift velocity profile calculated from the signal amplitude. Both measurements are performed using a not irradiated 100 μm thick sensor.

each injection depth y , the generated charge along the sensor depth is obtained:

$$Q(y) = \int_{t=0}^{t_{\text{int}}} I(y, t) dt \quad . \quad (4.1)$$

The window of the integration time needs to contain the full signal pulse but at the same time excluding imperfect impedance matching of electrical components. In this thesis, an integration time of 10 ns is used, where the value has been defined following the analysis described in Section 5.2.2 and from comparisons to previous measurements. Figure 4.9a represents an example of the collected charge along the sensor depth of a 100 μm thick sensor. The equation

$$\langle Q(y) \rangle = \frac{1}{d} \int_{y=0}^{y=d} Q(y) dy \quad (4.2)$$

describes the collected charge averaged over the depth y . The full sensor depth equals the sensor thickness d . At the time, when the carriers are generated in a single point location, trapping $\tau_{\text{eff},e,h}$ can be neglected, resulting in $\exp(-t/\tau_{\text{eff},e,h}) \approx 1$ and the induced current can be written as, following Equation 2.13 from Section 2.2.5

$$I(y(t)) = q N_{e,h} \frac{v_e(y_e) + v_h(y_h)}{d} \quad \text{and} \quad t = 0 \Leftrightarrow y = y_e = y_h \quad (4.3)$$

leading to the induced current being proportional to the sum of the drift velocities at a given depth $y = y_e = y_h$ at $t \approx 0$. If measured immediately after the pulse before the carriers drift away from the location of the laser beam, $v(y)$ is the velocity sum of the holes and electrons in depth y . Hence, it is possible to obtain the velocity profile from the increase of the signal in the very first ns. An example is shown in Figure 4.9b. From the velocity profile the electric field shape can be inferred.

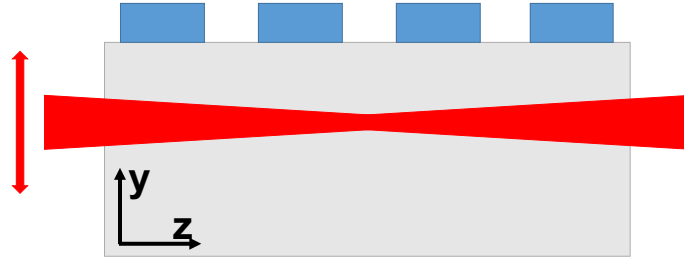


Figure 4.10: Typical case of focus finding. The sketch shows a sensor with the pixel implants as blue squares. The red area corresponds to the shape of the laser beam and the arrows represent the scanning axis in y and z .

Set-up calibration

For a correct interpretation of the results, the system needs to be calibrated for each device under investigation. The positioning in z is used to adjust the minimum of the beam size to be just below the read out pixel. To reach a narrow Full Width Half Maximum (FWHM) of 8-12 μm , the focus of the laser beam is adjusted by scans before the actual measurements, where a sketch is shown in Figure 4.10. An example is depicted in Figure 4.11. A y - z scan is performed leaving the beam spot at a fixed x position in the center of the implant. The detector needs to be biased above its depletion voltage during the focus measurements to allow for sufficient charge collection at every y value. The steps in z are chosen to be 500 μm at the beginning of the adjustment procedure for a determination of the rough position of the beam waist. Subsequently, the step size in z is gradually lowered down to a final 50 μm fine step size.

In the example of Figure 4.11 the starting position of the device is at a distance of 10 cm, defined as $z = 0 \mu\text{m}$. The z -coordinate is scanned in 180 steps of 50 μm size up to an end position of $z = 9000 \mu\text{m}$. For each step, the collected charge at the sensor depth y is obtained. In Figure 4.11a, the results of the collected charge at six steps in z are shown. The uncertainties in the collected charge at a particular sensor depth are discussed at the end of this section. An error function describing the turning charge collection shape as a function of y is fitted to each individual charge profile depicted in Figure 4.11a and resulting in the parabola shown in Figure 4.11b. The FWHM for different values of z is plotted and shown in the range from $z = 6000 \mu\text{m}$ to $z = 8500 \mu\text{m}$ with a minimum at $z_m = 7200 \mu\text{m}$. The FWHM reaches a value of 10 μm at this z position that is chosen for successive measurements of this device. The value of the FWHM results from the maximum slope of the fitted error function in the charge profile. The z value with the optimal focus is always used as the focus distance for subsequent measurements. The parabola is described as:

$$\text{FWHM} = \text{FWHM}_0 + az + bz^2 \quad . \quad (4.4)$$

The FWHM corresponds to 2.35 times the standard deviation σ of the Gaussian distribution, which is related to the error function by [93]

$$P(y) = \frac{1}{2} + \frac{1}{2} \text{erf} \left(\frac{y - \mu}{\sigma\sqrt{2}} \right) \quad , \quad (4.5)$$

where μ is the mean of the distribution and about 60 μm (see Figure 4.11a). The error function is

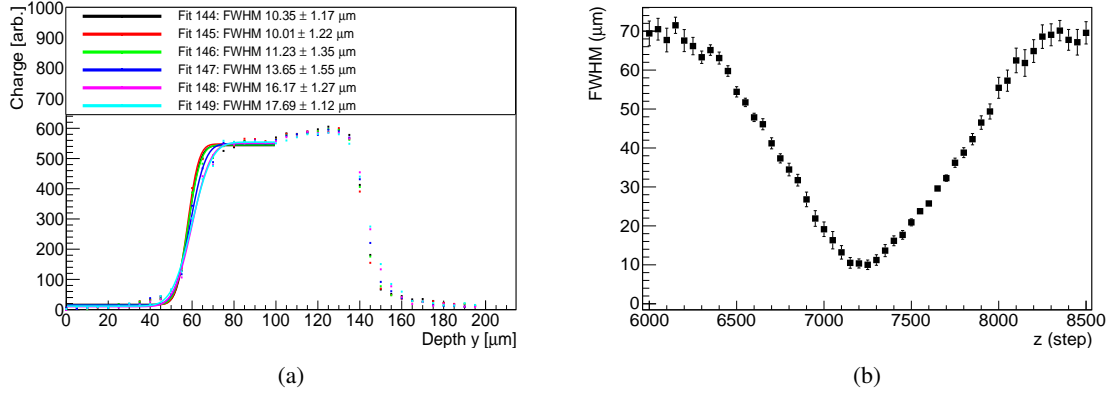


Figure 4.11: (a) error functions fitted to charge collection profiles of a $100 \mu\text{m}$ thick sensor before irradiation for different distances of $z = 7200 \mu\text{m}$ (corresponding to Fit 144) to $z = 7450 \mu\text{m}$ (corresponding to Fit 149) between device and laser output. (b) example of a FWHM of the beam as a function of different positions of the optical axis (z axis) is shown.

defined as:

$$\text{erf}(y) = \frac{2}{\sqrt{\pi}} \int_0^y e^{-v^2} dv \quad , \quad (4.6)$$

where v is the integration variable. The measurement of the charge collection and velocity profile is influenced by the quality of the focus and the x and y uncertainties. The uncertainty in x is only relevant for the two-dimensional charge collection maps. The contribution of their uncertainties is evaluated in the following for the example of a charge profile. The precision of the procedure of the focusing is obtained by the systematic uncertainty of $0.5 \mu\text{m}$ in the z position and by the statistical uncertainties in the fitting procedure, which is evaluated to be $1 \mu\text{m}$. With a $\text{FWHM} = 10 \mu\text{m}$, this results in an absolute uncertainty of 10% in the FWHM. To obtain the spread of the charge, resulting from the uncertainty of the FWHM, the deviation of the collected charge, obtained at a FWHM of $10 \mu\text{m}$ and $11 \mu\text{m}$, is calculated. Hence, an uncertainty in the FWHM of 10% leads to an uncertainty of the charge in a single point of less than 2%.

The uncertainties in the collected charge in depth y arise from two factors: a non-homogeneity of the sensor surface at the vertical sides and the scanning granularity of the y stage. The uncertainty in the collected charge emerging from the non-homogeneity of the surface of the sensor edge correlates with the focus of the beam, which slightly changes in case of a non-homogenous sensor edge. It is derived to be less than 3% by performing three independent y scans with the laser beam directed onto the middle of the pixel cell and $10 \mu\text{m}$ to the left and $10 \mu\text{m}$ to the right of the center of the pixel implant. The edges of the sensors tested in this thesis are not polished since test measurements on the quality of the surface at the beginning of each measurement showed satisfying results. Before every measurement, the edges are inspected under the microscope and the read out pixel is always chosen to be at the smoothest edge. This eliminated the risk of destroying the very thin samples with the polishing procedure. Uncertainties are also delineated in the scanning granularity in y for the one-dimensional charge profiles. For this reason, the typical scanning granularity of $5 \mu\text{m}$ in both directions is compared to scans with $2.5 \mu\text{m}$ and $10 \mu\text{m}$ spacing. The deviations are found to



Figure 4.12: The single chip cards for FE-I4B readout chips. The PCBs are designed at the University of Bonn and the University of Glasgow.

be smaller than 1%. In each charge collection and velocity measurement a global offset is induced by the noise of the electronic system and pick-up noise of the cable. Due to the fact that collected charge and carrier velocity are measured in arbitrary units, this uncertainty is not considered further. A total uncertainty of 4% is estimated for the collected charge, as well as for the velocity of the charge carriers within the Edge-TCT measurements.

As an additional factor, the influence of an estimated inclination of the sensor of up to 10° results in an uncertainty of $1.5 \mu\text{m}$ in the value of the depletion depths within the sensor in case of a $100 \mu\text{m}$ and $2.3 \mu\text{m}$ in case of a $150 \mu\text{m}$ thick sensor.

During individual measurements there is no calibration of the amount of generated charge, when scanning the laser along the sensor depth. The laser pulse is kept constant to $\approx 5\%$.

For an interpretation of the outcomes of the measurements, the offline analysis TCTAnalyse was used [94]. TCTAnalyse is a shared library dedicated to the analysis of TCT measurements. In this framework, a set of classes and functions, based on ROOT [95] are provided. The output files contain the signals within the sensor depth, see Figure 4.8, which are processed to obtain the charge collection or the charge carrier velocity profile.

4.3 Methodology for module characterisation

Single chip cards

After interconnection of the sensors to FE-I4 readout chips, which were introduced in Section 3.1.1, the assembled FE-I4 modules are wire bonded to Printed Circuit Boards (PCBs) at the electronics workshop hosted at MPP. Dedicated single chip cards, designed and manufactured at the University of Bonn and the University of Glasgow, enable readout of FE-I3, FE-I4A and FE-I4B readout chips. The single chip cards are equipped with an 8-pin Molex² connector, as well as a LEMO³ and an ethernet connector, as shown in Figure 4.12. The 8-pin Molex connection supplies a transmission of the analog and digital voltages, applied to power the chip, while the LEMO connection allows

²<http://de.rs-online.com/web/>

³www.lemo.com

for a transmission of the high voltage, applied to the sensors. With an ethernet connector and cable, the data stream is routed to a DAQ system steered by a computer.

DAQ systems

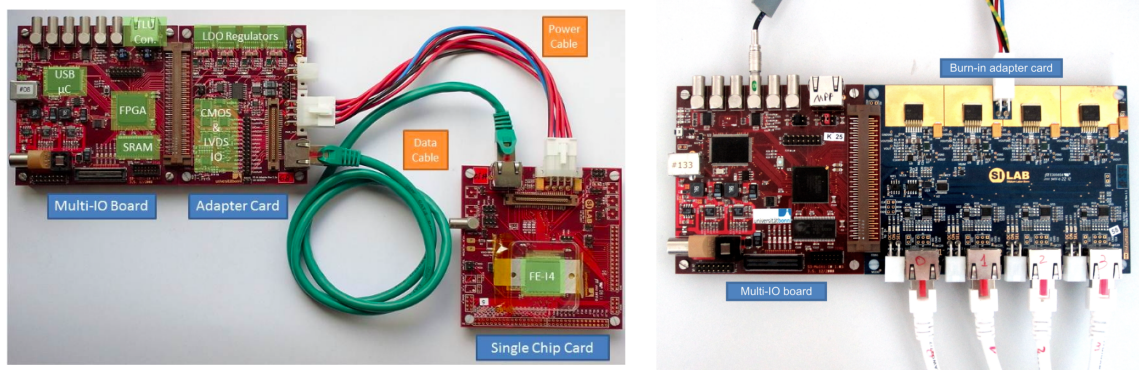
DAQ systems are used for tuning and data taking operations. To tune and read out the FE-I4 modules, analysed in this thesis, two different DAQ systems were employed, called USBPix and RCE. The USBPix2 and the successor USBPix3, with the MMC3 board available at MPP, are described together with the RCE in the following.

UBSPix The core component of the USBPix DAQ system [96] is a multi-purpose input/output field-programmable gate array (FPGA) board, the so-called Multi-IO board. The USBPix DAQ system was designed at the University of Bonn for the ATLAS pixel collaboration. With its dedicated adapter cards, it allows for the read out of different types of modules. In this thesis, the focus is on the read out of FE-I4 modules. The Multi-IO board with a single chip adapter card is shown in Figure 4.13a, connected to an FE-I4 module. The Burn-in adapter card can connect up to four FE-I4B front-ends, allowing for four single chip cards to be steered by one single board, as shown in Figure 4.13b. The MMC3 DAQ system, one of the versions of the USBPix3 generation, is shown in Figure 4.13c with eight ethernet connectors, allowing for a connection of up to eight single chip cards or two four-chip cards. The software, used to steer the DAQ system, is named STControl and is a C++ and ROOT based software application, controlling scans and measurements. It allows for configuration and operation of the connected FE-I4 assembly.

RCE The reconfigurable cluster element (RCE) system is a DAQ system [98], developed at the Stanford Linear Accelerator Center (SLAC) for ATLAS pixel development. The RCE is the main element for data transfer to and from an FE-I4 module and runs a software, which handles the data taking and processing. It uses an external high speed input/output (HSIO) module to drive the trigger signals and data stream of the FE-I4 modules. The HSIO acts as the intermediary between the optical signals, sent out and received by the RCE and the electrical signals, sent out and received by the FE-I4 module [55]. An adapter card, dedicated to FE-I4 modules, is connected to the HSIO and provides 16 ethernet connections to operate maximum 16 FE-I4 modules (or 4 four-chip modules) at the same time. The RCE system, including the HSIO board and adapter card, is illustrated in Figure 4.14. To allow for tuning and source scans of the FE-I4 module, the software package *calibGui* is implemented, while the software package *cosmicGui* is provided for data taking during beam test measurements.

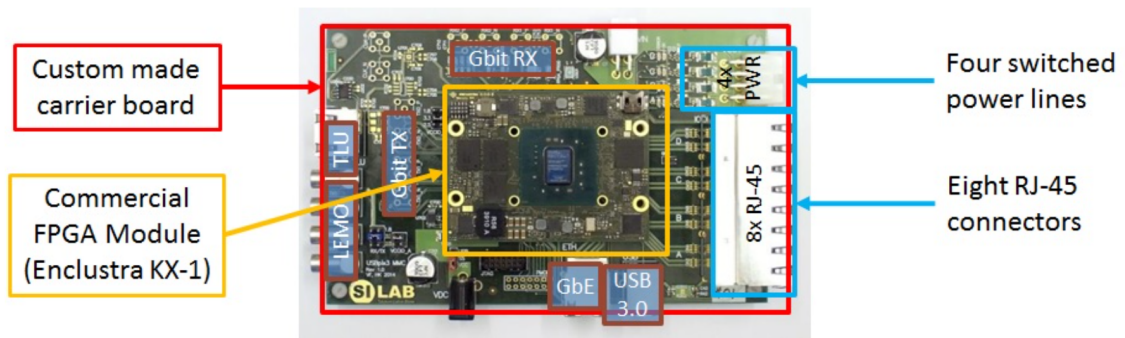
Tuning of readout chips

To reach a uniform response of the FE-I4 chip for all the pixel cells, a tuning procedure has to be applied. The differences in the pixel cells arise from unavoidable variations in the manufacturing process. The tuning algorithms aim to reduce the dispersion in the two most important tuning parameters: the threshold of the discriminator (see Section 3.1.1) of the chip, and the time over



(a) USBPix2 connected to FE-I4 module

(b) USBPix2 with BiC



(c) USBPix3 with MMC3 board

Figure 4.13: The USBPix2 DAQ system with a configuration for single chip FE-I4 cards shown in (a). It is composed of a Multi-IO board, an Adapter Card connected to a single chip FE-I4. The image is taken from Ref. [37]. In (b) the Multi-IO board is connected to a "Burn-in-card" (BiC) to read out four chips at the same time. In (c) the USBPix3 DAQ system with the MMC3 board is shown, taken from Ref. [97].

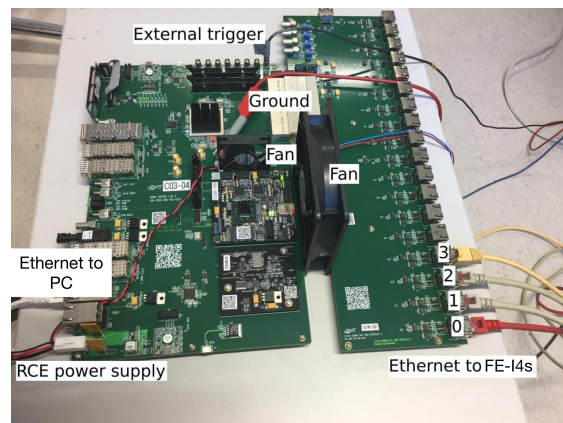


Figure 4.14: The RCE DAQ system. The HSIO module (left) is connected to the adapter card (right), which is dedicated to FE-I4 modules. The adapter card provides 16 ethernet connections to operate maximum 16 FE-I4 modules (or 4 four-chip modules) at the same time.

threshold (ToT). The set threshold value determines the minimum value of the collected charge, below which the hit is not registered, while the time spent by the signal above threshold (ToT) gives the information on the amount of collected charge. Figure 4.15 shows the strong dependence of the chip response of the collected charge, the threshold value and the feedback current. In the following, the tuning of the threshold and the ToT, are explained in more detail.

Threshold For testing purposes, a definite charge amount is injected via a charge injection circuit integrated in each FE channel. The value of the threshold for each pixel is measured with a dedicated scan. The pixel response is measured at different injected charges and fitted with a sigmoid curve for each pixel cell. An occupancy of 100% is obtained, when for a determined value of the injected charge, the chip channel always responds with a hit. Decreasing the charge value, a point is reached, where the channel responds with a hit only 50% of the times to the signal. By further decreasing the charge value, the pixel occupancy will reach 0%. In an ideal case, no hits would be recorded as soon as the signal is below the threshold, resulting into a step function. Due to the fact, that the shape of the threshold curve is affected by noise, a fluctuation of the obtained charge leads to some hits below the threshold being recorded, while others are not and vice versa. Hence, the distribution of the threshold is fitted with a convolution of a step function and a Gaussian distribution describing the probability to detect a hit releasing a certain amount of charge Q . The probability is described by the so-called S-curve:

$$P(Q) = \frac{1}{2} \operatorname{erfc} \left(\frac{Q_{\text{thresh}} - Q}{\sqrt{2}\sigma_{\text{noise}}} \right) , \quad (4.7)$$

where Q_{thresh} is the value of the charge set as threshold of the discriminator and σ_{noise} is the voltage fluctuation at the input of the discriminator. In this case, the noise is expressed in equivalent charge fluctuations at the input of the charge amplifier and hence, corresponds to the electronic noise of the pixel cell. The term *erfc* is the complementary error function and calculated using Equation 4.6:

$$\operatorname{erfc}(x) = 1 - \operatorname{erf}(x) . \quad (4.8)$$

Figure 4.16 shows an example of a typical outcome of a threshold measurement of a single pixel cell. The y axis shows the fraction of recorded pixel hits and the x axis the injected charge, where the threshold value of 1000 e is affected by a σ_{noise} of around 10% of the threshold value. It represents an example of one of the threshold targets, chosen for the tuning of the modules.

The threshold needs to be adjusted globally taking into account the average value across the pixel cells, as well as locally for every single pixel cell to ensure an equal and maximum efficiency over the entire module. For this, the tuning is performed by two digital to analog converters (DACs), a coarse and a fine DAC.

As the first step, the 8-bit wide global DAC (GDAC) register of the chip is set to a common value of the discriminator over the entire range of channels. The algorithm of the GDAC tune calculates the threshold value for every single pixel with Equation 4.7 by scanning over different values of injected charge. The threshold is monitored and, when the 50% value is reached for lower injected charges than the target threshold, the GADC value is increased and vice versa. At the end of the tuning procedure for the GDAC register, the setting is chosen in such a way, that it delivers the

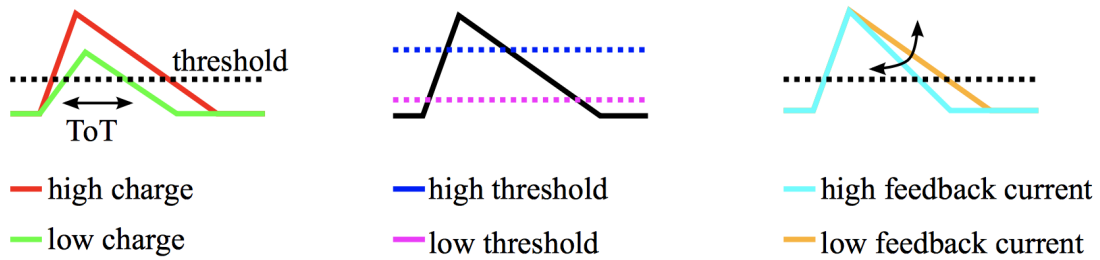


Figure 4.15: Preamplifier signal shapes depending on different values of injected charge, threshold and feedback current [99].

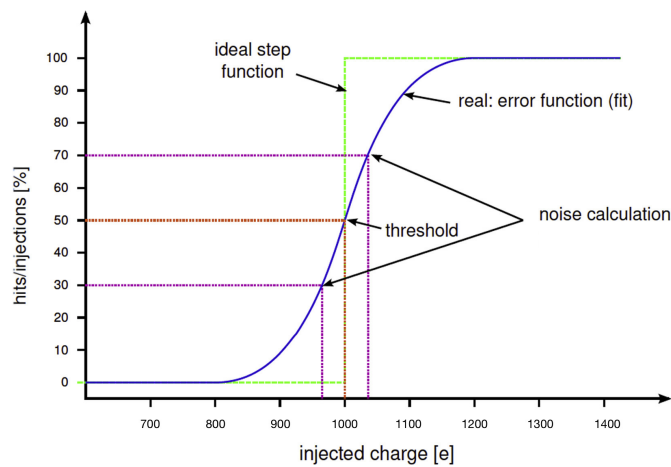


Figure 4.16: An example of a typical outcome of a threshold measurement of a single pixel cell, the so-called S-Curve. The Figure is adapted from Ref. [100].

average threshold closer to the target value. Then, every single pixel is fine tuned independently. The procedure, using a 5-bit TDAC setting, is called TDAC tune and is performed with the same algorithm as for the GDAC tune. As the threshold is influenced by the temperature by approximately 10 e/K , not irradiated modules are tuned at a set environment temperature of 20°C , while irradiated modules are tuned at -50°C . A decrease in temperature, when previously tuned at higher temperature, would result in a decrease of the target threshold.

Time over Threshold As well as the threshold, the tuning algorithm for the ToT exhibits a coarse, the so-called IF tune, and a fine tune, the so-called FDAC tune. Both tunings inject a specific charge and measure the ToT response globally or for each pixel. With its 4-bit register, the ToT features a range of values from zero to 15 and ToT target values in the central region, from 6 to 8, are chosen for the tuning. Depending on the sensor thickness, the corresponding charge is set to a value between $4\,000 \text{ e}$ and $14\,000 \text{ e}$.

ToT to charge calibration Since the ToT has a non-linear dependence on the charge, especially for higher ToT values, a calibration, correcting for the non-linearity, is performed. For identification of the released number of charge carriers within a sensor at a particular bias voltage, the STControl

Table 4.1: Parameters of the radioactive sources, ^{241}Am and ^{109}Cd , for ToT to charge calibration measurements. The charge released in silicon is given for the most significant line in the energy spectrum of the two radionuclides [102].

Nuclide	γ energy [keV]	released charge in silicon [ke]
^{241}Am	59.5	16.3
^{109}Cd	22.2	6.1

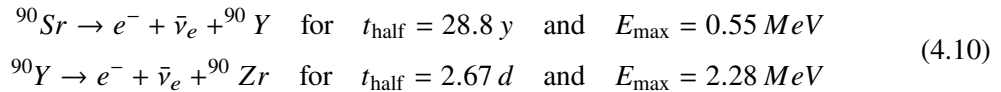
software employs a calibration scan, TOTcalib scan. This scan returns three fitting parameters a , b and c to correct for the non-linearity between ToT and charge. The fitting parameters are inserted in the empirical function, which describes the relation between the ToT and the charge [101]

$$Q = a + b \cdot \text{ToT} + c \cdot \text{ToT}^2 \quad (4.9)$$

to obtain the corresponding collected charge. Additional calibration measurements with radioactive γ sources are performed, which exhibit a defined γ peak at a particular energy corresponding to a certain released charge within the sensor. The γ sources and their corresponding energy peaks and the average signal in ke are summarised in Table 4.1. Since for not irradiated 100 μm thick sensors, a released charge of the order of around 6 500 -7 000 electrons is expected for a MIP, the ^{109}Cd source is used for the calibration correction. Instead, for the not irradiated 150 μm thick sensor the ^{241}Am source is used, exhibiting the highest intensity energy peak releasing 16.3 ke in silicon. The 150 μm thick sensor is expected to release around 12 000 electrons, when traversed by a MIP. The calibration correction measurements are performed at the highest voltage step of the previously performed charge collection measurements to ensure a saturation of the collected charge. The description on the charge collection measurements is summarised in the following.

4.3.1 Charge collection measurements

Charge collection measurements are carried out with strontium ^{90}Sr β -electrons using the USBPix [103] and RCE DAQ system [98]. The β -electrons traverse the silicon detector, as well as the scintillator placed underneath the module, as shown in Figure 4.17. The corresponding β -electrons result from the decay chain of ^{90}Sr of two β emissions to yttrium and zirconium with a characteristic three-body spectrum:



and taken from Ref. [24, 102]. The energy, resulting from the decay of ^{90}Y , is higher than the energy needed to traverse the silicon and to reach the scintillator. With the identification of the particle in the scintillator, the external triggering of the particle in the silicon device is enabled.

In case of a measurements with a γ -source, the low energy photons release all their energy at once when interacting with the silicon atoms. The energy loss of photons in silicon is at these energies mainly described by the photoelectric effect. Therefore, the photons are not able to reach the scintillator, which is placed below the module to be tested. Hence, an internal self-trigger of

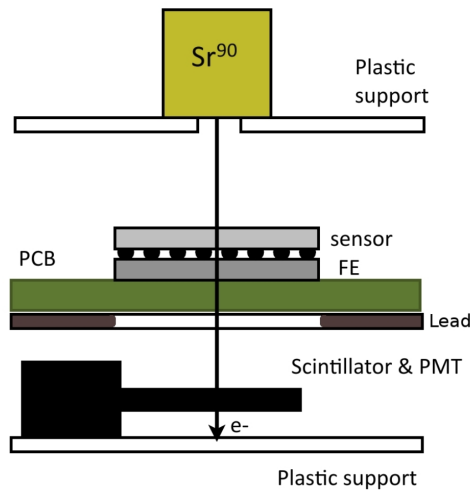


Figure 4.17: Setup to measure the collected charge in sensors. In a three-stage mechanical structure made of plastic the DUT is placed in between a source, which emits the particles, and a scintillator for triggering the readout. Figure taken from Ref. [37].

the readout chip is used, which records each signal above the set threshold value. However, the fact that all signals above threshold are registered has some drawbacks. After irradiation, it is necessary to mask noisy channels of the irradiated modules to avoid a buffer overflow of the internal trigger system, which stops further data taking.

The modules under test are operated inside a climate chamber at a stable ambient temperature of 20°C before irradiation and at a temperature of -50°C in case of irradiated devices. The resulting collected charge is affected by uncertainties arising from different sources. First, the statistical and systematic [104] uncertainties of the threshold value as well as the ToT value have to be counted in. Additional systematic uncertainties arise from the precision of the value of the injected charge, which itself is dependent on the injection capacitance of the readout chip. The spread of the injection capacitance was measured to be 4% [105]. Furthermore, statistical uncertainties arise from the relation between ToT and charge, described in Equation 4.9. As no pixel-by-pixel ToT to charge calibration is available, an additional global calibration (γ -correction) is introduced with γ -source measurements using γ -sources with a defined energy peak corresponding to the expected charge release in a particular sensor thickness. The goal of the γ -correction is to reduce systematic biases in the ToT to charge conversion. However, it introduces additional uncertainties originating from the limited precision in determining the value of the peak energy. Finally, all contributions sum up to a total uncertainty of 12% on the values of the collected charge [37].

4.3.2 Beam test measurements with particle beams

A beam test is the characterisation of devices with particle beams. With beam tests, properties of the devices are extracted that are not easy to be determined with laboratory measurements, as for example the hit efficiency and position resolution. Beam test measurements are a unique opportunity to verify the performance of particle detectors at real conditions of a high energy experiment. The

particle beams are obtained from accelerator facilities, providing test beams at a particular energy, as well as at a specific intensity. They are aligned with a series of tracking devices to ensure a crossing of the particles through the devices. The tracking devices form a so-called *beam telescope* and, in most cases, they are composed of well-known and characterised silicon pixel detectors with a good spatial resolution. A number of DUTs are mounted in the center in between the telescope planes, enabling a reconstruction of the trajectories of the traversing particles. With this, the impact point of the single particle on the DUT is precisely determined. In this section, a presentation of the beam test facilities at DESY and CERN-SpS and the telescope set-ups is given along with a discussion on the performed measurements and the analysis method.

Beam lines

In the following, the properties of the DESY test beam facility, as well as the one at the CERN-SpS are described. The measurements to obtain the results on the pixel detectors, discussed in this thesis, were performed at both facilities.

DESY The three provided beam lines at the Deutsches Elektronen-Synchrotron (DESY) in Hamburg offer a continuous particle beam of up to 1000 electrons or positrons per cm^2 with an energy ranging from 1 GeV to 6 GeV [106]. The energy spread is of around 5% and the divergence roughly 1 mrad. The DESY-II complex is depicted in Figure 4.18. The momentum discrimination for the final test beam reduces the instantaneous rate. During the beam test campaigns, a beam energy of 4 GeV is set, allowing for an appropriate particle rate and at the same time an appropriate beam energy. Due to the limited particle energy, multiple scattering, within either the telescope planes or the DUT, can not be neglected during measurements at DESY, allowing for simultaneous measurements of only two DUTs to avoid additional material. Due to the high number of particles per DESY-II bunch, the electron beam originating from DESY-II is directed to a thin carbon fiber, which is moved into the vacuum beam line. As a result, Bremsstrahlung radiation is generated, further directed to a secondary Cu or Al target and subsequently converted to electron and positron pairs. With a spectrometer magnet employing a collimator, a monoenergetic particle momentum is chosen, while with a spectrometer dipole magnet a selection of the preferred particle type is possible. Further information on the DESY beam test facility can be found in Ref. [107].

CERN-SpS The CERN-SpS provides a pion beam with an energy of either 120 GeV or 180 GeV, which allows for a minimisation of the influence of the multiple scattering. In this thesis, all beam test measurements were performed with a 120 GeV particle beam. The particle beam is delivered to four beam lines used as beam test facilities. Every beam line contains magnets for bending and beam focusing. To obtain a pion beam, protons from the SpS are accelerated to 400 GeV and directed to one of the three available targets. The generated pions traverse a spectrometer magnet filter, where their momenta are selected. Subsequently, they are directed to the beam lines with a maximum number of 2×10^8 particles per spill. The spill length and repetition frequency depend on the number of facilities used in parallel. The SpS is able to offer a spill length of 4.8 s to 9.6 s and

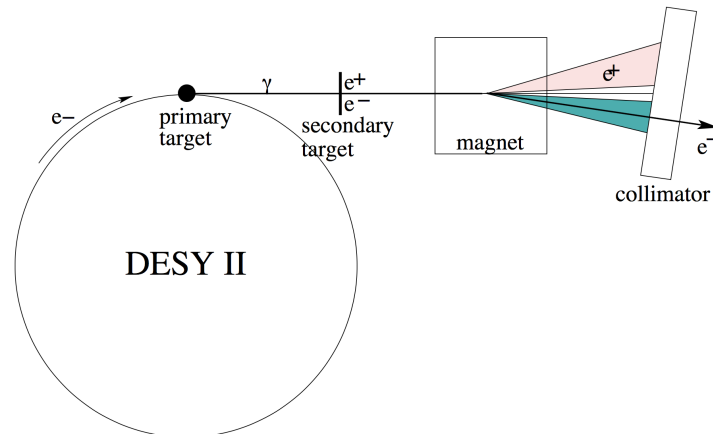


Figure 4.18: Schematic view of the generation of the test beam from the primary DESY-II beam. Bremsstrahlung is generated in a carbon fiber and converted into electron and positron pairs in a Cu or Al target. With the spectrometer dipole magnet a selection of the energy and type of the particles is possible. Subsequently, the final beam is collimated and delivered to the beam lines. The schematics are adapted from Ref. [107].

a repetition frequency every 14 s to 48 s. Due to the fact, that the CERN-SpS is serving multiple experiments, the beam is not continuously present.

The EUDET telescopes for particle tracking

The beam telescopes of the EUDET family are equipped with six fine-segmented MIMOSA26 detectors, which feature the architecture of monolithic active pixel sensors (MAPS) with fast binary readout and integrated zero suppression [108]. The EUDET telescopes provide a precise reference track trajectory using its 3 planes of the MIMOSA26 sensors upstream the Device Under Test (DUT) and another 3 planes downstream the DUTs. At CERN-SpS, the DUTs are mounted in a cooling box, developed and built at MPP, to ensure a stable temperature of 20°C, in case the devices are not irradiated, or a stable low temperature in the range of -30°C to -50°C to measure irradiated devices. The cooling box is made from aluminium and is connected to a chiller and a nitrogen source to allow for dry gas. An additional cooling box, designed at the University of Dortmund [109], is in use at CERN. The cooling box is made from foam and consists of two areas, which are separated from each other by an additional aluminium plate. The inner area is dedicated to the DUTs, while the outer area is used to place the dry ice close to the modules for cooling to temperatures down to about -50°C. The temperature is monitored during measurements using a temperature sensor inside the cooling box. The same type of cooling box is mounted at DESY, since it ensures lower material budget, important to reduce multiple scattering given the low beam energy available at this facility. The cooling boxes are illustrated in Figure 4.19. A high-precision xy-table is used to move the DUT through the active area of the telescope. In terms of readout of FE-I4 modules, the USBPix, as well as the RCE, are integrated in the telescope DAQ. In the front and back of the telescope four scintillators (two in the front, two in the back), with a total area close to the one of the MIMOSA26 pixel sensor, are placed to trigger the readout, when particles are crossing. The

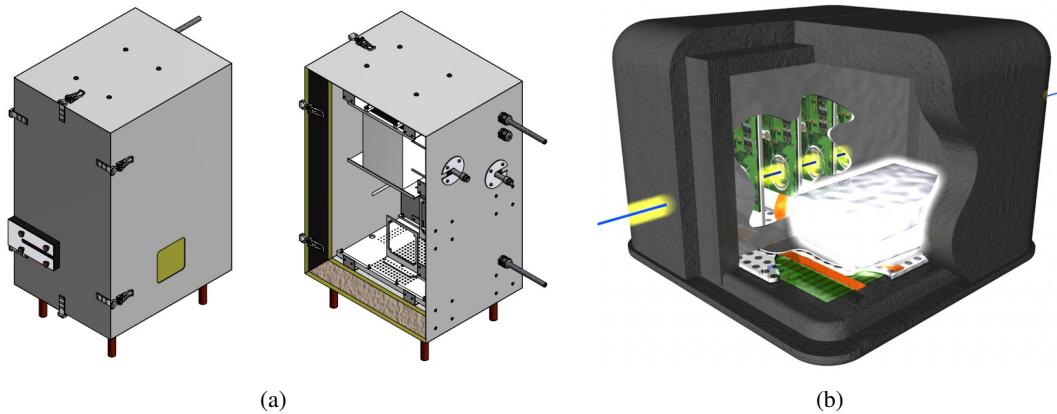


Figure 4.19: (a) MPP and (b) Dortmund cooling box [109]. The cooling box, manufactured by MPP, is situated at CERN, while the Dortmund cooling box is used at CERN and DESY.

size of the MIMOSA26 chip is $13.7 \text{ mm} \times 21.5 \text{ mm}$ and the sensor matrix is composed by 576×1152 pixels of $18.4 \mu\text{m}$ pitch with a thickness of only $25 \mu\text{m}$. A pixel pitch is defined to be the length from the center of one pixel cell to the center of the neighbouring one. Owing to this remarkably low thickness, the telescope allows for tracking of low energy particles with a reduced multiple scattering affecting the pointing resolution in a less relevant way.

For single pixel clusters, the sensor intrinsic resolution is estimated starting from the sensor pixel pitch. Using the term $p/\sqrt{12}$ [110] with p corresponding to the pixel pitch, an intrinsic resolution of $\sigma_{\text{int}} = 5.3 \mu\text{m}$ is reached by the telescope. Larger pixel clusters, obtained by lowering the threshold values of the MIMOSA26 chips, improves the intrinsic resolution. Doing so, each EUDET plane reaches up to $3.5 \mu\text{m}$ of spatial resolution in case of low energetic electrons and $2 \mu\text{m}$ for high energetic pions [111, 112]. The possibility to integrate readout micro-circuitry on the sensor, which is given by monolithic sensors, results in a very low readout noise and in a powerful signal processing capability. An operation point, resulting in an efficiency of $99.5 \pm 0.1\%$ for a MIP at a fake rate of 10^{-4} per pixel, can be reached at room temperature [113]. With a MIMOSA26 integration time of $115.2 \mu\text{s}$, the maximum possible rate is set to be 10 k hits per frame and second [108]. Due to the much smaller integration time of the FE-I4 readout chips, an FE-I4 module is included in the data taking as a reference device to select the tracks, which are in time with the DUT. A total number of seven EUDET-type beam telescopes was developed since 2009, of which AIDA and ACONITE are installed at CERN, owned by ATLAS, while DATURA and DURANTA are stationed at DESY.

Pointing resolution To achieve a spatial resolution much better than the pixel size, a minimal achievable pointing resolution of the telescope planes, which defines the precision of the determination of a particle trajectory, is crucial. The pointing resolution is influenced by parameters, such as the number of the available tracking planes, as well as by physical effects such as the multiple scattering. The latter is more relevant for lower energetic particles. Charged particles are deflected, when traversing material between the very first and the last telescope plane. The particle deflection is dependent on the detector material, as well as the path length in the surrounding air and is

described with the root mean square (RMS) of multiple scattering through small angles [114]:

$$\Theta_{\text{MS}}^{\text{RMS}} = \frac{13.6 \text{ MeV}}{\beta c p_{\text{mom}}} \cdot Z \sqrt{\epsilon_{\text{rad}}} \cdot (1 + 0.0038 \ln \epsilon_{\text{rad}}) \quad , \quad (4.11)$$

with βc representing the particle velocity, p_{mom} describing the momentum, and Z referring to the charge number of the traversing particle. The term $\epsilon_{\text{rad}} = \frac{t}{X_0}$ is the material budget in radiation length. In the case of measurements at the CERN-SpS, where 120 GeV pions are used (large p_{mom}), the effect of multiple scattering, due to Coloumb interactions with the nuclei of the traversed material, is negligible ($\Theta_{\text{MS}}^{\text{RMS}}$ is small). Instead, the lower energetic electrons with a maximum achievable energy of 6 GeV, are significantly affected by multiple scattering. Even though the multiple scattering is taken into account by the broken-line fit, introduced in the subsequent paragraph, the material in between the telescope planes needs to be reduced. Therefore, the foam based cooling box, designed by the University of Dortmund, is used for cooling at the set-up at DESY, while at CERN, a manufactured aluminium cooling box, with faster cooling and more precise achievable temperatures can be used.

Analysis chain of offline trajectory reconstruction

The particle trajectory is reconstructed from raw hit positions on the telescope planes and the DUTs by a sequential algorithm of the EU Telescope software framework [115–117]. In the following, the five main steps of the track reconstruction are summarised. As the first step, the events are defined from trigger information and hits in pixels, recorded with a time stamp, defined by the trigger logic unit (TLU), and converted into a EU Telescope internal data format. A hit is defined as a signal of a pixel above threshold. All noisy pixels are excluded before data taking. In case of further pixels exceeding the firing frequency threshold of 1%, the pixels are removed from the subsequent data analysis and their position is stored into the noisy pixel database. In the next step, a sparse pixel clustering algorithm groups together all hit pixels in close proximity, calculating the coordinates of the formed clusters. The following step, the hitmaker, transforms the hits in the local coordinate system of each detector plane to a global reference frame, in which the z axis is parallel to the beam direction. The geometry of pixels in x and y position, as well as their rotation are taken into account. Based on these coordinates and the resulting correlations between the devices, a coarse pre-alignment is done with a precision of a few hundred μm . With this, the pre-alignment corrects for any global misalignment and is used for the subsequent and crucial step, the alignment. In the second alignment iteration, an alignment processor tries to fit tracks through all telescope planes and DUTs in the set-up, taking into account the spatial resolutions of each device⁴. The requirement of how many and which telescope planes and DUTs are taken into consideration for alignment is set in this step. The first telescope plane is always fixed in its orientation and position to allow for a fixed starting point of the particle trajectory. The selected tracks are gathered and passed to the MILLEPEDE-II algorithm [118] that minimises the global χ^2 of the track residuals by trying all the possible combinations of hits. Tracks with $\chi^2 > 50$ are excluded from further track processing. In addition, the uncertainties of the fitted track parameters are minimised, while the constants of

⁴The respective telescope plane and DUT are excluded from the alignment.

the alignment for each telescope plane and DUT are returned. The final step is the track fitting, which is affected by false track candidates. Therefore, it is essential for track reconstruction, that track fitting algorithms allow for autonomous filtering of false track candidates. To overcome these difficulties, the deterministic annealing fitter (DAF) [119], which is based on a Kalman filter [120], is used. The track reconstruction is completed by finally fitting the tracks with the track model of the general broken lines [121] including effect of the multiple scattering in the initial particle trajectory. The data is stored in ROOT files on a per run basis with the reconstructed tracks, as well as with information on the telescope planes and DUTs, and is further reprocessed in TBmon [122, 123]. In this framework, a detailed analysis of the DUTs with their specific types of geometries, is conducted allowing for an analysis of a set of runs, which were taken under the same condition. The different analyses are introduced in the succeeding.

Cluster size A cluster is defined as an accumulation of hits in the sensor within close proximity in space and time, each of them assumed to be created by the same traversing particle. The number of hit pixels forming a cluster is defined as the cluster size, while the length of the pixels, fired in the two detector coordinates, is referred to as cluster width. To distinguish between multiple clusters in the same event, a threshold of the signal in the pixels is set as well as a minimum distance between two clusters to be identified as originating from separate tracks. Both restrictions cut out possible noise, appearing at the same time as the actual hits, where the first hit pixel in time is defined as the seed pixel. The local point, where the particle crosses the sensor, is defined as the geometrical center of the pixel cell. At perpendicular beam incidence, the average cluster size is between one and two. Two-hit clusters result from charge diffusion of the charge carriers, when the particle enters the detector in between two pixels or with an incidence angle slightly different than perpendicularly to the detector surface. The cluster size is further increased in case particles enter the detector surface with a higher incidence angle and is discussed in Section 5.2.6. In this case, the seeding point is deduced from averaging the center position by weighting the collected charge in the single clusters. In addition to the dependence of the cluster size on the entering point of the particle in the detector, the cluster size is dependent on the length of the pixel cell side. Two-hit clusters are mostly originating from the short pixel side, where the adjacent pixels below and above the seed pixel have a higher probability to record a signal. The total number of clusters in both pixel directions is obtained from the outputs of the EU Telescope software. Two-hit clusters in the short pixel direction are calculated to make up less than 10% of the total clusters, while two-hit clusters in the long pixel directions are calculated to be even less than 2% in case of a 150 μm thick sensor. Therefore, clusters, resulting from a perpendicular beam incidence, are interpreted as single-hit clusters.

Charge collection The charge collection can be measured as a function of the intra-pixel position or can be averaged over the full sensor area. To visualise particular pixel cell features, such as bias dot and rail, and their effect on the charge sharing within a pixel cell, the high-resolution tracking capability of the EUDET beam telescope is used. With the tracking information and the in-position resolved charge, it is possible to detect the device properties in terms of charge collection. In Section

5.2.2 of this thesis, the in x-y two-dimensional charge collection maps are displayed in ToT and not converted in e, since no charge calibration during beam tests is available. The over-all picture of the charge collection distributions within a pixel cell and between neighbouring pixel cells are analysed. When comparing the charge collection as a function of bias voltage obtained by beam tests to results from source scans and Edge-TCT measurements, the charge is averaged over the full sensor area and normalised to the highest voltage point of the measurement set.

Hit efficiency The hit efficiency of the DUTs is defined as the ratio of the number of reconstructed tracks with matching hits in the DUT to the total number of reconstructed tracks passing through the DUT :

$$\text{hit efficiency} = \frac{\# \text{ detected hits}}{\# \text{ expected tracks}} \quad , \quad (4.12)$$

where the symbol # represent the number of hits and tracks within a DUT. The tracks, passing through a DUT, are reconstructed from the particle trajectory, while the hits in the DUT are recorded as a signal in the projected impact point of the track of the sensor. The track-hit matching is defined within a given maximum distance between the two. The hit efficiency can be estimated for the entire module area, as well as within a pixel cell. As in the case of the charge collection, the effect of different designs on the sensor performance is investigated. Since the pointing resolution of the telescope is depending on to the energy of the particles traversing the telescope planes, the in-pixel efficiency maps obtained at CERN result in a better resolved distribution of the hit efficiency within the pixel cell. In Section 5.2.4, the efficiency averaged over the full sensor area as a function of bias voltage, as well the in-pixel efficiency maps of different module types, are shown. Additionally, the efficiency at the border of the sensors is determined; the results are summarised in Section 5.2.5, as well for multiple-hit clusters in case the particle beam traverses the DUT at a high inclined angle, see Section 5.2.6.

For all obtained hit efficiency results, an absolute systematic uncertainty is derived. Due to high statistics collected at each beam test, the systematic uncertainties are dominant. The systematic uncertainty is arising from three sources: the trajectory reconstruction, the subsequent DUT analysis and the fluctuations on the resulting efficiencies during the measurement time. During track reconstruction, different track parameters were used to reconstruct the tracks of different measurement set-ups. For the estimation of the uncertainties arising from the offline trajectory reconstruction, the resulting efficiencies are compared for different values of the *finder radius* and χ^2 . Using the finder radius, a track in the last track reconstruction step is reconstructed via a cone, that searches for hit points on every plane from a starting track candidate on the first hit plane of the telescope (plane 0). All hit points in the search area of the finder radius are included in the reconstruction analysis. For all track reconstructions performed for this work, the track parameters deviated by maximum 30% from the nominal values given by the EUTelescope software. With this deviation, an efficiency variation of 0.06% is observed. No fluctuations in efficiency are observed for different χ^2 settings. During a running time of above 2 hours, an additional fluctuation in efficiency of 0.04% is observed. In the subsequent DUT analysis, efficiency fluctuations up to 0.5% are obtained for track-hit matching values from 0.5 to 2 times the pixel cell size. To minimise the systemic

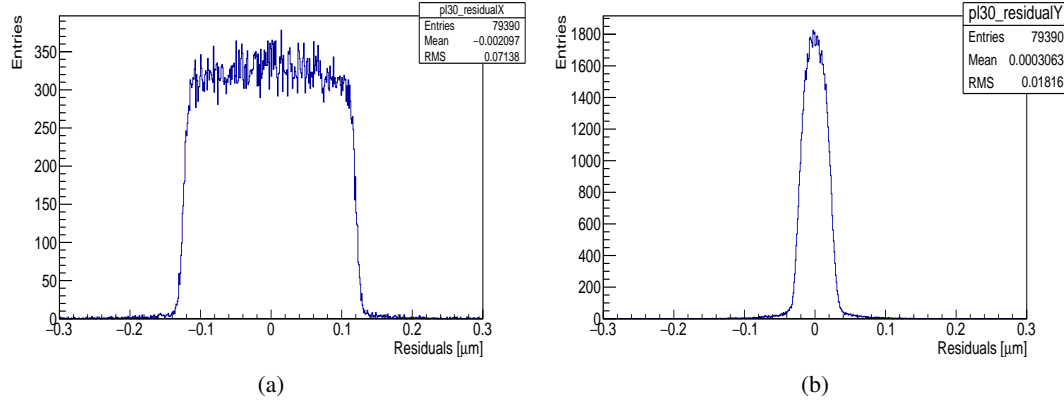


Figure 4.20: Residual distribution of an FE-I4 module with a $50 \times 250 \mu\text{m}^2$ pixel cell (a) in the long pixel side direction x and (b) in the short pixel side direction y. Beam test measurements performed at CERN with a perpendicular beam incidence.

uncertainty, the value of the track-hit matching in the DUT analysis is set to 1.5 times the pixel cell size of the device in each direction and not changed for different measurement set-ups. The total systematic uncertainty on all obtained hit efficiency values is calculated to be 0.3%. This value is well in agreement with previous estimations [111].

Spatial resolution For particle trajectory reconstruction, the spatial resolution of the telescope planes, as well as the DUTs is crucial. The spatial resolution of a detector is defined as the width of the unbiased residual distributions. The term *unbiased* in this case means, that these detectors are not taken into account for track fitting. The residual distribution is obtained from the distance between the extrapolated track of the particle, traversing the telescope and DUTs and the recorded position of the hit in the device. Hence, the residual in x is given by:

$$\Delta x = x_{\text{track}} - x_{\text{hit}} \quad , \quad (4.13)$$

and for the residual in y accordingly. The width of the residual, and hence the spatial resolution, is obtained by the RMS of the residual distribution. The residuals are calculated separately for x and y, given the FE-I4 rectangular shape. In the simplest case of single-hit clusters, the intrinsic spatial resolution for an FE-I4 pixel cell of $50 \times 250 \mu\text{m}^2$ pixel size are calculated to be $\sigma_{\text{int},X} \approx 72 \mu\text{m}$ and $\sigma_{\text{int},Y} \approx 14 \mu\text{m}$. In the ideal case of a uniform particle beam flux, box-shaped residuals with an RMS of $\sigma_{\text{int},X}$ and $\sigma_{\text{int},Y}$ are expected. Instead, the pointing resolution of the telescope introduces smearing at the edges of the residuals. In Figure 4.20, an example of residuals for the long and short pixel direction are given, measured at perpendicular beam incidence. The spatial resolutions, obtained from measurements, are close to the previously quoted values, with a slight discrepancy. This is explained by:

$$\sigma_{\text{meas}}^2 = \sigma_{\text{int}}^2 + \sigma_{\text{point}}^2 \quad , \quad (4.14)$$

The measured spatial resolution of the DUT σ_{meas} is influenced by the intrinsic resolution of the device, as well as by the pointing resolution σ_{point} , associated to the telescope performance. Since

multiple-hit clusters are more prone to occur in the short pixel direction, resulting in more charge sharing between the neighbouring pixel cells, the spatial resolution in the short pixel direction shows a slightly higher discrepancy. Nevertheless, the obtained spatial resolution is comparable with the intrinsic spatial resolution, as one-hit clusters dominate in case of perpendicular beam incidence.

PRODUCTION AND PERFORMANCE OF THIN PLANAR n^+ -IN-P PIXEL SENSORS

In this chapter properties of n^+ -in-p planar pixel modules with different sensor designs are investigated and compared. In Section 5.1, sensor productions from three producers are presented and in Section 5.2 the performance of the sensors before and after irradiation is discussed. The focus is in particular on the investigation of the radiation hardness as a function of the different sensor thicknesses, and on the study of the tracking capabilities at perpendicular beam incidence, as well as in the high- η regions of the pixel detector. The presented results are obtained by measurements partially performed within the framework of the RD50 collaboration [124], the AIDA-2020 project [125] and the Inner Tracker (ITk) group of ATLAS [126], focusing on the requirements for the ATLAS pixel detector upgrade at HL-LHC. Partial outcomes were already published in Refs. [127–131].

5.1 Production and processing

The ATLAS Inner Detector group at the MPP designed new n^+ -in-p planar pixel sensors in accordance with previously achieved and discussed results [37, 53, 67]. The designs of the pixel sensors, investigated and analysed in this thesis, are presented in this section and a description of the design and processing of the different sensor productions is provided with a following discussion on the sensor characteristics before and after irradiation. An overview of the sensor designs relevant for this thesis is presented in Table 5.1 along with tabular summaries of each production and the corresponding sensors at different irradiation fluences.

5.1.1 CiS productions

Four productions of planar pixel sensors were carried out at CiS Technology¹ on standard p-type FZ silicon, differing in sensor thickness, FE-I3 and FE-I4 compatibility, GR and biasing schemes, resistivity and wafer size employed in the production. The description and characterisation of the

¹<https://www.cismst.org>

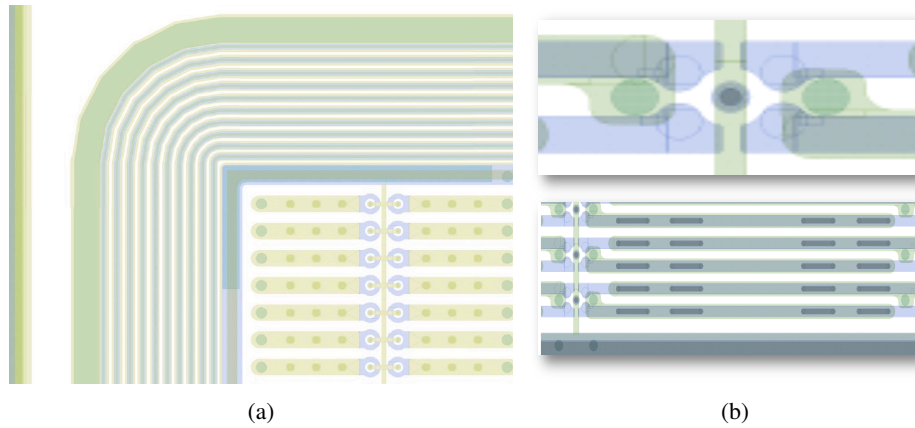


Figure 5.1: Guard ring layout with 10 GRs and one BR with a total edge distance of $d_e = 450 \mu\text{m}$ as implemented in the FE-I4 compatible structures. (a) the FE-I4 $50 \times 250 \mu\text{m}^2$ pixel cell and p-t design, and (b) the modified design with a $25 \times 500 \mu\text{m}^2$ pixel cell and the common p-t established in the CiS3 production. In (b), a zoom-in of the region around the bias dot is displayed on top.

first and second production (CiS1 and CiS2) were documented in Ref. [37,67]. The CiS3 production was for the most part investigated in Ref. [37] and these results are used for comparison in this thesis. The characterisation of the CiS3 production is completed together with the description and characterisation of the CiS4 production.

CiS3 production

The third CiS production is the first and up to now only CiS production, which was performed on 6-inch wafers. The wafers have a resistivity of $16 \text{ k}\Omega \text{ cm}$ and a thickness of $270 \mu\text{m}$. They are processed without the use of a handle wafer and thinned before the start of the processing. All pixel sensors are designed with the GR design adapted from the CiS2 production, with 10 implemented GRs and one BR with a total edge distance of $d_e = 450 \mu\text{m}$, defined as the distance between the UBM pad of the last pixel cell to the center of the dicing line. The sensor design with the GR structure, a $50 \times 250 \mu\text{m}^2$ pixel cell and single bias dot of $10 \mu\text{m}$ diameter is shown in Figure 5.1a. One sensor in each wafer of these productions has a modified layout with $25 \times 500 \mu\text{m}^2$ pixel cells still compatible to the FE-I4 chips. In this design a p-t design with a common bias dot, placed externally to the pixel implant and serving four neighbouring pixels, was implemented. A sensor cut-out of the $25 \times 500 \mu\text{m}^2$ pixel cell arrangement is illustrated in Figure 5.1b. To prevent the readout chip and the sensor surface from possible sparks, a thin BCB layer of $3 \mu\text{m}$ is used as a passivation layer. An easy processing of the thin film layer is possible due to the chemical reaction (polymerization) during manufacturing. The non-polar chemical structure of BCB leads to a low dielectric constant ($\epsilon_r = 2.65$) and a high breakdown voltage ($530 \text{ V}/\mu\text{m}$). Furthermore, BCB offers good planarization properties [132]. This coating involves an additional photolithographic process to open the electric contacts at the exact positions of the Under-Bump Metallisation (UBM) pads.

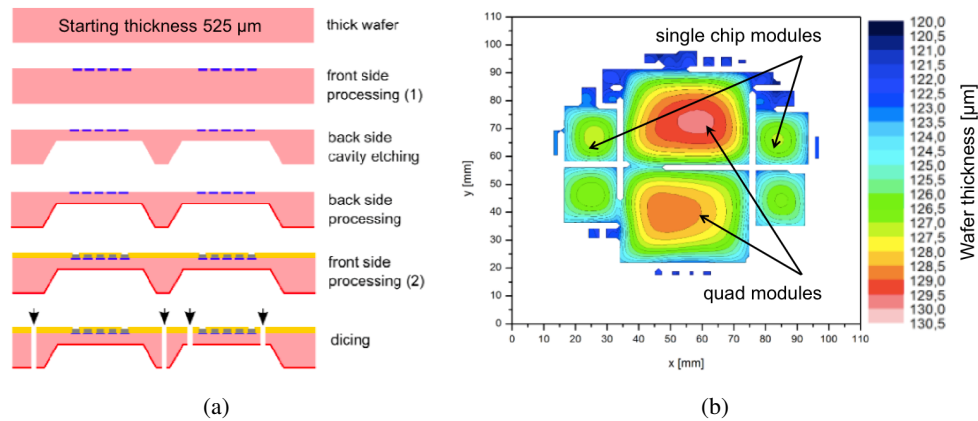


Figure 5.2: (a) production process flow at CiS technology, taken from Ref. [133], and (b) thickness fluctuations within one wafer.

The BCB and UBM are deposited at the Fraunhofer Institute for Reliability and Microintegration² (IZM), before the sensors are interconnected to FE-I4 chips.

CiS4 productions

For the fourth production an innovative method was explored to produce thin sensors without the use of a handle wafer. The technology employs anisotropic Potassium Hydroxide (KOH) etching [134] to create backside cavities within the wafer, leaving thicker frames around each single structure. Figure 5.2 describes the process flow beginning with a wafer starting thickness of 525 μm. As a next step, the front side is partially processed with n⁺-implants defining the electrodes. It is followed by the etching of cavities into the backside of the wafer. Below each single sensor the wafers are locally thinned to an active thickness of 100 μm or 150 μm. The backside is processed with an implantation of a p⁺ layer afterwards, while the front side is processed with additional p-spray. The process is continued with a common thermal annealing and finishes with the last metallisation and passivation steps on the front side [135]. Two different sets of dicing lines are implemented. One is designed in the center of the frames between the neighbouring sensors and the second one within the borders of the thinned membrane. The structures, studied in this thesis, were diced following the internal set of dicing lines and result in a homogenous thickness of either 100 μm or 150 μm. This technology does not need a handle wafer during the thinning process, thus being potentially cheaper, than the alternative methods employing SOI wafers. Thanks to the optimized procedure, only small thickness variations up to a maximum value of 10 μm in the cavities were measured as shown in Figure 5.2b. The production consists of 25 wafers with a resistivity of 20 kΩ cm. The depletion voltages for the sensors range from around 10 V in case of the 100 μm thick device to 30 V for the 150 μm thick device. Two pixel designs were implemented together with the common p-t design, which was found to retain the highest efficiencies after irradiation: the FE-I4 pixel cell size of 50×250 μm² cell and a modified pixel cell of 50×250 μm². The latter is composed of five

²<https://www.izm.fraunhofer.de>

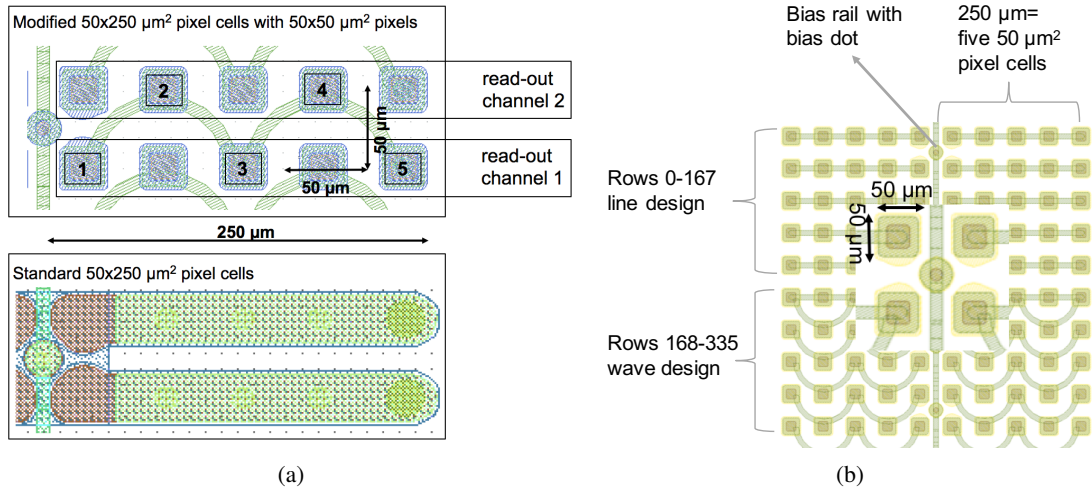


Figure 5.3: A modified 50 \times 250 μm^2 pixel cell composed by five 30 \times 30 μm^2 pixel implants with a 50 \times 50 μm^2 pixel cell is shown. The small implants are connected by metal lines allowing for a read-out by the FE-I4 chip: (a) (bottom) compared to an FE-I4 pixel cell and (b) cut-out of the sensor layout where the implementation of the line and wave designs is shown.

30 \times 30 μm^2 pixel implants in pixel cells of 50 \times 50 μm^2 connected by metal lines allowing for readout by the standard FE-I4 chip. A cut-out of the sensor layout is shown in Figure 5.3. Two layouts to link five 30 \times 30 μm^2 implants using a metal rail were designed and implemented in one single sensor of 336 rows and 80 columns allowing for a direct comparison of the performance. In the first 168 rows of the sensor, adjacent implants are linked creating the FE-I4 geometry and in the following is referred to as line design. Instead, in the last 168 rows, neighbouring pixel implants are read out by two different channels, with only every second pixel implant inside a 50 \times 250 μm^2 pixel cell being read out by the same channel. This is denoted as wave design. Therefore, the last-mentioned design makes it possible to investigate the effect of charge sharing in adjacent 50 \times 50 μm^2 pixels.

5.1.2 MPP/HLL productions

A production, henceforth referred to as SOI3, carried out at the Halbleiterlabor of the Max-Planck-Society³ (MPG HLL) was completed on 6-inch wafers in 2016 of standard p-type FZ silicon. The wafers are provided with a resistivity of 20-23 k Ω cm and sensor thicknesses of 100 μm or 150 μm . A total number of 11 GRs and one BR are realised in the sensors resulting in an edge distance of $d_e = 450 \mu\text{m}$. Sensors with reduced numbers of rings, 8 and 4, yielding $d_e = 300 \mu\text{m}$ and $d_e = 90 \mu\text{m}$ respectively, are also implemented. Homogenous p-spray is used for the inter-pixel isolation.

For the thinning process, developed at this facility and shown in Figure 5.4, Silicon on Insulator (SOI) wafers are employed. Accordingly, a handle wafer is attached to the active pixel wafer, serving as a mechanical support to ensure the rigidity of the structure for the subsequent processing steps [136]. After the backside of the active pixel wafer is processed with an oxidation and boron

³<https://www.hll.mpg.de>

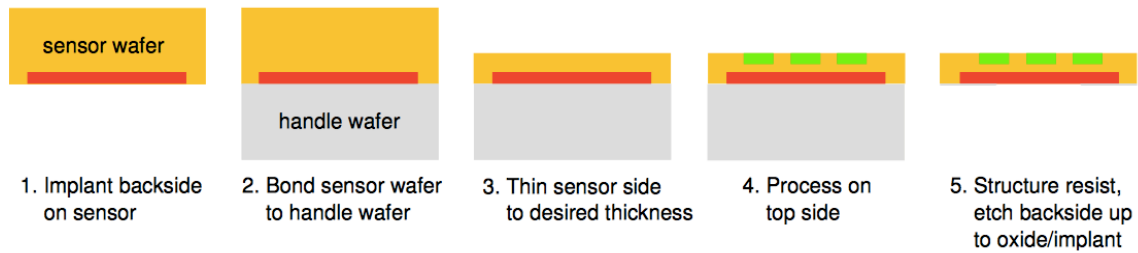


Figure 5.4: Sketch of the MPP/HLL process [136].

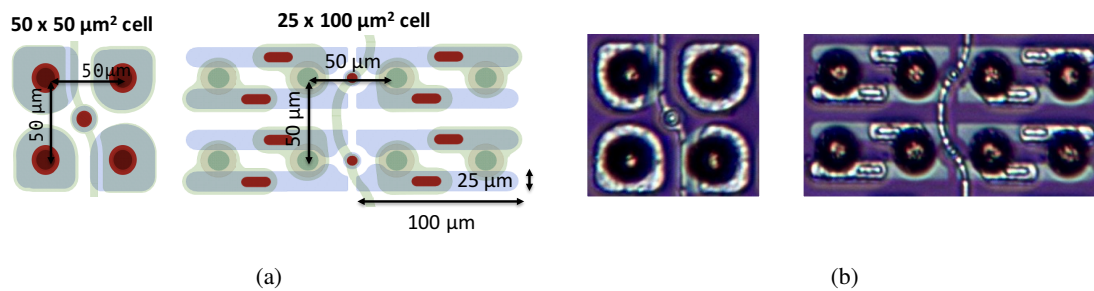


Figure 5.5: (a) novel pixel design of $50 \times 50 \mu\text{m}^2$ and $25 \times 100 \mu\text{m}^2$ pixel cells combining the common p-t design with the new arrangement of the bias rail being superimposed to the pixel implant as much as possible. (b) images of the $50 \times 50 \mu\text{m}^2$ and $25 \times 100 \mu\text{m}^2$ pixel cells.

implantation, it is directly bonded to the handle wafer. The thinning to the active thickness is then performed from the front side using the Chemical Mechanical Polishing (CMP) technique [137]. The front side is processed afterwards. As for the CiS production, a BCB passivation layer is used to coat the sensor to avoid possible sparks.

In the course of passivation, openings for the electrical contacts for the UBM pads are left open. Following the UBM processing, the handle wafer is completely grinded or etched away. The etching takes place up to the SiO_2 passivation layer that protects the active pixel wafer. Finally, the wafers are diced into sensors and are interconnected to FE-I4 chips. Sensors were produced with the FE-I4 pixel cell size of $50 \times 250 \mu\text{m}^2$ as well as with the RD53 compatible pixel cell size. The new pixel cells are designed to be compatible with the $50 \times 50 \mu\text{m}^2$ cells of the readout chip that is being developed by the RD53 Collaboration [76]: one with the same cell size and an alternative version with $25 \times 100 \mu\text{m}^2$ cell size. Both new RD53 layouts are depicted as schematics and as images in Figure 5.5. In both designs, FE-I4 and RD53 pixel cells, a p-t structure with a common bias dot is chosen together with the bias rail superimposed to the pixel implant. These specific designs of the bias dot and the bias rail were previously found to have the best performance after irradiation [37]. In the design of the FE-I4 pixel cell two varieties of BR interconnection are implemented. One design keeps the BR surrounding the pixels grounded. UBM openings are placed on the BR to allow for electric contact to the chip to supply ground potential. The BR then directs the grounding to the bias rail, as in all previous designs of the MPP productions. The other implementation includes a floating BR to investigate the possibility of reducing the effect of punch-through on the hit efficiency after

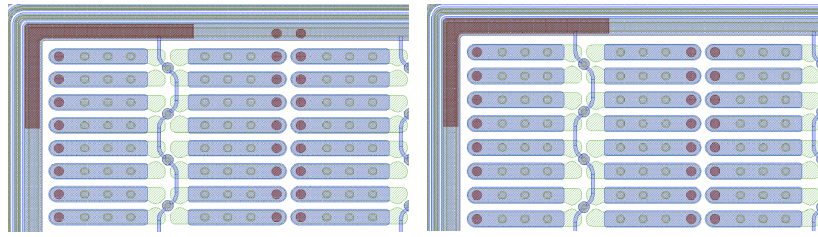


Figure 5.6: Two different sensor types: the standard design with the grounded BR (on the left) and the modified design (on the right) with the floating BR for FE-I4 compatible sensors with a pixel cell size of $50 \times 250 \mu\text{m}^2$. The two brown circles on the horizontal section of the BR in the left figure show the positions of the passivation openings to connect the BR to the chip.

irradiation. This is accomplished by not opening the passivation layer on the BR in correspondence of the bumps on the chip. For this reason, an electrical connection between the chip and BR on the sensor is avoided. An additional approach to prevent electrical contact modifies the chip bumping configuration. While growing the bump balls on the chip, the ones to be placed on the BR are left out in the bump ball processing. This makes a direct comparison between two different strategies to suppress electrical contact on the BR possible. A consequence from the floating BR, implemented in both designs, is, that higher currents from the edges directly flow into the edge columns with the possible risk of causing low breakdown voltages. Furthermore, increased leakage currents for the cells in these edge columns will occur. In Figure 5.6, the two different types of BR implementation on the sensor are shown.

Some of the sensors of the SOI3 and CiS4 production were connected to chips post-processed with BCB. The aim of this additional passivation layer on the chip side is again to prevent sparks between sensor and chip. This is particularly important in the case of the CiS4 production, where the thinning process with the cavities in the backside did not allow for the BCB deposition on the sensor side. For half of the chips the BCB is deposited only on the chip edges, where the chip faces the not active area of the sensor at high voltage potential, called frame BCB from here on. For the other half of the chips, the BCB coating is on the full surface (named full BCB) except for the openings for the bumps and wire bonding pads.

5.1.3 ADVACAM productions

The ADVACAM⁴ (Finland) production is a follow-up of the previous production at VTT (Finland), from which ADVACAM is a recently founded spin-off company. The second SOI run at ADVACAM employs 6-inch wafers with a FZ silicon active bulk and is focused on pixel sensors with active edges. The FZ wafers have an initial resistivity of 20-23 k Ω cm. This production has been designed to extend the research program, initiated with the VTT-FE-I3 compatible sensors, see Ref. [53], to FE-I4 geometries in the thickness range of 50 μm to 150 μm . The depletion voltages for the thicker devices correspond to the ones of the sensors from the other productions. The 50 μm thick sensors show an even lower depletion voltage at around 5 V. The thinning process at ADVACAM [138] resembles the one at MPP/HLL. After front side processing, trenches are realised around the

⁴<http://advacam.com>

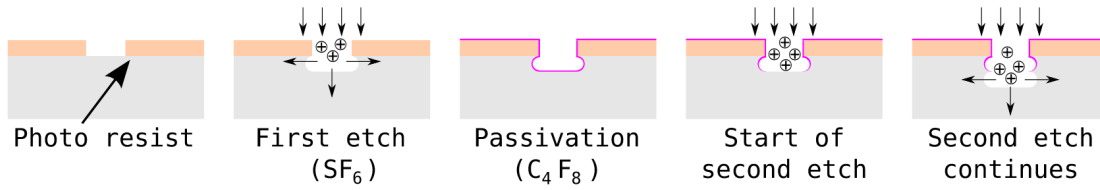


Figure 5.7: Depiction of the DRIE process in silicon structures, taken from Ref. [67]. The three main steps of the DRIE technique conducted on a wafer are: 1. coating with photoresist, 2. etching of the trenches with SF_6 , 3. passivation with C_4F_8 .

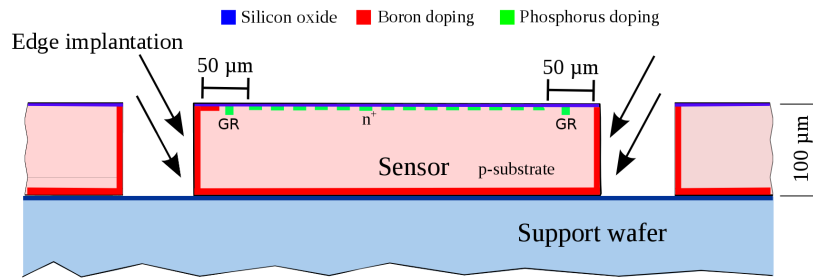


Figure 5.8: Schematic view of the sensor processing at ADVACAM, where four-quadrant Boron implantation in the trenches is used.

perimeter of each sensor with Deep Reactive Ion Etching (DRIE) [70] using the mechanical support, offered by the handle wafer of the SOI stack. The DRIE technique is illustrated in Figure 5.7. As the first processing step, the entire wafer is covered with a photoresist mask except on the areas where the trenches need to be created. The trenches are repeatedly etched with SF_6 and passivated with C_4F_8 . After the trenches have reached the SiO_2 layer, a four-quadrant ion implantation of Boron ions is performed extending the p^+ implant of the backside to the edges, indicated in Figure 5.8 [139]. As a final step, after UBM deposition, the handle wafer is fully removed and the sensors are interconnected to FE-I4 chips with solder bump bonding. After interconnection, the modules are coated with parylene at IZM to prevent from sparks between the readout chip and the sensor surface. In contrary to the BCB coating performed before module assembly, the parylene coating is performed afterwards. At the module edges, a $5 \mu\text{m}$ thick parylene layer penetrates into the region between the readout chip and the sensor to a depth of about $100 \mu\text{m}$ and forms a protective film between the two.

A slim edge and an active edge design are implemented, differing in the distance d_e of the last pixel implant to the sensor edge. Two variants of slim edge sensors with $d_e = 100 \mu\text{m}$ were produced: the first one with a single BR, the second one with a BR together with one GR at floating potential. In both designs the single p-t design is implemented, as well as the common p-t design in case of the single BR design. The active edge design characterised by $d_e = 50 \mu\text{m}$ employs only one GR at floating potential. No p-t structure is implemented in this design. Due to the non existent biasing structures, it is not possible to test the functionality of the pixel cells before interconnection. Furthermore, after bump bonding the pixels are only grounded via the connection to the chip. A

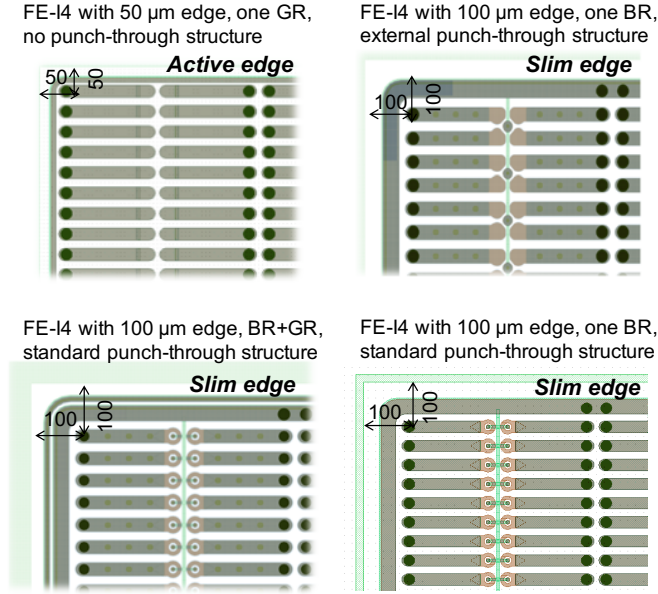


Figure 5.9: Four different sensor types of the ADVACAM SOI production: the active edge design with $d_e = 50 \mu\text{m}$, one GR and no p-t structure (top left), the slim edge design with $d_e = 100 \mu\text{m}$, one grounded BR and the common p-t structure (top right), the slim edge design with one BR and GR and the single p-t design (bottom left) and the slim edge design with only one BR and the single p-t structure (bottom right).

disconnected channel will cause a local modification of the electric field, which may lead to a lower breakdown voltage. On the other side the absence of the biasing rail avoids the efficiency loss after high irradiation doses, observed in the area where these structures are placed [37]. The four different sensor types are illustrated in Figure 5.9.

5.1.4 Overview of the modules and the irradiations performed on them

In this section an overview of the modules, pertinent to the thesis, of the CiS, HLL/MPP and ADVACAM productions is given emphasizing their unique characteristics in terms of sensor design. This is summarised in Table 5.1. For the investigation of the performance at the conditions foreseen at HL-LHC of various sensor designs and thicknesses, irradiations were carried out at CERN, the University of Birmingham, at Karlsruhe Institute for Technology and Jožef Stefan Institute. Irradiations were performed at these four irradiation facilities as described in Section 4.1 and are marked as CERN, UoB, KIT and JSI in the tables. The particles used for irradiation are protons, except for the latter one, where the irradiation is performed with neutrons. For a better comparison of the irradiations at the different facilities, the radiation doses are expressed in MeV equivalent neutron fluences. The irradiation of the devices takes place at module level to avoid severe annealing on sensor level during the high temperature interconnection to the readout chips. Annealing of the module will occur, when temperatures as high as 250°C need to be applied to solder the chip bumps on the sensor UBM. This circumstance involves the irradiation of the readout chips, which are known to be sensitive to high radiation doses [140]. Sensor and readout chip see identical irradiation, as in the case in the ATLAS detector. The chips are more prone to irradiation damage

Table 5.1: Summary of the single chip modules from the CiS3, CiS4, SOI3, ADVACAM and VTT productions relevant for this thesis. The different sensor characteristics are included in this overview. Values that do not change with row are only listed at first occurrence in this and all following tables.

Production	Thickness [μm]	Pixel cell [μm^2]	P-t design	Edge distance [μm]
CiS3	270	50×250	single	450
		25×500	external	
CiS4	150	50×250	external	450
		50×50		
	100	50×250		
SOI3	150	50×250	external + wave	450
				300
	100	50×250		450
			300	
ADVACAM	150	50×250	external	100
			no	50
	100	50×250	external	100
			no	50
	50	50×250	external	100
no			50	
VTT [37]	100	50×250	single	450

for ionising particles, and especially at low energies. This fact limits the selection for the irradiation to higher fluences than $5 \cdot 10^{15} \text{ n}_{\text{eq}} \text{ cm}^{-2}$ to the CERN-PS irradiation facility, since at KIT and the UoB the irradiation is performed with MeV protons. Furthermore, an irradiation of assembled FE-I4 modules is not possible at the Jožef Stefan Institute, since the presence of tantalum in the FE-I4 chip will be highly activated during neutron irradiation. In this thesis, only the sensors before interconnection were irradiated at the TRIGA Mark II research reactor.

An overview of the irradiations performed for the single chip modules is given in three tables divided according to the production run. The summary of the single chip modules from the CiS production is divided into modules from the CiS3 and CiS4 production. The results from the CiS3 production were mainly presented in [37] and are completed in this thesis, focusing on the devices with the modified pixel cells of a size of $25 \times 500 \mu\text{m}^2$. The performance of modified $50 \times 250 \mu\text{m}^2$ pixel cells with smaller $30 \times 30 \mu\text{m}^2$ implants in $50 \times 50 \mu\text{m}^2$ pixel cells implemented in the succeeding CiS4 production are compared to the standard pixel cell for different thicknesses. The selection of modules for this study is given in Table 5.2. The SOI3 production, the third production carried out at HLL/MPP, focuses on the investigation of different types of biasing designs. The results of the SOI3 modules with an external p-t design and a modified bias rail running superimposed to the

Table 5.2: Overview of the irradiated single chip modules of the CiS production. All sensors have a standard edge distance of $d_e = 450 \mu\text{m}$. Both modules with $50 \times 50 \mu\text{m}^2$ pixel cells have an FE-I4 $50 \times 250 \mu\text{m}^2$ pixel cell geometry and are compatible to the FE-I4 chip, such as the rest of the modules in the table.

Production	Module	Thickness [μm]	Pixel cell [μm^2]	Irradiation at	Fluence [$10^{15} \text{ n}_{\text{eq}} \text{ cm}^{-2}$]
CiS3	W14-6	270	50×250	KIT	3+2+3
	W11-10		25×500		
CiS4	W6-4	150	50×250	CERN	10
	W7-6		50×50	UoB	3
	W11-4	100	50×250		5
	W16-6		50×50		

Table 5.3: Overview of the irradiated single chip modules from the HLL/MPP SOI3 production. All sensors have an FE-I4 pixel cell of $50 \times 250 \mu\text{m}^2$ and an external p-t design with a modified bias rail running as much as possible on top of the pixel implants.

Name	Thickness [μm]	Grounded BR	Chip coating	Irradiation at	Fluence [$10^{15} \text{ n}_{\text{eq}} \text{ cm}^{-2}$]	Edge distance [μm]
W7-2	150	yes	no	UoB	2	450
W7-1		no (sensor)		CERN		
W4	100	yes	frame	CERN	5	300
W6		no (sensor)				

pixel implants are compared to the CiS4 modules with the previous linear design of the standard bias rail. The focus of this production is on the investigations of the new implementation of the BR which is either forced to ground, or on a floating potential, and on the two ways of BCB coatings. The modules investigated in this thesis are listed in Table 5.3. In this production, as well as in the CiS4 production, the external p-t design is implemented with a bias dot size of $d_b = 23 \mu\text{m}$, whereas the bias dot size is $d_b = 18 \mu\text{m}$ in the ADVACAM production. The results obtained with these different geometries from beam tests are compared. An overview of the modules of the ADVACAM production is given in Table 5.4. The main characteristics of this production are the differing edge designs along with the varying implementations of p-t design. The latest external p-t design is confronted with the previous single p-t design and with the design without any p-t structure, implemented in the active edge design. Due to a low breakdown voltage after irradiation caused by the reduced pixel-edge distance, the modules of the ADVACAM productions are, differently than in other productions, only irradiated to fluences up to $3 \cdot 10^{15} \text{ n}_{\text{eq}} \text{ cm}^{-2}$.

Table 5.4: Overview of the irradiated single chip modules with active edges from the ADVACAM production. The module from the VTT production is included at the bottom of this table.

Name	Thickness [μm]	P-t design	Edge distance [μm]	Irradiation at	Fluence [$10^{15} \text{ n}_{\text{eq}} \text{ cm}^{-2}$]
6-1B	150	no	50	BIRM	1+2
2-3B	100	single	100	UoB	3
7-2B		external		CERN	
2-1D		no	50		
3-1A	50	no	50	UoB	1
VTT	100	single	450	JSI	10

5.2 Performance of thin sensors

5.2.1 IV characteristics

Electrical properties of thin sensors from different productions with thicknesses of 50 μm , 100 μm and 150 μm are investigated before and after irradiation.

Before irradiation, the leakage currents of bare sensors are measured at an environmental temperature of 20°C. Their IV characteristics after irradiation are obtained at bare sensor level keeping the backside in contact with the cold chuck of a probestation at an environmental temperature of -25°C. The module characterisation after irradiation in a climate chamber is performed without direct contact between the sensor and a solid cooling element. The sensor self-heating therefore induces a local temperature increase that cannot be estimated with high precision. For this reason, the exact leakage current values are extracted in the MPP set-up only at bare sensor level.

Figure 5.10 shows the results of the SOI3 production for different sensor designs with an FE-14 pixel cell of $50 \times 250 \mu\text{m}^2$ and sensor thicknesses of 100 μm and 150 μm for measurements performed on sensor and module level. All sensor types with 100 μm thick sensors show in general 20-40 V lower breakdown voltages throughout the different edge distances. This is due to the higher electric field in sensors with smaller distance between the two sides, where the ground and high voltage potential are applied. In thin sensors, critical values for the electric field are reached earlier and consequently lead to a lower breakdown. In thicker sensors, the voltage drop occurs over a wider electrode distance and therefore increases the range of operational bias voltage. The highest breakdown voltages around 120 V are reached for 150 μm thick sensors and an edge distance of $d_e = 450 \mu\text{m}$. This is well above the depletion voltage of 10 V to 30 V expected from the high bulk resistivity. Due to the higher electric field, originating from the voltage drop within the smaller distance between the ground potential of the BR and the high voltage at the sensor edge, the range of operational voltage decreases for shorter edge distances. In the case of a 100 μm thick sensor and the shortest edge distance of $d_e = 90 \mu\text{m}$ the operational voltage decreases down to 40 V. Given their high breakdown voltages, only sensors with edge distances of $d_e = 300 \mu\text{m}$ and $d_e = 450 \mu\text{m}$ were

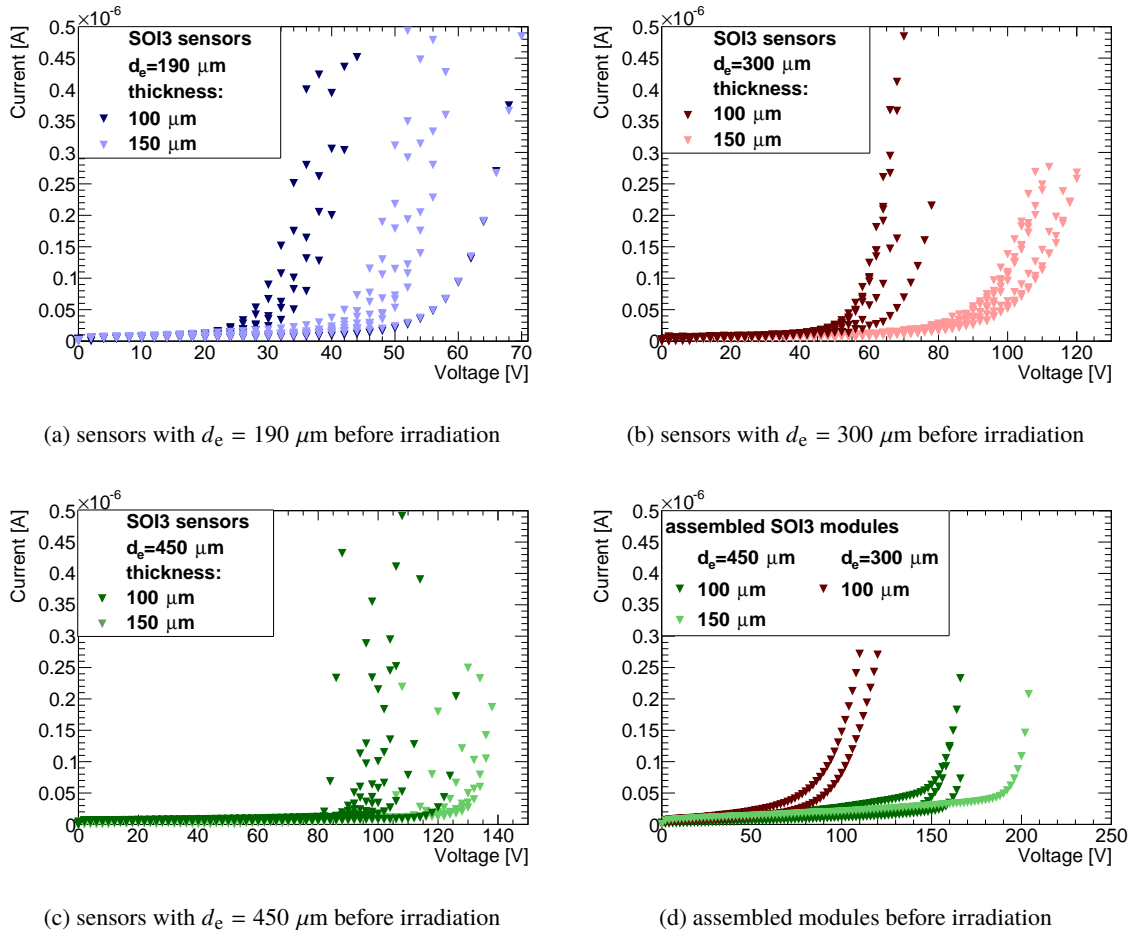


Figure 5.10: Leakage current as a function of bias voltage before irradiation (a-c) for bare sensors from the SOI3 production with different edge designs and (d) after interconnection to readout chips. Results of sensor thicknesses of $100 \mu\text{m}$ (always darker color) and $150 \mu\text{m}$ are shown. Currents for bare sensors were measured at 20°C on a cooled chuck, whereas for assemblies the local temperature is not perfectly determined.

interconnected to readout chips. The IV curves of the sensors after interconnection are summarised in Figure 5.10d for both sensor edge distances and thicknesses. The difference in the potential between the pixel implants and the surrounding area increases the breakdown voltages for the sensors after interconnection to readout chips. Before interconnection, the backside of the sensor is biased and the front side of the sensor, including the pixel implants, is grounded via the BR and the punch-through mechanism. The potential of the pixels results in a slightly more negative value being closer to the backside potential, when compared to the p-t structure. After interconnection, each pixel implant is grounded by each channel of the chip via the bump balls. Potential differences between the pixel implants and the surrounding area is minimized resulting in a more homogenous distribution of ground potential over the sensor surface. The sensors consequently show a more stable performance in terms of breakdown voltage.

The CiS4 sensors with standard edge distances of $d_e = 450 \mu\text{m}$ show higher leakage current levels ($0.5\text{-}1 \mu\text{A}$) and breakdown voltages mostly above 200 V in the case of the $150 \mu\text{m}$ thick sensors,

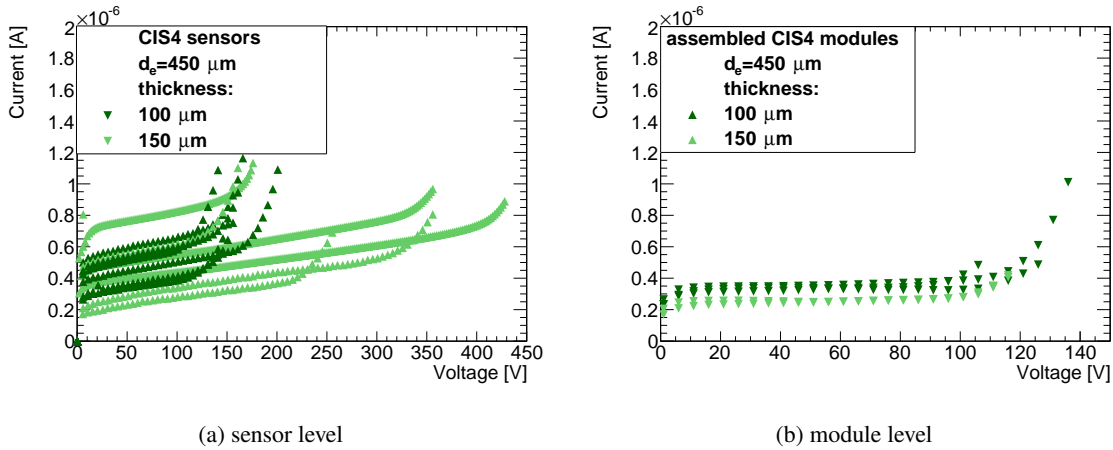


Figure 5.11: Leakage current as a function of bias voltage before irradiation (a) for bare sensors from the CiS4 production with thicknesses of 100 μm and 150 μm and (b) after interconnection to readout chips.

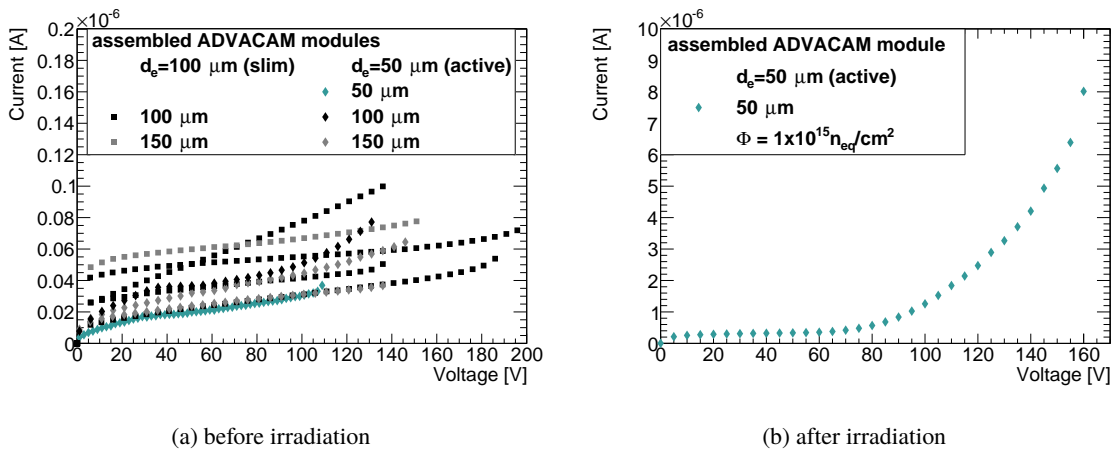


Figure 5.12: Properties of FE-I4 pixel modules from the ADVACAM production with sensors of 50 μm , 100 μm and 150 μm thickness in terms of leakage current as a function of bias voltage (a) before and (b) after irradiation to a fluence of $10^{15} \text{ n}_{\text{eq}} \text{ cm}^{-2}$ of a module with a 50 μm thick sensor and $d_e = 50 \mu\text{m}$. The measurements in (a) were performed at a temperature of 20°C, while the one for the irradiated module in (b) was performed at around -50°C. For some modules the measurements were stopped shortly before the breakdown to avoid sparks between the sensor and chip.

see Figure 5.11. After interconnection, IV curves were recorded for the modules built with these sensors and they showed breakdown voltages around 100 V, for both 100 μm and 150 μm thick sensors.

Sensors with active edges from the ADVACAM production and their IV characteristics are presented in Figure 5.12. The measurements were performed at module level because no bare sensors were delivered for this production. Thanks to their special side activation process, the ADVACAM sensors with small edge distances of $d_e = 100 \mu\text{m}$ and $d_e = 50 \mu\text{m}$ feature higher breakdown voltages than the short edge sensors of the SOI3 production. The breakdown voltages of around

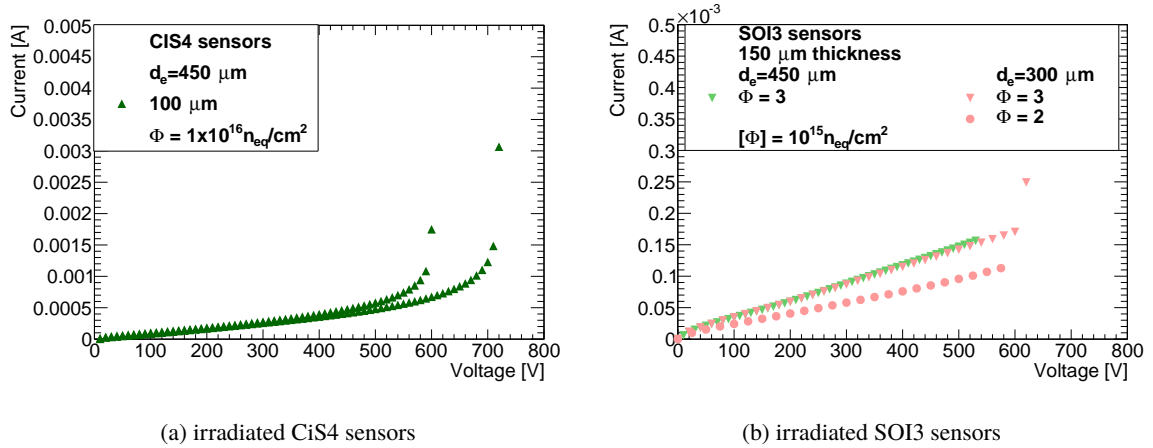


Figure 5.13: Leakage currents of CiS4 and SOI3 sensors as a function of bias voltage after irradiation. (a) the breakdown voltages of the 100 μm thick CiS4 sensors after an irradiation to a fluence of $10^{16} \text{ n}_{\text{eq}} \text{ cm}^{-2}$ are 600-700 V. (b) for both SOI3 sensors with an edge distance of $d_e = 300 \mu\text{m}$ the breakdown voltages are around 600 V after an irradiation to fluences of $2 \cdot 10^{15} \text{ n}_{\text{eq}} \text{ cm}^{-2}$ and $3 \cdot 10^{15} \text{ n}_{\text{eq}} \text{ cm}^{-2}$. The IV curve for the sensor with the largest edge was stopped before breakdown, which is expected to be shortly after 600 V. The scales in leakage currents are different with respect to each other.

150 V are well above the thickness dependent depletion voltage of 5 V to 30 V, which is the case for all sensor productions. No significant difference in breakdown voltage between active and slim edge designs is detected before irradiation. The module with the thinnest sensor of 50 μm thickness shows a breakdown voltage of 110 V before irradiation. As no ADVACAM sensors are irradiated before interconnection, the IV curves of an ADVACAM module with a 50 μm edge are measured after irradiation in the climate chamber with an ambient temperature of -50°C . The readout chip is not powered, since otherwise the powered chip would further increase the temperature in addition to the sensor self-heating. The ADVACAM module shows a breakdown voltage slightly above 100 V after an irradiation to $10^{15} \text{ n}_{\text{eq}} \text{ cm}^{-2}$. For the thicker ADVACAM modules, irradiated at a higher fluences of $3 \cdot 10^{15} \text{ n}_{\text{eq}} \text{ cm}^{-2}$, a low breakdown voltage at around 200 V is observed. This is due to the high electric field present at the edges of these sensors and leads to a reduced range of bias voltage. Compared to the IV measurements on irradiated bare sensors from the CiS4 and SOI3 production, with the same sensor thickness, the breakdown voltages for the active edge sensors are lower. The IV measurements on the irradiated ADVACAM modules were performed with a voltage scan during a test beam campaign, discussed in Section 5.2.5.

The results of the IV characterisation of CiS4 sensors with a sensor thickness of 100 μm are summarised in Figure 5.13 after an irradiation to a fluence of $10^{16} \text{ n}_{\text{eq}} \text{ cm}^{-2}$ together with SOI3 sensors with a sensor thickness of 150 μm irradiated up to a fluence of $3 \cdot 10^{15} \text{ n}_{\text{eq}} \text{ cm}^{-2}$. The sensors can not be directly compared since the irradiated samples of the different productions do not have the same thickness and were not exposed to the same irradiation dose. The leakage currents of the CiS4 and SOI3 sensors scale with the irradiation fluence. The breakdown voltages of the 100 μm thick CiS4 sensors after an irradiation up to $10^{16} \text{ n}_{\text{eq}} \text{ cm}^{-2}$ are 600-700 V. This is in good agreement

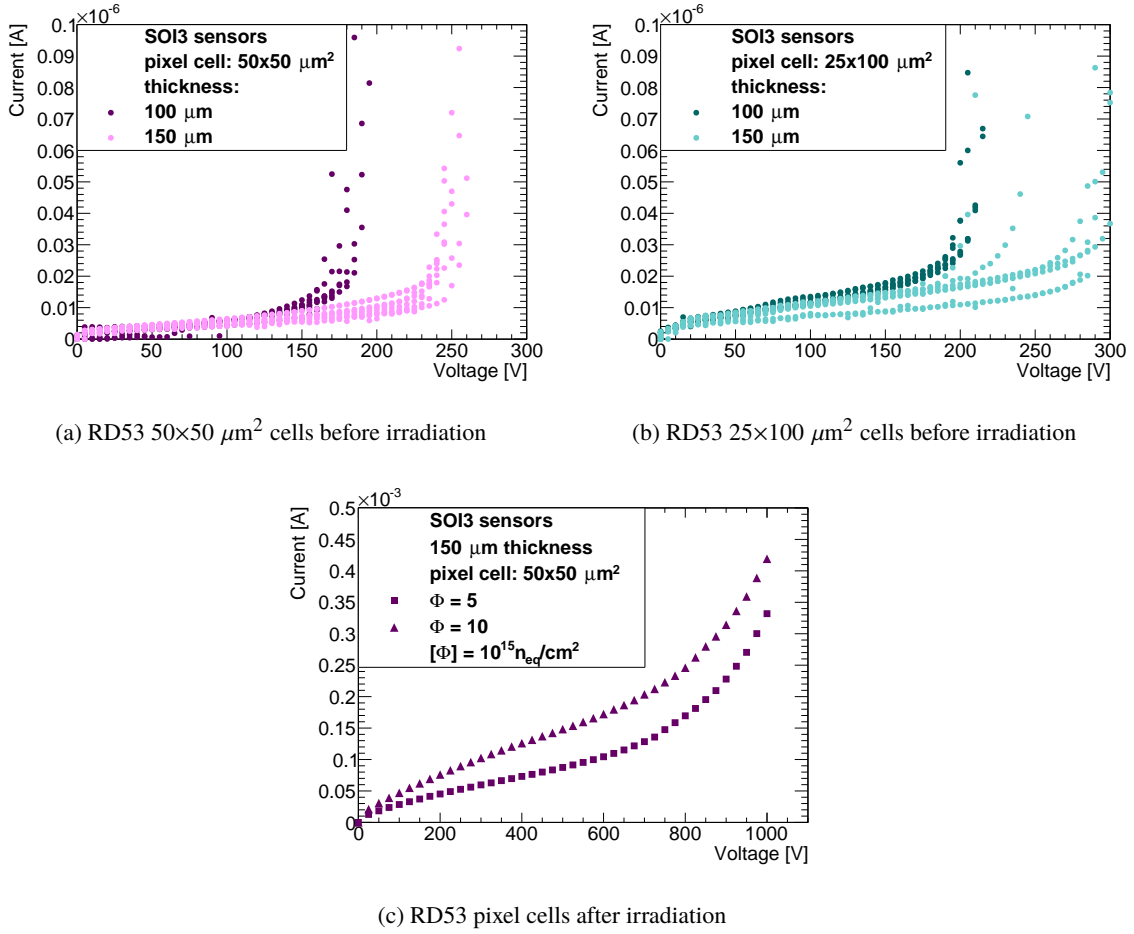


Figure 5.14: Leakage current as a function of bias voltage of the RD53 sensors from the SOI3 production. Sensors with a thicknesses of 100 μm and 150 μm and with pixel cells of (a) 50x50 μm^2 and (b) 25x100 μm^2 are summarised before irradiation. The sensors with the 25x100 μm^2 pixel cells show higher breakdown voltages compared to the sensors with the 50x50 μm^2 pixel cells before irradiation. (c) sensors with 100 μm thickness and a pixel cell of 50x50 μm^2 are shown after irradiations to fluences of $5 \cdot 10^{15} n_{\text{eq}} \text{cm}^{-2}$ and $10^{16} n_{\text{eq}} \text{cm}^{-2}$. After irradiation, the RD53 sensors can be biased up to 1000 V.

with previous results [37]. The same accounts for the breakdown voltages of the 150 μm thick SOI3 sensors irradiated up to a fluence of $3 \cdot 10^{15} n_{\text{eq}} \text{cm}^{-2}$ with breakdown voltages up to 600 V. No significant difference in terms of leakage current performance is observed for the different edge distances.

Particularly relevant for ITk are the results of the IV measurements of the RD53A compatible sensors. The curves relative to 100 μm and 150 μm thicknesses are shown in Figure 5.14. They present comparably low currents below 20 nA. The breakdown voltages are in the range of 150-250 V and well above the depletion voltage. The IV curves of pixels with a cell size of 50x50 μm^2 are displayed in (a), 25x100 μm^2 pixel cells are shown in (b). Pixel cells of 25x100 μm^2 appear to have a higher breakdown voltage of roughly 50 V more compared to pixel cells of 50x50 μm^2 size. Sensors with 50x50 μm^2 pixel cells were measured after irradiation fluences of $5 \cdot 10^{15} n_{\text{eq}} \text{cm}^{-2}$ and

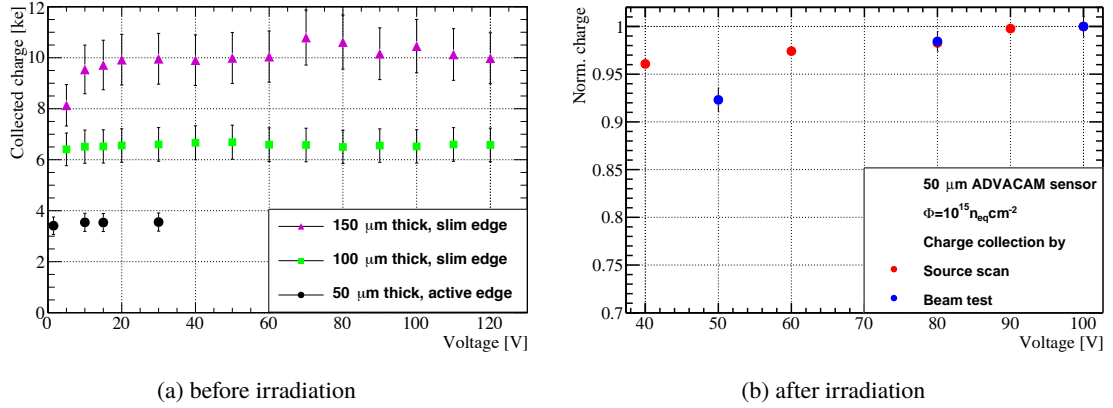


Figure 5.15: (a) collected charge as a function of bias voltage of FE-I4 pixel modules from the ADVACAM production with sensors of 50 μm , 100 μm and 150 μm thickness, measured in ^{90}Sr source scans. (b) comparison of the collected charge of an ADVACAM module with a 50 μm thick sensor irradiated to $10^{15} \text{ n}_{\text{eq}} \text{ cm}^{-2}$. The results were obtained with source scan measurements and particle beams. Where not visible, the statistical uncertainties in (b) are smaller than the marker size.

$10^{16} \text{ n}_{\text{eq}} \text{ cm}^{-2}$ and show no breakdown up to a voltage of 1000 V.

Comparing the outcomes of the FE-I4 to the RD53 sensors of the SOI3 production before irradiation, their performance is shown to be similar in terms of leakage currents and breakdown voltages. Thanks to the smaller distance between two neighbouring implants, the breakdown voltages of the sensors with the $25 \times 100 \mu\text{m}^2$ cells are by around 50 V higher.

5.2.2 Charge collection

In this section, the charge collection of a module before and after irradiation is discussed. Modules from all three productions are tested with particle beams and radioactive sources. Bare CiS4 and SOI3 sensors are measured by the Edge-TCT method. The outcomes of all three methodologies are investigated and compared. Charge collection and its dependency on the bias voltage and irradiation fluence are investigated by beam test measurements and compared to the results obtained by Edge-TCT measurements. In addition, the charge collection profile obtained from Edge-TCT studies is discussed.

Results obtained by beam test and source scan measurements

Beam test and source scan studies are performed on modules from all three productions with the FE-I4 pixel cell design of $50 \times 250 \mu\text{m}^2$ and on CiS4 modules with the modified pixel cell with $30 \times 30 \mu\text{m}^2$ pixel implants. In Figure 5.15a, the collected charge as a function of bias voltage is shown for unirradiated ADVACAM modules of different sensor thicknesses from 50 μm to 150 μm tested with a ^{90}Sr source. In case of source scan measurements, the charge is calibrated from ToT values and studied as a function of bias voltage.

A more detailed description of the method and the uncertainties are given in Section 4.3.1. Looking

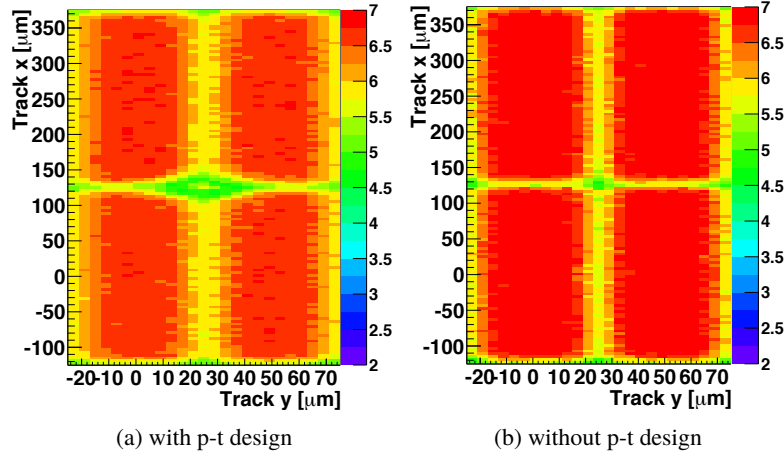


Figure 5.16: In-pixel charge collection map in ToT of 150 μm sensors with an FE-I4 pixel cell design of $50 \times 250 \mu\text{m}^2$ with (a) a sensor by CiS with a common p-t structure and (b) a sensor from ADVACAM with no punch-through implementation. Four pixel cells are displayed with the bias dot in the center of the map in (a). The voltage applied on the sensors is 50 V.

at the collected charge for different bias voltages in ^{90}Sr scans, it is flat for all sensor thicknesses after depletion and the measured values agree well with the expectations [53]: for 50 μm a charge of 3.1 ke is collected, for 100 μm 6.7 ke and for 150 μm 10.2 ke. Hence, this corresponds well to the principle that every 1 μm traversed in the silicon by a MIP 70-80 electrons-hole pairs are created, as introduced in Section 2.2.4. The 50 μm thick sensors gives a really low depletion voltage of around 5 V, the increase of the collected charge is not even visible in Figure 5.15a. The saturation of the collected charge starts at 20 V for the 150 μm device, showing a flat plateau after 20 V. In Figure 5.15b, the charge collection behaviour of an ADVACAM module with a 50 μm thick sensor and after an irradiation to $10^{15} \text{ n}_{\text{eq}} \text{ cm}^{-2}$ is depicted. The collected charge is obtained in two ways: by source scans measurements with ^{90}Sr , as well as by high energy particle beam measurements with pions of an energy in the GeV range. The outcomes are normalised to the value at the highest voltage step. Since charge calibration is not possible during beam test measurements, the charge normalisation serves for direct comparison of the collected charge dependence on the bias voltage. Both approaches show a saturation of the charge above 90 V. Only the point at 50 V obtained by beam test measurements is slightly off with respect to the source scan value, which may be due to slightly different tunings. Compared to the collected charge of the module with the 50 μm thick sensor before irradiation, the saturation of the charge is shifted from 5-10 V to around 90 V after an irradiation to a fluence of $10^{15} \text{ n}_{\text{eq}} \text{ cm}^{-2}$. The uncertainties restrict to statistical uncertainties for the not calibrated charge values. The beam test analysis framework additionally comprises a two-dimensional charge collection view of the pixel implants to allow for direct visibility of regions of high charge and low charge.

Figure 5.16a depicts the in-pixel charge collection map of four FE-I4 pixel cells with the bias dot in the center. The charge collection map is from a CiS4 module before irradiation. In Figure 5.16b it is shown for an unirradiated ADVACAM module without p-t design.

Both modules are assembled with 150 μm thick sensors and 10 000 to 12 000 electron-hole pairs are expected for a MIP. Therefore, the modules are tuned to 7 ToT at 14 ke to cover the range of possible collected charge. As no calibration of the charge is performed during beam test measurements, the collected charge is expressed in ToT from here on. Comparing both charge collection maps 7 ToT are registered in the $30 \times 230 \mu\text{m}$ pixel implant of both sensor producers whereas in a 5-10 μm frame around the pixel implant slightly less charge of 6 ToT is collected. In addition, 4 to 5 ToT are registered in the CiS4 sensor in the region of the bias dot, as well as in the area, in which the bias rail is implemented. The charge released in this area, is shared by the neighbouring implants and results in a lower charge in between implants. Therefore, the probability, that the collected charge in one of the two pixel cells is below threshold, is increased. The so-called charge sharing occurs in between the pixel implants for both sensors. For the CiS4 sensor, additional charge sharing between the bias dot and those corners on the implant close to the biasing structure further decreases the charge in this region. Hence, the area with less collected charge is increased for the CiS4 sensor around the bias dot.

Charge collection studies are also performed on modules, where $30 \times 30 \mu\text{m}^2$ implants are implemented in $50 \times 50 \mu\text{m}^2$ pixel cells forming a $50 \times 250 \mu\text{m}^2$ pixel cell. The modules with the modified pixel cell design, assembled with 100 μm and 150 μm thick sensors, are investigated before and after irradiation. The in-pixel charge collection maps before and after an irradiation to a fluence of $3 \cdot 10^{15} \text{ n}_{\text{eq}} \text{ cm}^{-2}$ are shown in Figure 5.17 for a single chip module with a 150 μm thick sensor. Figure 5.18 depicts the same type of in-pixel map for a module with a 100 μm thick sensor and up to an irradiation to a fluence of $5 \cdot 10^{15} \text{ n}_{\text{eq}} \text{ cm}^{-2}$. Before and after irradiation, the p-t design and the bias rail cause charge loss in the corner of the pixel being close to it in the modules with the 100 μm and 150 μm thick sensors. This is comparable with the previous results of the CiS4 module with a single FE-I4 $50 \times 250 \mu\text{m}^2$ pixel cell before irradiation.

As the neighbouring pixel implants in the wave design are read out by two different readout channels, charge sharing between the neighbouring pixel implants can appear. Charge loss between the pixel implants is visible before irradiation, as shown in Figures 5.17b and 5.18b. Due to the fact, that the metal rail connecting the pixel implants also acts as an additional connected pixel implant, it can partially compensate the charge loss. As in the case of the wave design, the metal rail runs in curves in the region between the long sides of the pixel cells (along the x-axis at $y \approx -10 \mu\text{m}$ to $y \approx 10 \mu\text{m}$ in Figure 5.17b), the charge loss is reduced in the corners of the pixel implant over which the metal rail is running. The signal of this region is summed up with the one of the neighbouring pixel along the diagonal, which is read out by the same readout channel. As in the case of the line design a straight metal rail connects the pixel implants running over the central region of the implants and the neighbouring pixel implants are read out by the same readout channel, no charge loss between the implants is visible before irradiation, as shown in Figures 5.17a and 5.18a. Instead, after irradiation, the charge loss is only partially compensated by the straight metal rail in the line design in the central regions of the pixel implants, where the metal rail is implemented. This is shown in Figures 5.17c and 5.18c. The pixel implants in the wave design after irradiation show an enhanced charge loss in the outer frames of the pixel implants. After an irradiation to a fluence of $3 \cdot 10^{15} \text{ n}_{\text{eq}} \text{ cm}^{-2}$, charge of 13-14 ToT is collected on the pixel implants itself. A clear line of

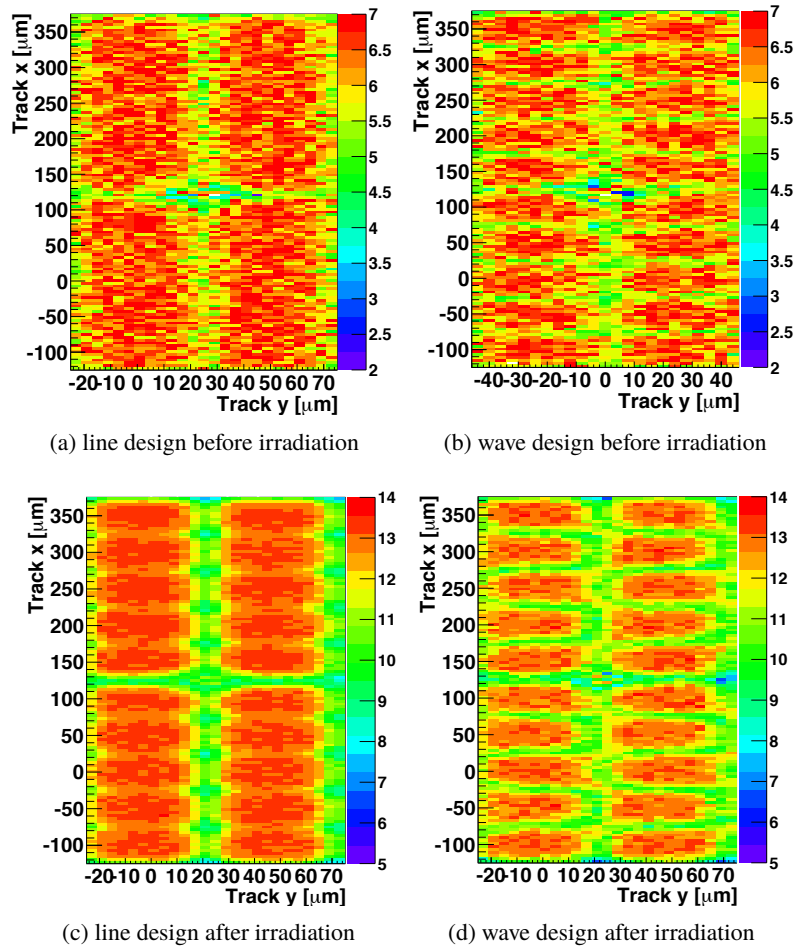


Figure 5.17: In-pixel charge collection map in ToT of $150 \mu\text{m}$ sensors (a,b) before and (c,d) after an irradiation to a fluence of $3 \cdot 10^{15} \text{ n}_{\text{eq}} \text{ cm}^{-2}$. 4 pixel cells are displayed with the bias dot in the center of the map. The line design is displayed in (a,c), the wave design is in (b,d). The charge collection map before irradiation is shown for the module biased at 50 V and a tuning of 7 ToT at 14 ke. The charge collection map of the irradiated module is displayed at a bias voltage of 500 V. From the tuning of the module 10 ToT correspond to 6 ke. Both modules were operated at full depletion.

1-2 ToT lower charge of around 12 ToT, surrounding the pixel implants, is observed.

Also in case of the module with the $100 \mu\text{m}$ thick sensor irradiated to a fluence of $5 \cdot 10^{15} \text{ n}_{\text{eq}} \text{ cm}^{-2}$, less charge is registered in the inter implant region after irradiation in the line and wave design, as shown in Figures 5.18c and 5.18d. In the wave design around 8 ToT charge is collected on the pixel implant itself, while in the frame around the implant 0.5-1 ToT less charge is collected after irradiation.

Comparing the line design to the wave design in both sensor thicknesses, there is an increased charge loss in the inter-implant region of the wave design before and after irradiation. The charge loss in the inter pixel region of the line design is only visible after irradiation.

In the following, the outcomes of the charge collection studies of the irradiated CiS4 modules with modified pixel cells are compared to the outcomes of irradiated SOI3 and ADVACAM modules with

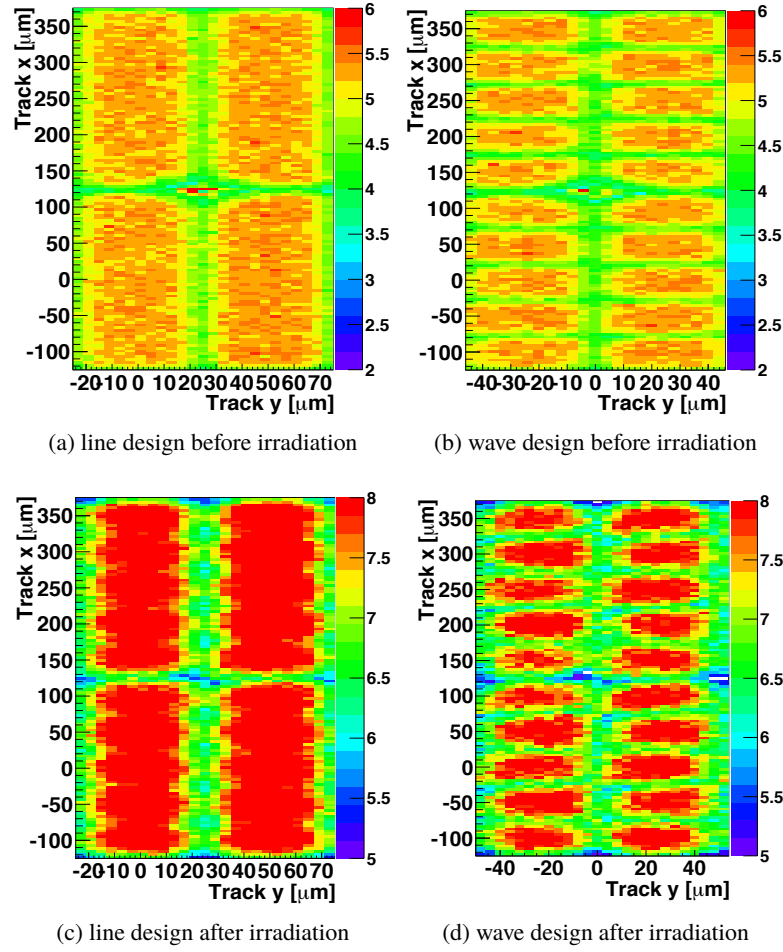


Figure 5.18: In-pixel charge collection map in ToT of a 100 μm thick sensor before and after irradiation to a fluence of $5 \cdot 10^{15} \text{ n}_{\text{eq}} \text{ cm}^{-2}$. The unirradiated module is biased with 60 V, the irradiated one with 600 V. 4 pixel cells are displayed with the bias dot in the center of the map. The line design is displayed in (a) before irradiation and (c) after irradiation, the wave design is displayed in (b) before irradiation and (d) after irradiation. From the tuning of the module 6 ToT corresponds to 6 ke before irradiation and 8 ToT correspond to 4 ke after irradiation.

standard $50 \times 250 \mu\text{m}^2$ pixel cells. The charge obtained by particle beams is normalised and shown as a function of bias voltage in Figure 5.19. In Figure 5.19a an ADVACAM module and a CiS4 module both with 150 μm thick sensors and after an irradiation to a fluence of $3 \cdot 10^{15} \text{ n}_{\text{eq}} \text{ cm}^{-2}$ are compared. The charge of the CiS4 sensor saturates at a higher voltage above 500 V. This performance is due to the smaller implants and is discussed in more detail in the subsequent section Section 5.2.4. The shorter edge distance of $d_e = 50 \mu\text{m}$, implemented in the ADVACAM sensor, limits the achievable bias voltage to values below 300 V. CiS4 and SOI3 modules with 100 μm thick sensors, irradiated to a higher fluence of $5 \cdot 10^{15} \text{ n}_{\text{eq}} \text{ cm}^{-2}$, are compared in Figure 5.19b and show a saturation of the charge at higher voltages above 600 V. The saturation of the charge in the SOI3 sensor is observed to be around 100 V lower compared to the modified CiS4 sensor, which fits well to the previously observed outcomes. A saturation voltage of more than 500 V for a module with a 150 μm thick

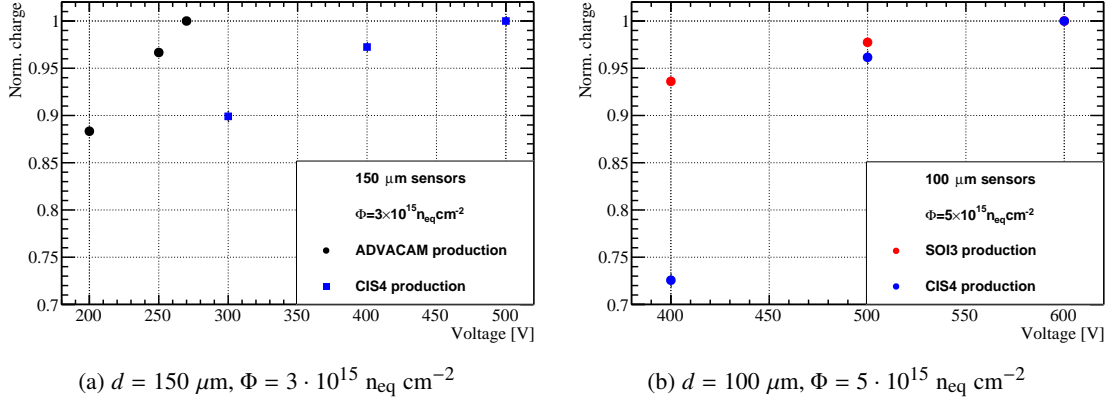


Figure 5.19: Comparison of normalised collected charge as a function of bias voltage (a) of CiS4 and ADVACAM modules with 150 μm thick sensors after an irradiation to a fluence of $3 \cdot 10^{15} \text{ n}_{\text{eq}} \text{ cm}^{-2}$ and (b) of CiS4 and SOI3 modules with 100 μm thick sensors after an irradiation to a fluence of $5 \cdot 10^{15} \text{ n}_{\text{eq}} \text{ cm}^{-2}$. Where not visible, the statistical uncertainties are smaller than the marker size.

sensor and FE-I4 pixels cells at the same irradiation level of $3 \cdot 10^{15} \text{ n}_{\text{eq}} \text{ cm}^{-2}$ is in good agreement with former studies, carried out with comparable devices [37].

Results obtained by edge transient current technique measurements

In this section, the collected charge of thin pixel sensors from the CiS4 production as a function of sensor depth is presented before and after irradiation by using the TCT set-up (see Section 4.2.2). The samples are irradiated with neutrons to fluences of $5 \cdot 10^{15} \text{ n}_{\text{eq}} \text{ cm}^{-2}$ and $10^{16} \text{ n}_{\text{eq}} \text{ cm}^{-2}$ and are annealed for 80 min at 60°C to complete the short term annealing of electrically active defects [68], see Section 2.3.2. The collected charge is defined as the time integral of the induced current with an uncertainty of 4% in the charge, previously defined in Section 4.2.2. The induced current is proportional to the number of generated charge carriers inside the sensor depth y . Its pulse shape is shown for different injection depths in an unirradiated 150 μm thick sensor in Figure 5.20. The sensor is kept at a voltage of 120 V and is therefore overdepleted. An injection depth of 0 μm corresponds to the front side position, whereas 150 μm correspond to the backside. The signal increases, when the laser is moving from the front side towards the middle of the sensor thickness and then decreases again towards the backside of the sensor. The contributions of electrons and holes is clearly seen and separated. At small y , the peak at the beginning of the signal is a superposition of the currents induced by the drift of electrons and holes in the high electric field close to the electrodes. As the laser beam is directed into the bulk (larger y) closer to the sensor backside, the contributions of electrons becomes wider and at the same time the long tail due to hole drift becomes shorter. This is in good agreement with previous studies [45]. Since the collected charge equals the integral of the signal, the integration time of the signal is an important parameter. The integration time is highly influenced by noise, and therefore investigations on the appropriate time interval for the collected charge are performed. Random noise of the electronic system and pick-up of the cables are the major contributions to the noise and cause fluctuations in the baseline of the waveform

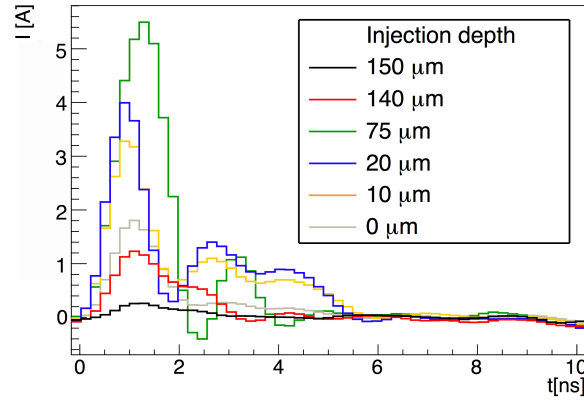


Figure 5.20: Induced current pulse shape of a $150\ \mu\text{m}$ thick sensor before irradiation. The sensor is biased at $120\ \text{V}$ and thus is operated at over depletion. The signal is shown for different injection depths inside the sensor in a time interval of $10\ \text{ns}$.

introduced in Section 4.2.2. Shrinking the integration window gives rise to a possible loss of charge. In contrast, enlarging leads to summing up more bins, entering a time range, where noise dominates over the signal. The impact of the integration time on the charge profile is discussed in the following. Integration times of $t = 1.5\ \text{ns}$ to $t = 10\ \text{ns}$ are chosen. In Figure 5.21, the collected charge as a function of voltage is summarised for $100\ \mu\text{m}$ and $150\ \mu\text{m}$ thick sensors before and after irradiation to fluences of $5 \cdot 10^{15}\ \text{n}_{\text{eq}}\ \text{cm}^{-2}$ and $10^{16}\ \text{n}_{\text{eq}}\ \text{cm}^{-2}$. The charge is normalised to the value obtained at the highest voltage point of each curve: the black dots represent the integration time of $t = 1.5\ \text{ns}$ increasing to the light blue dots, which show the results for an integration time of $t = 10\ \text{ns}$. The voltage, at which the plateau is reached, changes with integration time. Smaller integration times result in plateaus reached at larger voltages. Before irradiation, the charge saturates for all integration times equal or longer than $t = 10\ \text{ns}$ at a voltage of $20\ \text{V}$ for the $100\ \mu\text{m}$ thick sensor and at $30\ \text{V}$ for the $150\ \mu\text{m}$ thick sensor. These voltages are interpreted as the depletion voltages. These results fit well with depletion voltages obtained by source scan measurements previously discussed in Section 5.2.2. This integration time is chosen for all following measurements and is found to be in good agreement with previous investigations [141]. It is found, that the shape of the curves do not depend on the fluence. This is explained by trapping of charge carriers, which is known to happen after irradiation [51]. The average carrier lifetime is shorter than $1.5\ \text{ns}$ at these very high fluences. The charge saturation voltage of the $100\ \mu\text{m}$ thick sensor at a fluence of $5 \cdot 10^{15}\ \text{n}_{\text{eq}}\ \text{cm}^{-2}$ is found to be above $300\ \text{V}$. After irradiation to a fluence of $10^{16}\ \text{n}_{\text{eq}}\ \text{cm}^{-2}$ the charge saturates at about $500\ \text{V}$, as shown in Figure 5.21c and Figure 5.21e. For the thicker sensor, no saturation of the collected charge is observed at the same irradiation fluences. A higher bias voltage is needed for the thicker sensor to achieve a higher electric field throughout the bulk and in this case the drift velocity is still not saturated. Consequently, the collected charge, proportional to the drift velocity, still increases with the applied voltage up to the maximum value reached in these measurements. This is due to the fact, that the electric field increases with increasing bias voltage, resulting in a lower number of charge carriers to be lost due to trapping at high voltages.

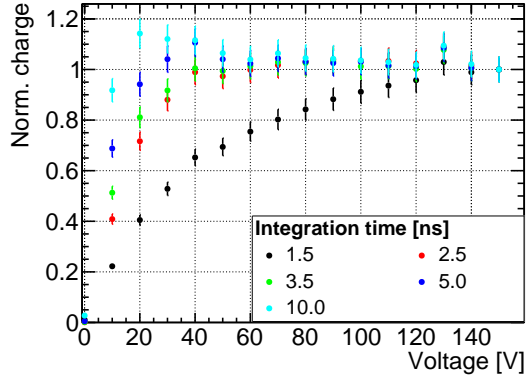
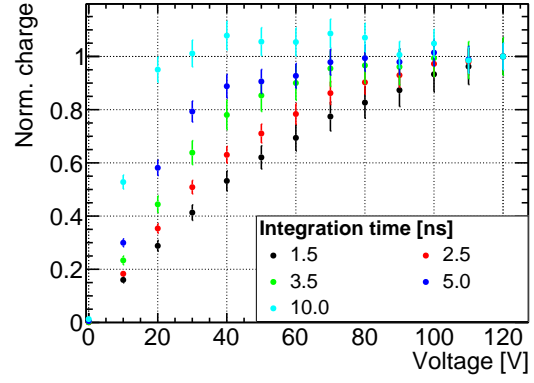
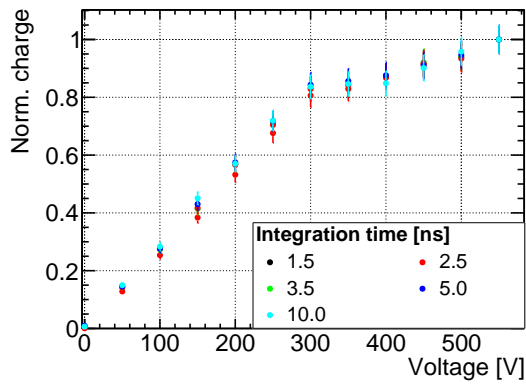
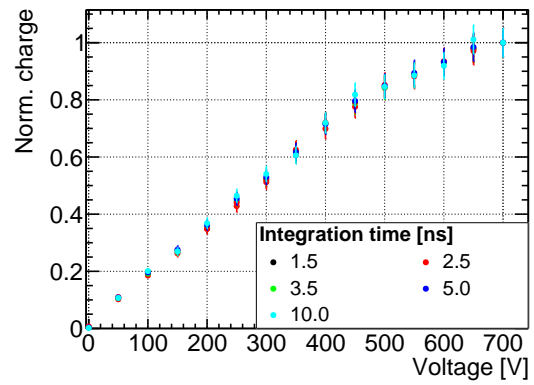
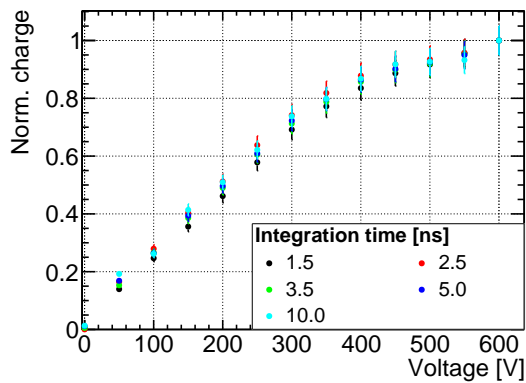
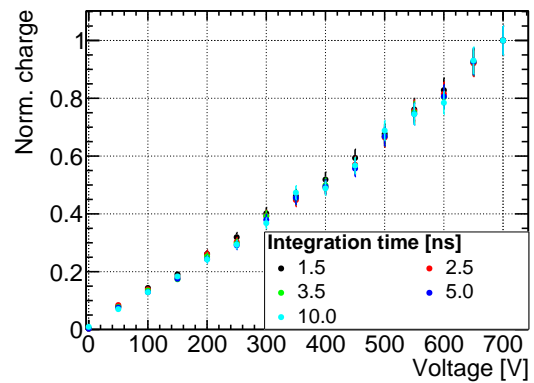
(a) $d = 100 \mu\text{m}$, $\Phi = 0$ (b) $d = 150 \mu\text{m}$, $\Phi = 0$ (c) $d = 100 \mu\text{m}$, $\Phi = 5 \cdot 10^{15} \text{ n}_{\text{eq}} \text{ cm}^{-2}$ (d) $d = 150 \mu\text{m}$, $\Phi = 5 \cdot 10^{15} \text{ n}_{\text{eq}} \text{ cm}^{-2}$ (e) $d = 100 \mu\text{m}$, $\Phi = 10^{16} \text{ n}_{\text{eq}} \text{ cm}^{-2}$ (f) $d = 150 \mu\text{m}$, $\Phi = 10^{16} \text{ n}_{\text{eq}} \text{ cm}^{-2}$

Figure 5.21: Charge collection as a function of bias voltage for 100 μm and 150 μm thick sensors before and after irradiation to fluences of $5 \cdot 10^{15} \text{ n}_{\text{eq}} \text{ cm}^{-2}$ and $10^{16} \text{ n}_{\text{eq}} \text{ cm}^{-2}$. The charge is normalised to the value obtained at the highest voltage point for the curve of each integration time.

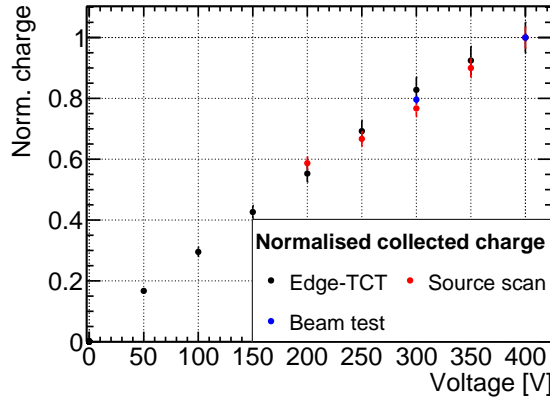


Figure 5.22: Comparison of collected charge as a function of bias voltage obtained by Edge-TCT, source scan and beam test measurements for a $100\ \mu\text{m}$ thick device after an irradiation to a fluence of $10^{16}\ \text{n}_{\text{eq}}\ \text{cm}^{-2}$. The results for each curve are normalised to the value obtained at the highest bias voltage. The Edge-TCT measurements are performed at sensor level before interconnection to readout chips, whereas the source scan and beam test measurements are performed after the sensors are interconnected to readout chips. Within their statistical uncertainties, the results are all in good agreement.

A comparison of the normalised charge obtained by Edge-TCT, source scan and beam test measurements of a $100\ \mu\text{m}$ thick device after an irradiation to a fluence of $10^{16}\ \text{n}_{\text{eq}}\ \text{cm}^{-2}$ is shown in Figure 5.22. Within their uncertainties, the results are all in good agreement. An uncertainty of 4% is associated to the collected charge obtained by Edge-TCT measurements and is discussed in Section 4.2.2. The uncertainties in the results obtained by beam test measurements are limited to statistical uncertainties. The collected charge obtained by source scan measurements is fraught with an uncertainty of 12% [37] and reviewed in Section 4.3.1. Due to lower breakdown voltages reached during source scan and test beam measurements, the achievable voltage is limited to 400 V. After interconnecting the sensor to a chip, the module was not passivated, neither with parylene, nor with BCB. Therefore, it was not possible to reach a voltage of more than 450 V with the module after an irradiation to a fluence of $10^{16}\ \text{n}_{\text{eq}}\ \text{cm}^{-2}$.

Figure 5.23 summarises the collected charge as a function of the sensor depth measured with the Edge-TCT set-up for $100\ \mu\text{m}$ and $150\ \mu\text{m}$ thick sensors before and after irradiation to fluences of $5 \cdot 10^{15}\ \text{n}_{\text{eq}}\ \text{cm}^{-2}$ and $10^{16}\ \text{n}_{\text{eq}}\ \text{cm}^{-2}$. Sensor front and backside are highlighted with red dashed lines, the sensor front side being on the left. The laser beam is directed onto the middle of the pixel implant, illustrated in Figure 4.5 of Section 4.2.2. The absolute value of the induced current is dependent on the exact laser focus and power, as well as the surface properties of the sensor edge. Therefore, the obtained values of the collected charge, listed in arbitrary units, are comparable within one set of measurements with the same sample and experimental conditions, but not across different samples. Before irradiation, shown in Figure 5.23a and b, for voltages above 20 V, the charge is nearly constant over the $100\ \mu\text{m}$ thick sensor. The $150\ \mu\text{m}$ thick sensor exhibits a charge saturation at a higher voltage of around 30 V before irradiation, seen in both Figures 5.21 and 5.23. Due to the higher electric field at the front side of the sensor, the charge is maximal at the front side

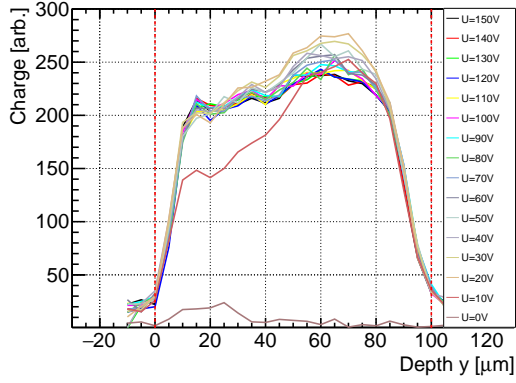
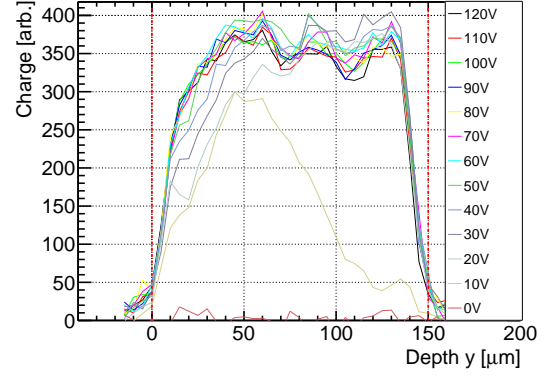
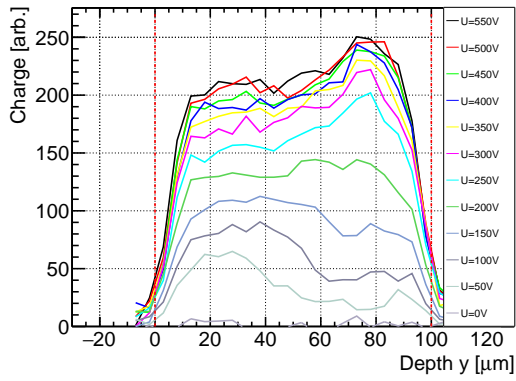
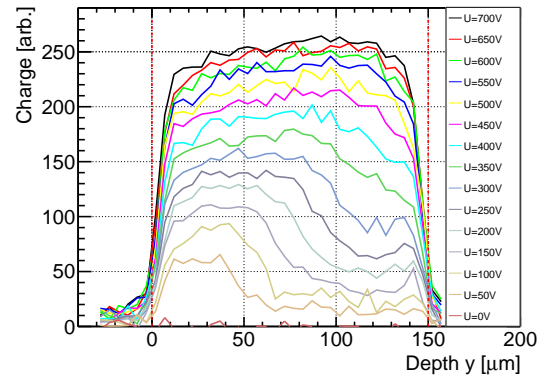
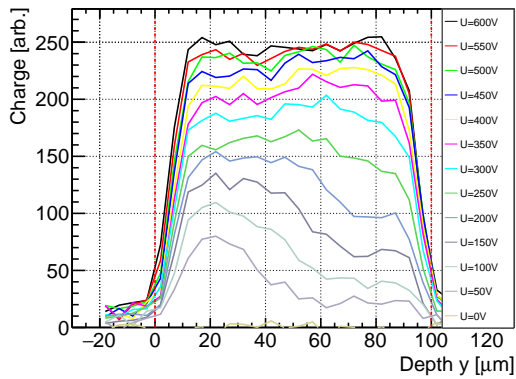
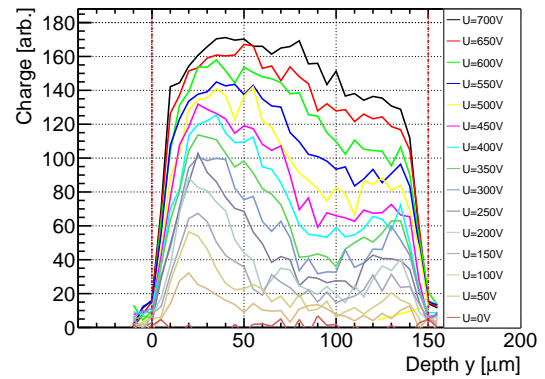
(a) $d = 100 \mu\text{m}$, $\Phi = 0$ (b) $d = 150 \mu\text{m}$, $\Phi = 0$ (c) $d = 100 \mu\text{m}$, $\Phi = 5 \cdot 10^{15} \text{ n}_{\text{eq}} \text{ cm}^{-2}$ (d) $d = 150 \mu\text{m}$, $\Phi = 5 \cdot 10^{15} \text{ n}_{\text{eq}} \text{ cm}^{-2}$ (e) $d = 100 \mu\text{m}$, $\Phi = 10^{16} \text{ n}_{\text{eq}} \text{ cm}^{-2}$ (f) $d = 150 \mu\text{m}$, $\Phi = 10^{16} \text{ n}_{\text{eq}} \text{ cm}^{-2}$

Figure 5.23: Collected charge as a function of sensor depth along the center of the pixel cell for 100 μm and 150 μm thick sensors (a, b) before and after irradiation to fluences of (c, d) $5 \cdot 10^{15} \text{ n}_{\text{eq}} \text{ cm}^{-2}$ and (e, f) $10^{16} \text{ n}_{\text{eq}} \text{ cm}^{-2}$. The voltage before irradiation ranges from 0 V to 120 V and reaches 700 V after irradiation.

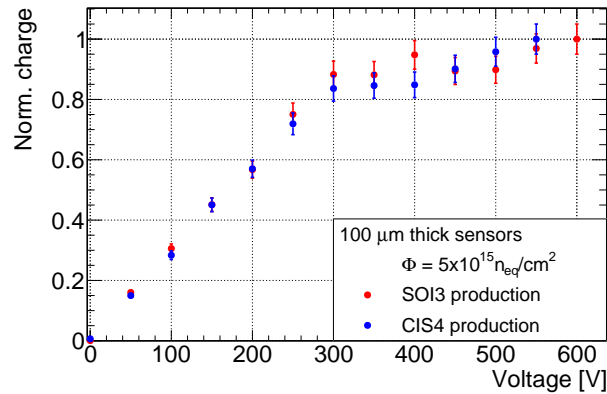


Figure 5.24: Comparison of the collected charge of 100 μm thick sensors from two different sensors producers, HLL and CiS. The collected charge of the CiS4 sensor is illustrated in red, while the SOI3 sensor is shown in black. Both sensors are irradiated to a fluence of $5 \cdot 10^{15} \text{ n}_{\text{eq}} \text{ cm}^{-2}$. The charge is normalised to the collected charge at 600 V. All results are obtained by Edge-TCT measurements.

before charge saturation. Furthermore, a charge increase is seen at the sensor backside for higher voltages, as shown in Figure 5.23b. The effect is enhanced after irradiation. Irradiating both sensors to a fluence of $5 \cdot 10^{15} \text{ n}_{\text{eq}} \text{ cm}^{-2}$ leads to higher saturation voltages, as discussed before. The charge is maximal at the front side. Applying higher voltages, the collected charge is independent of the sensor depth. Comparing the results for the two different sensor thicknesses after an irradiation to a fluence of $10^{16} \text{ n}_{\text{eq}} \text{ cm}^{-2}$, the charge is collected through the entire sensor already at a bias voltage of 50 V. These observations are in disagreement with the assumption of a constant effective doping concentration, that would result in a very thin depleted layer.

Instead, the measurements can be explained by the space charge polarization and low free carrier concentration in highly irradiated material [142]. The space charge polarization also results in the so-called "double peak" structure [44], visible in the 150 μm thick devices after irradiation and especially dominant at a fluence of $10^{16} \text{ n}_{\text{eq}} \text{ cm}^{-2}$, as shown in Figure 5.23f. Higher charge with respect to the central region of the sensor is collected at the sensor backside at bias voltages around 350 V. In case of the 100 μm thick sensor, a double peak structure is not clearly identified after exposure to high fluences. A plateau is visible at the backside for voltages below 200 V. From 300 V onwards the charge flattens over the entire sensor depth for the 100 μm thick device: For voltages above 450 V no significant change of the collected charge is observed, which points to a saturation of the drift velocity. Due to the lower electric field in thicker devices, this effect is not seen in the case of a 150 μm thick sensor over the full range of applied bias voltages. As the cooling capabilities were limited, it was not possible to apply higher voltages. The SOI3 sensors, as well as the CiS4 sensors, show similar charge collection, as shown in Figure 5.24. Two sensors, from HLL and CiS, with a 100 μm thickness, irradiated to a fluence of $5 \cdot 10^{15} \text{ n}_{\text{eq}} \text{ cm}^{-2}$ are compared. Within the uncertainties in the collected charge, both sensors show a saturation in their collected charge from voltages of 300 V or more. This saturation voltage is in accordance with beam test results [37].

The response uniformity within a pixel cell is important for a pixel detector. The Edge-TCT analysis framework additionally comprises a two-dimensional scan, where the position of the laser beam

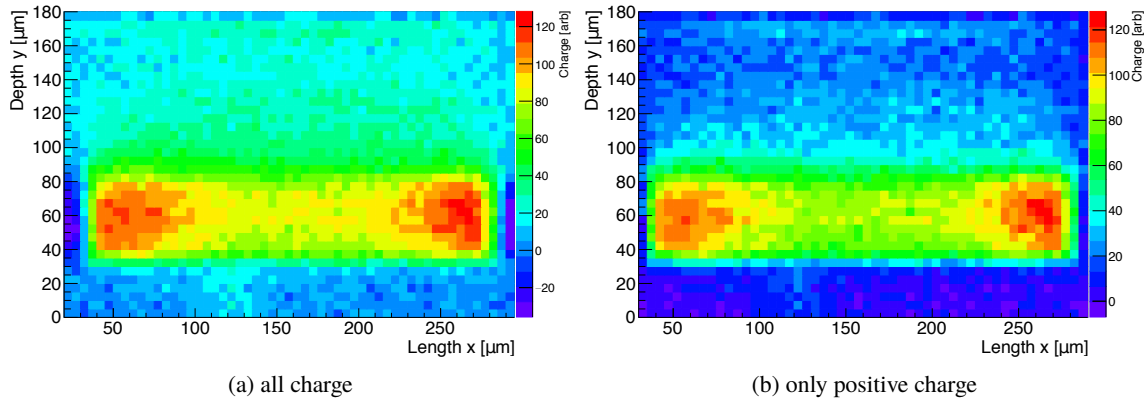


Figure 5.25: Example of a two-dimensional representation of a charge collection measurement with the Edge-TCT method for one single pixel cell in a $150 \mu\text{m}$ thick sensor irradiated to a fluence of $5 \cdot 10^{15} \text{ n}_{\text{eq}} \text{ cm}^{-2}$ and operated at 100 V. The y-axis represent the sensor depth, while the x-axis represents the long pixel side. The sensor front side is at $y \approx 30 \mu\text{m}$. It serves for a direct comparison of a two-dimensional charge profile with (a) all charge and (b) only positive charge.

is varied along the sample depth (y-coordinate), as well as along the pixel implant (x-coordinate). Figure 5.25 is the first example of two-dimensional charge profiles along the sensor depth (y) and in the pixel direction of the longer pixel side (x). The charge profile is shown for a $150 \mu\text{m}$ thick sensor, irradiated to a fluence of $5 \cdot 10^{15} \text{ n}_{\text{eq}} \text{ cm}^{-2}$ and operated at a low bias voltage of 100 V. The laser beam is directed perpendicularly onto the x-y plane of the 2-dimensional maps. The sensor front side is at lower y with a pixel cell width of $250 \mu\text{m}$ in x. The depth of the sensor is along the y-axis with the detector surface being at $y \approx 30 \mu\text{m}$.

The backside corresponds to about $y = 180 \mu\text{m}$. Red areas represent regions of high charge and the blue colour corresponds to regions of low charge. The negative charge is an artifact from charges collected by the neighbouring pixel. In Figure 5.25a, all charge is shown in the two-dimensional charge profile, while Figure 5.25b only depicts the positive charge. Since after irradiation charge is trapped before drifting through the entire weighting field (introduced in Section 2.2.5), it is found, that negative charge is more prone to appear at lower bias voltages. At higher bias voltages, the drift is faster and less charge is trapped, so one could expect the charge collected at high bias voltages to be less negative, as derived in [143]. Hence, for higher bias voltages no significant regions of negative charge are observed. In the following, all two-dimensional charge profiles are illustrated only with positive charge for a better comparison. The small charge measured at low y (i.e. when the laser beam is outside the detector surface) is caused by light reflected by the wire bond attached to the read out pixel. For all devices under study the region of high charge on the front side is increasing with voltage. This is depicted in Figure 5.26, where two-dimensional charge collection maps are shown for a $150 \mu\text{m}$ thick sensor after an irradiation to a fluence of $5 \cdot 10^{15} \text{ n}_{\text{eq}} \text{ cm}^{-2}$. The comparison is for bias voltages from 100 V to 780 V. The increase of the region of high charge is clearly seen in addition to the increase of the amount of collected charge at each higher voltage step. At 100 V and 200 V, the higher electric field regions at the edge of the pixel implant result in an accumulation of the of high charge in the corners of the pixel implant. This effect flattens

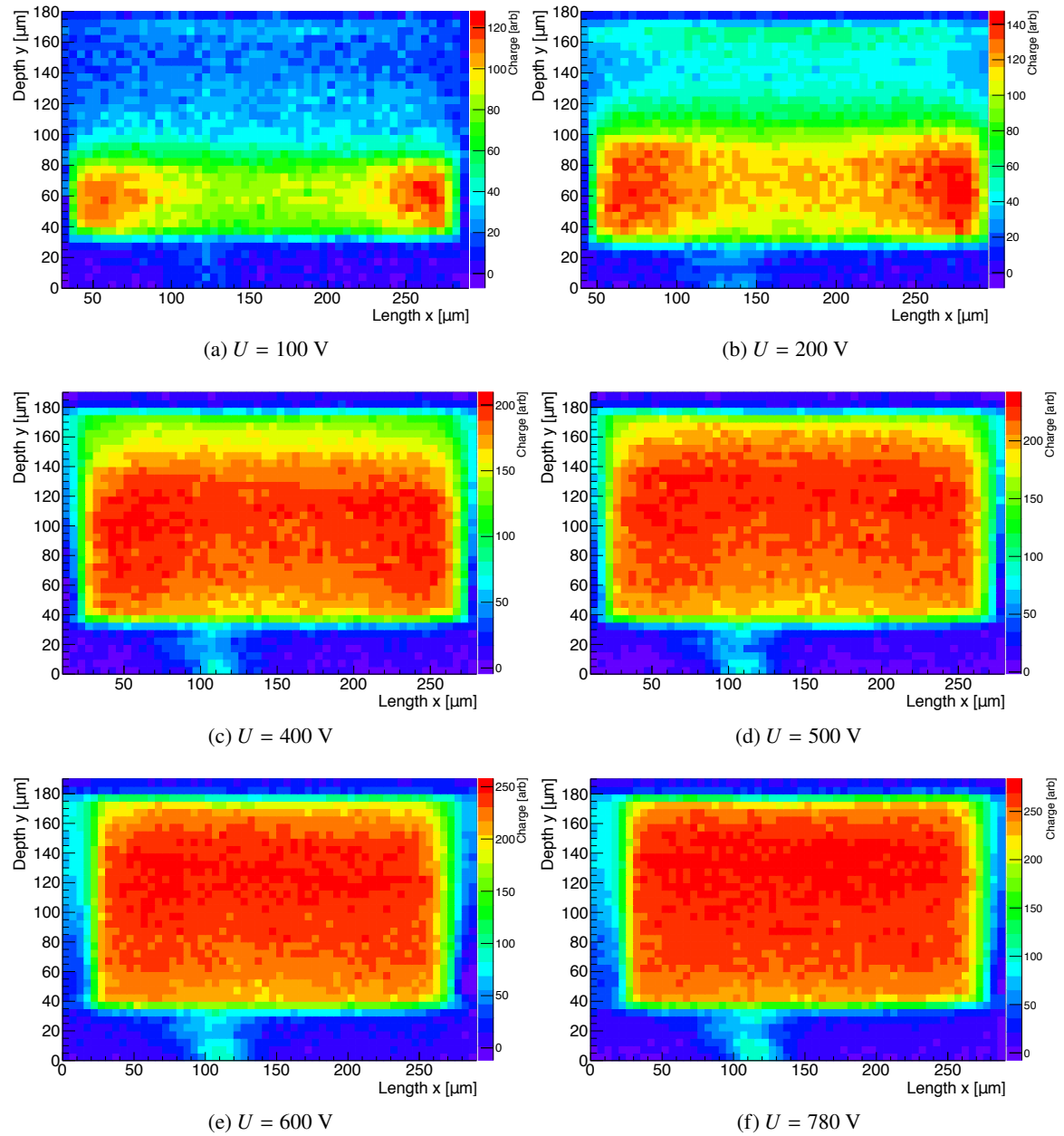


Figure 5.26: Two-dimensional representation of a charge collection measurement with the Edge-TCT method for one single pixel cell in a $150 \mu\text{m}$ thick sensor irradiated to a fluence of $5 \cdot 10^{15} \text{ n}_{\text{eq}} \text{ cm}^{-2}$. The increase of the depleted region is clearly visible for an increase of voltage from (a) 100 V to (d) 780 V. The collected charge is color-coded and is high below the pixel cell (lower y) before charge saturation and constant along the sensor depth after charge saturation.

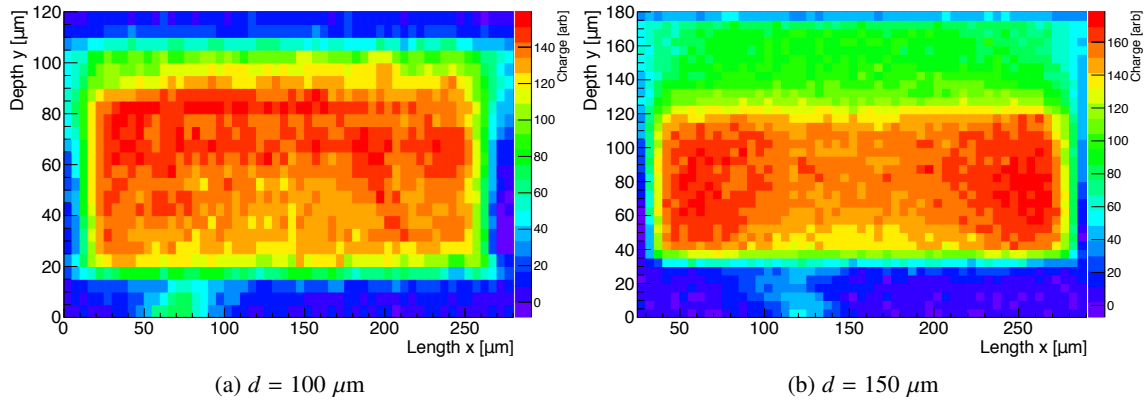


Figure 5.27: Comparison of two-dimensional charge collection maps of a (a) 100 μm and (b) 150 μm thick sensors, both irradiated to a fluence of $5 \cdot 10^{15} \text{ n}_{\text{eq}} \text{ cm}^{-2}$. Both sensors are biased at a voltage of 300 V for direct comparison. An area of around 85 μm of the total sensor depth of the 100 μm thick sensor is fully saturated. The saturation area in the 150 μm thick sensor shows only 85 μm of saturated region of its total thickness.

out at higher bias voltages. The double peak structure is visible at a voltage of 200 V, where a significant amount of collected charge is obtained in case the laser is directed onto the backside of the sensor ($y \approx 160$). Moving the laser towards the front side, a 20-30 μm wide region of low charge is observed, before it increases again, when being closer to the electrodes. This allows for a clear observation of the double peak. An increase of voltage results in an expansion of the charge region up to a full saturation of the collected charge at a voltage of 500 V. This is also in good agreement with previous studies [37].

In Figure 5.27, the 150 μm thick sensor is compared to a 100 μm thick sensor irradiated at the same fluence of $5 \cdot 10^{15} \text{ n}_{\text{eq}} \text{ cm}^{-2}$. The two-dimensional maps both show the collected charge of the sensors biased at 300 V. An area of around 85 μm of the total sensor depth of the 100 μm thick sensor is fully saturated. The sensor is almost fully depleted at a voltage of 300 V. The 150 μm thick sensor also displays a saturated region of around 85 μm below the pixel electrode. The difference between the 100 μm and 150 μm thick sensor is, that there is still a region of low charge of additional 40 μm in the 150 μm thick device. At a bias voltage of 300 V the charge within the 100 μm is almost saturated leading to an efficient operation after 300 V. This agrees well with the outcomes shown in Figures 5.24 and 5.21. In contrast, in the 150 μm thick sensor only roughly two thirds of the entire volume are fully saturated. Therefore, full operation at 300 V with suitable detector performance is not possible.

In Figure 5.28 the collected charge of sensors with the same sensor thicknesses but at a higher irradiation level of $10^{16} \text{ n}_{\text{eq}} \text{ cm}^{-2}$ are compared. It is observed, that in the 100 μm thick sensor the region of the high charge extends deeper at all three voltages of 200, 400 and 600 V.

In addition to sensors with the FE-I4 pixel cell of $50 \times 250 \mu\text{m}^2$ cell size, the charge collection properties of modified sensors with the wave design subdivided into five $50 \times 50 \mu\text{m}^2$ pixel implants are investigated before irradiation. Figure 5.29 shows the two-dimensional maps of the sensor with the wave design. Previous results from sensors with FE-I4 pixels showed a 150 μm thick sensor

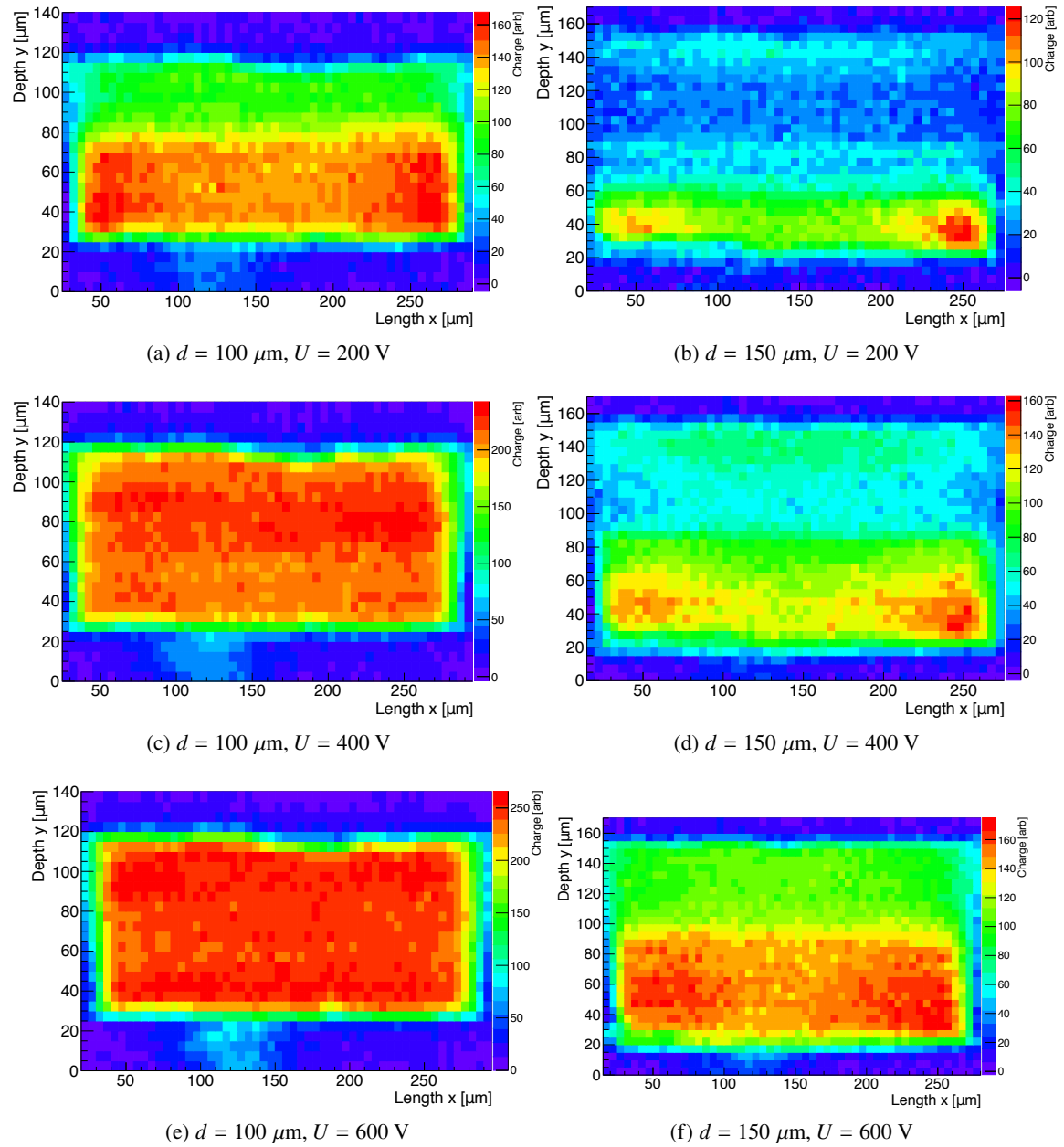


Figure 5.28: Comparison of two-dimensional charge collection maps for one single pixel cell in a $100 \mu\text{m}$ and $150 \mu\text{m}$ thick sensor after an irradiation to a fluence of $10^{16} \text{ n}_{\text{eq}} \text{ cm}^{-2}$. Both sensors are biased with voltages from 200 to 600 V for direct comparison. The collected charge is constant along the sensor depth at 600 V only in case of the $100 \mu\text{m}$ thick sensor.

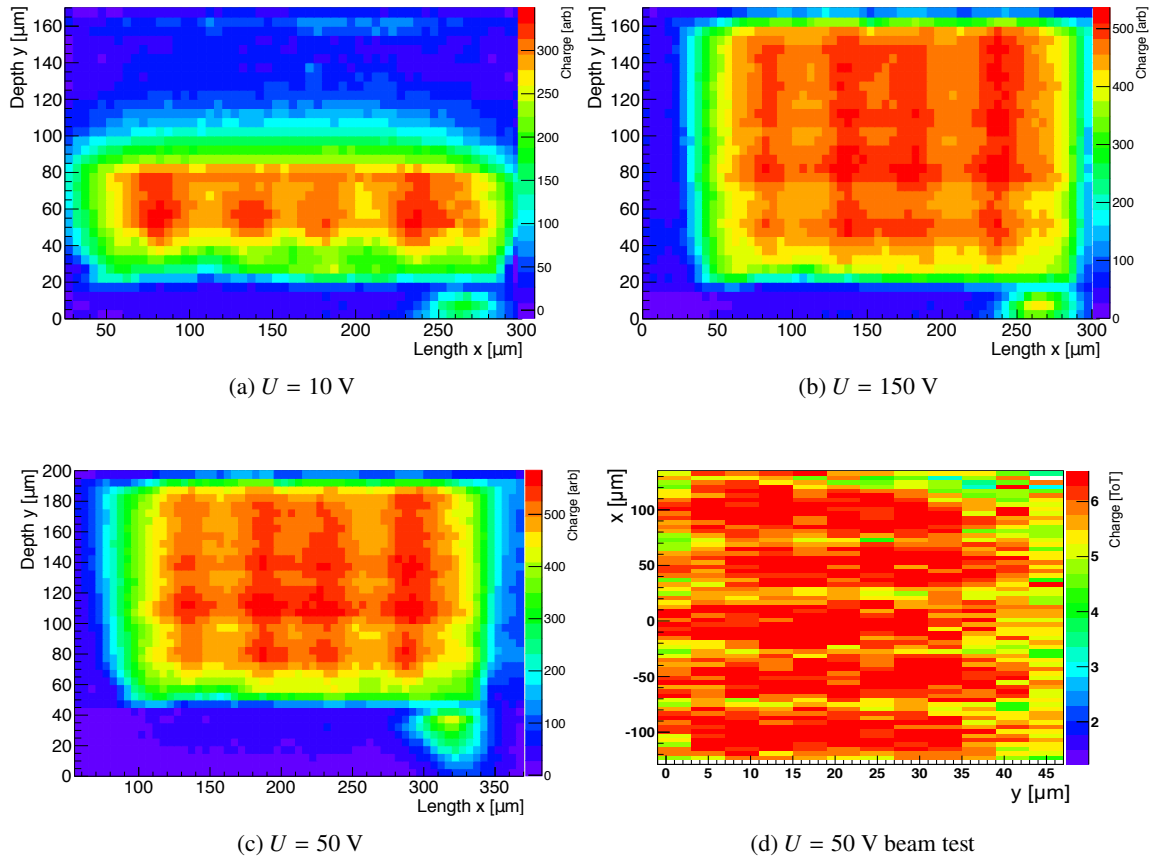


Figure 5.29: Charge collection of a $150\ \mu\text{m}$ CiS4 sensor with a modified pixel FE-I4 geometry subdivided into five $50\times 50\ \mu\text{m}^2$ pixel cells illustrated in a two-dimensional map: (a) shows the collected charge at a low voltage of 10 V before full charge saturation and (b) at a high voltage of 150 V after full charge saturation. The collected charge of the same Edge-TCT set at 50 V is shown in (c). During this set of Edge-TCT measurements the position of the device is changed for the different voltage steps. The X-Y range is increased to allow for a larger view on the pixel cell. Therefore, the X-Y coordinates in the maps are not in exact correspondence to each other. It does not bias or influence the measurements. The outcome of (c) is compared to the one obtained at beam test measurements with a FE-I4 module assembled with the same type of sensor (d). Different to (a)-(c), in (d) y represents the length of the pixel cell in y.

depleting around 30-40 V. This is in good agreement with this device.

The region of high charge is at 10 V before saturation and after full saturation at 150 V. In addition to the development of the depleted region within the sensor depth, four regions of high charge are observed along the x direction. They are interpreted as the inter-pixel regions. The geometry of the TCT set-up is the reason for the effect of regions of high charge between the pixel implants. The laser traverses the sensor parallel to the pixel cells. Due to the wave design with the displaced $50\times 50\ \mu\text{m}^2$ pixel cells (for layout details see Section 5.1.1) it is probable that the laser traverses two implants when shining on the inter-pixel region creating more charge in this area. This effect is more prone to happen, when the beam is slightly defocused leading to a halo around the beam spot. Comparing the charge collection maps obtained by Edge-TCT measurements (see Figure 5.29a-c) to the ones obtained by beam test measurements (see Figure 5.29d) with the same type of sensor

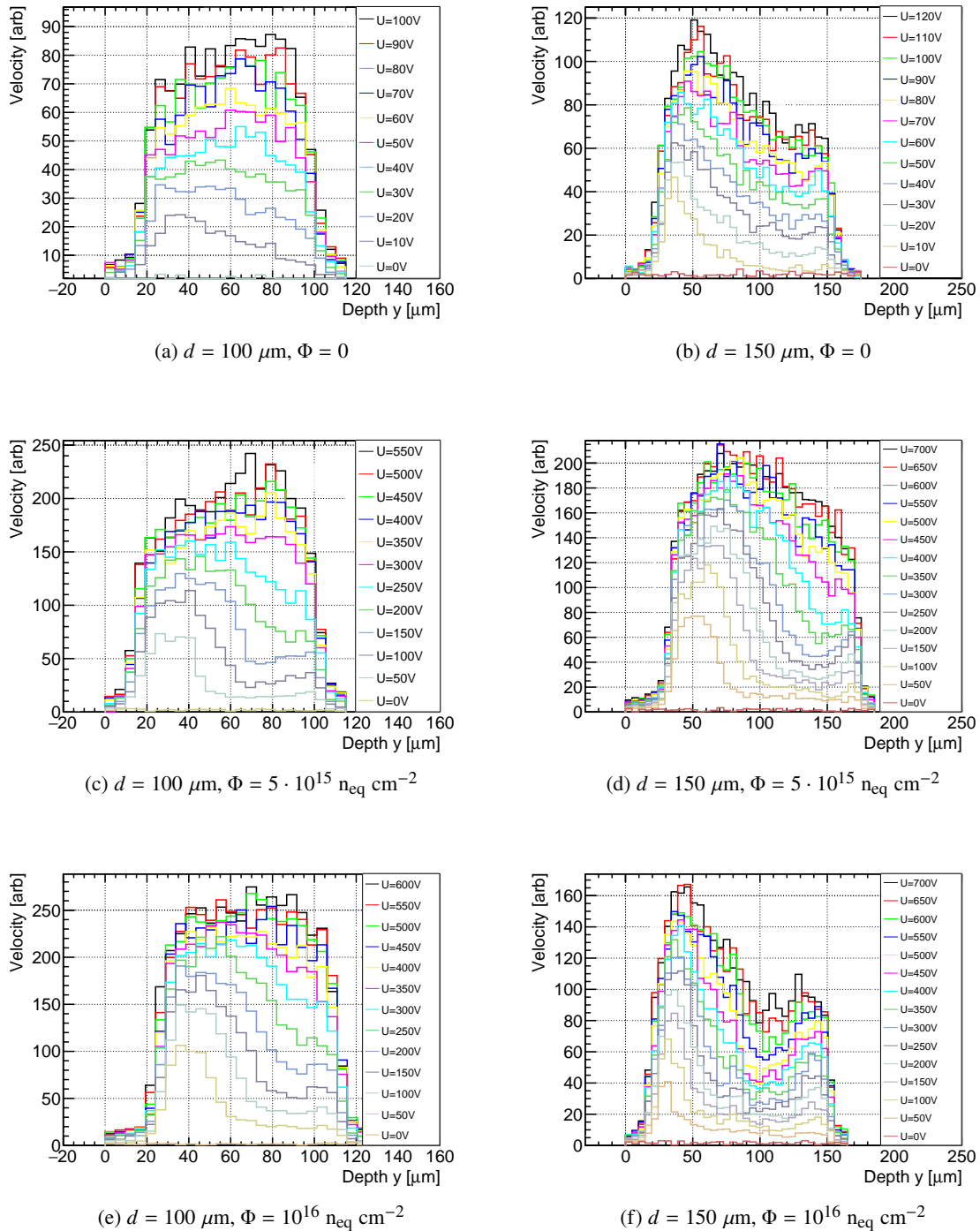


Figure 5.30: Velocity profile as a function of sensor depth for 100 μm and 150 μm thick sensors (a,b) before irradiation and after an irradiation to fluences of (c,d) $5 \cdot 10^{15} \text{ n}_{\text{eq}} \text{ cm}^{-2}$ and (e,f) $10^{16} \text{ n}_{\text{eq}} \text{ cm}^{-2}$. Before irradiation, the electric field of the 100 μm thick sensor appears to be flatter in the chosen range of voltages. After irradiation, the double peak effect in the electric field is visible at lower voltages before charge saturation. The values of the velocity correspond to arbitrary units. The range of the scale of the sensor depth differs for the 100 μm and 150 μm devices. In addition, both sensors irradiated to a fluences of $5 \cdot 10^{15} \text{ n}_{\text{eq}} \text{ cm}^{-2}$ were measured in different measurement campaigns and hence at slightly different positions. This explains the different values of y for sensor front and backside.

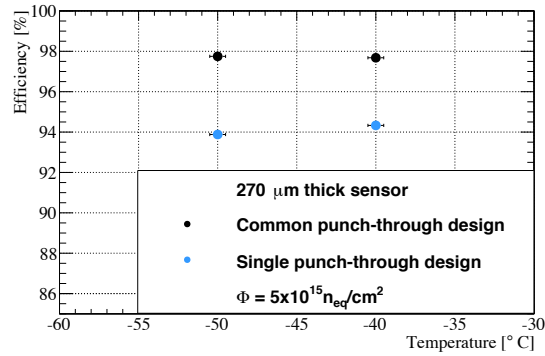


Figure 5.31: Hit efficiencies of CiS3 sensors of 270 μm thickness with an FE-I4 pixel cell, as well as the modified $25 \times 500 \mu\text{m}^2$ pixel cell are shown after an irradiation of the modules to a fluence of $5 \cdot 10^{15} \text{ n}_{\text{eq}} \text{ cm}^{-2}$. The obtained hit efficiencies are shown for different temperatures of -50°C and -40°C .

and at the same bias voltage, the total number of five implants is visible in the charge collection map, as shown in Figure 5.29. The beam traverses the sensor perpendicularly in this case and the charge sharing effect leads to a charge decrease in between the pixel implants.

5.2.3 Electric field properties

The velocity profile is obtained by looking at the slope of the signal in the very first ns giving insights in the electrical field of the sensor (see Section 4.2.2). From the velocity profile the shape of the electric field is inferred. In Figure 5.30, the velocity profiles of a 100 μm and 150 μm thick sensor before and after an irradiation to fluences of $5 \cdot 10^{15} \text{ n}_{\text{eq}} \text{ cm}^{-2}$ and $10^{16} \text{ n}_{\text{eq}} \text{ cm}^{-2}$ are compared. A high carrier velocity at the front side at lower voltages is observed for both thicknesses before irradiation. Due to a more uniform electric field in thinner devices, the distribution is flatter for the 100 μm thick device at higher voltages, both before and after irradiation. One sees the existence of the electric field at the back side of the sensor, meaning that the devices are fully depleted at 10 V in case of the 100 μm detector and at 20 V for the 150 μm thick detector. The velocity profiles after irradiation confirm the hypothesis from the previous section, that an electric field in the entire sensor thickness already exists at low bias voltages. A double peak electric field distribution is observed for both sensor thicknesses at low to moderated bias voltages, but the field flattens at higher bias voltages. However, the electric field at the back is much weaker with respect to the main junction at the pixels. The double peak effect after irradiation for thicker sensors was reported in several publications, see for example [44].

5.2.4 Hit efficiency

One of the key features of tracking systems is the hit efficiency of devices, when they are traversed by charged particles. After high radiation doses, the performance of the tracking detectors is degraded due to the effects described in Section 2.3. A lower hit efficiency influences the precision of the track and vertex reconstruction and induces a loss in the overall particle detection efficiency and fake track rejection. The primary reason for the loss in efficiency is the decrease of the collected

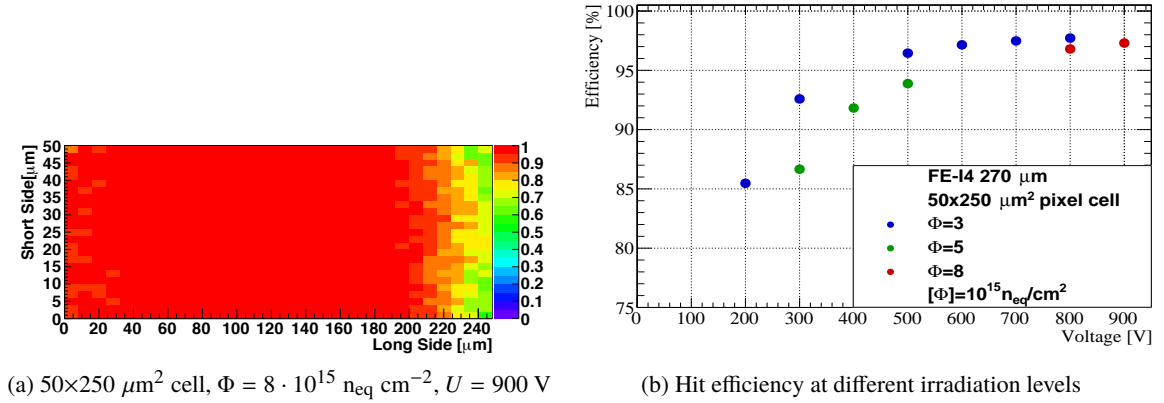


Figure 5.32: (a) in-pixel hit efficiency map for a module with a $270 \mu\text{m}$ thick sensor with an FE-I4 pixel cell and single p-t design after an irradiation to a fluence of $8 \cdot 10^{15} \text{ n}_{\text{eq}} \text{ cm}^{-2}$. The measurements were performed at DESY. The in-pixel hit efficiency map is not to scale. (b) hit efficiency as a function of bias voltage after an irradiation to fluences of $3 \cdot 10^{15} \text{ n}_{\text{eq}} \text{ cm}^{-2}$, $5 \cdot 10^{15} \text{ n}_{\text{eq}} \text{ cm}^{-2}$ and $8 \cdot 10^{15} \text{ n}_{\text{eq}} \text{ cm}^{-2}$. The results of the two lower irradiation steps are adapted from Ref. [37].

charge in the sensor, caused by trapping and partial charge saturation in the bulk. The lower the value of the collected charge, the higher the probability to fall below the threshold of the readout chip, such that the particles stay undetected. This effect is more important in case of charge sharing among neighbouring pixels. If the charge is below threshold in one of the pixel cells, the determined hit position is biased, which also affects the track resolution.

The hit efficiency of modules from the different productions is investigated in beam tests at the CERN-SpS and at the DESY facility. Thanks to the high resolution of the telescopes of the EUDET family (see Section 4.3.2), it is further possible to investigate the spatially resolved in-pixel hit efficiency, charge sharing properties and the performance of the sensor edge. An absolute systematic uncertainty of 0.3% , as estimated in Ref. [111] and introduced in Section 4.3.2, is associated to all hit efficiency measurements. Due to high statistics usually collected at beam tests, this systematic uncertainty is dominant. The outcomes of the measurements of different sensor productions implementing different sensor designs and thicknesses are discussed in this section.

CiS3: Beam test results on irradiated modules with $25 \times 500 \mu\text{m}^2$ pixel cells

CiS3 modules with a $270 \mu\text{m}$ thick sensor and a FE-I4 pixel cell of $50 \times 250 \mu\text{m}^2$ together with a single p-t structure per cell are compared to modules with a modified pixel cell of $25 \times 500 \mu\text{m}^2$ and an external p-t design. The modified pixel cell was implemented to make first predictions on the performance of the RD53 pixel cell of a $25 \times 100 \mu\text{m}^2$ cell size after irradiation still maintaining the compatibility to the FE-I4 readout chip. The modules are investigated in beam tests at DESY or the CERN-SpS. They are kept cool with dry ice in a styrophor box or in an isolated cooling box (see Section 4.3.2) at a temperature of -50° or -40° depending on the set-up used. It is shown, that the hit efficiency is not influenced by a difference in temperature, as shown in Figure 5.31. The in-pixel hit efficiency of the module with the FE-I4 pixel cell after an irradiation to a fluence

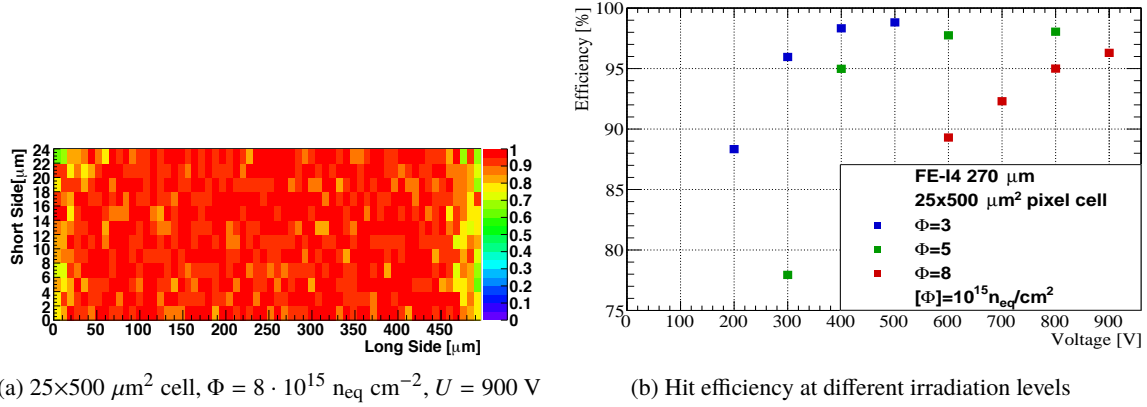


Figure 5.33: (a) in-pixel hit efficiency map for a module with a $270 \mu\text{m}$ thick sensor with a modified pixel cell and external p-t design after an irradiation to a fluence of $8 \cdot 10^{15} \text{ n}_{\text{eq}} \text{ cm}^{-2}$. The measurements were performed at DESY. The in-pixel hit efficiency map is not to scale. Note the pixel cell size of $25 \times 500 \mu\text{m}^2$. (b) hit efficiency as a function of bias voltage after an irradiation to fluences of $3 \cdot 10^{15} \text{ n}_{\text{eq}} \text{ cm}^{-2}$, $5 \cdot 10^{15} \text{ n}_{\text{eq}} \text{ cm}^{-2}$ and $8 \cdot 10^{15} \text{ n}_{\text{eq}} \text{ cm}^{-2}$.

Table 5.5: Summary of the hit efficiency results of CiS3 modules with $270 \mu\text{m}$ thick sensors employing $50 \times 250 \mu\text{m}^2$ and $25 \times 500 \mu\text{m}^2$ pixel cells. The hit efficiencies are shown for the irradiation fluences of $3 \cdot 8 \cdot 10^{15} \text{ n}_{\text{eq}} \text{ cm}^{-2}$ at bias voltages steps of 500 V , 800 V and 900 V .

Production	Pixel cell [μm^2]	Φ [$10^{15} \text{ n}_{\text{eq}} \text{ cm}^{-2}$]	Hit efficiency at		
			$U = 500 \text{ V}$	$U = 800 \text{ V}$	$U = 900 \text{ V}$
CiS3	50×250	3	$96.4 \pm 0.3\%$	$97.7 \pm 0.3\%$	
		5	$93.9 \pm 0.3\%$		
		8		$96.8 \pm 0.3\%$	$97.3 \pm 0.3\%$
	25×500	3	$98.8 \pm 0.3\%$		
		5		$98.0 \pm 0.3\%$	
		8		$95.0 \pm 0.3\%$	$96.3 \pm 0.3\%$

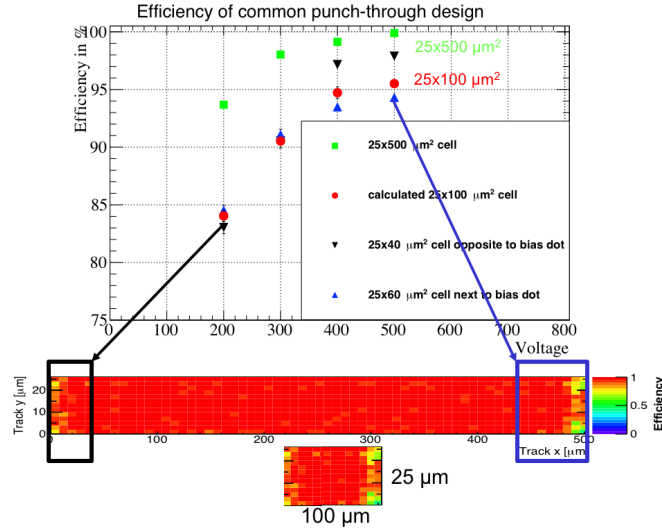


Figure 5.34: Estimated hit efficiency of a $25 \times 100 \mu\text{m}^2$ pixel cell irradiated to a fluence of $3 \cdot 10^{15} \text{ n}_{\text{eq}} \text{ cm}^{-2}$ and compared to the hit efficiency of the larger $25 \times 500 \mu\text{m}^2$ pixel cell. Efficiencies at the edges are also shown separately.

of $8 \cdot 10^{15} \text{ n}_{\text{eq}} \text{ cm}^{-2}$ together with a summary of the hit efficiencies as a function of bias voltages at different fluences is depicted in Figure 5.32. The results after an irradiation to fluences of $3 \cdot 10^{15} \text{ n}_{\text{eq}} \text{ cm}^{-2}$ and $5 \cdot 10^{15} \text{ n}_{\text{eq}} \text{ cm}^{-2}$ are extracted from Ref. [37]. The in-pixel hit efficiency map and the summary plot of hit efficiencies at different fluences up to $8 \cdot 10^{15} \text{ n}_{\text{eq}} \text{ cm}^{-2}$ of a module with a modified pixel cell is seen in Figure 5.33. The results after an irradiation to a fluence of $3 \cdot 10^{15} \text{ n}_{\text{eq}} \text{ cm}^{-2}$ are also extracted from Ref. [37].

The irradiation steps of $3 \cdot 10^{15} \text{ n}_{\text{eq}} \text{ cm}^{-2}$, $5 \cdot 10^{15} \text{ n}_{\text{eq}} \text{ cm}^{-2}$ and $8 \cdot 10^{15} \text{ n}_{\text{eq}} \text{ cm}^{-2}$ are identical for both modules allowing for a direct comparison. The hit efficiency results are summarised in Table 5.5 for the voltages of 500 V, 800 V and 900 V. At lower fluences, the modified $25 \times 500 \mu\text{m}^2$ cell shows a better hit efficiency. The obtained efficiencies are up to 2.4% higher compared to the standard pixel cell at every voltage step. At $3 \cdot 10^{15} \text{ n}_{\text{eq}} \text{ cm}^{-2}$, the hit efficiency of the module with the $25 \times 500 \mu\text{m}^2$ pixel cell saturates at a value of $98.8 \pm 0.3\%$ and a bias voltage of 500 V, whereas the module with the FE-I4 pixel cell design reaches a hit efficiency of $97.7 \pm 0.3\%$ at a bias voltage of 800 V. This behaviour is related to the better performance of the external bias dot after irradiation, as well as the fact, that the pixel cell is double the size along the long pixel direction in x.

In contrast, at the maximum applied fluence of $8 \cdot 10^{15} \text{ n}_{\text{eq}} \text{ cm}^{-2}$ and highest bias voltage of 900 V a lower hit efficiency is observed for the module with modified pixel cells. This is explained with the differently tuned threshold values of both modules during the beam test at DESY. The module with modified pixel cells was tuned to a slightly higher threshold affecting the charge collection efficiency over the full pixel cell. This is observed for the efficiency loss over the entire pixel cell. To make first predictions on the performance of RD53A compatible pixel cells, the hit efficiency for a $25 \times 100 \mu\text{m}^2$ pixel cell at an irradiation fluence of $3 \cdot 10^{15} \text{ n}_{\text{eq}} \text{ cm}^{-2}$ is estimated based on the existing prototype of the $25 \times 500 \mu\text{m}^2$ pixel cell, as illustrated in Figure 5.34. The hit efficiencies in 40 μm of the pixel cell in the region opposite to the bias dot (with efficiency losses caused by

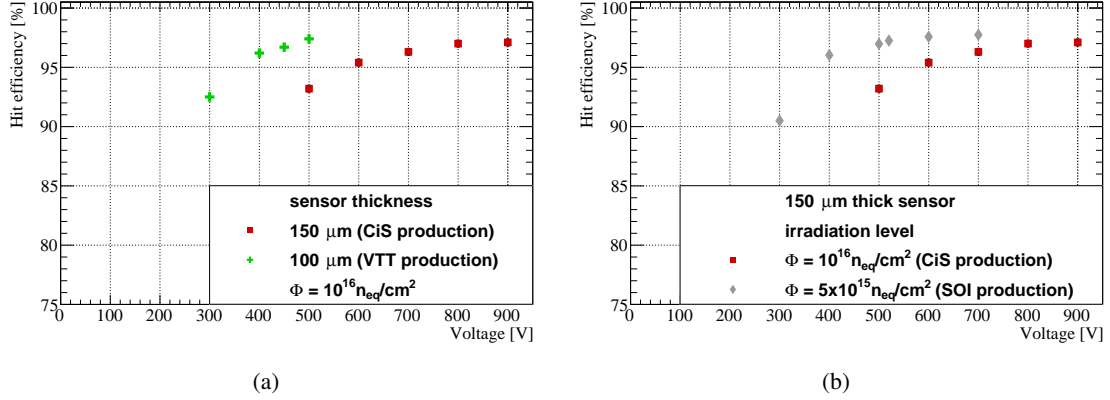


Figure 5.35: Hit efficiency of a CiS4 module with a 150 μm thick sensor irradiated to a fluence of $10^{16} \text{ n}_{\text{eq}} \text{ cm}^{-2}$ and tested at CERN compared to (a) a VTT module with a 100 μm thick sensor irradiated to the same fluence, but at the Jožef Stefan Institute and tested at DESY. In (b) the CiS4 module is compared to an SOI2 module with a 150 μm thick sensor irradiated to a fluence of $5 \cdot 10^{15} \text{ n}_{\text{eq}} \text{ cm}^{-2}$ at LANSCE in New Mexico [144] and tested at a beam test at CERN. The results from this module are taken from Ref. [37]. Where not visible, the uncertainties are smaller than the marker size.

charge sharing in an effective pixel cell of $25 \times 40 \mu\text{m}^2$) and in 60 μm of the pixel cell in the region next to the bias dot (with efficiency losses caused by the p-t structure in an effective pixel cell of $25 \times 60 \mu\text{m}^2$) are combined to estimate the hit efficiency for an effective pixel cell of $25 \times 100 \mu\text{m}^2$. A value of $95.5 \pm 0.3\%$ is obtained and is lower compared to the full $25 \times 500 \mu\text{m}^2$ pixel cell at $3 \cdot 10^{15} \text{ n}_{\text{eq}} \text{ cm}^{-2}$ but is still in a suitable performing hit efficiency range meeting the requirements by the performance of physics analysis for the ITk [29].

CiS4: Beam test results on highly irradiated modules with thin sensors

The hit efficiency of an FE-I4 module of the CiS4 production with a 150 μm thick sensor irradiated to a fluence of $10^{16} \text{ n}_{\text{eq}} \text{ cm}^{-2}$ at CERN is investigated in a beam test at CERN. The sensor employs the FE-I4 grid of $50 \times 250 \mu\text{m}$ pixel cells with the common p-t design. To isolate the sensor edges against sparks at the high voltages needed after high irradiation, the sensor surface is covered with parylene. The results are compared to an FE-I4 module of the VTT production irradiated to the same fluence at the Jožef Stefan Institute, but assembled with a 100 μm thick sensor with FE-I4 pixel cells and the single p-t structure. The VTT module is not covered with any layer, which would prevent from sparks, when applying high bias voltages, needed at this fluence. Therefore, it can only be biased up to 450 V. Both sensors are designed with a standard edge distance of $d_e = 450 \mu\text{m}$. The detailed sensor designs and the description of the BCB and parylene layers were introduced in Section 5.1. In Fig. 5.35a, the hit efficiency as a function of bias voltage is illustrated. At the highest voltage of 500 V, the VTT module with the 100 μm thick sensor reaches a hit efficiency of $97.4 \pm 0.3\%$. The hit efficiency of the module with a 150 μm thick sensor saturates at a similar value of $97.0 \pm 0.3\%$. Considering only the pixel region excluding the p-t structures, hit efficiencies of 98.4% for the module with the 100 μm thick sensor and of 97.8% in the case of the module with

Table 5.6: Summary of the hit efficiency results of a VTT module with 100 μm thick sensor and a CiS4 module with a 150 μm thick sensor after an irradiation to $10^{16} \text{ n}_{\text{eq}} \text{ cm}^{-2}$. The hit efficiency results of the CiS4 module with a 150 μm thick sensor are further compared to a module with the same sensor thickness irradiated to a fluence of $5 \cdot 10^{15} \text{ n}_{\text{eq}} \text{ cm}^{-2}$. The results are shown for the voltage steps of 500 V, 700 V and 900 V.

Production	Thickness [μm]	Φ [$10^{15} \text{ n}_{\text{eq}} \text{ cm}^{-2}$]	Hit efficiency at		
			$U = 500 \text{ V}$	$U = 700 \text{ V}$	$U = 900 \text{ V}$
VTT	100	10	$97.4 \pm 0.3\%$		
CiS4	150	10	$93.2 \pm 0.3\%$	$96.3 \pm 0.3\%$	$97.0 \pm 0.3\%$
SOI2 [37]		5		$97.8 \pm 0.3\%$	

the 150 μm thick sensor were measured. However, to achieve the saturation, a higher bias voltage of 800 V to 900 V is needed. The findings support the results from charge collection studies, obtained with the Edge-TCT set-up. They evidenciate a sufficient hit efficiency of 100 μm thick sensors in the range of fluences expected at the innermost layers at HL-LHC. The study of power dissipation in Section 5.2.7 completes the analysis that demonstrates the feasibility of employing these devices in L_0 and L_1 of the ITk detector.

The results from the CiS4 module for the highest fluence of $10^{16} \text{ n}_{\text{eq}} \text{ cm}^{-2}$ are compared to those obtained with an SOI2 module irradiated to a fluence of $5 \cdot 10^{15} \text{ n}_{\text{eq}} \text{ cm}^{-2}$ with a 800 MeV proton beam at the Los Alamos Neutron Science Center (LANSCE) [144]. At 700 V, this module, tested at the CERN beam test, retains a hit efficiency of $97.8 \pm 0.3\%$, as reported in Ref. [37]. The hit efficiency for the module irradiated to a fluence of $10^{16} \text{ n}_{\text{eq}} \text{ cm}^{-2}$ is found to be $96.3 \pm 0.3\%$ at the same bias voltage. As shown in Figure 5.35b, the saturation of the hit efficiency at a fluence of $5 \cdot 10^{15} \text{ n}_{\text{eq}} \text{ cm}^{-2}$ and at 700 V is 0.8% higher than at a fluence of $10^{16} \text{ n}_{\text{eq}} \text{ cm}^{-2}$ at 900 V. The hit efficiency results are summarised in Table 5.6 for voltage steps at 500 V, 700 V and 900 V.

The in-pixel hit efficiency map of the CiS4 module with a 150 μm thick sensor irradiated to a fluence of $10^{16} \text{ n}_{\text{eq}} \text{ cm}^{-2}$ is illustrated in Figure 5.36 as an 8-pixel map. The correspondence of efficiency loss and p-t structure is clearly observed. The p-t structure leads to a hit efficiency of only 10% in the most central part of the bias dot to around 60% in the region surrounding the bias dot. At the other cell corner below the bias rail, but opposite to bias dot, the combined effect of charge sharing results in an efficiency of 60%. As the charge released by crossing particles is shared among four pixels, the corners of the pixel cells are affected by charge sharing. In contrary, in the central part of the pixel cell a hit efficiency of $99 \pm 0.3\%$ is achieved.

The perpendicular incidence, corresponding to $\eta = 0$ in the ATLAS ITk, is considered as the most pessimistic case among the possible track directions. In fact, in this condition the particle path in the silicon bulk is minimal, and therefore also the charge release is lower than for inclined tracks. To study the dependence of the hit efficiency as a function of the track-module angle, an inclination angle analysis is performed inclining a module at an angle of 45° with respect to the beam direction. The results for a module with a 150 μm thick sensor irradiated to a fluence of $10^{16} \text{ n}_{\text{eq}} \text{ cm}^{-2}$ are

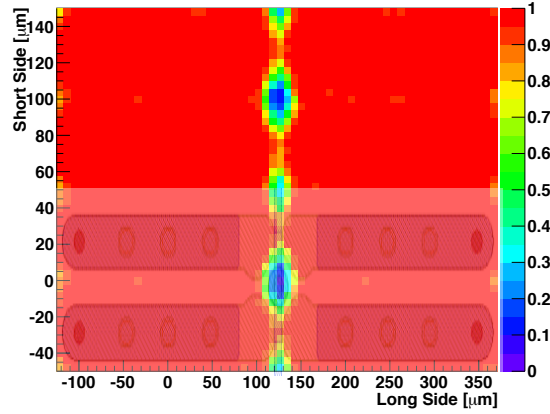


Figure 5.36: Hit efficiency in an 8-pixel map of a CiS4 module with a $150\ \mu\text{m}$ thick sensor irradiated to a fluence of $10^{16}\ \text{n}_{\text{eq}}\ \text{cm}^{-2}$ and biased at 900 V. The inefficiencies due to the p-t structure are visible as the two larger regions with the blue center. A sketch with four pixel implants sharing a bias dot is overlaid. The sensor employs a pixel cell size of $50 \times 250\ \mu\text{m}^2$.

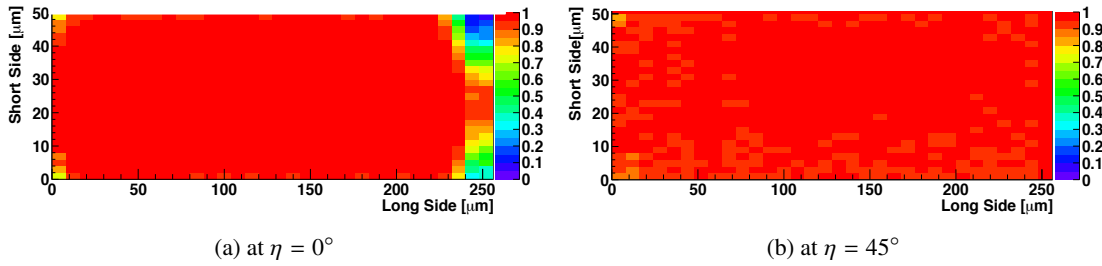


Figure 5.37: In-pixel hit efficiency map of a $150\ \mu\text{m}$ thick sensor irradiated at $10^{16}\ \text{n}_{\text{eq}}\ \text{cm}^{-2}$ placed (a) perpendicular to the beam and (b) at an angle of 45° . The efficiencies obtained at a bias voltage of 900 V are (a) $97.0 \pm 0.3\%$ and (b) $98.7 \pm 0.3\%$.

shown as single in-pixel hit efficiency maps in Figure 5.37. As the biasing structure is kept at ground potential, but is not connected to the readout, a fraction of the charge carriers drift towards the biasing structures. This results in main inefficiency regions inside the single pixel cell, located at the bias dot area and the bias rail. This effect is reduced for inclined tracks by tilting the module, thanks to the fact, that a track can partially cross the area below the biasing structure and the regions of the cells below the pixel implant. Therefore, the hit efficiency at 900 V is increased from $97.0 \pm 0.3\%$ at $\eta = 0$ to $98.7 \pm 0.3\%$ at an angle of 45° .

CiS4: Beam test results on irradiated modules with $50 \times 50\ \mu\text{m}^2$ pixel cells

In addition to the performance of FE-I4 $50 \times 250\ \mu\text{m}^2$ pixel cells at high fluences, the performance of small pixel cells is investigated. The CiS4 production also contains sensors, where an FE-I4 pixel cell is subdivided into smaller implants. This allows for investigation of the expected performance of the $50 \times 50\ \mu\text{m}^2$ cells with a pixel implant size of $30 \times 30\ \mu\text{m}^2$ for the ITk. The design is introduced in Section 5.1.1 and is illustrated in Figure 5.3.

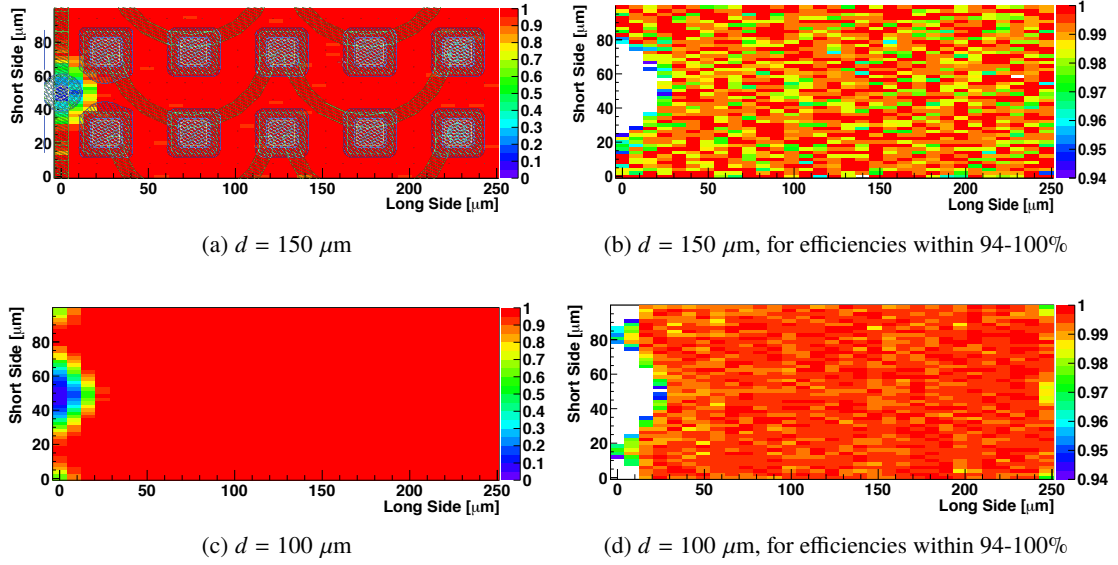


Figure 5.38: In-pixel hit efficiency map for (a) ((c)) a 150 μm thin sensor (100 μm thin sensor) at 60 V for all efficiencies and (b) ((d)) for efficiencies within a scale of 94-100%, all before irradiation. In (a) the design is overlaid. The module with the 150 μm thick sensor reaches a hit efficiency of $97.6 \pm 0.3\%$ and the one with the 100 μm thick sensor $97.8 \pm 0.3\%$.

Before irradiation, the charge is still above threshold, although the charge released by a particle is splitted between two adjacent pixel readout channels. Therefore, the charge sharing among neighbouring pixels observed in Section 5.2.2 has no impact. Correspondingly, the hit efficiency is not affected. Figure 5.38 shows the in-pixel hit efficiency map before irradiation for (top) a 150 μm thin sensor and (bottom) a 100 μm thin sensor, both operated at a bias voltage of 60 V. The design is overlaid on the pixel cell. The scale is displayed for efficiencies within 94-100% to enhance the very small efficiency loss in between the pixel cells due to charge sharing. This effect is more significant in the in-pixel efficiency map of the 100 μm thick sensor. The module with the 150 μm thick sensor reaches a hit efficiency of $97.6 \pm 0.3\%$ and the one with the 100 μm thick sensor $97.8 \pm 0.3\%$. The efficiency loss is mainly concentrated at the bias dot and the inter-implant regions of the small implants.

The sensor design with small implants employs two different ways of connecting the $30 \times 30 \mu\text{m}^2$ implants to FE-I4 readout channels in two halves of the same module, separated along the row direction. The performance of the two sensor sides are compared in the following, and also to the one of the sensors with an FE-I4 pixel cell. In particular, the discussion will be focused on the study of a module with a 100 μm thick sensor irradiated to a fluence of $5 \cdot 10^{15} \text{ n}_{\text{eq}} \text{ cm}^{-2}$ and a 150 μm thick sensor irradiated to a fluence of $3 \cdot 10^{15} \text{ n}_{\text{eq}} \text{ cm}^{-2}$.

In Figure 5.39a, the hit efficiency after an irradiation to a fluence of $5 \cdot 10^{15} \text{ n}_{\text{eq}} \text{ cm}^{-2}$ of the pixel cells in the line and wave design are compared. As shown for the charge collection efficiency in Section 5.2.2, less charge is collected in the inter-implant region of the wave design. This happens especially after irradiation and results in an efficiency loss of up to 20% for the wave design before

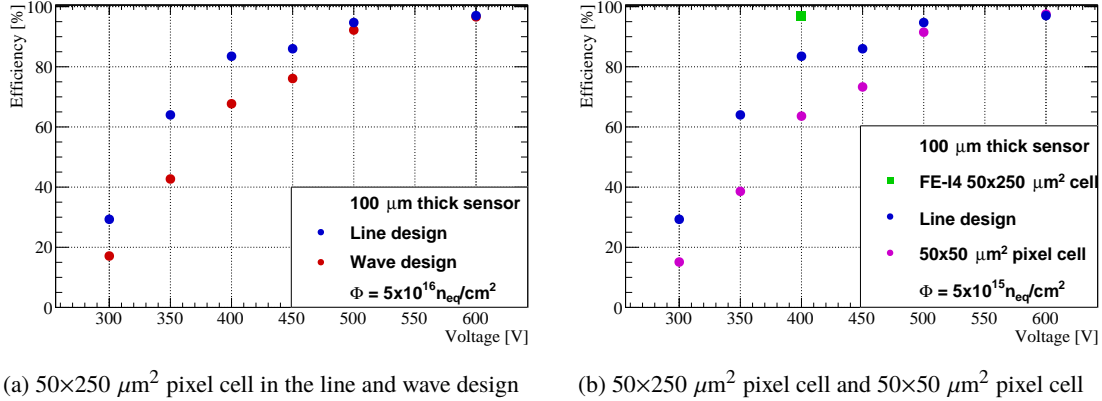


Figure 5.39: Hit efficiencies as a function of voltage of a 100 μm thick sensor after an irradiation to a fluence of $5 \cdot 10^{15} \text{ n}_{\text{eq}} \text{ cm}^{-2}$. (a) the hit efficiency of a $50 \times 250 \text{ μm}^2$ pixel cell for different voltages obtained with the line and wave design, averaged over the five implants read out by the same channel, (b) hit efficiency of the $50 \times 250 \text{ μm}^2$ pixel cell of the line design and the last $50 \times 50 \text{ μm}^2$ pixel implant in the wave design, situated opposite to the bias dot. If not visible, the uncertainties are smaller than the marker size.

saturation, when averaged over the five implants with respect to the $50 \times 250 \text{ μm}^2$ pixel cell of the line design. In the range of voltages, where the saturation of the hit efficiency is observed, i.e. for bias voltages of more than 500 V, the discrepancy in efficiency decreases to less than 3%. At a maximum bias voltage of 600 V a hit efficiency of $96.6 \pm 0.3\%$ is reached for the $50 \times 250 \text{ μm}^2$ pixel cell of the wave design and is, within the uncertainties, comparable with the achieved efficiency of $97.0 \pm 0.3\%$ for the line design.

To derive the expected performance of the RD53A cell without any p-t structure, the $50 \times 50 \text{ μm}^2$ pixel cell of the wave design, situated at the edge, is taken as the closest approximation. It is surrounded by eight other pixel cells, seven of which are read out by different readout channels, and only one is read out by the same channel. Given, that for one channel the charge sharing effect is not realistically reproduced, the quoted hit efficiency is always slightly higher than the one expected for the RD53A modules. The performance of this cell is compared to the FE-I4 $50 \times 250 \text{ μm}^2$ pixel cells in Figure 5.39b. In the graph the efficiencies are shown as a function of bias voltage. The FE-I4 $50 \times 250 \text{ μm}^2$ pixel cell as a single implant yields the highest hit efficiency of $97.0 \pm 0.3\%$ at a voltage of 400 V compared to $83.5 \pm 0.3\%$ achieved for the $50 \times 250 \text{ μm}^2$ pixel cell inside the line design and $68.1 \pm 0.3\%$ achieved in the wave design. A hit efficiency of $63.6 \pm 0.3\%$ is achieved for the single $50 \times 50 \text{ μm}^2$ pixel cell. The obtained hit efficiency is verified with results previously presented in Ref. [37]. There, the same hit efficiency value is obtained at a bias voltage of 400 V. The charge saturation of a module with a 100 μm thick sensor was quoted to be around 200-300 V. Summarising the results at the voltage point at 400 V, a significant deviation in hit efficiency is observed, comparing the line and wave design, the single FE-I4 $50 \times 250 \text{ μm}^2$ pixel cell and the $50 \times 50 \text{ μm}^2$ pixel cell. An efficiency loss between the implants in the line design after irradiation is only partially compensated by the metal rail, connecting the implants in a straight line. However, due to the metal rail running in curves in the wave design and the fact, that the neighbouring implants are

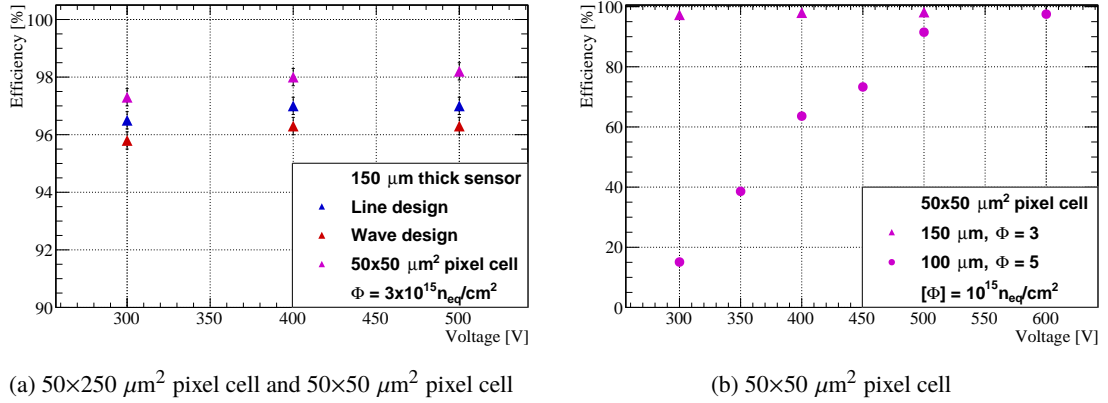


Figure 5.40: Hit efficiencies as a function of voltage of a 150 μm thick sensor after an irradiation to a fluence of $3 \cdot 10^{15} \text{ n}_{\text{eq}} \text{ cm}^{-2}$. (a) the hit efficiency of a $50 \times 250 \mu\text{m}^2$ pixel cell in the line and wave design is compared to $50 \times 50 \mu\text{m}^2$ pixel cell in the wave design in the hit efficiency range 90-100%. (b) hit efficiencies of $50 \times 50 \mu\text{m}^2$ pixel implant in modules with 100 μm and 150 μm thick sensors at different irradiation levels are compared and are shown in the hit efficiency range 0-100%. If not visible, the uncertainties are smaller than the marker size.

not read out by the same channel, an even lower hit efficiency is reached. These outcomes support the observed charge loss in the line and wave designs in between the implants in Section 5.2.2. The single $50 \times 50 \mu\text{m}^2$ cell suffers from the full effect of charge sharing, since a larger proportion of the small pixel cell, compared to the larger pixel cell of single or segmented $50 \times 250 \mu\text{m}^2$ pixel, is affected by the charge sharing, as investigated in Section 5.2.2.

Instead, at the highest voltage of 600 V, the hit efficiency of the single $50 \times 50 \mu\text{m}^2$ cell saturates at a value of $97.5 \pm 0.3\%$ and surpasses the hit efficiency obtained by the line design by 0.5%. At this voltage, the modified CiS4 module shows a saturation of the hit efficiency for both designs. This means, that the saturation of the hit efficiency of the sensor with the modified pixels is observed at an around 300-400 V higher voltage with respect to the one with the FE-I4 pixel design. The values of the saturated hit efficiencies of the module with the single FE-I4 $50 \times 250 \mu\text{m}^2$ pixel and with the $50 \times 50 \mu\text{m}^2$ cell are the same within their uncertainties.

Similar investigations are carried out for a module of the same type, but assembled with a 150 μm thick sensor with the modified geometry, irradiated to a fluence of $3 \cdot 10^{15} \text{ n}_{\text{eq}} \text{ cm}^{-2}$. In this case, the saturation of the hit efficiency is reached around 400 V, see Figure 5.40. This is around the expected saturation voltage for a module of the same sensor thickness with the FE-I4 pixel cell. No exact comparison is drawn, since outcomes on modules with 150 μm thick sensors were previously shown after an irradiation to fluences of $2 \cdot 10^{15} \text{ n}_{\text{eq}} \text{ cm}^{-2}$ (charge saturation around 300 V) and $4 \cdot 10^{15} \text{ n}_{\text{eq}} \text{ cm}^{-2}$ (efficiency saturation around 500 V) in Ref. [37], but not after an irradiation to a fluence of $3 \cdot 10^{15} \text{ n}_{\text{eq}} \text{ cm}^{-2}$. Hence, the discrepancy in the saturation voltages is not as significant as for modules irradiated to higher fluences. At the highest voltage of 500 V, a hit efficiency of $98.2 \pm 0.3\%$ is obtained for the single $50 \times 50 \mu\text{m}^2$ pixel cell, see Figure 5.40b. The hit efficiency values obtained for the full $50 \times 250 \mu\text{m}^2$ pixel cell are affected by the efficiency

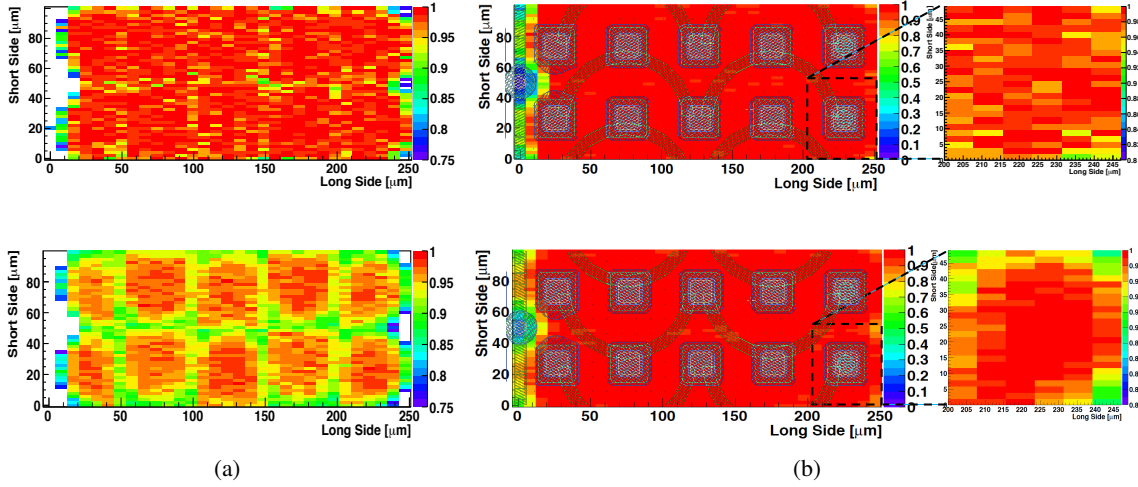


Figure 5.41: In-pixel hit efficiency map for a $150\ \mu\text{m}$ thick sensor (top) at (a) 300 V and (b) 500 V irradiated to a fluence of $3 \cdot 10^{15}\ \text{n}_{\text{eq}}\ \text{cm}^{-2}$ and a $100\ \mu\text{m}$ thick sensor (bottom) at (a) 500 V and (b) 600 V irradiated to a fluence of $5 \cdot 10^{15}\ \text{n}_{\text{eq}}\ \text{cm}^{-2}$. In (a) the scale is zoomed to enhance the efficiency loss of 5% to 15% in between the pixel cells. In (b) the design is overlaid and the efficiency of the edge implant is calculated for the closest approximation of the geometry of a RD53A $50 \times 50\ \mu\text{m}^2$ pixel cell without p-t structure.

loss by the p-t design. Therefore, at this irradiation fluence the $50 \times 50\ \mu\text{m}^2$ pixel cell, selected as the closest approximation of the RD53A cell with no biasing structure implemented, performs better than the $50 \times 250\ \mu\text{m}^2$ pixel cell in the line design with a 1.0% higher hit efficiency at the same bias voltage. Compared to the module with the $100\ \mu\text{m}$ thick sensor irradiated to a fluence of $5 \cdot 10^{15}\ \text{n}_{\text{eq}}\ \text{cm}^{-2}$, the hit efficiency of the module with the $150\ \mu\text{m}$ thick sensor, irradiated to a lower fluence of $3 \cdot 10^{15}\ \text{n}_{\text{eq}}\ \text{cm}^{-2}$, consequently reaches a higher hit efficiency. At the bias voltage of 500 V, its hit efficiency is almost 7% higher and reaches $98.2 \pm 0.3\%$. At 600 V, the hit efficiency of the module with the $100\ \mu\text{m}$ thick sensor increases up to a value of $97.5 \pm 0.3\%$.

The in-pixel hit efficiency maps of the two modules after an irradiation to fluences of $3 \cdot 10^{15}\ \text{n}_{\text{eq}}\ \text{cm}^{-2}$ and $5 \cdot 10^{15}\ \text{n}_{\text{eq}}\ \text{cm}^{-2}$ are shown in Figure 5.41 at 300 V and 500 V (a) and at 500 V and 600 V (b). The pixel cell at the edge, chosen to be the closest approximation of the RD53A cell, is highlighted in Figure 5.41. The hit efficiency of the other pixel implants is influenced by the metal rail, connecting the small $30 \times 30\ \mu\text{m}^2$ implants in curves and summing up the signal of the neighbouring pixel cells along the diagonal. This is especially the case for the three inner implants of the $50 \times 250\ \mu\text{m}^2$ pixel cell. With this modified geometry of the FE-I4 compatible sensor design, it is therefore possible to make first predictions on the performance of a $50 \times 50\ \mu\text{m}^2$ pixel cell after irradiation, when considering the edge pixel implant opposite to the bias dot.

An efficiency loss up to 10% in the lower right corner of the $50 \times 50\ \mu\text{m}^2$ pixel cell in the module irradiated to a fluence of $3 \cdot 10^{15}\ \text{n}_{\text{eq}}\ \text{cm}^{-2}$ is clearly seen in the cut-out of the in-pixel hit efficiency map when zooming into the scale. Due to the implemented geometry entailing the charge sharing with 7/8 of the neighbouring channels, the upper left corner is not affected by charge sharing. In the device irradiated to a higher fluence of $5 \cdot 10^{15}\ \text{n}_{\text{eq}}\ \text{cm}^{-2}$, the charge loss is enhanced and appears in

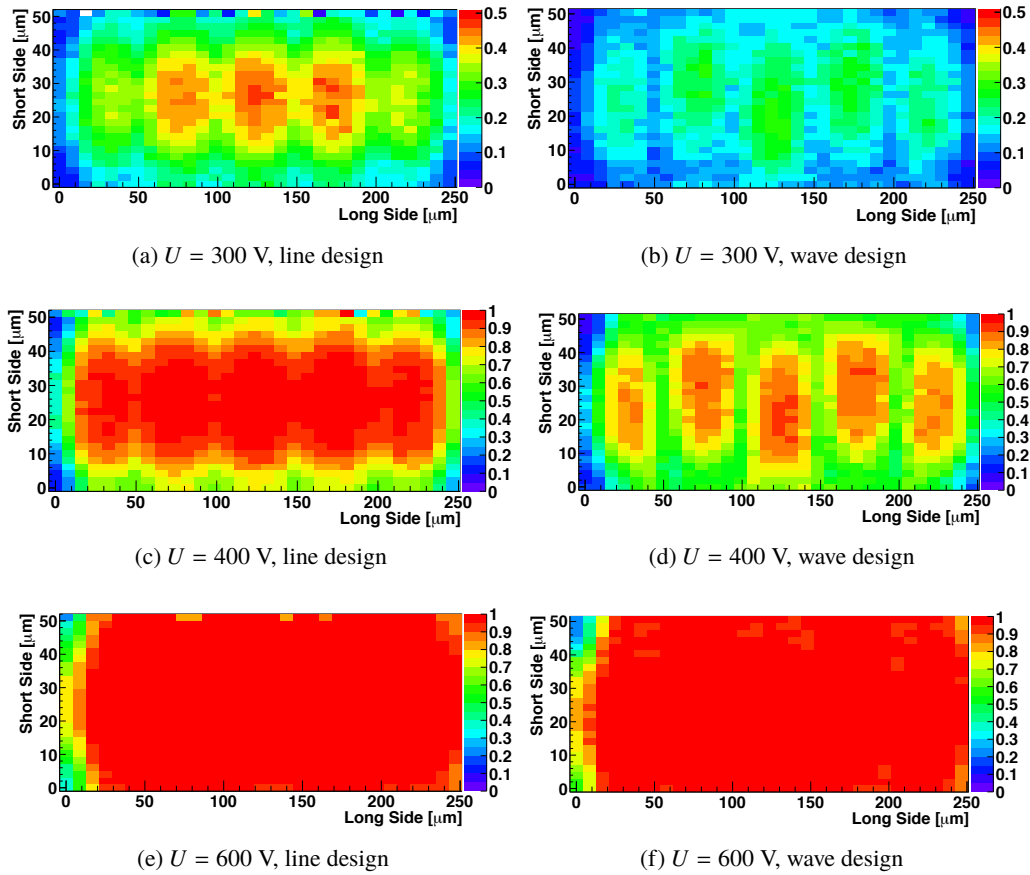


Figure 5.42: In-pixel hit efficiency maps of a $50 \times 250 \mu\text{m}^2$ pixel cell in the line (a,c,e) and wave design (b,d,f) at a bias voltage of 300 V, 400 V and 600 V after an irradiation to a fluence of $5 \cdot 10^{15} \text{ n}_{\text{eq}} \text{ cm}^{-2}$. The module is assembled with a sensor with a thickness of $100 \mu\text{m}$.

three corners except for the lower left corner. In the lower and upper right corners the efficiency loss is due to charge sharing with the neighbouring pixel implants, read out by different readout channels with respect to the pixel cell at the edge. In the upper left corner the efficiency loss is caused by charge sharing with the metal rail connected to the neighbouring pixel implant, which is readout by a different readout channel. Instead, in the lower left corner, the metal rail attached to the pixel implant compensates the charge loss resulting in no significant decrease of the hit efficiency in this region.

For a more detailed investigation of the efficiency loss at different bias voltage steps, Fig. 5.42 depicts the in-pixel efficiencies of a $50 \times 250 \mu\text{m}^2$ pixel cell in the line (a,c,e) as well as in the wave design (b,d,f) of the module with a $100 \mu\text{m}$ thick sensor irradiated to a fluence of $5 \cdot 10^{15} \text{ n}_{\text{eq}} \text{ cm}^{-2}$. The results are shown for bias voltages of 300 V, 400 V before saturation and 600 V after saturation. With respect to the single FE-I4 $50 \times 250 \mu\text{m}^2$ pixel cell, the higher saturation voltage of the hit efficiency in the line design is clearly seen in the in-pixel hit efficiency maps. Efficiency loss appears in the inter-implant region even though the $30 \times 30 \mu\text{m}^2$ implants of the $50 \times 50 \mu\text{m}^2$ pixel cells are connected by a straight line. Only at 600 V the effect of the small implants is recovered,

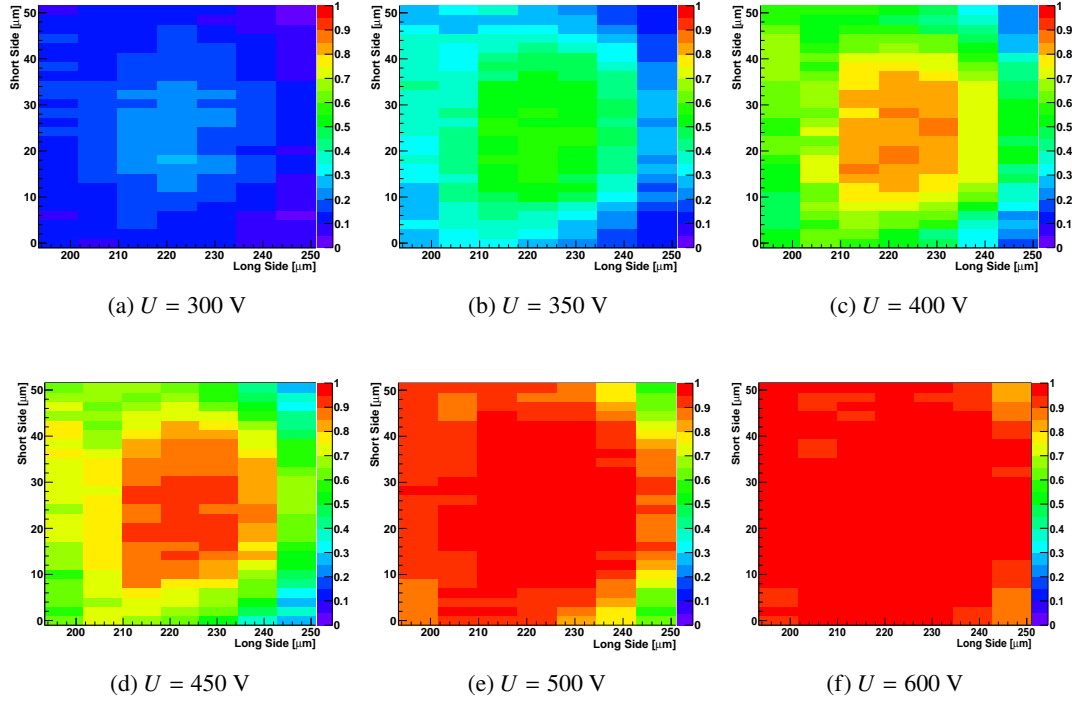


Figure 5.43: In-pixel hit efficiency maps of the outer $50 \times 50 \mu\text{m}^2$ pixel implant of the wave design, chosen to be the closest approximation to the RD53A compatible pixel cell design without punch-through structure, at different voltages ranging from 300 V to 600 V. The scale of the hit efficiency ranges from 0 to 1 for all maps to allow for a direct comparison of the hit efficiency distribution within the pixel cell. The module, assembled with a $100 \mu\text{m}$ thick sensor, is irradiated to a fluence of $5 \cdot 10^{15} \text{ n}_{\text{eq}} \text{ cm}^{-2}$.

explaining the high saturation voltage of the hit efficiency of the $50 \times 250 \mu\text{m}^2$ pixel cell in the line design compared to a single FE-I4 $50 \times 250 \mu\text{m}^2$ pixel cell with no subdivisions. Comparing the performance of the line and the wave design at a lower voltage of 400 V before saturation, the hit efficiency in the line design is increased due to the straight metal rail in the inter-pixel region with respect to the inter-pixel region in the wave design, where the efficiency loss in this region is still clearly visible. At 600 V the effect of an efficiency loss in between the pixel implants is completely recovered for the pixel cell in the line, as well as in the wave design. This is also seen in Figure 5.39. Hence, after irradiation the effect of charge sharing for smaller pixel cells is evident at lower bias voltages.

In Figure 5.43, the performance of the small pixel cell of the module irradiated to a fluence of $5 \cdot 10^{15} \text{ n}_{\text{eq}} \text{ cm}^{-2}$ is illustrated in in-pixel hit efficiency maps for the entire bias voltage range. The hit efficiency scales are all set from 0 to 1 for a direct comparison of the in-pixel hit efficiency at different voltage steps. Only at a voltage of 450 V a hit efficiency of $90.0 \pm 0.3\%$ is obtained on the implant, but only covering an area of not more than $20 \times 20 \mu\text{m}^2$. At this voltage a sensor with an FE-I4 pixel cell size is at full saturation.

At 500 V, the hit efficiency in this region is increased up to 97%, but the surrounding implant frame still remains at an average hit efficiency of $90.0 \pm 0.3\%$. At 600 V, finally a hit efficiency of $98.6 \pm 0.3\%$

Table 5.7: Summary of the hit efficiency results of CiS4 modules with 100 μm and 150 μm thick sensors after an irradiation to $3 \cdot 10^{15} \text{ n}_{\text{eq}} \text{ cm}^{-2}$ and $5 \cdot 10^{15} \text{ n}_{\text{eq}} \text{ cm}^{-2}$. The results are summarised for the single $50 \times 50 \mu\text{m}^2$ pixel cell at the highest voltage steps of 500 V and 600 V.

Production	Pixel cell [μm^2]	Thickness [μm]	Φ [$10^{15} \text{ n}_{\text{eq}} \text{ cm}^{-2}$]	Hit efficiency at	
				$U = 500 \text{ V}$	$U = 600 \text{ V}$
CiS4	50×50	100	5	$91.5 \pm 0.3\%$	$97.5 \pm 0.3\%$
		150	3	$98.2 \pm 0.3\%$	

is achieved over the entire implant. Still at the corners (3 out of 4) of the $30 \times 30 \mu\text{m}^2$ implant the hit efficiency decreases to $95.0 \pm 0.3\%$. The hit efficiencies obtained for the $50 \times 50 \mu\text{m}^2$ pixel cell in the CiS4 modules with 100 μm and 150 μm thick sensors after an irradiation to $3 \cdot 10^{15} \text{ n}_{\text{eq}} \text{ cm}^{-2}$ and $5 \cdot 10^{15} \text{ n}_{\text{eq}} \text{ cm}^{-2}$ are summarised in Table 5.7 at the highest voltage steps.

SOI3: Beam test results on irradiated modules with a floating bias rail

With the modules of the MPG/HLL production, investigations on the reduction of the effect of the p-t design on the hit efficiency before and after irradiation are made. The SOI3 sensors are developed with a p-t structure with a common bias dot, connected to bias rail partially superimposed to the pixel implant. Additionally, two varieties of bias ring (BR) interconnection are implemented: one with a grounded BR, the other one with a floating BR, as described in more detail in Section 5.1.2. Biasing structures in general are described in more detail in Section 2.4.1.

Result of modules with a grounded, as well as a floating BR are presented. In Figures 5.44 and 5.45, the hit efficiency is shown for modules with 150 μm and 100 μm thick sensors before irradiation. The modules were all tuned to a threshold of 1000 e and measured at a beam test at DESY. Since the particle beam has an energy of 5 GeV and therefore leads to a large contribution of multiple scattering, the in-pixel hit efficiency maps are derived with a lower spatial resolution, see Section 4.3.2.

The benefit of the floating BR is still significant in the in-pixel hit efficiency maps for both thicknesses of the sensors. A hit efficiency of $99.7 \pm 0.3\%$ is achieved in case of the floating BR implemented in the 150 μm thick sensor. Instead, the grounded BR results in a 0.8% lower hit efficiency of $98.9 \pm 0.3\%$. An inefficient region in the bias dot area is clearly visible. In the module with the 100 μm thick sensors the difference between the two types of BR implementation is even more significant. A hit efficiency of $99.6 \pm 0.3\%$ is reached in case of a floating BR, being 1.5% higher with respect to the module with the 100 μm thick sensor and the grounded BR. Furthermore, a better hit efficiency is detected for the module with the thicker sensor at the same operational bias voltage of 60 V before irradiation. The p-t design has a larger impact on the inefficiencies in thinner sensors before irradiation. The performance of irradiated sensors with the grounded or floating BR is also investigated in beam test campaigns at CERN and compared, see Figure 5.46. After irradiation, the larger effect of trapping in thicker sensors equalises the reached hit efficiency to approximately the same value for 100 μm and 150 μm thick sensors at the saturation voltage, as previously shown in

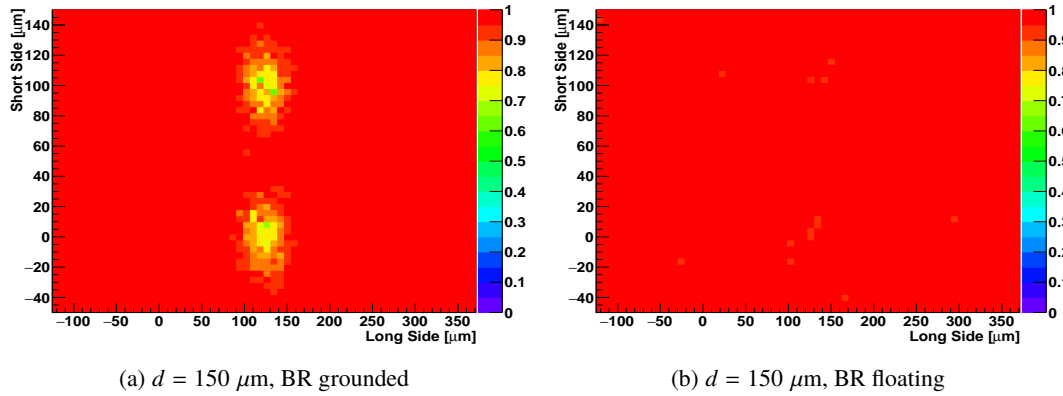


Figure 5.44: Comparison of in-pixel hit efficiency map with 8 pixels of SOI3 modules with sensor thicknesses of $150 \mu\text{m}$. The module is assembled with a sensor with the grounded BR, the standard implementation, and is displayed in (a), the module with the modified sensor with a floating BR is shown in (b). Both modules are operated at full saturation at a voltage of 60 V and were measured at a beam test at DESY.

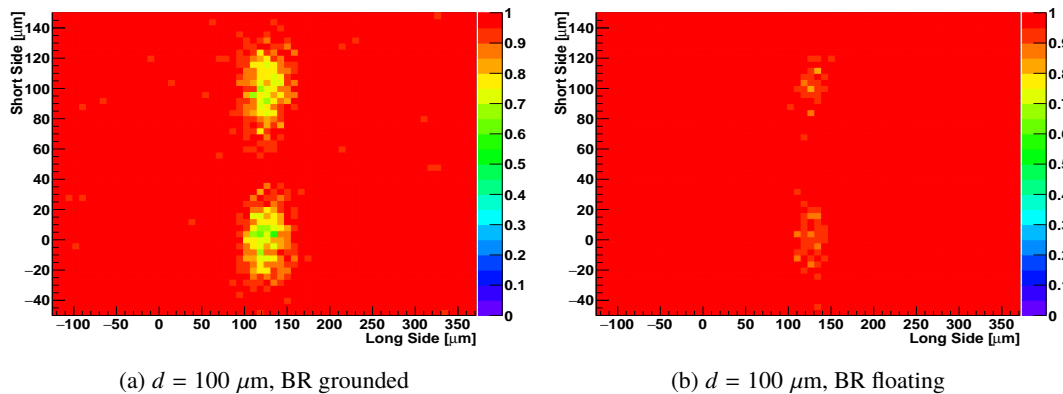


Figure 5.45: Comparison of in-pixel hit efficiency map with 8 pixels of SOI3 modules with sensor thicknesses of $100 \mu\text{m}$. The module assembled with a sensor with the grounded BR, the standard implementation, is displayed in (a), the module with the modified sensor with a floating BR is shown in (b). Both modules are operated at full saturation at a voltage of 60 V and were measured at a beam test at DESY.

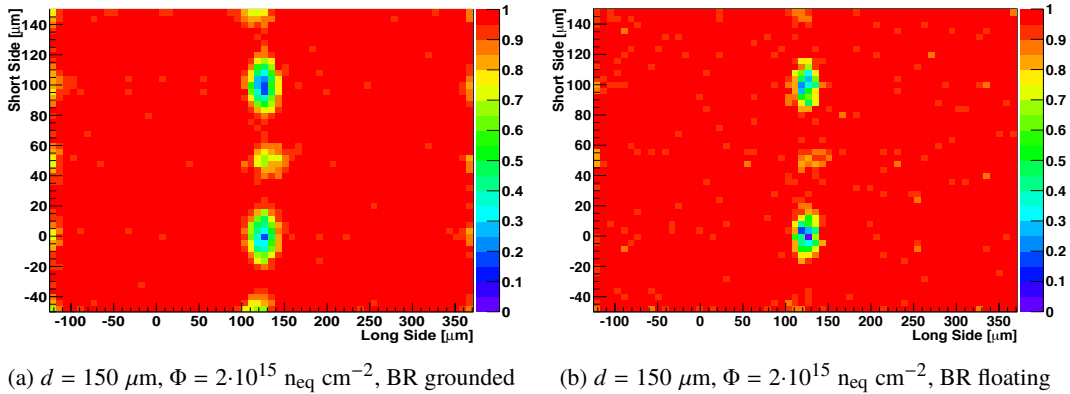


Figure 5.46: Comparison of the in-pixel hit efficiency maps of SOI3 modules with $150 \mu\text{m}$ thick sensors after an irradiation to $2 \cdot 10^{15} \text{ n}_{\text{eq}} \text{ cm}^{-2}$ at 500 V: (a) with an implementation of a grounded BR and (b) with a floating BR. The modules were measured at a beam test at CERN.

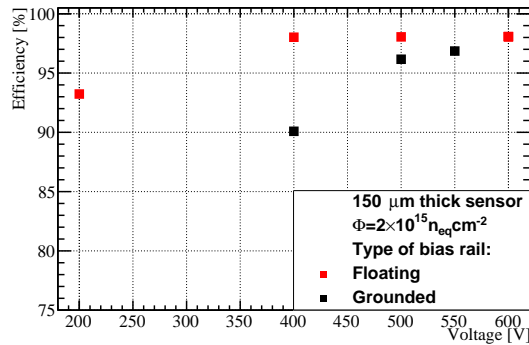


Figure 5.47: Comparison of the hit efficiency of SOI3 modules with $150 \mu\text{m}$ thick sensors after an irradiation to $2 \cdot 10^{15} \text{ n}_{\text{eq}} \text{ cm}^{-2}$ in a voltage range up to 600 V with an implementation of a floating BR and with a standard BR. The uncertainties are included but smaller than the marker size.

Section 5.2.4.

In Figure 5.46, the in-pixel hit efficiency maps of two modules, both assembled with $150 \mu\text{m}$ thick sensors, are shown after an irradiation to $2 \cdot 10^{15} \text{ n}_{\text{eq}} \text{ cm}^{-2}$. They are biased at 500 V to ensure full saturation of the charge within the sensor. In contrast to the in-pixel hit efficiency maps before irradiation in Figures 5.44 and 5.45, both modules show clear inefficient regions in the area of the bias dot. However, the inefficient regions are smaller for the module with the sensor with the floating BR, resulting in a hit efficiency of $98.0 \pm 0.3\%$ at 500 V. The grounded BR is the reason for an efficiency loss of 1.6% compared to the previous results at the same bias voltage. This module shows additional inefficiencies in the area without bias dot, but close to the bias rail. The inefficiencies due to charge sharing in the corners of the pixel cells in the module with the sensor with the grounded BR can also be caused by the slightly higher threshold tuned to 850 e compared to a threshold of 800 e of the other device. However, the grounded BR, implemented in the sensor, still gives the larger contribution to the efficiency loss. Figure 5.47 summarises the hit efficiencies

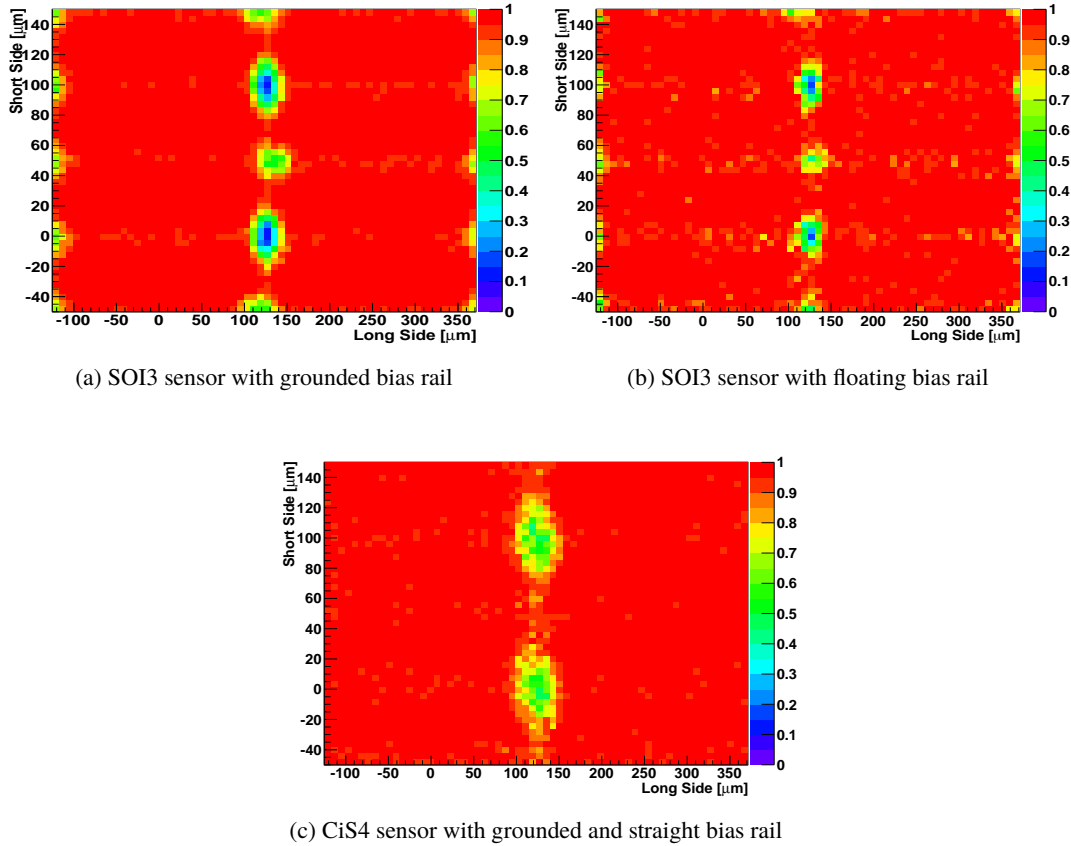


Figure 5.48: Comparison of the hit efficiency of SOI3 and CiS4 modules with $100\ \mu\text{m}$ thick sensors after an irradiation to a fluence of $5 \cdot 10^{15}\ \text{n}_{\text{eq}}\ \text{cm}^{-2}$ at 400 V. (a) SOI3 module with an implementation of a grounded bias rail, (b) with a floating bias rail and (c) CiS4 module with a grounded and straight bias rail. The modules were measured at a beam test at CERN. If not visible, the uncertainties are smaller than the marker size.

of both modules at different bias voltages. At 400 V the module with the floating BR already reaches a saturated hit efficiency of $98.0 \pm 0.3\%$. With this investigation, the saturation voltage for a module with a $150\ \mu\text{m}$ thick sensor after an irradiation to $2 \cdot 10^{15}\ \text{n}_{\text{eq}}\ \text{cm}^{-2}$ was found to be 400 V. In contrast, the other module shows a saturation voltage of around 550 V reaching a hit efficiency of $97.1 \pm 0.3\%$ at this point.

The same types of modules with a grounded and floating BR, but instead assembled with $100\ \mu\text{m}$ thick sensors and irradiated to a fluence of $5 \cdot 10^{15}\ \text{n}_{\text{eq}}\ \text{cm}^{-2}$, are compared to a CiS4 module at the same conditions and with the same properties. The CiS4 module instead employs a sensor with a grounded and straight bias rail. In Figure 5.48, the in-pixel hit efficiency maps for all three modules are compared at a voltage of 400 V. The inefficiencies occur in the region of the bias dot. Depending on the design, the spread of the inefficient region differs. The SOI3 module with the floating bias rail, running as much as possible over the implants, shows the smallest inefficient regions around the bias dot compared to both modules with a grounded bias rail.

A comparison of the CiS4 and SOI3 modules with the grounded BRs shows a larger inefficient

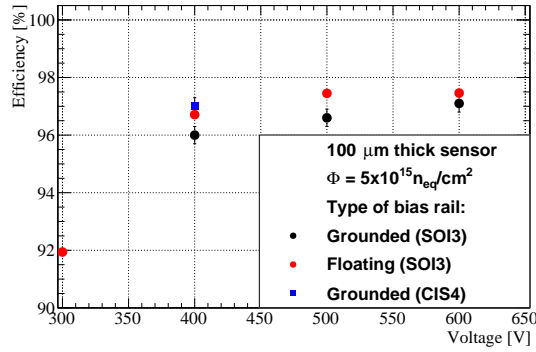


Figure 5.49: Comparison of the hit efficiency as a function of bias voltage of modules from the SOI3 and CiS4 production after an irradiation to a fluence of $5 \cdot 10^{15} \text{ n}_{\text{eq}} \text{ cm}^{-2}$. The SOI3 module with a grounded bias rail is represented in black, the one with a floating bias rail in red, while the CiS4 module with a grounded and straight bias rail is depicted in blue. The range of the y scale is from 90% to 100% to enhance the difference in hit efficiencies between the three devices.

Table 5.8: Summary of the hit efficiency results of SOI3 modules with 100 μm and 150 μm thick sensors after an irradiation to $2 \cdot 10^{15} \text{ n}_{\text{eq}} \text{ cm}^{-2}$ and $5 \cdot 10^{15} \text{ n}_{\text{eq}} \text{ cm}^{-2}$. The results are summarised for the sensor with a floating and grounded BR at the highest voltage steps of 500 V and 600 V.

Production	BR	Thickness [μm]	Φ [$10^{15} \text{ n}_{\text{eq}} \text{ cm}^{-2}$]	Hit efficiency at	
				$U = 500 \text{ V}$	$U = 600 \text{ V}$
SOI3	floating	150	2	$98.0 \pm 0.3\%$	$98.0 \pm 0.3\%$
	grounded			$96.4 \pm 0.3\%$	
	floating	100	5	$97.5 \pm 0.3\%$	$97.5 \pm 0.3\%$
	grounded			$96.1 \pm 0.3\%$	$96.5 \pm 0.3\%$

region around and where the bias dot is implemented. In the CiS4 module it leads to an efficiency decrease down to 50% and in the SOI3 module the hit efficiency even drops to 20% in the very center of this area. The inefficient region does not concentrate only around the bias dot, but extends to the bias rail line running in between the two pixel columns. In opposition to the CiS4 module, both SOI3 modules show inefficiencies due to charge sharing in the four corners of the pixel cell. The SOI3 module with the 100 μm thick sensor with the floating BR additionally employs a short sensor edge of $d_e = 300 \mu\text{m}$ from the last pixel column to the edge of the sensor. The 100 μm thick sensors of the other two modules with the grounded BR are designed with $d_e = 450 \mu\text{m}$. In Figure 5.49 it is shown, that the shorter edge distance does not influence the performance of the SOI3 module in terms of breakdown voltage. The SOI3 module with $d_e = 300 \mu\text{m}$ shows a good breakdown performance for voltages higher than 600 V. At 600 V, a hit efficiency of 97.5% is reached for the SOI3 module with a floating BR. The SOI3 module with the grounded BR shows a 1% lower hit efficiency at the same bias voltage. Similar to the modules irradiated to a fluence of $2 \cdot 10^{15} \text{ n}_{\text{eq}} \text{ cm}^{-2}$, the saturation of the efficiency is shifted towards higher voltages for the SOI3 module with the grounded BR. Since the hit efficiency of the CiS4 module was measured at a single

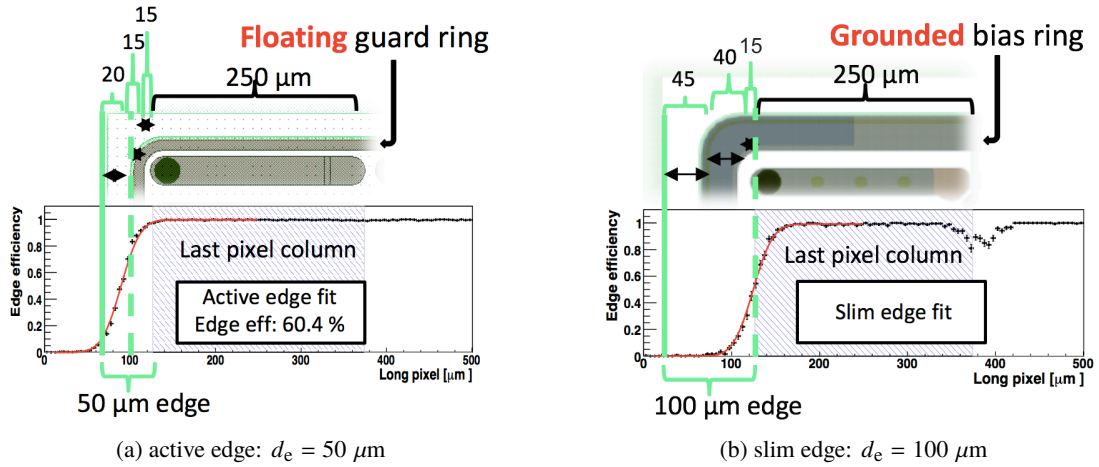


Figure 5.50: Hit efficiency at the sensor edge of the $100 \mu\text{m}$ thin sensor (a) with $50 \mu\text{m}$ active edge and (b) $100 \mu\text{m}$ slim edge design before irradiation. The pixel cell has an FE-I4 cell size of $50 \times 250 \mu\text{m}^2$ and the hit efficiency is evaluated as a function of the distance from the last pixel column to the edge region. Smearing of the position of approximately $18 \mu\text{m}$ is due to the telescope resolution.

point of 400 V , a comparison between the three modules at this bias voltage is performed. The CiS4 module reaches a hit efficiency of $97.0 \pm 0.3\%$ and shows the best performance. Within the uncertainties, the SOI3 module with the floating BR reaches the same hit efficiency. The SOI3 module with the grounded BR again shows a 1% lower hit efficiency at the same bias voltage. Hence, no benefit was observed following the implementations of the grounded bias rail running on top of the pixel implant. The hit efficiency results after irradiation are summarised in Table 5.8 for the two highest voltage points at 500 V and 600 V .

5.2.5 Hit efficiency at the sensor edge

Sensors produced by ADVACAM were employed to perform an analysis of the hit efficiency at the periphery of the devices. The modules are investigated before and after irradiation to fluences of $10^{15} \text{ n}_{\text{eq}} \text{ cm}^{-2}$, and $3 \cdot 10^{15} \text{ n}_{\text{eq}} \text{ cm}^{-2}$ for sensor thicknesses of $50 \mu\text{m}$, $100 \mu\text{m}$ and $150 \mu\text{m}$. Not irradiated devices of a sensor thickness of $100 \mu\text{m}$ were studied during a beam test with 5 GeV electrons at DESY. The slim edge design with one BR and common p-t structure and the active edge design with one GR and no p-t structure are both displayed in Figure 5.50.

Furthermore, the achieved efficiencies for the pixel cells within and outside the last column in the two designs are indicated. The plots on the bottom show the efficiency curve within and outside the last pixel column. For the active edge sensor an in-pixel hit efficiency of $99.8 \pm 0.3\%$ and an average hit efficiency of $60.4 \pm 0.4\%$ from the border of the pixel implant up to the sensor edge was achieved before irradiation. The uncertainties given on the edge efficiencies are uncertainties of the mean. The slim edge sensor yields an in-pixel hit efficiency of $99.2 \pm 0.3\%$. Compared to the active edge design, the slim edge design shows an active region only up to the BR, which is $25 \mu\text{m}$ away from the last pixel implant. This behaviour is also visible in Figure 5.51a. Two $150 \mu\text{m}$ thick sensors with active and slim edge implementation were measured in a beam test at CERN-SpS and the

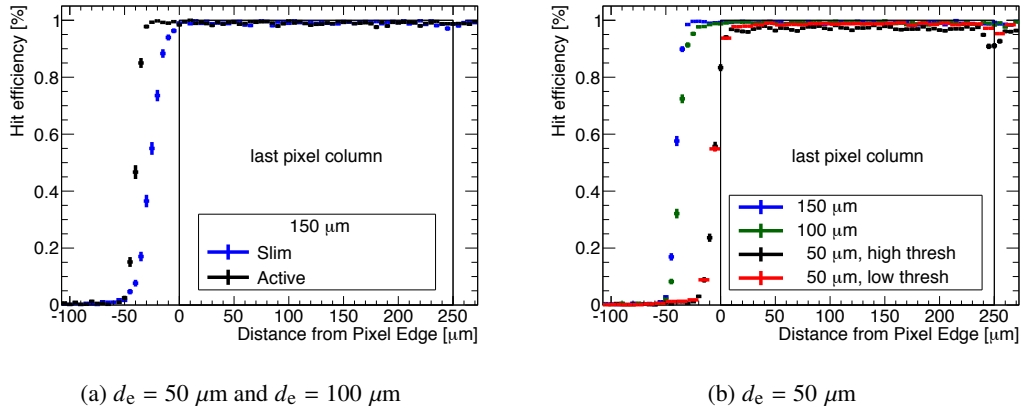


Figure 5.51: Hit efficiency at the edge of the sensor with (a) the active and slim edge design in a $150\ \mu\text{m}$ thick sensor before irradiation and (b) with $50\ \mu\text{m}$, $100\ \mu\text{m}$ and $150\ \mu\text{m}$ thickness, employing a $50\ \mu\text{m}$ active edge design before irradiation. The hit efficiency at the edge of a $50\ \mu\text{m}$ thick sensor is measured with high ($800\ \text{e}$) and low ($380\ \text{e}$) threshold. Smearing of the position of approximately $5\ \mu\text{m}$ is due to the telescope resolution at the CERN-SpS.

results are compared in this graph. The black curve, representing the hit efficiency in the last pixel column up to the edge in an active edge design, shows a highly efficient region up to the $50\ \mu\text{m}$ edge of the sensor. Both, the active and slim edge design with $150\ \mu\text{m}$ thick sensors, show an in-pixel hit efficiency of $99.5 \pm 0.3\%$ and result, within the uncertainties, in the same hit efficiency as the $100\ \mu\text{m}$ thick device.

Figure 5.51b summarises the performance of unirradiated active edge sensors for all three thicknesses from $50\ \mu\text{m}$ to $150\ \mu\text{m}$. A thicker sensor results in a higher overall efficiency and larger active regions up to the edge. The ADVACAM module with the $50\ \mu\text{m}$ thick sensor is analysed in more detail. Results of the module tuned to $800\ \text{e}$, here called high threshold, lead to a rather low overall efficiency of $96.9 \pm 0.3\%$. Charge sharing in between the pixel cells results in an efficiency loss, visible at $x = 250\ \mu\text{m}$ in Figure 5.51. Tuning the chip threshold down to $380\ \text{e}$ increases the efficiency between neighbouring pixels and improves the overall efficiency to $98.7 \pm 0.3\%$. In direct comparison to the thicker sensor, the edge efficiency of a $50\ \mu\text{m}$ thick device is lower, which is in good agreement with previous investigations [145]. The tracking resolution obtained at CERN-SpS in Figure 5.51 is estimated to be $5\ \mu\text{m}$, while the one obtained at DESY is estimated to be $18\ \mu\text{m}$.

The hit efficiency at the edge of an active edge module of $150\ \mu\text{m}$ sensor thickness is analysed after an irradiation to $10^{15}\ \text{n}_{\text{eq}}\ \text{cm}^{-2}$ and $3 \cdot 10^{15}\ \text{n}_{\text{eq}}\ \text{cm}^{-2}$. Both irradiation steps were carried out at the University of Birmingham. The measurements after an irradiation to $10^{15}\ \text{n}_{\text{eq}}\ \text{cm}^{-2}$ were performed at CERN and therefore show a better resolution compared to the measurements after an irradiation to the fluence of $3 \cdot 10^{15}\ \text{n}_{\text{eq}}\ \text{cm}^{-2}$ which were performed at DESY. Due to the lower resolution and lower statistics during the measurements at DESY, a larger bin size was chosen for the results of the hit efficiency.

In both diagrams of Figure 5.52 the hit efficiency in the last pixel column up to the sensor edge is given for different voltages from $100\ \text{V}$ to $250\ \text{V}$. Since a higher saturation voltage is reached after

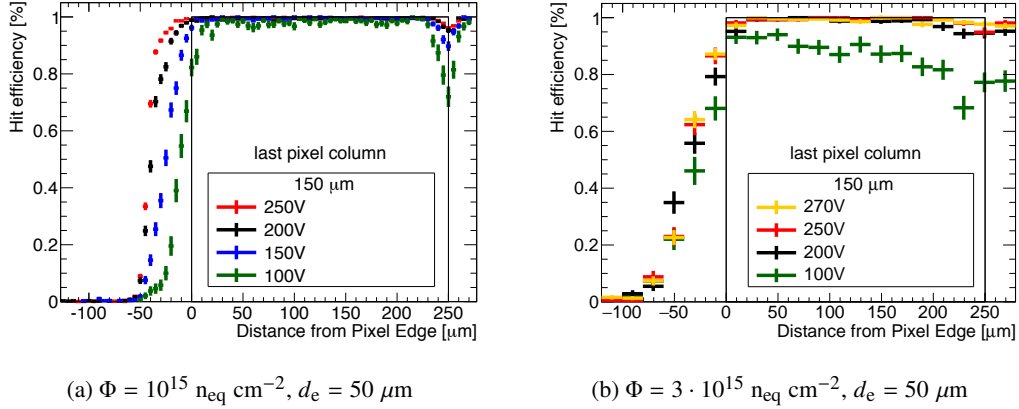


Figure 5.52: Hit efficiency at the edge of a $150 \mu\text{m}$ thick sensor employing a $50 \mu\text{m}$ active edge design after an irradiation to fluences of (a) $10^{15} \text{ n}_{\text{eq}} \text{ cm}^{-2}$ (measured at CERN) and (b) $3 \cdot 10^{15} \text{ n}_{\text{eq}} \text{ cm}^{-2}$ (measured at DESY). The hit efficiency obtained at voltages from 100 V to 250 V, and 270 V for the case of irradiation to the higher fluence of $3 \cdot 10^{15} \text{ n}_{\text{eq}} \text{ cm}^{-2}$, are summarised. A lower resolution at DESY and lower statistics result in larger bin sizes in (b).

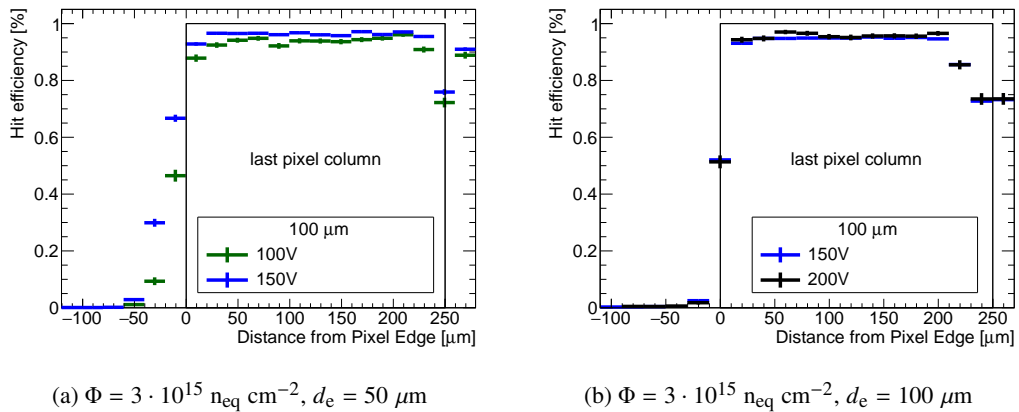


Figure 5.53: Hit efficiency at the edge of two $100 \mu\text{m}$ thick sensors after an irradiation to a fluence of $3 \cdot 10^{15} \text{ n}_{\text{eq}} \text{ cm}^{-2}$, with (a) a $50 \mu\text{m}$ active edge design and with (b) a $100 \mu\text{m}$ slim edge design. The hit efficiency are shown at voltages of (a) 100 V and 150 V, and (b) 150 V and 200 V for the case of the module with the slim edge design. Due to low breakdown voltages, a saturation of the hit efficiency was not achieved.

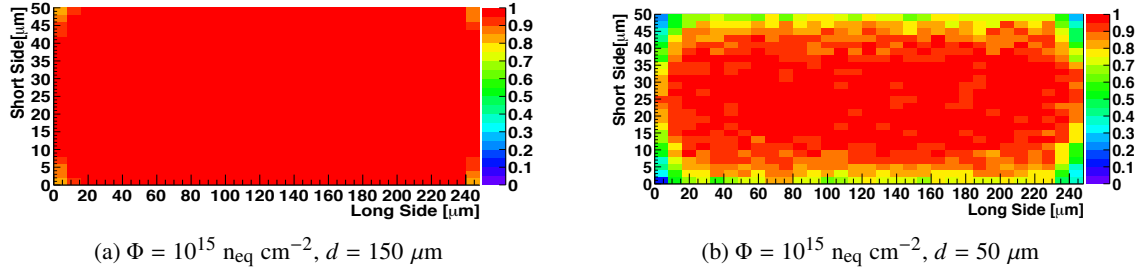


Figure 5.54: In pixel efficiency maps of a $50 \times 250 \mu\text{m}^2$ pixel cell inside an active edge module without p-t structure (a) assembled with a $150 \mu\text{m}$ thick sensor and (b) assembled with a $50 \mu\text{m}$ thick sensor. Both modules are irradiated to a fluence of $10^{15} \text{ n}_{\text{eq}} \text{ cm}^{-2}$ and are biased at (a) 250 V and (b) 120 V after irradiation.

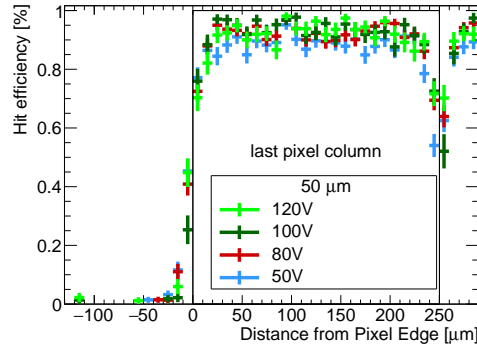


Figure 5.55: Hit efficiency at the edge of a $50 \mu\text{m}$ thick sensor, assembled with a $50 \mu\text{m}$ active edge design after an irradiation to fluences of $10^{15} \text{ n}_{\text{eq}} \text{ cm}^{-2}$, measured at CERN. The results on the hit efficiencies at voltages from 50 V to 120 V are taken from Ref. [146] and summarised. Due to low statistics, the uncertainties on the hit efficiency are larger.

irradiation to higher fluences, the module irradiated to a fluence of $3 \cdot 10^{15} \text{ n}_{\text{eq}} \text{ cm}^{-2}$ is pushed to 270 V to achieve efficiencies as high as possible. An average hit efficiency from the edge of the pixel cell up to the sensor edge of $73.1 \pm 0.8\%$ was obtained at a voltage of 250 V for the active edge module after an irradiation to $10^{15} \text{ n}_{\text{eq}} \text{ cm}^{-2}$ and of $58.1 \pm 2.4\%$ for the one after an irradiation to $3 \cdot 10^{15} \text{ n}_{\text{eq}} \text{ cm}^{-2}$ at a voltage of 270 V. The larger uncertainty on the result in the latter is due to less statistics. Higher voltages were not possible due to a low breakdown voltage of slim and active edge modules.

An example of low efficiencies obtained due to too low voltages applied are shown in Figure 5.53. The active and slim edge device, both $100 \mu\text{m}$ thick, would have needed higher voltages applied to the sensor to reach saturated hit efficiency values after an irradiation to $3 \cdot 10^{15} \text{ n}_{\text{eq}} \text{ cm}^{-2}$. Instead, the modules had a low breakdown voltage and only reached voltages up to 150 V and 200 V. Furthermore, the limited biasing could not overcome the efficiency loss, caused by charge sharing. This is clearly visible in the inefficient regions around the p-t design in the slim edge design and in between the pixel cells in the active edge design.

The in-pixel hit efficiencies of the active edge module with $150 \mu\text{m}$ and $50 \mu\text{m}$ thick sensors are

Table 5.9: Summary of the hit efficiency results of ADVACAM modules with 50 μm 100 μm and 150 μm thick active edge sensors before and after irradiations up to $3 \cdot 10^{15} \text{ n}_{\text{eq}} \text{ cm}^{-2}$. The results on the in-pixel efficiency over the entire module and the edge efficiency are summarised after hit efficiency saturation.

Production	Thickness [μm]	Φ [$10^{15} \text{ n}_{\text{eq}} \text{ cm}^{-2}$]	Hit efficiency [%]	Edge efficiency [%]
ADVACAM	50	0	98.7 ± 0.3	28.6 ± 0.4
	100		99.8 ± 0.3	60.4 ± 0.5
	150		99.5 ± 0.3	78.3 ± 0.8
	50	1	93.2 ± 0.3	26.8 ± 3.3
	150		98.4 ± 0.3	73.1 ± 0.8
	150	3	98.0 ± 0.3	58.1 ± 2.4

displayed in Figure 5.54 after an irradiation to $10^{15} \text{ n}_{\text{eq}} \text{ cm}^{-2}$. As seen from the edge efficiency plots of the module assembled with the 150 μm thick sensor, a good hit efficiency of more than $98.0 \pm 0.3\%$ is achieved. No significant efficiency loss appears thanks to the fact, that no biasing structures were implemented in the active edge design. A slight efficiency loss due to charge sharing is detected in the corners of the pixel cell. The active edge module with the 50 μm thick sensor irradiated to the same fluence of $10^{15} \text{ n}_{\text{eq}} \text{ cm}^{-2}$ and biased at 120 V shows a significantly lower overall in-pixel hit efficiency of $93.2 \pm 0.3\%$.

In Figure 5.55 the distribution of its efficiency over the last pixel implant as well as up to the sensor edge is shown for voltages from 50 V up to 120 V. At all voltage steps, a clear efficiency drop appears between the two neighbouring pixel implants. In this area, an efficiency down to 50% is visible at the lowest voltage of 50 V and is increased to an efficiency of 70% at the highest voltage of 120 V. Before irradiation, the effect of charge sharing decreases the efficiency at the corners of the pixel cell by only 10%, as seen in Figure 5.51b.

The results for all investigated modules are summarised in Table 5.9.

5.2.6 Hit efficiency and charge collection at high pseudorapidity

Especially for the tracking in high pseudorapidity regions (high η), the decrease of pixel size results in an increase of detector occupancy. Therefore, the charge collection and hit efficiency for a cell of $50 \times 50 \mu\text{m}^2$ are investigated in a set-up that reproduces the track inclination in this η region. This technique is known as the grazing angle technique. FE-I4 modules are placed in the beam at DESY and CERN-SpS in such a way, that they allow for particles to cross the pixel along their short side (50 μm) at an angle of $\vartheta = 80^\circ$ ($\eta \approx 2.4$ for the complementary angle). Such measurements are performed with unirradiated modules of 50 μm , 100 μm , 150 μm and 200 μm sensor thicknesses from the CiS, ADCAVAM and VTT productions. The cluster width, the number of pixel crossed by a particle, along η strongly depends on the sensor thickness: thinner sensors lead to smaller clusters and result in a lower pixel occupancy, as shown in Figure 5.56a. In this figure, the cluster width y for sensor thicknesses from 50 μm to 250 μm is calculated for different beam incidence angles

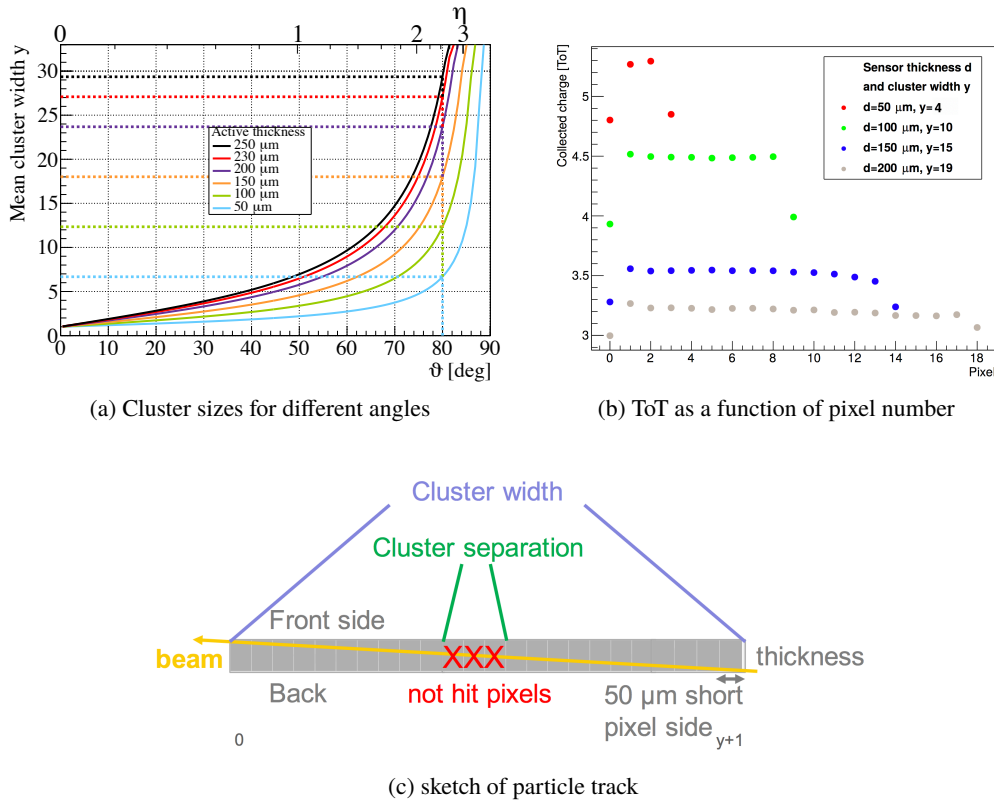


Figure 5.56: (a) expected mean cluster width along the short pixel cell direction (50 μm) in y direction for an FE-I4 module as a function of beam incidence angle. (b) charge collection in units of Time over Threshold (ToT), as a function of pixel number for different cluster widths obtained with unirradiated FE-I4 modules assembled with sensor thicknesses of 50 μm , 100 μm , 150 μm and 200 μm . The statistical uncertainties of the points are smaller than the marker size. (c) exemplary sketch of a particle traversing the sensor with a high incidence angle. The definitions of the properties used in the analysis are illustrated.

from $\vartheta = 0^\circ$ to $\vartheta = 90^\circ$ [37]. At $\vartheta = 80^\circ$ a vertical dashed line is shown for easier reading of the cluster widths for different thicknesses. The colours identify the different thicknesses from light blue (50 μm) to black (250 μm). A 50 μm thick sensor results in a cluster width of around 7 pixels at an angle of $\vartheta = 80^\circ$. For a thickness of 100 μm the cluster width is increased to around 13 pixels and increasing the thickness further to 250 μm results in around 29 pixels. These are crossed at high beam incidence angle.

Given this set-up, there is no possibility to match the tracks reconstructed by the telescope with the hits in the DUT. Therefore, the analysis needs to be performed using only the hit information of the long clusters compatible with the hypothesis of a single particle passing through the sensor.

In Figure 5.56b, the most probable value (MPV) of the ToT distribution for modules with different sensor thicknesses at high incidence angle are summarised. All modules are tuned to a threshold of 1000 e. Pixel number zero always corresponds to the sensor front side and is characterised by a lower charge since it is only partially traversed, as illustrated in Figure 5.56c. An average cluster width of 4 pixels for a 50 μm thick sensor, of 10 pixels for a 100 μm thick sensor (well in agreement with Ref. [37]) and of 15 pixels for a 150 μm thick device is reconstructed. The values are slightly

lower than the values expected, i.e. the values expected for a 150 μm thick sensor would be in the range of 17-18 clusters, which can be traced back to a misplacement of 1-5° of the modules with respect to the nominal position of $\vartheta = 80^\circ$.

The charge is almost constant over the sensor depth for all thicknesses, except for the entrance and exit pixels which are not entirely crossed by the track. The MPV of the collected charge increases from 3.1 ToT for a 200 μm thick sensor to 3.5 ToT for a 150 μm and further to 4.5 ToT for a 100 μm thick sensor. With a 50 μm thick sensor, it is possible to achieve even higher ToT values of 5.3 ToT. The increase of charge in ToT is explained with a reduced effect of charge sharing due to a smaller lateral diffusion of charge carriers in thinner sensors.

In addition to the studies above, investigations on the hit efficiency of $50 \times 50 \mu\text{m}^2$ pixel cells, crossed by particles with high incidence angle, are conducted. The hit efficiency E_{eff} for a single pixel is defined as [37]:

$$E_{\text{eff}} = 1 - \sum_{n_{\text{cluster}}=1}^N \frac{n_{\text{holes}}}{w_{\text{cluster}} - 2} \quad (5.1)$$

with n_{cluster} representing the number of clusters and n_{holes} the number of holes inside a cluster with a width w_{cluster} . Dividing the number of holes within a cluster by w_{cluster} subtracting the first and the last pixels, that are 100% efficient by definition, results in the hit inefficiency E_{ineff} . Hence, the hit efficiency per pixel is obtained from the hit inefficiency by $E_{\text{eff}} = 1 - E_{\text{ineff}}$. As shown in Ref. [37] for a 100 μm thick sensor, the hit efficiency as a function of the number of holes within the cluster width saturates for missing hits in more than three pixels. For a cluster width of 10 pixels, the ratio of cluster width and number of holes is around then 30%. In this thesis, it is found, that a ratio of 50% is suitable to be applied on all investigated sensor thicknesses investigated. Therefore, the hit efficiencies are calculated with the requirement on the allowed number of holes between two hit pixels inside the cluster of 50% of the expected cluster width. The systematic uncertainties arise from the choice of the number of allowed holes for each sensor thickness. They are derived from the fluctuation of hit efficiencies for the number of holes ranging from 3 to the maximum cluster width depending on each sensor thickness. The systematic uncertainties are calculated to be at most 0.5%. Due to high statistics collected, the statistical uncertainties are negligible.

The hit efficiency of an ADVACAM module with a 150 μm thick sensor at high incidence angle at different target threshold is shown in Figure 5.57. The ADVACAM module is tuned to different threshold targets of 600 e, 800 e and 1 ke. The two lower threshold targets are in the range considered routinely achievable by the future RD53A readout chip. By lowering the threshold to 600 e instead of 1 ke, the hit efficiency increases by 2% to $98.0 \pm 0.5\%$.

Furthermore, the grazing angle technique is performed with irradiated modules to make predictions on the hit efficiency of a $50 \times 50 \mu\text{m}^2$ pixel cell at high incidence angle after irradiation. A CiS device assembled with a 200 μm thick sensor is irradiated to $2 \cdot 10^{15} \text{ n}_{\text{eq}} \text{ cm}^{-2}$. The hit efficiencies are shown in Figure 5.58a for voltages from 300 V to 800 V, where an increase of 22% in hit efficiency to an average value of $89.0 \pm 0.5\%$ is achieved. At voltages above saturation of around 400 V, a nearly flat hit efficiency distribution throughout the sensor thickness is seen, whereas at 300 V an increased hit efficiency at the front side of the sensor (lower pixel numbers) is significant. The hit efficiency drops to $38 \pm 0.5\%$ going closer to the backside and then slightly increases again showing

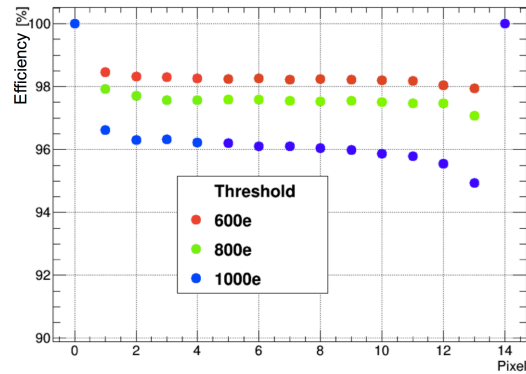


Figure 5.57: Hit efficiency as a function of pixel number at different target thresholds of 600 e, 800 e and 1 ke for an unirradiated FE-I4 module with a sensor thickness of $150 \mu\text{m}$ tilted by 80° with respect to the beam direction. The efficiencies of the first and the last pixels are by construction 100%, since they define the start and the end of the cluster. The uncertainties on the hit efficiency values are included but smaller than the marker size.

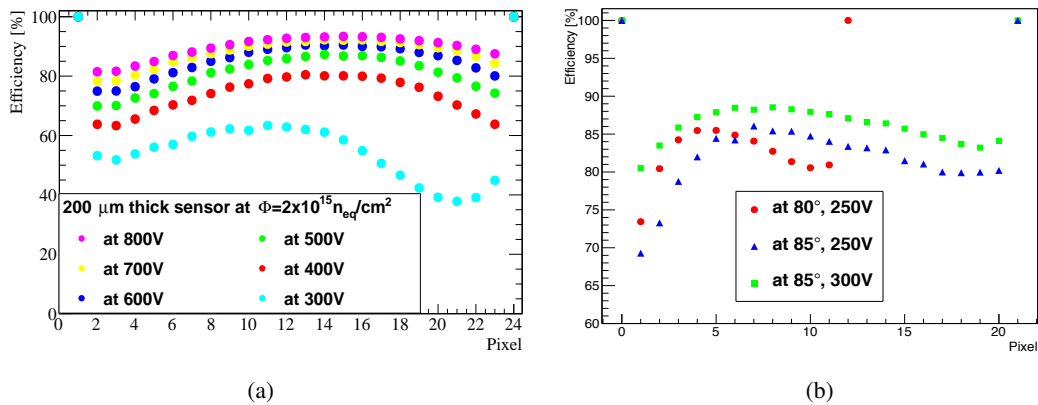


Figure 5.58: Hit efficiencies of (a) a CiS module with a $200 \mu\text{m}$ thick sensor after an irradiation to $2 \cdot 10^{15} \text{ n}_{\text{eq}} \text{ cm}^{-2}$ and (b) an ADVACAM module with a $150 \mu\text{m}$ thick sensor after an irradiation to $10^{15} \text{ n}_{\text{eq}} \text{ cm}^{-2}$ for different high incidence angles. In (b) the hit efficiency scale is zoomed and ranges from 60% to 100%. Both modules are presented at different voltage steps. Low pixel numbers correspond to the sensor front side in both cases. The uncertainties on the hit efficiency values are included but smaller than the marker size.

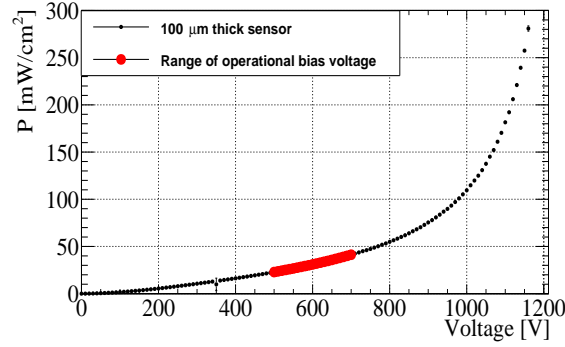


Figure 5.59: Power dissipation as a function of voltage of a 100 μm thick sensor irradiated to a fluence of $10^{16} \text{ n}_{\text{eq}} \text{ cm}^{-2}$. The range of operational bias voltage is marked in red.

an indication of a double peak at the backside of the sensor after irradiation, being in agreement with the TCT results after irradiation in Section 5.2.3.

In Figure 5.58b, at an angle of $\vartheta = 80^\circ$ the ADVACAM module, irradiated to $10^{15} \text{ n}_{\text{eq}} \text{ cm}^{-2}$ and assembled with a sensor thickness of 150 μm , results in a maximal hit efficiency of $85 \pm 0.5\%$ close to the sensor front side, decreasing by 5% towards the sensor backside and then slightly increasing again. Going to a higher incidence angle of $\vartheta = 85^\circ$ ($\eta \approx 3.1$), the maximum hit efficiency stays the same at the same voltage of 250 V applied. The number of pixels crossed increases by 9 pixels at higher incidence angle. Applying a voltage of 300 V increases the hit efficiency to $90.0 \pm 0.5\%$. Due to low breakdown voltage of the ADVACAM modules after irradiation, discussed in Section 5.2.5, higher voltages were not possible to be reached.

5.2.7 Power dissipation

The sensors in the ATLAS pixel detector will be exposed to high irradiation doses during their lifetime. Moreover, the sensors in the ITk will have to cope with an even higher irradiation dose environment in the HL-LHC phase. The radiation induces an increase of sensor leakage current. As high detection efficiency needs to be ensured even after exposure to high irradiation, an increase of the sensor operational bias voltage is essential. However, an increased operational bias voltage results in a further increase of the leakage current. Both parameters result in an increase of the power dissipation P_{diss} during detector operation. The power dissipation density P is described by the quotient of power dissipation and active area A_{active} . With the power dissipation as a product of I and U , P can be written as:

$$P = \frac{I_{\text{leak}} U}{A_{\text{active}}} \quad , \quad (5.2)$$

where P is expressed in units of mW/cm^2 . The total P_{diss} of a module is arising from both the readout chip and the sensor. For ITk pixel modules, P_{diss} is dominated by the readout chip with an expected value of $P = 700 \text{ mW}/\text{cm}^2$ [29, 147]. However, an increased P_{diss} of the sensor results in an increase of temperature and a further increase of the leakage current up to thermal runaway. Therefore, controlled cooling of the detector is crucial for stable operation.

Table 5.10: Power dissipation density of 100 μm and 150 μm thick sensors after irradiation to a fluence of $10^{16} \text{ n}_{\text{eq}} \text{ cm}^{-2}$, given for the expected operational bias voltages at $T = -25^\circ\text{C}$.

Thickness [μm]	Operational U [V]	I_{leak} per area [$\mu\text{A}/\text{cm}^2$]	P [mW/cm^2]	Annealing [days]
100	500-700	46-59	23-41	6-11
150	700-900	86-121	60-110	8

Nevertheless, the modules need to fulfil the requirements and constraints given by the cooling systems. For that, the sensor technologies need to be optimised to ensure low operational bias voltages. At the same time high tracking efficiency after high irradiation needs to be guaranteed. Low operational bias voltages are obtained with thin sensors. With their reduced electrode distance of 100 μm and 150 μm , they ensure less charge trapping from radiation-induced effects.

Results on their power dissipation after an irradiation to the highest fluence of $10^{16} \text{ n}_{\text{eq}} \text{ cm}^{-2}$ are obtained by combining the corresponding hit efficiency results from Section 5.2.4 with leakage current measurements of bare sensors. The leakage current measurements of the bare sensors are performed at a controlled temperature. From the hit efficiency results the range of the operational bias voltage after high irradiation is derived. The operational bias voltages are defined to be adequate, when a hit efficiency of above 97% is obtained, which reflects the requirements dictated by the performance of physics analysis for the ITk [29].

Figure 5.59 shows the power dissipation of the VTT module operated at a temperature of $T = -25^\circ\text{C}$ as a function of the applied bias voltage up to 1200V. The power dissipation is normalised to the active area of an FE-I4 module of 3.4 cm^2 . Finally, the resulting power dissipation for a 100 μm thick sensor operated at voltages of 500 V to 700 V is determined to be 23 mW/cm^2 to mW/cm^2 .

These low values make the thin n^+ -in-p planar pixel sensor technology an ideal candidate for use in the innermost layers, most probably foreseen to instrument L_1 and L_2 of the ITk [29], up to the end of lifetime of the HL-LHC. The power dissipation densities for 100 μm and 150 μm thick sensors after an irradiation to a fluence of $10^{16} \text{ n}_{\text{eq}} \text{ cm}^{-2}$ are summarised in Table 5.10. Compared to the operational bias voltage range of the 100 μm , the 150 μm thick sensor requires a higher operational bias voltage range from 700 V to 900 V, resulting in higher leakage currents of 86-121 μA . With respect to the 100 μm thick sensor, this is an increase in leakage current by a factor of 2. The resulting power dissipation density is found to be in the range between 60 mW/cm^2 to 110 mW/cm^2 . These results do not meet the restrictions imposed on the power dissipation in the regime of high irradiation. In the regime of lower irradiation, expected in the layers from L_2 onward, 150 μm thick sensors are foreseen to instrument these layers.

CONCLUSIONS AND OUTLOOK

The inner detector of the ATLAS experiment plays a fundamental role in the identification of charged particles and reconstruction of their tracks. Especially the innermost element, the pixel detector, will be challenged by increasing track densities and greater radiation damage during data taking at HL-LHC.

Pixel modules based on the thin n^+ -in-p planar pixel sensor technology were presented to address the issues of high occupancy and radiation damage. Thin sensors are crucial to ensure radiation hardness, smaller pixel cell sizes are essential to guarantee low occupancy, while a sensor periphery with reduced inactive areas is implemented to maximise the sensitive sensor area very important in a region closer to the interaction zone.

For the investigation of the performance of thin n^+ -in-p planar pixel modules at realistic operation conditions, comprehensive characterisations at sensor as well as at module level of different prototypes were performed. Their performance before and after high irradiation to fluences up to $10^{16} \text{ n}_{\text{eq}} \text{ cm}^{-2}$ was studied in terms of charge collection and hit efficiency with high energy particle beams and in terms of charge collection and electric field distributions using the transient current technique. The focus was mainly on the investigation of $100 \mu\text{m}$ and $150 \mu\text{m}$ thick sensors and the results were compared to the ones previously obtained in Refs. [37, 53].

The radiation hardness of FE-I4 planar pixel modules with sensor thicknesses ranging from $50 \mu\text{m}$ to $270 \mu\text{m}$ thickness was examined. It was demonstrated, that the $100 \mu\text{m}$ thick sensors are able to sustain an irradiation fluence of $10^{16} \text{ n}_{\text{eq}} \text{ cm}^{-2}$ with a hit efficiency of $97.4 \pm 0.3\%$ already starting from a voltage of 500 V . With moderate operational bias voltages of 500 V to 700 V , the resulting power dissipation per sensor is in the range of $25\text{-}50 \text{ mW/cm}^2$. The modules with the $150 \mu\text{m}$ thick sensors were shown to reach a hit efficiency of $97.0 \pm 0.3\%$, but at higher bias voltage around 900 V . For both types of modules, the main efficiency loss appears in the areas of the pixel cell, where the biasing structures are implemented. To improve the hit efficiency especially after irradiation, sensors were designed and characterised with a combination of the best performing biasing structures, investigated previously in Ref. [37]: an external bias dot and a bias rail superimposed to the pixel implant. An alternative biasing scheme was implemented to keep the bias ring floating.

After an irradiation to a fluence of $5 \cdot 10^{15} \text{ n}_{\text{eq}} \text{ cm}^{-2}$ the module with a $100 \mu\text{m}$ thick sensor and a floating bias rail superimposed to the pixel implant was observed to reach a hit efficiency of

$97.5 \pm 0.3\%$ at 600 V. The hit efficiency is increased by 1.0% compared to the same module type but employing a grounded bias rail. However, the hit efficiency is still affected by the implementation of a biasing structure.

A possible alternative option, that is being explored, is the modification of the production process with the addition of a temporary metal. This would allow for the measurements of the sensor leakage current by shorting all pixels. This additional layer is removed after the device characterisation before further processing.

The charge collection and electric field properties obtained by transient current measurements were shown to support the test beam measurements for 100 μm and 150 μm thick sensors. Due to a shorter distance between sensor front and backside, a higher electric field is established in 100 μm thick sensors, resulting in a reduced probability of charge trapping. Furthermore, thin sensors show an earlier signal saturation at lower bias voltage. A more homogenous distribution of the charge collection and electric field within the sensor depth was found for the 100 μm thick sensors before and after high irradiation. In contrast, in thicker sensors, the maximum charge and the highest electric field were reached at the sensor front side before and after high irradiation.

In addition, a double peak structure after irradiation to fluences of $5 \cdot 10^{15} \text{ n}_{\text{eq}} \text{ cm}^{-2}$ and $10^{16} \text{ n}_{\text{eq}} \text{ cm}^{-2}$ with two local maxima close to the sensor front and backside was observed for the 150 μm thick sensor at moderate voltages. This finding is in agreement with high incidence angle measurements, where the high energy particle beam traverses the sensor depth while passing through many pixels. An increase of the hit efficiency was found at the backside of a 200 μm thick sensor irradiated to a fluence of $2 \cdot 10^{15} \text{ n}_{\text{eq}} \text{ cm}^{-2}$.

In these measurements, it was also demonstrated, that thinner sensors are also beneficial in terms of low occupancy at high incidence angles, especially for the innermost layers, where a higher track density is expected. In unirradiated 100 μm thick sensors clusters as long as 10 pixel cells are measured at a track angle of 80° compared to 15 cells for 150 μm thick sensors.

Due to the excellent performance in terms of hit efficiency and power dissipation, 100 μm thick sensors are foreseen to instrument the second innermost layer of the ITk, while 150 μm thick sensors are foreseen to instrument the remaining layers. Due to an even lower power dissipation arising from the smaller collection electrode distance, 3D sensors are the baseline technology to instrument the innermost layer.

The future ATLAS ITk chip will implement a smaller pixel cell size of $50 \times 50 \mu\text{m}^2$ to cope with the higher track density. To investigate the performance of small pixel cells before and after irradiation, even without the availability of the future readout chip, a sensor design with $50 \times 50 \mu\text{m}^2$ pixel cells compatible to the FE-I4 readout chip was developed and investigated. A hit efficiency of $98.2 \pm 0.3\%$ at 500 V for a module with a 150 μm thick sensor, irradiated to a fluence of $3 \cdot 10^{15} \text{ n}_{\text{eq}} \text{ cm}^{-2}$ and of $97.5 \pm 0.3\%$ at 600 V for a module with a 100 μm thick sensor, irradiated to $5 \cdot 10^{15} \text{ n}_{\text{eq}} \text{ cm}^{-2}$ was reached for a $50 \times 50 \mu\text{m}^2$ pixel cell. These results are obtained with a pixel cell without any biasing structure implemented.

For systematic evaluation of the performance of $50 \times 50 \mu\text{m}^2$ and alternative $25 \times 100 \mu\text{m}^2$ pixel cells, future measurements need to be carried out with modules assembled with the RD53A readout chip

and compatible sensors. At the point of writing, the RD53A modules have just been received by the ITk groups and the first characterisation is under way.

For the investigation of the feasibility of reducing the inactive area at the sensor periphery, devices produced with the active edge technology were characterised before and after irradiation. The implantation of Boron ions on the sides allows to extend the backside p^+ layer in this region. In this way the depleted volume reaches the edges, while the guard ring structure is omitted or strongly reduced.

In particular, an active edge design, with a pixel distance of $d_e = 50 \mu\text{m}$ was studied, together with a slim edge design with one bias ring and $100 \mu\text{m}$ distance between the last pixel implant and the sensor edge. Modules with sensor thicknesses of $50 \mu\text{m}$, $100 \mu\text{m}$ and $150 \mu\text{m}$ were investigated in terms of their hit efficiency. For the active edge module assembled with a $150 \mu\text{m}$ thick sensor an average edge efficiency in the region between last pixel column and sensor edge of $78.3 \pm 0.8\%$ was achieved. Due to the effect of charge sharing in between the pixel implants, the module with $50 \mu\text{m}$ thick sensor showed an in-pixel hit efficiency of $98.7 \pm 0.3\%$ over the entire sensor, which was 0.8% lower, when compared to thicker sensors before irradiation. After irradiation to a fluence of $10^{15} \text{ n}_{\text{eq}} \text{ cm}^{-2}$, the effect on charge sharing was increased and lead to a decreased hit efficiency of the edge pixel cell of $93.2 \pm 0.3\%$ at a voltage of 120 V in the case of the module with the $50 \mu\text{m}$ thick sensor and $98.0 \pm 0.3\%$ at a voltage of 270 V in the case of the module with the $150 \mu\text{m}$ thick sensor. Many results presented in this thesis were included in the ATLAS Pixel Technical Design Report and were used, together with other studies, as basis of the choice of the baseline sensor technologies in the different pixel layers.

ACKNOWLEDGEMENTS

These last pages are dedicated to all the people, who contributed with their support and efforts to the successful finalisation of this work. It is therefore my greatest pleasure to offer my sincere gratitude to them all.

Foremost, I would like to express my deepest gratitude to my supervisor Richard Nisius who gave me the opportunity to conduct my work in his research group at MPP and accompanied and supported me along all the way. Thank you, Richard, for the knowledgeable advice, all valuable comments and challenging questions during (I counted 18!) rehearsals and all the many conferences you let me participate in. Every single bit contributed to my professional scientific and personal growth.

Anna, my-day-to-day-supervisor, my coach and my restaurant-advisor. From sharing your great knowledge on silicon detector, helping me in the organisation throughout my PhD, pushing me to my limits to get the most of my work within the three years, hard working together during 13 (!) testbeams up to proof-reading through every single page of my thesis multiple times... I could never be grateful enough to Anna Macchiolo. Your door was always open and your laptop and phone always on- during day, night and weekend. Most of this work would not have been possible without your experience and human support. Grazie, Anna.

I would like to convey my warmest gratitude to the colleagues from the ATLAS-SCT group and the MPP, especially to Stefano Terzo, my mentor in the very beginning of my PhD, Andreas Maier, who was always willing to help me, Ben Pearson, Tom McCarthy and Tim Brunst, who were proof-reading parts of my thesis and finally, but by no means least Julien Beyer. Julien, keinen einzigen Tag am MPP oder Testbeam mit Dir möchte ich missen, und ich freue mich, dass ich Deine Teamkollegin und nun gute Freundin sein darf. Furthermore, I want to thank all other students and interns who worked with me and supported the group and myself with valuable contributions to measurements.

Ohne die fleißige Arbeit der MPP-Werkstattler, vor allem Carina Schlammer, Christoph Knust und Enrico Töpfer, wären nie so viele Module geklebt und gebondet worden, deren Ergebnisse ich nun in meiner Arbeit zusammenfassen konnte. Für die große Unterstützung bei langwierigen Installationen der Track-Rekonstruktionsprogramme danke ich Dir, Arthur Erhardt, von Herzen. Auch möchte ich ein großes Dankeschön an meinen "External Supervisor" Frank Simon ausrichten. Danke für Deine wertvollen Kommentare während meiner APS-Meetings und das Korrekturlesen eines Teiles meiner Doktorarbeit.

A very special gratitude goes to the members of the ITk group and RD50 collaboration. I would like to thank the testbeam team and its organisers and the EUTelescope developers, especially I am grateful to Andre Rummler, who was always on the scene to support during testbeam campaigns. For all the discussions on testbeam reconstruction and the girls time at CERN and LPNHE in Paris, I am very thankful to Audrey Ducourthial.

My sincere thanks go to the CERN-crew, I had the chance working and socialising with during my

stay at CERN. With a special mention to the 007-office, Alessandro La Rosa and Markus Lippert. None of the modules could have been irradiated without the help of Igor Mandić and Vlado Cindro at JSI, Laura Gonella at UoB, Frederico Ravotti at CERN and Alexander Dierlamm at KIT.

Not only for the irradiation I am thankful to you Igor, but also for the opportunity you and Gregor Kramberger gave me to perform edge-TCT measurements at JSI in Ljubljana. Za mene je bilo nešto posebno raditi sa Vama i diskutirati o fizici na hrvatskom jeziku. Vrijeme provedno kod Vas u Ljubljani neću nikada zaboraviti. Bili ste jako ljubazni prema meni i odmah ste me primili kao Vašu kolegicu. Od srca Vam se zahvaljujem. Posebno sam zahvalna Igoru za njegovu pomoć u svakom slučaju. Und auch Dir, Bojan Hiti, möchte ich für Deine große Unterstützung bei der Einführung in die TCT-Welt danken.

Die allerletzten Worte möchte ich meiner Familie widmen: meinen Eltern und meinem kleinen Bruder. Ohne Eure Unterstützung von der Zeit an, als ich mich für das Physikstudium entschied, hätte ich nun diese letzte Seite meiner Doktorarbeit nicht schreiben können. Ihr drei habt mir immer den nötigen Rückhalt gegeben. Und nun zu Dir, moj Fran. Mein Dank an Dich ist schwer in Worte zu fassen. Du bist meine Stütze und mein Retter in jeder Lebenslage und standest mir vom allerersten Tag dieser Arbeit mit Rat und Tat zur Seite. Ich danke Dir auch für das Tolerieren der 30 Reisen und 174 Tage, die ich nicht zu Hause war, während meiner Promotion. Und für Deine unfassbare Unterstützung besonders in der letzten Zeit der Schreibphase und das akribische Durchlesen großer Teile meiner Arbeit bin ich Dir unendlich dankbar. Hvala.

Natascha Savić
München im Dezember 2017

LIST OF FIGURES

1.1	The LHC accelerator complex is composed of the LHC shown in black and smaller accelerators, which help boost the particles to their final energies. The image is taken from Ref. [7].	4
1.2	(a) peak instantaneous luminosity expressed in $10^{33} \text{cm}^{-2} \text{s}^{-1}$ at a center-of-mass energy of 13 TeV shown for the second half of 2017. (b) delivered integrated luminosity expressed in fb^{-1} as a function of time from the year 2011 up to now, year 2017, for the proton-proton collisions. The luminosity is obtained using counting rates evaluated by the luminosity detectors. Both figures show the luminosities, delivered to the ATLAS detector. The images are taken from Ref. [9].	5
1.3	The cross section of the ATLAS Experiment with the Inner Detector, Calorimeter and the Muon Spectrometer (from inner to outer region). The images is taken from Ref. [16].	7
1.4	The LHC schedule for the upcoming high luminosity decade. The schedule plan starts from year 2011 and shows the energy of the collision in the upper red lines and the luminosity in the lower green lines. The first long shutdown (LS1) took place in 2013-2014, where the accelerator complex was upgraded to reach higher beam energies above 8 TeV (center-of-mass energy before LS1) and luminosities. The second long shutdown (LS2) is foreseen for 2019-2020, in which the luminosity will be consolidated und the LHC injectors and detectors will be upgraded. From 2026, after the third long shutdown (LS3) the LHC will be operated in the high luminosity configuration and will be named the HL-LHC from then on.	10
1.5	Schematic layout of the ITk of ATLAS for the HL-LHC phase, as presented in Ref. [2, 29]. The horizontal axis is parallel to the beam line, while the vertical axis represents the radial distance from the center of the detector, placed at point (0,0) in the figure. Only the active detector elements of the first quadrant are shown.	12
2.1	Schematics of the energy levels in p-type (left) and n-type (center) silicon. The valence band is shown in green colour, while the conduction band is shown in orange. With the introduction of donor electrons, the accompanied energy level E_D is created, while for the introduction of acceptor electrons E_A is created. Combining the differently doped segments results in a p-n junction with a balanced Fermi level in between the two segments. The sketch is taken from Ref. [33].	15
2.2	(a) depiction zone inside a silicon sensor with p-type bulk and (b) charge generation within the depleted bulk, taken from Ref. [34].	16
2.3	(a) example of the most probable energy loss of 500 MeV pions in silicon detectors of different sensor thicknesses. The width w is the full width at half maximum. The figure is taken from Ref. [36]. (b) the MPV of electron-hole pairs generated by particles of different energies as a function of the sensor thickness. The energies of the particles are given. The curves for electrons of 6 GeV and pions of 120 GeV, drawn in the same colour, coincide. The sensor thicknesses, shown as vertical lines, are highlighted with different colours, where in the scope of this thesis, the investigations are mainly focused on 100 μm and 150 μm thick sensors. The figure is taken from Ref. [37].	18
2.4	Charge carrier mobility shown as a function of the electric field. Figure taken from Ref. [30].	20
2.5	Depletion voltage of an n-type 300 μm thick sensor as a function of absolute effective doping concentration and irradiation fluence. Figure taken from Ref. [47].	21

2.6	Variation of the effective doping concentration $ N_{\text{eff}} $ as a function of time after annealing at 60°C. Figure taken from Ref. [51].	23
2.7	Schematic view of a pixel cell in a hybrid pixel detector. This detector is composed of a sensor and a readout chip interconnected via a bump ball in between the under bump metallisations on chip and sensor side. The figure is taken from Ref. [30].	24
2.8	(a) n^+ -in-n sensor design with an n-type bulk and n^+ implants. The guard rings are situated on the backside. (b) n^+ -in-p sensor design with a p-type bulk and n^+ implants. Images taken from Ref. [53].	26
2.9	Layout of a pixel sensor: (a) cut-out of a sensor corner with GRs in the periphery of the active area of the sensor, (b) cut-out of four pixels from the active area of the sensor. A bias rail runs in between the short side of the pixels. It is situated on the same side as the bias dots, implemented either in an opening of the pixel implant (as shown in the figure) or in close proximity. Such design is called standard single punch-through design. On the other side of the pixel cell the bump pad for the interconnection to the readout channels is located. Images taken from Ref. [37].	27
3.1	(a) (top) the current ATLAS pixel detector with its four layers and (bottom) the radial position of each layer. (b) (top) the IBL detector housing 14 staves depicted as a 3D schematic and (bottom) a sketch of the top-view of one IBL stave with the location of the two different module types. In the 3D schematic some staves are removed for a better visibility of the inner part of IBL. The images are adapted from Ref. [59].	30
3.2	Schematic diagram of the FE-I4 pixel analog circuitry [66].	31
3.3	The present ATLAS module displaying a sensor in the thickness range from 200 μm (FE-I4 sensor) to 250 μm (FE-I3 sensor). Figure taken from Ref. [67].	32
3.4	(top) the current ATLAS sensor design and (bottom) the IBL sensor design, adapted from Ref. [66]. The front side and the guard rings on the backside of the sensor are superimposed.	33
3.5	The two sensor technologies: (a) planar n^+ -in-n and (b) 3D n^+ -in-p sensors. The n^+ electrodes are illustrated in green, while the p^+ electrodes are coloured red. In the IBL, the charge collection distance d_c is 200 μm for the planar sensors and 67 μm for the 3D sensors. Images taken from Ref. [37].	34
3.6	Schematics of the two 3D sensor options presently operational in the ATLAS IBL. The 3D sensor (a) with columns, etched partially through the bulk (CNM design) and (b) with full-through columns (FBK design). Both sensors are processed double-sided. The 3D sensor designs are taken from Ref. [66].	35
3.7	A possible schematic layout of the pixel detector for Phase II taken from Ref. [29]. It represents the inclined layout with a pseudo-rapidity coverage up to $\eta = 4 $. The horizontal axis is parallel to the beam line, while the vertical axis is the radius from the the beam line at $R = 0$ in the diagram. Only the active detector elements of the first quadrant are shown.	36
4.1	Photographs of the mountings of modules during irradiation at KIT. At KIT the modules are placed on an aluminium plate which is inserted into a cooling box. The modules are shielded by aluminium with an opening of 2x2 cm^2 in the sensor area. A maximum number of two devices are placed behind each other.	40
4.2	Photographs of the mountings of modules during irradiation at CERN-PS. At CERN multiple modules (in case of the shown irradiation in August 2015 there are two modules) are placed on a plastic frame behind each other fixed with plastic pins. The PCB does not have to be shielded, since the beam does not cover an area larger than 2x2 cm^2	41
4.3	Measurements of the Beam Profile Monitor (BPM) at CERN-PS during irradiation for a module on August 4th in 2015. The sum of all voltages in the X and Y projections of the Gaussian beam profile is proportional to the integral of the proton spill. The integral of all readout channels corresponds to the beam intensity. The blue Gaussian is the beam shape at the focus position with a FWHM of 20.6x13.6 mm^2 , while the red line represents the last proton spill monitored. The beam profile in x is given in (a) and in y in (b).	42
4.4	(a) the probe station and (b) the sensor inside the probe station placed at the center of the chuck with the HV-needle in contact with the sensor.	43

4.5	The Edge-TCT set-up from <i>Particulars</i> [88]: (a) schematics of the experimental set-up taken from Ref. [89] and (b) detector side view with an illustration of the laser beam penetrating at the detector edge.	44
4.6	Placement of the sensor on the PCB via a manual component placement station [90] shown in (a) as a larger view and (b) as a zoom-in shortly before placing the sensor onto the PCB.	45
4.7	Photographs of the Edge-TCT set-up: (a) general view of the instrumentation, (b) placement of the detector with the laser beam pointing at its edge, (c) mounting of the device on a copper support and placement inside an aluminium frame with a connector for biasing and readout and (d) a microscope image of the sensor front side with one single pixel connected to readout via a wirebond.	45
4.8	Induced current pulse at a position of 50 μm inside the sensor depth for a sensor with a thickness of 100 μm before irradiation. In the pulse shape, at increasing times, a peak, an undershoot and a tail is observed.	46
4.9	(a) collected charge (integrated current pulse over time) as a function of depth for a bias voltage of 100 V. The red lines indicate the sensor depth with front (lower depth numbers) and sensor backside. (b) charge carrier drift velocity profile calculated from the signal amplitude. Both measurements are performed using a not irradiated 100 μm thick sensor.	47
4.10	Typical case of focus finding. The sketch shows a sensor with the pixel implants as blue squares. The red area corresponds to the shape of the laser beam and the arrows represent the scanning axis in y and z.	48
4.11	(a) error functions fitted to charge collection profiles of a 100 μm thick sensor before irradiation for different distances of $z= 7200\mu\text{m}$ (corresponding to Fit 144) to $z= 7450\mu\text{m}$ (corresponding to Fit 149) between device and laser output. (b) example of a FWHM of the beam as a function of different positions of the optical axis (z axis) is shown.	49
4.12	The single chip cards for FE-I4B readout chips. The PCBs are designed at the University of Bonn and the University of Glasgow.	50
4.13	The USBPix2 DAQ system with a configuration for single chip FE-I4 cards shown in (a). It is composed of a Multi-IO board, an Adapter Card connected to a single chip FE-I4. The image is taken from Ref. [37]. In (b) the Multi-IO board is connected to a "Burn-in-card" (BiC) to read out four chips at the same time. In (c) the USBPix3 DAQ system with the MMC3 board is shown, taken from Ref. [97].	52
4.14	The RCE DAQ system. The HSIO module (left) is connected to the adapter card (right), which is dedicated to FE-I4 modules. The adapter card provides 16 ethernet connections to operate maximum 16 FE-I4 modules (or 4 four-chip modules) at the same time.	52
4.15	Preamplifier signal shapes depending on different values of injected charge, threshold and feedback current [99].	54
4.16	An example of a typical outcome of a threshold measurement of a single pixel cell, the so-called S-Curve. The Figure is adapted from Ref. [100].	54
4.17	Setup to measure the collected charge in sensors. In a three-stage mechanical structure made of plastic the DUT is placed in between a source, which emits the particles, and a scintillator for triggering the readout. Figure taken from Ref. [37].	56
4.18	Schematic view of the generation of the test beam from the primary DESY-II beam. Bremsstrahlung is generated in a carbon fiber and converted into electron and positron pairs in a Cu or Al target. With the spectrometer dipole magnet a selection of the energy and type of the particles is possible. Subsequently, the final beam is collimated and delivered to the beam lines. The schematics are adapted from Ref. [107].	58
4.19	(a) MPP and (b) Dortmund cooling box [109]. The cooling box, manufactured by MPP, is situated at CERN, while the Dortmund cooling box is used at CERN and DESY.	59
4.20	Residual distribution of an FE-I4 module with a $50\times 250 \mu\text{m}^2$ pixel cell (a) in the long pixel side direction x and (b) in the short pixel side direction y. Beam test measurements performed at CERN with a perpendicular beam incidence.	63

5.1	Guard ring layout with 10 GRs and one BR with a total edge distance of $d_e = 450 \mu\text{m}$ as implemented in the FE-I4 compatible structures. (a) the FE-I4 $50 \times 250 \mu\text{m}^2$ pixel cell and p-t design, and (b) the modified design with a $25 \times 500 \mu\text{m}^2$ pixel cell and the common p-t established in the CiS3 production. In (b), a zoom-in of the region around the bias dot is displayed on top.	66
5.2	(a) production process flow at CiS technology, taken from Ref. [133], and (b) thickness fluctuations within one wafer.	67
5.3	A modified $50 \times 250 \mu\text{m}^2$ pixel cell composed by five $30 \times 30 \mu\text{m}^2$ pixel implants with a $50 \times 50 \mu\text{m}^2$ pixel cell is shown. The small implants are connected by metal lines allowing for a readout by the FE-I4 chip: (a) (bottom) compared to an FE-I4 pixel cell and (b) cut-out of the sensor layout where the implementation of the line and wave designs is shown.	68
5.4	Sketch of the MPP/HLL process [136].	69
5.5	(a) novel pixel design of $50 \times 50 \mu\text{m}^2$ and $25 \times 100 \mu\text{m}^2$ pixel cells combining the common p-t design with the new arrangement of the bias rail being superimposed to the pixel implant as much as possible. (b) images of the $50 \times 50 \mu\text{m}^2$ and $25 \times 100 \mu\text{m}^2$ pixel cells.	69
5.6	Two different sensor types: the standard design with the grounded BR (on the left) and the modified design (on the right) with the floating BR for FE-I4 compatible sensors with a pixel cell size of $50 \times 250 \mu\text{m}^2$. The two brown circles on the horizontal section of the BR in the left figure show the positions of the passivation openings to connect the BR to the chip.	70
5.7	Depiction of the DRIE process in silicon structures, taken from Ref. [67]. The three main steps of the DRIE technique conducted on a wafer are: 1. coating with photoresist, 2. etching of the trenches with SF_6 , 3. passivation with C_4F_8	71
5.8	Schematic view of the sensor processing at ADVACAM, where four-quadrant Boron implantation in the trenches is used.	71
5.9	Four different sensor types of the ADVACAM SOI production: the active edge design with $d_e = 50 \mu\text{m}$, one GR and no p-t structure (top left), the slim edge design with $d_e = 100 \mu\text{m}$, one grounded BR and the common p-t structure (top right), the slim edge design with one BR and GR and the single p-t design (bottom left) and the slim edge design with only one BR and the single p-t structure (bottom right).	72
5.10	Leakage current as a function of bias voltage before irradiation (a-c) for bare sensors from the SOI3 production with different edge designs and (d) after interconnection to readout chips. Results of sensor thicknesses of $100 \mu\text{m}$ (always darker color) and $150 \mu\text{m}$ are shown. Currents for bare sensors were measured at 20°C on a cooled chuck, whereas for assemblies the local temperature is not perfectly determined.	76
5.11	Leakage current as a function of bias voltage before irradiation (a) for bare sensors from the CiS4 production with thicknesses of $100 \mu\text{m}$ and $150 \mu\text{m}$ and (b) after interconnection to readout chips.	77
5.12	Properties of FE-I4 pixel modules from the ADVACAM production with sensors of $50 \mu\text{m}$, $100 \mu\text{m}$ and $150 \mu\text{m}$ thickness in terms of leakage current as a function of bias voltage (a) before and (b) after irradiation to a fluence of $10^{15} \text{ n}_{\text{eq}} \text{ cm}^{-2}$ of a module with a $50 \mu\text{m}$ thick sensor and $d_e = 50 \mu\text{m}$. The measurements in (a) were performed at a temperature of 20°C , while the one for the irradiated module in (b) was performed at around -50°C . For some modules the measurements were stopped shortly before the breakdown to avoid sparks between the sensor and chip.	77
5.13	Leakage currents of CiS4 and SOI3 sensors as a function of bias voltage after irradiation. (a) the breakdown voltages of the $100 \mu\text{m}$ thick CiS4 sensors after an irradiation to a fluence of $10^{16} \text{ n}_{\text{eq}} \text{ cm}^{-2}$ are $600\text{-}700 \text{ V}$. (b) for both SOI3 sensors with an edge distance of $d_e = 300 \mu\text{m}$ the breakdown voltages are around 600 V after an irradiation to fluences of $2 \cdot 10^{15} \text{ n}_{\text{eq}} \text{ cm}^{-2}$ and $3 \cdot 10^{15} \text{ n}_{\text{eq}} \text{ cm}^{-2}$. The IV curve for the sensor with the largest edge was stopped before breakdown, which is expected to be shortly after 600 V . The scales in leakage currents are different with respect to each other.	78

5.14	Leakage current as a function of bias voltage of the RD53 sensors from the SOI3 production. Sensors with a thicknesses of 100 μm and 150 μm and with pixel cells of (a) 50 \times 50 μm^2 and (b) 25 \times 100 μm^2 are summarised before irradiation. The sensors with the 25 \times 100 μm^2 pixel cells show higher breakdown voltages compared to the sensors with the 50 \times 50 μm^2 pixel cells before irradiation. (c) sensors with 100 μm thickness and a pixel cell of 50 \times 50 μm^2 are shown after irradiations to fluences of 5 \cdot 10 ¹⁵ n _{eq} cm ⁻² and 10 ¹⁶ n _{eq} cm ⁻² . After irradiation, the RD53 sensors can be biased up to 1000 V.	79
5.15	(a) collected charge as a function of bias voltage of FE-I4 pixel modules from the ADVACAM production with sensors of 50 μm , 100 μm and 150 μm thickness, measured in ⁹⁰ Sr source scans. (b) comparison of the collected charge of an ADVACAM module with a 50 μm thick sensor irradiated to 10 ¹⁵ n _{eq} cm ⁻² . The results were obtained with source scan measurements and particle beams. Where not visible, the statistical uncertainties in (b) are smaller than the marker size.	80
5.16	In-pixel charge collection map in ToT of 150 μm sensors with an FE-I4 pixel cell design of 50 \times 250 μm^2 with (a) a sensor by CiS with a common p-t structure and (b) a sensor from ADVACAM with no punch-through implementation. Four pixel cells are displayed with the bias dot in the center of the map in (a). The voltage applied on the sensors is 50 V.	81
5.17	In-pixel charge collection map in ToT of 150 μm sensors (a,b) before and (c,d) after an irradiation to a fluence of 3 \cdot 10 ¹⁵ n _{eq} cm ⁻² . 4 pixel cells are displayed with the bias dot in the center of the map. The line design is displayed in (a,c), the wave design is in (b,d). The charge collection map before irradiation is shown for the module biased at 50 V and a tuning of 7 ToT at 14 ke. The charge collection map of the irradiated module is displayed at a bias voltage of 500 V. From the tuning of the module 10 ToT correspond to 6 ke. Both modules were operated at full depletion.	83
5.18	In-pixel charge collection map in ToT of a 100 μm thick sensor before and after irradiation to a fluence of 5 \cdot 10 ¹⁵ n _{eq} cm ⁻² . The unirradiated module is biased with 60 V, the irradiated one with 600 V. 4 pixel cells are displayed with the bias dot in the center of the map. The line design is displayed in (a) before irradiation and (c) after irradiation, the wave design is displayed in (b) before irradiation and (d) after irradiation. From the tuning of the module 6 ToT corresponds to 6 ke before irradiation and 8 ToT correspond to 4 ke after irradiation.	84
5.19	Comparison of normalised collected charge as a function of bias voltage (a) of CiS4 and ADVACAM modules with 150 μm thick sensors after an irradiation to a fluence of 3 \cdot 10 ¹⁵ n _{eq} cm ⁻² and (b) of CiS4 and SOI3 modules with 100 μm thick sensors after an irradiation to a fluence of 5 \cdot 10 ¹⁵ n _{eq} cm ⁻² . Where not visible, the statistical uncertainties are smaller than the marker size.	85
5.20	Induced current pulse shape of a 150 μm thick sensor before irradiation. The sensor is biased at 120 V and thus is operated at over depletion. The signal is shown for different injection depths inside the sensor in a time interval of 10 ns.	86
5.21	Charge collection as a function of bias voltage for 100 μm and 150 μm thick sensors before and after irradiation to fluences of 5 \cdot 10 ¹⁵ n _{eq} cm ⁻² and 10 ¹⁶ n _{eq} cm ⁻² . The charge is normalised to the value obtained at the highest voltage point for the curve of each integration time.	87
5.22	Comparison of collected charge as a function of bias voltage obtained by Edge-TCT, source scan and beam test measurements for a 100 μm thick device after an irradiation to a fluence of 10 ¹⁶ n _{eq} cm ⁻² . The results for each curve are normalised to the value obtained at the highest bias voltage. The Edge-TCT measurements are performed at sensor level before interconnection to readout chips, whereas the source scan and beam test measurements are performed after the sensors are interconnected to readout chips. Within their statistical uncertainties, the results are all in good agreement.	88
5.23	Collected charge as a function of sensor depth along the center of the pixel cell for 100 μm and 150 μm thick sensors (a, b) before and after irradiation to fluences of (c, d) 5 \cdot 10 ¹⁵ n _{eq} cm ⁻² and (e, f) 10 ¹⁶ n _{eq} cm ⁻² . The voltage before irradiation ranges from 0 V to 120 V and reaches 700 V after irradiation.	89

5.24	Comparison of the collected charge of 100 μm thick sensors from two different sensors producers, HLL and CiS. The collected charge of the CiS4 sensor is illustrated in red, while the SOI3 sensor is shown in black. Both sensors are irradiated to a fluence of $5 \cdot 10^{15} \text{ n}_{\text{eq}} \text{ cm}^{-2}$. The charge is normalised to the collected charge at 600 V. All results are obtained by Edge-TCT measurements.	90
5.25	Example of a two-dimensional representation of a charge collection measurement with the Edge-TCT method for one single pixel cell in a 150 μm thick sensor irradiated to a fluence of $5 \cdot 10^{15} \text{ n}_{\text{eq}} \text{ cm}^{-2}$ and operated at 100 V. The y-axis represent the sensor depth, while the x-axis represents the long pixel side. The sensor front side is at $y \approx 30 \mu\text{m}$. It serves for a direct comparison of a two-dimensional charge profile with (a) all charge and (b) only positive charge.	91
5.26	Two-dimensional representation of a charge collection measurement with the Edge-TCT method for one single pixel cell in a 150 μm thick sensor irradiated to a fluence of $5 \cdot 10^{15} \text{ n}_{\text{eq}} \text{ cm}^{-2}$. The increase of the depleted region is clearly visible for an increase of voltage from (a) 100 V to (d) 780 V. The collected charge is color-coded and is high below the pixel cell (lower y) before charge saturation and constant along the sensor depth after charge saturation.	92
5.27	Comparison of two-dimensional charge collection maps of a (a) 100 μm and (b) 150 μm thick sensors, both irradiated to a fluence of $5 \cdot 10^{15} \text{ n}_{\text{eq}} \text{ cm}^{-2}$. Both sensors are biased at a voltage of 300 V for direct comparison. An area of around 85 μm of the total sensor depth of the 100 μm thick sensor is fully saturated. The saturation area in the 150 μm thick sensor shows only 85 μm of saturated region of its total thickness.	93
5.28	Comparison of two-dimensional charge collection maps for one single pixel cell in a 100 μm and 150 μm thick sensor after an irradiation to a fluence of $10^{16} \text{ n}_{\text{eq}} \text{ cm}^{-2}$. Both sensors are biased with voltages from 200 to 600 V for direct comparison. The collected charge is constant along the sensor depth at 600 V only in case of the 100 μm thick sensor.	94
5.29	Charge collection of a 150 μm CiS4 sensor with a modified pixel FE-I4 geometry subdivided into five $50 \times 50 \mu\text{m}^2$ pixel cells illustrated in a two-dimensional map: (a) shows the collected charge at a low voltage of 10 V before full charge saturation and (b) at a high voltage of 150 V after full charge saturation. The collected charge of the same Edge-TCT set at 50 V is shown in (c). During this set of Edge-TCT measurements the position of the device is changed for the different voltage steps. The X-Y range is increased to allow for a larger view on the pixel cell. Therefore, the X-Y coordinates in the maps are not in exact correspondence to each other. It does not bias or influence the measurements. The outcome of (c) is compared to the one obtained at beam test measurements with a FE-I4 module assembled with the same type of sensor (d). Different to (a)-(c), in (d) y represents the length of the pixel cell in y.	95
5.30	Velocity profile as a function of sensor depth for 100 μm and 150 μm thick sensors (a,b) before irradiation and after an irradiation to fluences of (c,d) $5 \cdot 10^{15} \text{ n}_{\text{eq}} \text{ cm}^{-2}$ and (e,f) $10^{16} \text{ n}_{\text{eq}} \text{ cm}^{-2}$. Before irradiation, the electric field of the 100 μm thick sensor appears to be flatter in the chosen range of voltages. After irradiation, the double peak effect in the electric field is visible at lower voltages before charge saturation. The values of the velocity correspond to arbitrary units. The range of the scale of the sensor depth differs for the 100 μm and 150 μm devices. In addition, both sensors irradiated to a fluences of $5 \cdot 10^{15} \text{ n}_{\text{eq}} \text{ cm}^{-2}$ were measured in different measurement campaigns and hence at slightly different positions. This explains the different values of y for sensor front and backside.	96
5.31	Hit efficiencies of CiS3 sensors of 270 μm thickness with an FE-I4 pixel cell, as well as the modified $25 \times 500 \mu\text{m}^2$ pixel cell are shown after an irradiation of the modules to a fluence of $5 \cdot 10^{15} \text{ n}_{\text{eq}} \text{ cm}^{-2}$. The obtained hit efficiencies are shown for different temperatures of -50°C and -40°C	97
5.32	(a) in-pixel hit efficiency map for a module with a 270 μm thick sensor with an FE-I4 pixel cell and single p-t design after an irradiation to a fluence of $8 \cdot 10^{15} \text{ n}_{\text{eq}} \text{ cm}^{-2}$. The measurements were performed at DESY. The in-pixel hit efficiency map is not to scale. (b) hit efficiency as a function of bias voltage after an irradiation to fluences of $3 \cdot 10^{15} \text{ n}_{\text{eq}} \text{ cm}^{-2}$, $5 \cdot 10^{15} \text{ n}_{\text{eq}} \text{ cm}^{-2}$ and $8 \cdot 10^{15} \text{ n}_{\text{eq}} \text{ cm}^{-2}$. The results of the two lower irradiation steps are adapted from Ref. [37].	98

5.33	(a) in-pixel hit efficiency map for a module with a 270 μm thick sensor with a modified pixel cell and external p-t design after an irradiation to a fluence of $8 \cdot 10^{15} \text{ n}_{\text{eq}} \text{ cm}^{-2}$. The measurements were performed at DESY. The in-pixel hit efficiency map is not to scale. Note the pixel cell size of $25 \times 500 \mu\text{m}^2$. (b) hit efficiency as a function of bias voltage after an irradiation to fluences of $3 \cdot 10^{15} \text{ n}_{\text{eq}} \text{ cm}^{-2}$, $5 \cdot 10^{15} \text{ n}_{\text{eq}} \text{ cm}^{-2}$ and $8 \cdot 10^{15} \text{ n}_{\text{eq}} \text{ cm}^{-2}$	99
5.34	Estimated hit efficiency of a $25 \times 100 \mu\text{m}^2$ pixel cell irradiated to a fluence of $3 \cdot 10^{15} \text{ n}_{\text{eq}} \text{ cm}^{-2}$ and compared to the hit efficiency of the larger $25 \times 500 \mu\text{m}^2$ pixel cell. Efficiencies at the edges are also shown separately.	100
5.35	Hit efficiency of a CiS4 module with a 150 μm thick sensor irradiated to a fluence of $10^{16} \text{ n}_{\text{eq}} \text{ cm}^{-2}$ and tested at CERN compared to (a) a VTT module with a 100 μm thick sensor irradiated to the same fluence, but at the Jožef Stefan Institute and tested at DESY. In (b) the CiS4 module is compared to an SOI2 module with a 150 μm thick sensor irradiated to a fluence of $5 \cdot 10^{15} \text{ n}_{\text{eq}} \text{ cm}^{-2}$ at LANSCE in New Mexico [144] and tested at a beam test at CERN. The results from this module are taken from Ref. [37]. Where not visible, the uncertainties are smaller than the marker size.	101
5.36	Hit efficiency in an 8-pixel map of a CiS4 module with a 150 μm thick sensor irradiated to a fluence of $10^{16} \text{ n}_{\text{eq}} \text{ cm}^{-2}$ and biased at 900 V. The inefficiencies due to the p-t structure are visible as the two larger regions with the blue center. A sketch with four pixel implants sharing a bias dot is overlaid. The sensor employs a pixel cell size of $50 \times 250 \mu\text{m}^2$	103
5.37	In-pixel hit efficiency map of a 150 μm thick sensor irradiated at $10^{16} \text{ n}_{\text{eq}} \text{ cm}^{-2}$ placed (a) perpendicular to the beam and (b) at an angle of 45° . The efficiencies obtained at a bias voltage of 900 V are (a) $97.0 \pm 0.3\%$ and (b) $98.7 \pm 0.3\%$	103
5.38	In-pixel hit efficiency map for (a) ((c)) a 150 μm thin sensor (100 μm thin sensor) at 60 V for all efficiencies and (b) ((d)) for efficiencies within a scale of 94-100%, all before irradiation. In (a) the design is overlaid. The module with the 150 μm thick sensor reaches a hit efficiency of $97.6 \pm 0.3\%$ and the one with the 100 μm thick sensor $97.8 \pm 0.3\%$	104
5.39	Hit efficiencies as a function of voltage of a 100 μm thick sensor after an irradiation to a fluence of $5 \cdot 10^{15} \text{ n}_{\text{eq}} \text{ cm}^{-2}$. (a) the hit efficiency of a $50 \times 250 \mu\text{m}^2$ pixel cell for different voltages obtained with the line and wave design, averaged over the five implants read out by the same channel, (b) hit efficiency of the $50 \times 250 \mu\text{m}^2$ pixel cell of the line design and the last $50 \times 50 \mu\text{m}^2$ pixel implant in the wave design, situated opposite to the bias dot. If not visible, the uncertainties are smaller than the marker size.	105
5.40	Hit efficiencies as a function of voltage of a 150 μm thick sensor after an irradiation to a fluence of $3 \cdot 10^{15} \text{ n}_{\text{eq}} \text{ cm}^{-2}$. (a) the hit efficiency of a $50 \times 250 \mu\text{m}^2$ pixel cell in the line and wave design is compared to $50 \times 50 \mu\text{m}^2$ pixel cell in the wave design in the hit efficiency range 90-100%. (b) hit efficiencies of $50 \times 50 \mu\text{m}^2$ pixel implant in modules with 100 μm and 150 μm thick sensors at different irradiation levels are compared and are shown in the hit efficiency range 0-100%. If not visible, the uncertainties are smaller than the marker size.	106
5.41	In-pixel hit efficiency map for a 150 μm thick sensor (top) at (a) 300 V and (b) 500 V irradiated to a fluence of $3 \cdot 10^{15} \text{ n}_{\text{eq}} \text{ cm}^{-2}$ and a 100 μm thick sensor (bottom) at (a) 500 V and (b) 600 V irradiated to a fluence of $5 \cdot 10^{15} \text{ n}_{\text{eq}} \text{ cm}^{-2}$. In (a) the scale is zoomed to enhance the efficiency loss of 5% to 15% in between the pixel cells. In (b) the design is overlaid and the efficiency of the edge implant is calculated for the closest approximation of the geometry of a RD53A $50 \times 50 \mu\text{m}^2$ pixel cell without p-t structure.	107
5.42	In-pixel hit efficiency maps of a $50 \times 250 \mu\text{m}^2$ pixel cell in the line (a,c,e) and wave design (b,d,f) at a bias voltage of 300 V, 400 V and 600 V after an irradiation to a fluence of $5 \cdot 10^{15} \text{ n}_{\text{eq}} \text{ cm}^{-2}$. The module is assembled with a sensor with a thickness of 100 μm	108
5.43	In-pixel hit efficiency maps of the outer $50 \times 50 \mu\text{m}^2$ pixel implant of the wave design, chosen to be the closest approximation to the RD53A compatible pixel cell design without punch-through structure, at different voltages ranging from 300 V to 600 V. The scale of the hit efficiency ranges from 0 to 1 for all maps to allow for a direct comparison of the hit efficiency distribution within the pixel cell. The module, assembled with a 100 μm thick sensor, is irradiated to a fluence of $5 \cdot 10^{15} \text{ n}_{\text{eq}} \text{ cm}^{-2}$	109

5.44	Comparison of in-pixel hit efficiency map with 8 pixels of SOI3 modules with sensor thicknesses of 150 μm . The module is assembled with a sensor with the grounded BR, the standard implementation, and is displayed in (a), the module with the modified sensor with a floating BR is shown in (b). Both modules are operated at full saturation at a voltage of 60 V and were measured at a beam test at DESY.	111
5.45	Comparison of in-pixel hit efficiency map with 8 pixels of SOI3 modules with sensor thicknesses of 100 μm . The module assembled with a sensor with the grounded BR, the standard implementation, is displayed in (a), the module with the modified sensor with a floating BR is shown in (b). Both modules are operated at full saturation at a voltage of 60 V and were measured at a beam test at DESY.	111
5.46	Comparison of the in-pixel hit efficiency maps of SOI3 modules with 150 μm thick sensors after an irradiation to $2 \cdot 10^{15} \text{ n}_{\text{eq}} \text{ cm}^{-2}$ at 500 V: (a) with an implementation of a grounded BR and (b) with a floating BR. The modules were measured at a beam test at CERN.	112
5.47	Comparison of the hit efficiency of SOI3 modules with 150 μm thick sensors after an irradiation to $2 \cdot 10^{15} \text{ n}_{\text{eq}} \text{ cm}^{-2}$ in a voltage range up to 600 V with an implementation of a floating BR and with a standard BR. The uncertainties are included but smaller than the marker size.	112
5.48	Comparison of the hit efficiency of SOI3 and CiS4 modules with 100 μm thick sensors after an irradiation to a fluence of $5 \cdot 10^{15} \text{ n}_{\text{eq}} \text{ cm}^{-2}$ at 400 V. (a) SOI3 module with an implementation of a grounded bias rail, (b) with a floating bias rail and (c) CiS4 module with a grounded and straight bias rail. The modules were measured at a beam test at CERN. If not visible, the uncertainties are smaller than the marker size.	113
5.49	Comparison of the hit efficiency as a function of bias voltage of modules from the SOI3 and CiS4 production after an irradiation to a fluence of $5 \cdot 10^{15} \text{ n}_{\text{eq}} \text{ cm}^{-2}$. The SOI3 module with a grounded bias rail is represented in black, the one with a floating bias rail in red, while the CiS4 module with a grounded and straight bias rail is depicted in blue. The range of the y scale is from 90% to 100% to enhance the difference in hit efficiencies between the three devices.	114
5.50	Hit efficiency at the sensor edge of the 100 μm thin sensor (a) with 50 μm active edge and (b) 100 μm slim edge design before irradiation. The pixel cell has an FE-I4 cell size of $50 \times 250 \mu\text{m}^2$ and the hit efficiency is evaluated as a function of the distance from the last pixel column to the edge region. Smearing of the position of approximately 18 μm is due to the telescope resolution.	115
5.51	Hit efficiency at the edge of the sensor with (a) the active and slim edge design in a 150 μm thick sensor before irradiation and (b) with 50 μm , 100 μm and 150 μm thickness, employing a 50 μm active edge design before irradiation. The hit efficiency at the edge of a 50 μm thick sensor is measured with high (800 e) and low (380 e) threshold. Smearing of the position of approximately 5 μm is due to the telescope resolution at the CERN-SpS.	116
5.52	Hit efficiency at the edge of a 150 μm thick sensor employing a 50 μm active edge design after an irradiation to fluences of (a) $10^{15} \text{ n}_{\text{eq}} \text{ cm}^{-2}$ (measured at CERN) and (b) $3 \cdot 10^{15} \text{ n}_{\text{eq}} \text{ cm}^{-2}$ (measured at DESY). The hit efficiency obtained at voltages from 100 V to 250 V, and 270 V for the case of irradiation to the higher fluence of $3 \cdot 10^{15} \text{ n}_{\text{eq}} \text{ cm}^{-2}$, are summarised. A lower resolution at DESY and lower statistics result in larger bin sizes in (b).	117
5.53	Hit efficiency at the edge of two 100 μm thick sensors after an irradiation to a fluence of $3 \cdot 10^{15} \text{ n}_{\text{eq}} \text{ cm}^{-2}$, with (a) a 50 μm active edge design and with (b) a 100 μm slim edge design. The hit efficiency are shown at voltages of (a) 100 V and 150 V, and (b) 150 V and 200 V for the case of the module with the slim edge design. Due to low breakdown voltages, a saturation of the hit efficiency was not achieved.	117
5.54	In pixel efficiency maps of a $50 \times 250 \mu\text{m}^2$ pixel cell inside an active edge module without p-t structure (a) assembled with a 150 μm thick sensor and (b) assembled with a 50 μm thick sensor. Both modules are irradiated to a fluence of $10^{15} \text{ n}_{\text{eq}} \text{ cm}^{-2}$ and are biased at (a) 250 V and (b) 120 V after irradiation.	118
5.55	Hit efficiency at the edge of a 50 μm thick sensor, assembled with a 50 μm active edge design after an irradiation to fluences of $10^{15} \text{ n}_{\text{eq}} \text{ cm}^{-2}$, measured at CERN. The results on the hit efficiencies at voltages from 50 V to 120 V are taken from Ref. [146] and summarised. Due to low statistics, the uncertainties on the hit efficiency are larger.	118

5.56	(a) expected mean cluster width along the short pixel cell direction ($50 \mu\text{m}$) in y direction for an FE-I4 module as a function of beam incidence angle. (b) charge collection in units of Time over Threshold (ToT), as a function of pixel number for different cluster widths obtained with unirradiated FE-I4 modules assembled with sensor thicknesses of $50 \mu\text{m}$, $100 \mu\text{m}$, $150 \mu\text{m}$ and $200 \mu\text{m}$. The statistical uncertainties of the points are smaller than the marker size. (c) exemplary sketch of a particle traversing the sensor with a high incidence angle. The definitions of the properties used in the analysis are illustrated.	120
5.57	Hit efficiency as a function of pixel number at different target thresholds of 600 e, 800 e and 1 ke for an unirradiated FE-I4 module with a sensor thickness of $150 \mu\text{m}$ tilted by 80° with respect to the beam direction. The efficiencies of the first and the last pixels are by construction 100%, since they define the start and the end of the cluster. The uncertainties on the hit efficiency values are included but smaller than the marker size.	122
5.58	Hit efficiencies of (a) a CiS module with a $200 \mu\text{m}$ thick sensor after an irradiation to $2 \cdot 10^{15} \text{ n}_{\text{eq}} \text{ cm}^{-2}$ and (b) an ADVACAM module with a $150 \mu\text{m}$ thick sensor after an irradiation to $10^{15} \text{ n}_{\text{eq}} \text{ cm}^{-2}$ for different high incidence angles. In (b) the hit efficiency scale is zoomed and ranges from 60% to 100%. Both modules are presented at different voltage steps. Low pixel numbers correspond to the sensor front side in both cases. The uncertainties on the hit efficiency values are included but smaller than the marker size.	122
5.59	Power dissipation as a function of voltage of a $100 \mu\text{m}$ thick sensor irradiated to a fluence of $10^{16} \text{ n}_{\text{eq}} \text{ cm}^{-2}$. The range of operational bias voltage is marked in red.	123

LIST OF TABLES

1.1	High Luminosity LHC parameters with the nominal values of the LHC and the ones planned for HL-LHC [8]. Both configurations are shown for a bunch-spacing time of 25 ns.	11
2.1	Example of a process flow for the production of n ⁺ -in-p silicon pixel sensors.	25
4.1	Parameters of the radioactive sources, ²⁴¹ Am and ¹⁰⁹ Cd, for ToT to charge calibration measurements. The charge released in silicon is given for the most significant line in the energy spectrum of the two radionuclides [102].	55
5.1	Summary of the single chip modules from the CiS3, CiS4, SOI3, ADVACAM and VTT productions relevant for this thesis. The different sensor characteristics are included in this overview. Values that do not change with row are only listed at first occurrence in this and all following tables.	73
5.2	Overview of the irradiated single chip modules of the CiS production. All sensors have a standard edge distance of $d_e = 450 \mu\text{m}$. Both modules with $50 \times 50 \mu\text{m}^2$ pixel cells have an FE-I4 $50 \times 250 \mu\text{m}^2$ pixel cell geometry and are compatible to the FE-I4 chip, such as the rest of the modules in the table.	74
5.3	Overview of the irradiated single chip modules from the HLL/MPP SOI3 production. All sensors have an FE-I4 pixel cell of $50 \times 250 \mu\text{m}^2$ and an external p-t design with a modified bias rail running as much as possible on top of the pixel implants.	74
5.4	Overview of the irradiated single chip modules with active edges from the ADVACAM production. The module from the VTT production is included at the bottom of this table.	75
5.5	Summary of the hit efficiency results of CiS3 modules with $270 \mu\text{m}$ thick sensors employing $50 \times 250 \mu\text{m}^2$ and $25 \times 500 \mu\text{m}^2$ pixel cells. The hit efficiencies are shown for the irradiation fluences of $3 \cdot 10^{15} \text{ n}_{\text{eq}} \text{ cm}^{-2}$ at bias voltages steps of 500 V, 800 V and 900 V.	99
5.6	Summary of the hit efficiency results of a VTT module with $100 \mu\text{m}$ thick sensor and a CiS4 module with a $150 \mu\text{m}$ thick sensor after an irradiation to $10^{16} \text{ n}_{\text{eq}} \text{ cm}^{-2}$. The hit efficiency results of the CiS4 module with a $150 \mu\text{m}$ thick sensor are further compared to a module with the same sensor thickness irradiated to a fluence of $5 \cdot 10^{15} \text{ n}_{\text{eq}} \text{ cm}^{-2}$. The results are shown for the voltage steps of 500 V, 700 V and 900 V.	102
5.7	Summary of the hit efficiency results of CiS4 modules with $100 \mu\text{m}$ and $150 \mu\text{m}$ thick sensors after an irradiation to $3 \cdot 10^{15} \text{ n}_{\text{eq}} \text{ cm}^{-2}$ and $5 \cdot 10^{15} \text{ n}_{\text{eq}} \text{ cm}^{-2}$. The results are summarised for the single $50 \times 50 \mu\text{m}^2$ pixel cell at the highest voltage steps of 500 V and 600 V.	110
5.8	Summary of the hit efficiency results of SOI3 modules with $100 \mu\text{m}$ and $150 \mu\text{m}$ thick sensors after an irradiation to $2 \cdot 10^{15} \text{ n}_{\text{eq}} \text{ cm}^{-2}$ and $5 \cdot 10^{15} \text{ n}_{\text{eq}} \text{ cm}^{-2}$. The results are summarised for the sensor with a floating and grounded BR at the highest voltage steps of 500 V and 600 V.	114
5.9	Summary of the hit efficiency results of ADVACAM modules with $50 \mu\text{m}$, $100 \mu\text{m}$ and $150 \mu\text{m}$ thick active edge sensors before and after irradiations up to $3 \cdot 10^{15} \text{ n}_{\text{eq}} \text{ cm}^{-2}$. The results on the in-pixel efficiency over the entire module and the edge efficiency are summarised after hit efficiency saturation.	119
5.10	Power dissipation density of $100 \mu\text{m}$ and $150 \mu\text{m}$ thick sensors after irradiation to a fluence of $10^{16} \text{ n}_{\text{eq}} \text{ cm}^{-2}$, given for the expected operational bias voltages at $T = -25^\circ\text{C}$	124

BIBLIOGRAPHY

- [1] L. Evans and P. Bryant (editors), *LHC Machine*, JINST **3** (2008) S08001.
- [2] ATLAS, Collaboration, *Letter of Intent for the Phase-II Upgrade of the ATLAS Experiment*, CERN-LHCC-2012-022, Dec, 2012, <http://cds.cern.ch/record/1502664>.
- [3] ALICE Collaboration, *Upgrade of the ALICE Experiment: Letter of Intent*, CERN-LHCC-2012-012, Aug, 2012, <https://cds.cern.ch/record/1475243>.
- [4] CMS Collaboration, *The CMS experiment at the CERN LHC*, JINST **3** (2008) S08004.
- [5] LHCb Collaboration, *LHCb VELO Upgrade Technical Design Report*, CERN-LHCC-2013-021. LHCb-TDR-013, Nov, 2013, <https://cds.cern.ch/record/1624070>.
- [6] H. Haberland and G. Kane, *The search for supersymmetry: probing physics beyond the standard model*, Physics Reports **117** (1985) 2-4 75–263.
- [7] C. Lefevre, *The CERN accelerator complex*, CERN-DI-0812015, Dec, 2008, <https://cds.cern.ch/record/1260465>.
- [8] G. Apollinari et al., *High-Luminosity Large Hadron Collider (HL-LHC): Technical Design Report V. 0.1*. CERN Yellow Reports: Monographs. 2017. <https://cds.cern.ch/record/2284929>.
- [9] ATLAS Collaboration, *ATLAS public results*, 2017, <https://twiki.cern.ch/twiki/bin/view/AtlasPublic/LuminosityPublicResultsRun2>.
- [10] G. Aad et al., *ATLAS pixel detector electronics and sensors*, JINST **3** (2008) 07 P07007.
- [11] G. Aad et al., *The ATLAS Inner Detector commissioning and calibration*, The European Physical Journal C **70** (2010) 3 787–821.
- [12] Y. Unno, *ATLAS silicon microstrip detector system (SCT)*, Nucl. Instr. Meth. A **511** (2003) 1 58–63.
- [13] T. Kohriki et al., *Development of the hybrid structure for the barrel module of the ATLAS silicon-microstrip tracker*, IEEE Transactions on Nuclear Science **49** (2002) 6 3278–3283.
- [14] E. Abat et al., *The ATLAS Transition Radiation Tracker (TRT) proportional drift tube: Design and performance*, JINST **3** (2008) 02 P02013.
- [15] JD Degenhardt, *ATLAS Transition Radiation Tracker (TRT) Electronics Operation Experience at High Rates*, ATL-INDET-SLIDE-2012-515, Sep, 2012, <https://cds.cern.ch/record/1477744>.
- [16] J. Pequeno, *Computer generated image of the whole ATLAS detector*, CERN-GE-0803012, Mar, 2008, <https://cds.cern.ch/record/1095924>.
- [17] ATLAS Collaboration, *ATLAS liquid-argon calorimeter: Technical Design Report*. Technical Design Report ATLAS. CERN/LHCC, 1996. <https://cds.cern.ch/record/331061>.
- [18] ATLAS Collaboration, *Calorimeter performance technical design report*. Technical Design Report ATLAS. 1996. <https://cds.cern.ch/record/331061>.
- [19] C. Bini, *Study of the performance of the ATLAS Muon Spectrometer*, Nuclear Science Symposium and Medical Imaging Conference (NSS/MIC) (2011) 1265–1268.

- [20] C. Gabaldon, *Performance of the atlas trigger system*, JINST **7** (2012) 01 C01092.
- [21] G. Apollinari et al., *High-Luminosity Large Hadron Collider (HL-LHC): Preliminary Design Report*. CERN Yellow Reports: Monographs. 2015. <https://cds.cern.ch/record/2116337>.
- [22] ATLAS Collaboration, *Observation of a new particle in the search for the Standard Model Higgs boson with the ATLAS detector at the LHC*, Phys. Lett. B **716** (2012) 1.
- [23] S. Glashow, *Partial-symmetries of weak interactions*, Nuclear Physics **22** (1961) 4 579–588.
- [24] D. Groom et al., *Review of particle physics. Particle data group*, European Physical Journal C **15** (2000) 1-4 1–878.
- [25] L. Arnaudon et al., *Linac4 technical design report*, CERN-AB-2006-084, Dec, 2006, <https://cds.cern.ch/record/1004186>.
- [26] P. Vankov, *ATLAS Upgrade for the HL-LHC: meeting the challenges of a five-fold increase in collision rate*, EPJ Web of Conferences **28** (2012) 12069.
- [27] G. Aad et al., *Technical design report for the phase-I upgrade of the ATLAS TDAQ system*, CERN-LHCC-2013-018, Sep, 2013, <https://cds.cern.ch/record/1602235>.
- [28] A. Loginov, *ATLAS upgrade: meeting the challenges of the sLHC*, ATL-COM-UPGRADE-2011-002, Jan, 2011, <https://cds.cern.ch/record/1321570>.
- [29] ATLAS Collaboration, *Technical Design Report for the ATLAS Inner Tracker Strip Detector*, CERN-LHCC-2017-005, Apr, 2017, <https://cds.cern.ch/record/2257755>.
- [30] L. Rossi et al., *Pixel detectors: From fundamentals to applications*. Springer Science & Business Media, 2006.
- [31] S. Sze and K. Ng, *Physics of semiconductor devices*. John wiley & sons, 2006.
- [32] G. Lutz et al., *Semiconductor radiation detectors*, vol. 40. Springer, 1999.
- [33] S. Spannagel, *Test Beam Measurements for the Upgrade of the CMS Pixel Detector and Measurement of the Top Quark Mass from Differential Cross Sections*. PhD thesis, PhD thesis, DESY, 2016. <http://cms.desy.de/e128524/e269717/PhDThesisSimonSpannagel.pdf>.
- [34] T. Wittig, *Slim edge studies, design and quality control of planar ATLAS IBL pixel sensors*. PhD thesis, Universitätsbibliothek Dortmund, 2013. <https://eldorado.tu-dortmund.de/bitstream/2003/30362/1/Dissertation.pdf>.
- [35] K. Roy et al., *Leakage current mechanisms and leakage reduction techniques in deep-submicrometer CMOS circuits*, Proceedings of the IEEE **91** (2003) 2 305–327.
- [36] D. Groom and SR Klein, *Passage of particles through matter*, The European Physical Journal C **15** (2000) 1-4 163–173.
- [37] S. Terzo, *Development of radiation hard pixel modules employing planar n-in-p planar silicon sensors with active edges for the ATLAS detector at HL-LHC*. PhD thesis, Technische Universität München, 2015. <https://publications.mppmu.mpg.de/2015/MPP-2015-291/FullText.pdf>.
- [38] L. Davidovich Landau, *On the energy loss of fast particles by ionization*, J. Phys. **8** (1944) 201–205.
- [39] PV Vavilov, *Ionization losses of high-energy heavy particles*, Soviet Phys. JETP **5** (1957) .
- [40] C. Canali et al., *Electron and hole drift velocity measurements in silicon and their empirical relation to electric field and temperature*, IEEE Transactions on Electron Devices **22** (1975) 11 1045–1047.
- [41] C. Jacoboni et al., *A review of some charge transport properties of silicon*, Solid-State Electronics **20** (1977) 2 77–89.
- [42] W. Shockley, *Currents to conductors induced by a moving point charge*, Journal of applied physics **9** (1938) 10 635–636.
- [43] S. Ramo, *Currents induced by electron motion*, Proceedings of the IRE **27** (1939) 9 584–585.

- [44] G. Kramberger et al., *Electric field modeling in heavily irradiated silicon detectors based on Edge-TCT measurements*, Proceedings of Science, Vertex **2012** (2013) .
- [45] G. Kramberger et al., *Investigation of irradiated silicon detectors by edge-TCT*, IEEE transactions on Nuclear Science **57** (2010) 4 2294–2302.
- [46] G. Kramberger, *Signal development in irradiated silicon detectors*. PhD thesis, Jozef Stefan Inst., Ljubljana, 2001. <http://cds.cern.ch/record/1390490>.
- [47] R. Wunstorf, *Systematische Untersuchungen zur Strahlenresistenz von Silizium-Detektoren für die Verwendung in Hochenergiephysik-Experimenten*. PhD thesis, Universität Hamburg, see also DESY FHIK-92-01, 1992. <https://cds.cern.ch/record/243081>.
- [48] JR Srour et al., *Review of displacement damage effects in silicon devices*, IEEE Transactions on Nuclear Science **50** (2003) 3 653–670.
- [49] A. Van Ginneken, *Nonionizing energy deposition in silicon for radiation damage studies*, FERMILAB-FN-522, 1989, <http://cds.cern.ch/record/203592>.
- [50] H. Pernegger, *High mobility diamonds and particle detectors*, physica status solidi (a) **203** (2006) 13 3299–3314.
- [51] M. Moll, *Radiation damage in silicon particle detectors: Microscopic defects and macroscopic properties*. PhD thesis, Hamburg U., 1999. <http://www-library.desy.de/cgi-bin/showprep.pl?desy-thesis99-040>.
- [52] J. Kemmer, *Improvement of detector fabrication by the planar process*, Nucl. Instr. Meth. A **226** (1984) 1 89–93.
- [53] P. Weigell, *Investigation of Properties of Novel Silicon Pixel Assemblies Employing Thin n-in-p Sensors and 3D-Integration*. PhD thesis, Technische Universität München, 2013. <https://publications.mppmu.mpg.de/2013/MPP-2013-5/FullText.pdf>.
- [54] F. Hüggling, *Der ATLAS Pixelsensor: Der state-of-the art Pixelsensor für teilchenphysikalische Anwendungen mit extrem hohen Strahlungsfeldern*. PhD thesis, Technische Universität Dortmund, 2001. <http://cds.cern.ch/record/529691>.
- [55] ATLAS IBL Collaboration, *ATLAS Pixel IBL: Stave Quality Assurance*, . <https://cds.cern.ch/record/1754509>.
- [56] S. Parker et al., *3D: A proposed new architecture for solid-state radiation detectors*, Nucl. Instr. Meth. A **395** (1997) 3 328–343.
- [57] C. Da Via et al., *3D silicon sensors: Design, large area production and quality assurance for the ATLAS IBL pixel detector upgrade*, Nucl. Instr. Meth. A **694** (2012) 321–330.
- [58] M. Capeans et al., *ATLAS Insertable B-Layer Technical Design Report*, CERN-LHCC-2010-013, Sep, 2010, <https://cds.cern.ch/record/1291633>.
- [59] M. Backhaus et al., *The upgraded Pixel Detector of the ATLAS Experiment for Run 2 at the Large Hadron Collider*, Nucl. Instr. Meth. A **831** (2016) 65–70.
- [60] I. Peric et al., *The FEI3 readout chip for the ATLAS pixel detector*, Nucl. Instr. Meth. A **565** (2006) 1 178–187.
- [61] A. Macchiolo et al., *Thin n-in-p pixel sensors and the SLID-ICV vertical integration technology for the ATLAS upgrade at the HL-LHC*, Nucl. Instr. Meth. A **731** (2013) 210–215.
- [62] W. Fernando, *Overview and status of ATLAS pixel detector*, Nucl. Instr. Meth. A **596** (2008) 1 58–62.
- [63] M. Garcia-Sciveres et al., *The FE-I4 pixel readout integrated circuit*, Nucl. Instr. Meth. A **636** (2011) 1 S155–S159.
- [64] M. Barbero et al., *FE-I4 ATLAS pixel chip design*, PoS (2009) 027.
- [65] M. Karagounis, *Development of the ATLAS FE-I4 pixel readout IC for b-layer Upgrade and Super-LHC*, CERN-2008-008, Sep, 2008, <https://cds.cern.ch/record/1158505>.
- [66] ATLAS IBL collaboration, *Prototype ATLAS IBL modules using the FE-I4A front-end readout chip*, JINST **7** (2012) 11 P11010.

- [67] M. Beimforde, *Development of thin sensors and a novel interconnection technology for the upgrade of the atlas pixel system*. PhD thesis, Technische Universität München, 2010.
<https://publications.mppmu.mpg.de/2010/MPP-2010-115/FullText.pdf>.
- [68] G. Lindström et al., *Radiation hard silicon detectors-developments by the RD48 (ROSE) collaboration*, Nucl. Instr. Meth. A **466** (2001) 2 308–326.
- [69] J. Kemmer and G. Lutz, *New structures for position sensitive semiconductor detectors*, Nucl. Instr. Meth. A **273** (1988) 2-3 588–598.
- [70] Lärmer, F and Schilp, A, *Verfahren zum anisotropen Ätzen von Silicium*, Deutsches Patent DE **42** (1994) 41 045.
- [71] G. Pellegrini et al., *First double-sided 3-D detectors fabricated at CNM-IMB*, Nucl. Instr. Meth. A **592** (2008) 1 38–43.
- [72] E. Vianello et al., *Optimization of double-side 3D detector technology for first productions at FBK*, Nuclear Science Symposium and Medical Imaging Conference (NSS/MIC) (2011) 523–528.
- [73] C. Da Via et al., *3D active edge silicon sensors: Device processing, yield and QA for the ATLAS-IBL production*, Nucl. Instr. Meth. A **699** (2013) 18–21.
- [74] A. Macchiolo et al., *Development of thin pixel sensors and a novel interconnection technology for the SLHC*, Nucl. Instr. Meth. A **591** (2008) 1 229–232.
- [75] M. Garcia-Sciveres et al., *The RD53A Integrated Circuit*, CERN-RD53-PUB-17-001, Oct, 2017,
<https://cds.cern.ch/record/2287593>.
- [76] RD-53 Collaboration. <http://rd53.web.cern.ch/RD53/>.
- [77] N. Demaria et al., *Recent progress of RD53 Collaboration towards next generation Pixel Read-Out Chip for HL-LHC*, JINST **11** (2016) 12 C12058.
- [78] J. Lange et al., *3D silicon pixel detectors for the High-Luminosity LHC*, JINST **11** (2016) 11 C11024.
- [79] N. Wermes and ATLAS CMOS Collaboration, *Depleted CMOS pixels for LHC proton–proton experiments*, Nucl. Instr. Meth. A **824** (2016) 483–486.
- [80] L. Snoj et al., *Computational analysis of irradiation facilities at the JSI TRIGA reactor*, International Journal of Radiation Applications and Instrumentation. Part A **10** (2012) 03 483–488.
- [81] L. Snoj et al., *Computational analysis of irradiation facilities at the JSI TRIGA reactor*, Applied Radiation and Isotopes **70** (2012) 3 483–488.
- [82] I. Mandic et al., *Bulk Damage in DMILL npn Bipolar Transistors Caused by Thermal Neutrons Versus Protons and Fast Neutrons*, IEEE Transactions on Nuclear Science **51** (2004) 1752–1758.
- [83] A. Dierlamm, *Untersuchung zur Strahlungshärte von Siliziumsensoren*. PhD thesis, 2003.
<https://ekp-invenio.physik.uni-karlsruhe.de/record/45039>.
- [84] P. Dervan et al., *Upgrade to the Birmingham Irradiation Facility*, Nucl. Instr. Meth. A **796** (2015) 80–84.
- [85] P. Allport et al., *Recent results and experience with the Birmingham and MC40 irradiation facility*, JINST **12** (2017) 03 C03075.
- [86] F. Ravotti et al., *A New High-Intensity Proton Irradiation Facility at the CERN PS East Area*, PoS (2014) 354.
- [87] B. Gkotse et al., *The Beam Profile Monitoring System for the IRRAD Proton Facility at the CERN PS East Area*, .
<https://cds.cern.ch/record/2235836>.
- [88] Particulars, *Advanced measurement systems*, <http://www.particulars.si>.
- [89] I. Mandic et al., *Edge-TCT measurements with the laser beam directed parallel to the strips*, JINST **10** (2015) 08 P08004.
- [90] kurtz ersa, *Electronics Production Equipment*, <http://www.kurtzersa.com>.
- [91] B. Hiti et al., *Charge collection properties in an irradiated pixel sensor built in a thick-film HV-SOI process*, JINST **12** (2017) P10020.

- [92] Picosecond Pulse Labs, *Model 5531 High Voltage Bias Tee Product Specification*, <http://datasheets.globalspec.com/ds/3765/PicosecondPulseLabs/>.
- [93] M. Milovanovic, *Electric Field and Charge Multiplication in Radiation-damaged Silicon Detectors*. PhD thesis, Jozef Stefan Inst., Ljubljana, 2015. <https://repozitorij.uni-lj.si/IzpisGradiva.php?id=83819>.
- [94] TCTAnalyse, *A ROOT based analysis library for TCT measurements*, <http://www.particulars.si/TCTAnalyse>.
- [95] ROOT data analysis framework. <http://root.cern.ch>.
- [96] M. Backhaus et al., *Development of a versatile and modular test system for ATLAS hybrid pixel detectors*, Nucl. Instr. Meth. A **650** (2011) 1 37–40.
- [97] V. Filimonov et al., *A serial powering pixel stave prototype for the ATLAS ITk upgrade*, JINST **12** (2017) 03 C03045.
- [98] The Reconfigurable Cluster Element. <http://www.slac.stanford.edu/exp/atlas/upgrade/RCE-distribution-2015Mar.html>.
- [99] D. Dobos, *Production accompanying testing of the ATLAS Pixel module*. PhD thesis, Technische Universität Dortmund, 2004. <http://cds.cern.ch/record/1016933>.
- [100] M. Stramaglia et al., *Calibration analysis software for the ATLAS Pixel Detector*, Nucl. Instr. Meth. A **824** (2016) 50–52.
- [101] J. Rieger, *Comparison of Thin n- and p-type Bulk Silicon Sensors*, Master thesis, Georg-August-Universität Göttingen (2012) .
- [102] L. C. of Nuclides. <https://www-nds.iaea.org/relnsd/vcharthtml/VChartHTML.html>.
- [103] *USBpix-USB based readout system for ATLAS FE-I3 and FE-I4*, <http://icwiki.physik.uni-bonn.de/twiki/bin/view/Systems/UsbPix>.
- [104] J. Große-Knetter, *Vertex measurement at a hadron collider. The ATLAS pixel detector*, Habilitation, Universität Bonn (2008) . http://www.iaea.org/inis/collection/NCLCollectionStore/_Public/39/088/39088841.pdf.
- [105] M. Backhaus, *Characterization of the FE-I4B pixel readout chip production run for the ATLAS Insertable B-layer upgrade*, JINST **8** (2013) 03 C03013.
- [106] *DESY Test Beam - Deutsches Elektron Synchrotron DESY*, testbeam.desy.de/.
- [107] T. Behnke et al., *Test beams at DESY*, EUDET-Memo-2007-11 (2007) .
- [108] I. Rubinskiy et al., *An EUDET/AIDA pixel beam telescope for detector development*, Physics Procedia **37** (2012) 923–931.
- [109] G. Troska, *Development and operation of a testbeam setup for qualification studies of ATLAS pixel sensors*. PhD thesis, Technische Universität Dortmund, 2012. <https://eldorado.tu-dortmund.de/handle/2003/29351>.
- [110] R. Turchetta, *Spatial resolution of silicon microstrip detectors*, Nucl. Instr. Meth. A **335** (1993) 1-2 44–58.
- [111] J. Weingarten et al., *Planar pixel sensors for the ATLAS upgrade: beam tests results*, JINST **7** (2012) 10 P10028.
- [112] H. Jansen et al., *Performance of the EUDET-type beam telescopes*, EPJ Techniques and Instrumentation **3** (2016) 1 7.
- [113] J. Baudot et al., *First test results of MIMOSA-26, a fast CMOS sensor with integrated zero suppression and digitized output*, Nuclear Science Symposium Conference Record (NSS/MIC) (2009) 1169–1173.
- [114] K. Olive and Particle Data Group, *Review of particle physics*, Chinese physics C **38** (2014) 9 090001.
- [115] A Generic Pixel Telescope Data Analysis Framework. <http://eutelescope.web.cern.ch>.
- [116] T. Bisanz et al., *EUTelescope 1.0: Reconstruction Software for the AIDA Testbeam Telescope*, AIDA-NOTE-2015-009, Mar, 2015, <http://cds.cern.ch/record/2000969>.

- [117] H. Perrey, *EUDAQ and EUTelescope Software Frameworks for Testbeam Data Acquisition and Analysis*, PoS Proc. Sci.,(TIPP2014) **353** (2014) .
- [118] V. Blobel, *Software alignment for tracking detectors*, Nucl. Instr. Meth. A **566** (2006) 1 5–13.
- [119] S. Fleischmann, *Track Reconstruction in the ATLAS Experiment: The deterministic annealing filter*. PhD thesis, Universität Wuppertal.
- [120] R. Kalman et al., *A new approach to linear filtering and prediction problems*, Journal of basic Engineering **82** (1960) 1 35–45.
- [121] C. Kleinwort, *General Broken Lines as advanced track fitting method*, Nucl. Instr. Meth. A **673** (2012) 107–110.
- [122] K. Sjøbæk, *Full simulation of a testbeam experiment including modeling of the Bonn ATLAS Telescope and ATLAS 3D pixel silicon sensors*. PhD thesis, University of Oslo, 2010.
<https://www.duo.uio.no/handle/10852/10980>.
- [123] M. George, *Testbeam Measurements with Pixel Sensors for the ATLAS Insertable b-Layer Project*. PhD thesis, Georg-August-Universität Göttingen, 2014.
<https://ediss.uni-goettingen.de/handle/11858/00-1735-0000-0022-5F07-A>.
- [124] RD-50 Collaboration. <http://rd50.web.cern.ch>.
- [125] AIDA-2020 project, Advanced European Infrastructure for Detectors and Accelerators.
<http://aida2020.web.cern.ch>.
- [126] ITk Pixel Group. <https://twiki.cern.ch/twiki/bin/view/Atlas/ITkPixel>.
- [127] A. Macchiolo et al., *Optimization of thin n-in-p planar pixel modules for the ATLAS upgrade at HL-LHC*, JINST **12** (2017) 01 C01024.
- [128] A. Macchiolo et al., *Development of n-in-p pixel modules for the ATLAS Upgrade at HL-LHC*, Nucl. Instr. Meth. A **A831** (2016) 111–115.
- [129] N. Savic et al., *Thin n-in-p planar pixel modules for the ATLAS upgrade at HL-LHC*, Nucl. Instr. Meth. A **A845** (2017) 154–158.
- [130] N. Savic et al., *Investigation of thin n-in-p planar pixel modules for the ATLAS upgrade*, JINST **11** (2016) 12 C12008.
- [131] N. Savic et al., *Performance of irradiated thin n-in-p planar pixel sensors for the ATLAS Inner Tracker upgrade*, JINST **12** (2017) 12 C12007.
- [132] M. Woehrmann and M. Toepper, *Polymerization of thin film polymers*, in *New Polymers for Special Applications*. InTech, 2012.
- [133] T. Wittig et al., *Large area thinned planar sensors for future high-luminosity-LHC upgrades*, JINST **11** (2016) 12 C12046.
- [134] K. Bean, *Anisotropic etching of silicon*, IEEE Transactions on Electron Devices **25** (1978) 10 1185–1193.
- [135] T. Wittig, *Ongoing activities at CiS*, 2015. <https://indico.cern.ch/event/456679/>.
- [136] L. Andricek et al., *Processing of ultra-thin silicon sensors for future e+ e- linear collider experiments*, IEEE Trans. Nucl. Sci. **51** (2004) 1117–1120.
- [137] A. Nenandic and R. W. Pasco, *Method of chemical-mechanical polishing an electronic component substrate and polishing slurry therefor*, IEEE Transactions on Electron Devices **25** (1992) 10 1185–1193.
- [138] S. Eränen et al., *3D processing on 6in. high resistive SOI wafers: Fabrication of edgeless strip and pixel detectors*, Nucl. Instr. Meth. A **607** (2009) 1 85–88.
- [139] X. Wu et al., *Recent advances in processing and characterization of edgeless detectors*, JINST **7** (2012) 02 C02001.
- [140] A. La Rosa, *Irradiation induced effects in the FE-I4 front-end chip of the ATLAS IBL detector*, Nuclear Science Symposium and Medical Imaging Conference: NSS/MIC (2016) 1–4.

- [141] J. Bronuzzi et al., *Principle and modelling of Transient Current Technique for interface traps characterization in monolithic pixel detectors obtained by CMOS-compatible wafer bonding*, JINST **11** (2016) 08 P08016.
- [142] G. Kramberger et al., *Modeling of electric field in silicon micro-strip detectors irradiated with neutrons and pions*, JINST **9** (2014) 10 P10016.
- [143] G. Kramberger and D. Contarato, *Simulation of signal in irradiated silicon pixel detectors*, Nucl. Instr. Meth. A **511** (2003) 1 82–87.
- [144] P. Lisowski et al., *The Los Alamos national laboratory spallation neutron sources*, Nuclear Science and Engineering **106** (1990) 2 208–218.
- [145] N. Alipour Tehrani, *Test-beam measurements and simulation studies of thin pixel sensors for the CLIC vertex detector*. PhD thesis, ETH Zurich, Nov, 2016. <http://cds.cern.ch/record/2270788>.
- [146] R. Taibah, *Characterization of thin planar sensors for the ATLAS pixel detector upgrade to operate at the high luminosity LHC*, Master thesis in progress, Ludwig-Maximilians-Universität München .
- [147] R. Klingenberg et al., *Power dissipation studies on planar n+-in-n pixel sensors*, Nucl. Instr. Meth. A **831** (2016) 105–110.